The Negatively Charged Tin Vacancy Centre In Diamond: A Good Quantum Bit?

Dissertation

zur Erlangung des Grades
des Doktors der Naturwissenschaften
der Naturwissenschaftlich-Technischen Fakultät
der Universität des Saarlandes

von

Johannes Görlitz

Saarbrücken

2022

Tag des Kolloquiums: 25.05.2022

Dekan: Univ.-Prof. Dr. rer. nat. Jörn Walter

Berichterstatter: Prof. Dr. Christoph Becher, Dr. Florian Kaiser

Vorsitz: Prof. Dr. Rolf Pelster

Akad. Mitarbeiter: Dr. Stephan Kucera

Abstract

The rapidly developing field of quantum information processing demands for qubit and quantum network node systems exhibiting outstanding characteristics such as exceptional spin and optical coherence. This thesis investigates the recently emerged negatively charged tin vacancy (SnV) centre in diamond as a promising candidate addressing those needs. On that account we conduct a detailed spectroscopic study revealing its single photon and zero-phonon line emission properties, the centre-phonon interactions impacting the phonon sideband and Debye-Waller factor as well as the energetic position of a higher lying excited state. Furthermore, we unveil the charge cycle of the SnV centre based upon which we realise highly efficient and rapid initialisation of the desired negative charge state. This charge control enables studying the optical and spin coherence of single centres, which we show to outperform other group IV vacancy emitters in diamond at temperatures of 1.7 K. The close to ideal optical coherence is preserved for hours, while the spin life- and dephasing times amount to $T_1 \approx 20\,\mathrm{ms}$ and $T_2^* \approx 5\,\mu\mathrm{s}$, respectively, even for large angles between magnetic field and the centre's symmetry axis. Furthermore, we demonstrate single-shot readout of spin states enabled by highly cycling spin-conserving transitions with a fidelity of $\mathcal{F} = 74\,\%$. Eventually, we explore the possibility of two-photon interference as a crucial prerequisite of remote entanglement and many quantum communication protocols.

Zusammenfassung

Das sich rapide entwickelnde Themengebiet der Quanteninformationsverarbeitung bedarf Qubit- und Quantennetzwerkknotensystemen, welche herausragende Eigenschaften wie bspw. exzeptionelle optische sowie Spinkohärenz aufweisen. Diese Arbeit untersucht das kürzlich entdeckte Zinn-Fehlstellen (SnV) Zentrum in Diamant als einen vielversprechenden Kandidaten. Dazu führen wir detaillierte spektroskopische Untersuchungen der Eigenschaften seiner Einzelphotonen- und Null-Phononen-Linienemission, des Einflusses der Zentrum-Phonon Wechselwirkungen auf phononisches Seitenband und Debye-Waller Faktor sowie der energetischen Lage eines höher liegenden angeregten Zustandes durch. Basierend auf unserem experimentell verifizierten Modell des Ladungszyklusses des SnV Zentrums initialisieren wir den negativen Ladungszustand schnell und hocheffizient. Diese Ladungskontrolle erlaubt die Untersuchung der optischen und Spinkohärenz bei einer Temperatur von 1.7 K, welche anderen Guppe IV Zentren überlegenen sind. Die nahezu perfekte optische Kohärenz ist über Stunden erhalten, während die Spinlebens- bzw. Dephasierungsdauer selbst für große Winkel zwischen Magnetfeld und Symmetrieachse des Zentrums $T_1 \approx 20\,\mathrm{ms}$ bzw. $T_2^* \approx 5\,\mu\mathrm{s}$ beträgt. Weiterhin demonstrieren wir Spinzustandsauslese mit nur einem optischen Puls und Fidelity von $\mathcal{F} = 74\,\%$. Abschließend untersuchen wir die Möglichkeit von Zwei-Photonen Interferenz, welche Grundlage für die Verschränkung entfernter Zentren sowie vielen Quantenkommunikationsprotokollen ist.

Contents

Chapter 1

Introduction

In recent years, the interest in quantum technologies, especially quantum information processing (QIP) and quantum sensing, has risen tremendously and funding of research projects increased considerably. It is an interesting question to ask about the origin of these dynamics as only few commercialised applications in these fields exist up until now. On a fundamental level it is based on the assumption that since the immensely successful classical information science is just a special limit of quantum mechanics, even greater advances are potentially achievable in the realm of quantum science. While the exploitation of the quantum advantage over classical science, called "Quantum supremacy", is challenging, it has recently been demonstrated by using Google's Scyamore processor in a proof-of-principle experiment [1]. The fact that global players of major importance such as Google and IBM are investing heavily in QIP research is a real-world argument convincing governments of the importance of nurturing quantum technologies in their respective countries. In particular, a prominent initiative to propel European researchers to the forefront of quantum science is the "Quantum Flagship" [2, 3], providing one billion euro over the duration of ten years to achieve its proposed goals. Within this initiative, quantum technologies are divided into four foundational pillars, namely **Quantum Sensing and Metrology**, **Quantum Simulation**, **Quantum Computation** and **Quantum Communication**, all of which are supported by advances in basic and enabling science research. The progress in Quantum Sensing and Metrology in the recent past has pushed this field to the intermediate state where technology achievements in fields such as optical and lattice clocks [4] or magnetic field sensing and imaging based on solid state colour centres [5–7] are being commercialised [8, 9], while the ultimate performance of these devices may still be significantly enhanced by further research efforts. Nevertheless, this branch of quantum technologies is on the verge of crossing the border from basic research to industrialisation. In comparison, Quantum Simulation has not reached this point quite yet. Its main focus is the exploitation of a well controlled quantum system in order to simulate a different quantum system on which it is challenging to impose a significant degree of control. The need for such a quantum simulator arises from the fact that the modelling of a quantum manybody system on a classical computer requires not only computer memory exponentially growing with the system's size but capturing e.g. the temporal evolution demands for a variety of operations that also scale exponentially with the system dimensions [10]. The latter is called the "exponential explosion", which can be avoided when exploring the resources of a quantum simulator, with the idea having been brought forward by Feynman in 1982 [11]. Intuitively, a quantum simulator is associated with a quantum computer, i.e. a device consisting of a multitude of quantum particles replacing the classical bits, so called qubits. While it is true that an ideal quantum computer would be also feasible of

simulating other quantum systems, it is however not necessary to utilise such a powerful device which will not be realistically achievable in the near future. Instead it suffices to rely on a quantum manybody state suitable to simulate a fixed rather than a universal set of Hamiltonians allowing for the mimicking of the dynamics of specific different quantum systems. Great advances have been made in the recent past by realising a quantum simulator with more than 51 Rydberg atoms [12] or 53 trapped ions [13], both of which provided new insights in phase transitions. Furthermore, quantum simulations have been performed in optical lattices filled with fermionic atoms [14–16]. These advancements in the field open up pathways for the simulation of exotic materials, understanding the dynamics of chemical reactions, and even in validation of String theory predictions [17, 18]. While quantum simulation will be of major importance in the future, there are nevertheless tasks requiring a quantum computer, the realisation of which is the aim of the Quantum Computation pillar. As mentioned before, a quantum computer's computational resources are quantum rather than classical bits. As the computation on classical bits relies on the digital values 0 and 1, that is, different voltage levels, a quantum bit covers a much larger computational space spanned by the basis states labeled $|0\rangle$ and $|1\rangle$ in analogy to its classical counterpart. However, these basis states span a two-dimensional vector space, called Hilbert-space, since superposition states of the form $\alpha\,|0\rangle + \beta\,|1\rangle$ can be realised with α and β being complex valued. As a convention, such a state is normalised by the restriction that $\alpha^2 + \beta^2 = 1$. The probability to find the quantum bit in state $|0\rangle$ ($|1\rangle$) is then given by α^2 (β^2). It has to be emphasised that this probability has no classical interpretation, but its meaning is that the qubit is in both states at the same time with the given probabilities and it will be determined only upon measuring whether it remained in $|0\rangle$ or $|1\rangle$. This is called the projective nature of the quantum mechanical measurement process [19]. In a quantum computer it is mandatory that each qubit can be prepared reliably in any possible superposition state at any time. Additionally, there is also the need for an interaction of several qubits with each other. Let's assume that there are two qubits and both of them are prepared in the equally weighed state $\frac{1}{\sqrt{2}}(|0\rangle + |1\rangle)$. The whole system can be intuitively described by the product state $\frac{1}{2}(|00\rangle + |01\rangle + |10\rangle + |11\rangle)$. However, in quantum mechanics it is even possible, and for many quantum algorithms necessary, that the states of the qubits are dependent on each other, a phenomenon which is called entanglement [20]. This means that the overall state, as opposed to the previous one, cannot be factorised in a product of the two single qubit states, e.g. $\frac{1}{\sqrt{2}}(|00\rangle + |11\rangle)$. The measurement of the state of one qubit will therefore instantaneously determine the other one's, meaning when measuring qubit one in state $|0\rangle$, qubit two will be found in the same state and vice versa. The physical realisation of qubits is manifold [21, 22] and has been demonstrated for instance in trapped single atoms [23, 24] and ions [25], superconducting qubits [26, 27], semiconductor quantum dots [28], rare earth ions [29, 30], defect centres in silicon carbide [31] and colour centres in diamond [32–34]. The reason for this variety of realised platforms is founded in the search for the ideal qubit system. In 2000, David P. DiVincenzo put forth a guideline on the requirements a quantum computer's hardware and thus a qubit needs to fulfill, since called DiVincenzos criteria [35], which read:

1. A scalable physical system with well characterised qubits
   This criterion encompasses two important requirements. The term "well characterised" means that the coupling of the qubit states to each other has to be well known but also the coupling to other states potentially present. It is very challenging to design a physical system actually consisting of only two quantum states, typically, there is a variety of them and the qubit states are suitably chosen from them. However, the remaining states may have influence on the system's dynamics

and thus the full level structure needs to be thorougly investigated. Furthermore, the coupling of the qubit states to external fields, its environment and to other qubits has to be well known. While this requirement is certainly important it has been demonstrated that it can be met especially in isolated systems such as single trapped ions and atoms. However, there remains the second requirement being the scalability of the system. In a quantum computer, suitable qubit systems need to be added up in large numbers to achieve meaningful computations. Typical qubit systems, however, tend to differ in their physical properties when packing them closely together, individual control becomes increasingly difficult and unwanted interactions between neighbouring qubits disturb the protocols. Scalability and the remaining DiVincenzo criteria (following below) thus have proven very difficult to achieve at the same time [10], posing a major hurdle for the implementation of a large scale quantum computer

2. The ability to initialise the state of the qubits to a simple fiducial state
   At the beginning of any quantum computation it is necessary to advance from a well defined starting point. The easiest way to achieve this is by preparing each qubit of the quantum computers computational infrastructure in a pure, non-superposition state e.g. $|0\rangle$, resulting in an overall state $|000...\rangle$ of all qubits. In most qubit systems this initialisation can be achieved fairly easy for single qubits by means of optical pumping [36, 37], laser [38] or microwave [39] sideband cooling and measurement based schemes [40]. With respect to quantum error correction [41, 42] (a way of mitigating errors occuring in a quantum computation) it is necessary to perform this initialisation at great speed in order to provide a constant supply of qubits needed for most protocols [43, 44].

3. Long relevant decoherence times
   The superposition states introduced above do not persist ultimately but are prone to decoherence. Consequently, the fixed phase relation between states $|0\rangle$ and $|1\rangle$ is lost over time and the system undergoes the transition to a statistical mixture. The decoherence is induced for instance by noise processes shifting the energy of the two states differently, e.g. magnetic and electric field fluctuations, or by interactions with phonons in optical traps and solid state systems. However, loosing coherence is equivalent to loosing the quantum advantage of a system and rather performing classical computations in a very complex, inefficient way. It is therefore necessary that decoherence time scales need to be significantly longer than typical manipulations of the qubit, so called quantum gates which are explained in the following.

4. A universal set of quantum gates
   The key ingredients of a quantum computation algorithm are the individual computational tasks, the quantum gates. These gates correspond to unitary transformation matrices. A universal set of the latter on the single qubit level means that by combining these operations every possible superposition state between the two qubit levels can be implemented. However, on the two qubit level a further quantum gate is necessary enabling a controlled interaction between two qubits. It has been shown that the single qubit gates need to be complemented by only one two qubit gate, typically chosen to be the cNOT gate, in order to constitute a complete architecture for any quantum computation [45, 46]. All of these quantum gates need to be performed with high accuracy (quantified by the gate fidelity) as gate errors can be seen as a further source of decoherence in the system that needs to be minimised. In order to

achieve this accuracy, the gate duration has to be much faster than the decoherence time scale thus opening up the way for implementation of quantum error correction.

5. A qubit-specific measurement capability
   As it is necessary to evaluate the output of a quantum computation a readout of the qubit state is required. There are two key factors a readout needs to fulfill. It is important that its accuracy is close to unity, meaning that it yields reliably the correct result. If this is not the case the computation needs to be repeated several times until the needed computational accuracy is reached. This is either time consuming or demands for parallel computing on redundant qubits thus increasing the number of qubits above the minimum required. The second key characteristic of the readout is the speed with which it can be achieved, being an important figure of merit in order to minimise the duration of a computation.

While these criteria should suffice to implement quantum computation including quantum error correction [44], there is an overlap with the requirements for Quantum Communication. This field is dedicated to enabling secure long-range communication based on quantum physics. It can be shown that quantum cryptography [47], as a special area of this field, enables concealment of the transmitted data fundamentally guaranteed by the laws of quantum mechanics. In the technically least challenging way, this can be used for the distribution of an encrypted key (quantum key distribution, QKD) in prepare-and-measure protocols, in which a certain qubit state is prepared at location A, transmitted via a quantum channel, and measured at the target location B. In the long run, these schemes should be upgraded in order to enable the formation of quantum memory or even quantum computing networks [48] in which the quantum devices used can be largely untrusted, making the protocols device independent [49]. The basic element of such a network is a quantum network node (QNN), with the different nodes constituting the network having to be linked with each other, meaning that they share long-lived entanglement. The most promising way to establish these links is to utilise photons as flying qubits which are entangled with an internal degree of freedom of the QNNs via e.g. their polarisational [50], temporal [51], or energetical [52–54] degree of freedom or by utilising which-path [50] or angular momentum [55] information. There are other approaches for realising flying qubits [56], however, due to the existing optical fibre telecommunication infrastructure and the corresponding know-how it is very likely that photons will be the flying qubits of choice in future applications. For the practical realisation [57, 58] of a quantum network link, two photons that are entangled with a QNN each are sent to a measurement station where a Bell-state measurement [59] is performed. Upon this, entanglement between the two remote QNNs is established. This approach suffers from photon losses in optical fibres exponentially increasing with the distance and thus limiting the protocol speed, the losses being minimised but not avoided by utilising photons in the telecom C-band. The imposed rate limit depending on the spatial separation of two QNNs is called the TGW bound [60,61] which needs to be overcome for realisation of a global scale quantum network. As quantum information encoded in flying qubits cannot be amplified in an analogous way as classical voltage signals due to the no-cloning theorem [62], the application demands for specifically designed quantum repeaters [63]. The basic idea is to split distances between two QNNs exceeding the TGW bound corresponding to the required repetition rate into smaller connections well within its limits. At each intersection point another QNN is situated. In a first step, each QNN is entangled with one of its nearest neighbours using the above-mentioned scheme. Subsequently, making use of the concept of entanglement swapping, a projective measurement on two neighbouring but not entangled QNNs trans-

fers the entanglement onto the outer nodes. By repeating this procedure, entanglement between the remote QNNs at the ends of the connection is established. The realisation of these quantum communication schemes imposes two additional criteria [33, 64] for QNNs, that are

6. An efficient optical photon - qubit interface
   Having an optical photon - qubit interface at hand, perferrably for photons in the low loss telecom C-band, enables the generation of remote entanglement with high rates. This interface can be either photon absorptive or emissive, depending on the application, however, deterministic interactions are required. In emissive schemes it is necessary that the linewidth of generated photons is limited either by the excited state lifetime or imposed by a cavity the emitters are situated in. In absorptive schemes, e.g. reflection of photonic qubits at a strongly coupled emitter-cavity system, the linewidth is typically governed by the cavity. Alternatively, strong light-matter interactions can be implemented by using dense ensembles of quantum emitters rather than relying on cavities.

7. The capability to store and operate several entangled states per node
   Eventually, quantum error correction will be necessary to implement in a large scale quantum network. This can be achieved if multiple entangled states can be stored per QNN and it is possible to perform high fidelity quantum gates between them.

For a typical qubit system, these seven criteria are not fulfilled at the same time. For example, trapped ion qubits have been shown to excel in terms of well characterised level structures, efficient initialisation [65], long coherence times [66], high fidelity quantum gates [65, 67], and efficient single-shot readout [68]. However, it remains very challenging to demonstrate all these favourable properties with merely one ion species. Additionally, it proves hard to scale systems such as these beyond certain limits imposed by the trap and the surrounding technical infrastructure. Furthermore, protocol repetition times are typically rather low [25, 69] and thus the overall computational speed is limited. Regarding their use as QNN, lifetime limited photons can be generated with reasonable repetition rates only in the blue or ultraviolet spectral range. This is disadvantageous as in these frequency regimes fibre losses are more than two orders of magnitude larger compared to the telecom C-band. Superconducting qubits have similar strengths [70], except that coherence times are shorter and efficient readout is more complicated [71], and extend the portfolio to very fast quantum gates [70]. The scalability of these systems is again a limiting factor as they need to be kept at ultracold temperatures requiring a dilution refrigerator. With an increasing number of qubits being addressed by microwaves, the heatload increases and thus again poses a boundary condition on the size of such a processor. Although constituting a major breakthrough, the only quantum computer device that ever demonstrated quantum supremacy up to now consists of "only" 53 superconducting qubits [1]. On top of this, an efficient microwave to optical photon conversion still needs to be demonstrated and thus criterion six imposes a severe obstacle for the application of superconducting qubits as QNNs. Instead utilising semiconductor quantum dots as qubits lowers the demand for ultralow temperatures as typical operational temperatures are about $4-8\,\mathrm{K}$, however, coherence times are severely limited as these artificial atoms are impacted by charge noise and a vast fluctuating nuclear spin bath interacting with the qubit [28]. Additionally, the fabrication of quantum dots with identical and favourable properties is rather challenging [28]. On the upside, their potential for use as QNNs [72] has been demonstrated by realisation of quantum dots emitting in the telecom C band frequency range [73, 74] and

ultrafast quantum control [75]. Furthermore, highly coherent photons at impressive repetition rates can be retrieved [76]. In comparison, rare earth ion qubits can exhibit ultralong coherence times [77] but typically suffer from poor optical readout in bulk material [22], thus realisation of an efficient photon - qubit interface requires the fabrication of highly advanced nanophotonic cavities [78] or large ensembles of emitters [79]. Defect centres in silicon carbide are recently discovered and promising new qubit systems [31] which have great potential in terms of scalability as silicon carbide is a well investigated material in manufacturing high-quality single crystalline wafer for classical electronic devices [80]. Recently, favourable optical [81] as well as spin properties [81, 82] even in nanophotonic structures [81] and up to temperatures of 20 K [83] have been demonstrated. However, the optical readout capabilities for centres exhibiting long spin coherence are typically rather limited [31]. In summary, each of these (potential) qubit realisations is characterised by its inherent flaws as well as advantages. While the systems for the greater part underwent extensive testing, the most promising approach could not yet be reliably determined.

Within this thesis, we focus on colour centres in diamond as qubit systems, consisting of an impurity atom substituting for a carbon atom in combination with an adjacent lattice vacancy. Among these, the state of the art is set by the negatively charged nitrogen vacancy (NV^-) and silicon vacancy (SiV^-) centre. The NV^- centre can be efficiently initialised [84], exhibits long spin coherence times ranging from several milliseconds even at room temperature [85] to seconds at cryogenic temperatures [86], and can be controlled with high fidelity single qubit quantum gates [87]. Utilising spin-to-charge conversion yields rather high fidelity single-shot readout [88]. An additional feature of the NV^- centre is its efficient interaction with ^{13}C nuclear spins, with gate fidelities reaching 99.2 % [87]. This is favourable as these nuclear spins are especially long-lived and decohere on time scales of seconds [89] to minutes [90], making them ideally suited as long-lived quantum memory qubits for the multimode storage of entangled states addressed in criterion seven. The manipulation itself is mediated by the communication qubit constituted by the electron spin of the NV^- centre. Interfacing of up to nine fully connected memory qubits with a single NV^- centre has been demonstrated [90], which exceeds the typical requirement for logical qubits in basic quantum error correction schemes [91]. On the other hand, the NV^- centre is severely impacted by crystal strain and fluctuating fields in the crystal environment, which contradicts the wish for well defined and well characterised qubits. While both of these effects can be turned into a benefit by strain [92] or electric field [93, 94] tuning of optical resonances resulting in a recent demonstration of up to three remote centres being brought to a common frequency in a small network [95], the spectral diffusion of the resonances still limit the fidelities of optical two qubit gates to below 90 % [95, 96]. Unfortunately, the NV^- centre being embedded in a solid state matrix is prone to interactions with lattice vibrations (phonons), which limits the fraction of photons being coherently emitted into the zero phonon line (ZPL) to about 3 % [97, 98]. This sets a major boundary condition on the achievable repetition rates on remote interactions of two qubits in state-of-the-art experiments, forcing them to be restricted to the mHz to several Hz regime [95, 96]. Both limitiations of the NV^- centre can be mitigated by choosing a group IV vacancy (G4V) colour centre as qubit system. In contrary to the NV centre, where the nitrogen is situated at the lattice site of the carbon atom it replaces, the G4V centres feature an inversion symmetry with the impurity atom being in an interstitial position between two vacant lattice sites [99,100]. The major benefits of the symmetrical configuration are the vanishing permanent dipole moment rendering the centres insensitive to first-order Stark shifts and the similar electron distribution in ground and excited state ensuring that a larger fraction of photons are emitted into the ZPL without emission or absorption of phonons [100]. The

most studied G4V centre is the SiV^- centre, which can be highly efficiently initialised [36, 37] and exhibits long spin coherence times albeit at temperatures below 0.4 K [36] while full control over single qubit rotations has been demonstrated optically [37] as well as by direct microwave driving [36]. In nanophotonic devices, readout of spin states can be obtained in single-shot schemes approaching unity efficiency [101]. The low inhomogeneous broadening [102] resulting from the inversion symmetry and close to lifetime limited optical transitions [102] are crucial prerequisites for generation of indistinguishable single photons and thus photonic Bell-state measurements. Therefore, in principle, the implementation of photon-mediated two qubit gates between remote SiV^- centres should be significantly facilitated. Nevertheless, this remains elusive up to now due to the low quantum efficiency and the technically challenging compensation for remaining shifts in central resonance frequencies of the centres. Only basic steps towards this aim have been realised with two emitters being independently addressed though situated in the same sample [103] or by coupling them to the same mode of an optical resonator [104]. Also, interactions with nearby nuclear spin memories are limited to significantly lower fidelities [101, 105, 106] than is the case for the NV^- centre. Nonregarding remaining imperfections, the SiV^- centre has been utilised to successfully demonstrate the first quantum memory enhanced quantum communication protocol which outperforms the direct transmission scheme [101]. This is particularly enabled by the inversion symmetry protection of the resonance lines of G4V centres from fluctuating charges in its environment, which allows for integration in optical resonators [107]. For future applications it would nevertheless be fortunate to significantly reduce the technical overhead imposed by cooling the qubit to millikelvin temperatures and utilise a system exhibiting a larger quantum efficiency, thus enabling higher repetition rates. While the next heavier G4V centre, the germanium vacancy centre (GeV^-), yields only moderate improvements at best in both aspects [108–112], the tin vacancy centre (SnV^-) promises to overcome both limitations [113, 114] whereas the lead vacancy centre (PbV^-) is only spectroscopically investigated up to now [115–119]. All of these G4V centres share the same fine structure consisting of two ground and two excited states [100]. However, the splittings between these states and their absolute position within the diamond band gap distinguish them from each other. The need for millikelvin temperatures in order to extend the spin coherence of the SiV^- centre arises from single phonon driven transitions [120] between the two orbital ground states that are separated by about 50 GHz [99, 102, 121]. As the spin-orbit coupling intensifies with the atomic number, this ground state splitting increases to about 820 GHz for the SnV^- centre and thus reduces the temperature limitation for similar spin coherence times to below 2 K [113, 114]. Such a temperature can be more conveniently achieved by closed-cycle liquid helium cryostats and thus reduces the technical overhead significantly. Additionally, its quantum efficiency was estimated in the first fundamental study conducted on this new colour centre to amount to about 80 %, approaching unity. The reason for this increased quantum efficiency is not clear, however, it is speculated that it is a result of the reduced amount of non-radiative phononic decays as multiphonon processes become less likely with higher ZPL energy [122, 123]. The latter is about 0.3 eV larger for the SnV^- compared to the SiV^- centre [100]. The likeliness with which non-radiative charge transitions occur and the time that a G4V centre spends in an unfavourable charge state under certain excitation conditions are another possible explanation for the reduced quantum efficiency of G4V centres. These processes are dependent on the absolute energy positions of the electronic states within the diamond band gap and thus the SnV^- centre might be positioned favourably. However, as the SnV^- centre is a very recently discovered colour centre, many open questions remain and its internal dynamics as well as interactions with its host lattice remain elusive. This

thesis is dedicated to reveal its fundamental properties such as the above-mentioned charge dynamics and gain insights into pathways to applicability of the SnV^- centre as a promising qubit candidate in QIP.
These objectives of the thesis are organised as follows:

- Chapter 2 is dedicated to introducing the fundamental concepts constituting the foundation of this study. In a first step, we highlight the underlying processes and the state of the art of fabricational techniques to create G4V centres in a controlled manner. Subsequently, their structural symmetry, possible charge states, and the general electronic structure are discussed. Building on this, we highlight the phonon-induced decoherence mechanism, the brightness of photon emission, and the impact of spectral diffusion on G4V centres. This subsection is concluded by a comparison of the individual members of the G4V family and the experimental state of the art of their applicability. In the second part, we discuss light-matter interactions with a special focus on the dynamics that are of importance for the conducted experiments on the SnV^- centre within this thesis. The third part completes chapter 2 by introducing the theory of two-photon interference (TPI) and the derivation of a model for analysing experiments with photons extracted from a single SnV^- centre.

- Chapter 3 focuses on the sample preparation and the experimentally employed optical setups. Different components and devices are presented and their characteristics relevant to this thesis are discussed.

- Chapter 4 is an extensive study revealing fundamental properties of the SnV^- centre covering photophysics such as the single photon nature of the emission of single centres, a discourse about their radiative lifetime, and the temperature dependence of the ZPL emission. Furthermore, photoluminescence spectra of SnV^- centres in samples that were subject to different annealing conditions are compared and the polarisation of the photon emission in low strained bulk environment is investigated. The chapter concludes with an in-depth analysis of the phonon sideband and the resulting Debye-Waller factor as well as a spectroscopic analysis of a higher lying excited state.

- The main subject of chapter 5 is the understanding of the charge dynamics that a single SnV^- centre is subject to under resonant excitation. We investigate the photodynamics of the charge transfer to an unwanted charge state as well as the mitigation of this process. In the end, the findings within this chapter enable the derivation of a charge cycle of the SnV^- centre explaining all charge dynamics and being potentially applicable to understand these effects also for different G4V centres.

- Chapter 6 builds upon the results obtained in chapter 5, encompassing a thorough analysis of the optical coherence of charge stabilised SnV^- centres. This is extended by probing the cyclicity of spin-conserving transitions and exploitation of the latter for implementation of a single-shot readout scheme. Finally, we use an all-optical coherent population trapping protocol in order to quantify the spin dephasing time of the potential ground state qubit.

- In chapter 7 we focus on the applicability of the SnV^- centre in quantum communication schemes. We firstly quantify effects limiting the contrast in TPI by extensively characterising the photon emission properties and how they are impacted by spectral diffusion. Finally, we realise TPI of photons emitted by a single SnV^- centre, probe

the time scales on which the interference contrast is reduced, and eventually compare it to the case of completely distinguishable photons.

Chapter 2

Fundamental concepts

2.1 Group IV vacancy centres in diamond

2.1.1 Fabrication processes

While only a small fraction of the focus within the experimental part of this thesis is set on fabrication of G4V centres, we want to use this section to review the requirements that will ultimately be imposed for use in QIP. Furthermore, we discuss the state of the art of fabrication techniques to give an overview on the advances in the field. This section is not meant to be a complete review but rather to put forth an intuition and an outlook of what is feasible at present and what might be achievable in the future.
Coming back to the criteria proposed by D. P. DiVincenzo, the first one emphasises the need for scalability of qubits in a quantum computer. This encompasses the feasibility of producing colour centres with the following features, in light of which we will evaluate the diverse fabrication methods:

1. **Well defined location:**
   If chip-like colour centre devices are to be realised, it is mandatory to create G4V centres at well defined positions. The exact value of the spatial resolution hinted at by the labelling "well defined" depends on the outline of the device. For example if each colour centre is to be positioned under a standard solid immersion lens ([124–126]) for improved light exctraction, a lateral and depth resolution of a few hundreds of nanometer is typically sufficient. In comparison, placing a single colour centre in the centre of a photonic crystal structure or Fabry-Perot cavity which enhance the light matter interaction requires lateral positioning accuracy of <50-100 nm [127–129]. If the chip design aims at generation of entangled spins due to magnetic dipolar interactions of the colour centres, the individual colour centres have to be placed within a few nanometers to each other [130].

2. **Creation yield:**
   The creation yield of the colour centres needs to be as high as possible in order to achieve scalability. For example, a typical creation yield of G4V centres in bulk diamond upon ion implantation and standard annealing is on the order of a few percent [116, 118, 131, 132]. That means, assuming a yield of 10 %, creation of a pattern of 10 single colour centres requires on average $\frac{1}{0.1^{10}} = 10^{10}$ trials until a working device is achieved. Therefore, it is crucial to reach a quasi-deterministic creation yield close to unity for industrial scale chip production. Alternatively, it is possible to fabricate modular "quantum microchiplets" that can be precharacterised while working

chiplets containing a colour centre are transferred to a multichip module [133]. However, also this fabrication technique benefits from high creation yields by improved numbers of fully functioning chiplets.

3. **Optimised diamond environment:**
   This requirement refers to the "well defined" part of the first as well as the third DiVincenzo criterion. Only in an optimised diamond host lattice, colour centres that are introduced into such an environment will exhibit very similar physical properties. For inhomogeneous strain, impurities and lattice defect distributions within the diamond, the optical transition frequencies will be statistically spread for the different qubits [134–136] and their charge states will vary, see supplementary information in [104] and [137, 138]. Furthermore, the quantum phase of superposition states and thus the spin coherence is strongly influenced by the presence of nearby electron or nuclear spins [36, 129, 139, 140]. It is therefore necessary to incorporate colour centres in a diamond matrix that exhibits exactly the wished-for amounts of impurities, defects and strain.

4. **Industrial production:**
   In the end, a commercially available quantum computing device will require the compatibility with wafer-scale chip production,which kind of combines the upper three requirements but extends it to sizing up the chip. The latter is non-trivial even though major advances in single crystalline diamond wafer production have been recently made [141].

Given the requirements stated above, we will discuss the different approaches made to achieve them for the two dominant production methods. These are the incorporation of colour centres during the growth in a plasma enhanced chemical vapour deposition (PECVD) process and the use of ion implantation to insert impurities into a preselected diamond substrate.
We will start highlighting the PECVD process:
This bottom up approach is based on utilising regular growth techniques for single crystalline diamond but under the addition of the desired group IV element X into the plasma. The incorporated impurities have to be post fabricationally treated in order to create the desired XV centre. Therefore, introduction of vacancies into the sample is needed. Several approaches emerged over the past years to achieve this aim, among these are the irradiation with electrons [142, 143], implantation of other elements such as helium [144] or carbon [145] and intense laser pulses [146]. All of these methods introduce vacancies in the diamond and a typically needed subsequent thermal annealing step ensures that mobile vacancies are captured by the impurities and the XV centres are formed.
In the context of scalability, the PECVD growth has the major disadvantage that incorporation of impurities during growth is a probabilistic effect and hardly any control of the lateral positioning is achieved in situ. Only the depth confinement can be very precise, when making use of so-called δ-doping. In this process the element X is inserted into the plasma only during a defined period of the growth process. The thickness of the impurity layer can then be controlled via the time and the intensity of the exposure of the sample to element X. The depth resolution can thus be precise up to a few nanometers, but the technical overhead differs depending on the element of choice being inserted and whether there is a suitable gas available for addition into the plasma in a controlled manner. Lateral resolution can be improved by controlling the resolution of the vacancy creation for example by using focused electron or ion beams [143–145]. However, it will be either limited by the distribution of the impurity atoms, where a too high density

of element X being inserted will prevent resolving individual colour centres, while a too low density will result in many empty locations on a chip, where a colour centre is desired to be. A further approach to achieve lateral positioning accuracy, is either growing nanodiamonds [147–149] instead of bulk diamond or reducing a grown bulk diamond to small nanodiamond pieces [134, 150, 151]. These nanodiamonds can be put to a specific location by using pick-and-place techniques such as employing an atomic force microscope (AFM) [152]. The disadvantage of this method is twofold. First of all, the nanodiamonds created in the bottom up as well as the top down approaches will exhibit a size and strain distribution. It has been shown, that colour centres in such nanodiamonds tend do differ heavily in their physical properties [134]. Furthermore, the positioning of the nanodiamonds imposes an additional technical overhead limiting the scalability.

Regarding the second of our fabricational requirements, creation yields after PECVD growth are hard to estimate, as it requires knowledge about how many impurity atoms were incorporated and which fraction of them was converted to an XV centre. While the amount of XV centres can be determined by e.g. optical microscopy, measuring the amount of impurities that were not converted is challenging. Using a combination of determining the concentration of SiV^- centres and secondary ion mass spectrometry a yield of 15 % of the incorporated silicon being in the form of SiV^- centres was determined [153].

The major advantage of the PECVD growth is that the impurities are situated in a diamond environment which can be controlled by the parameters of the growth process. Furthermore, typically very little additional strain is excerted by the process and thus the colour centres will be situated in a relatively low strain environment. This also depends on the gentleness of the subsequent vacancy creation process where electron irradiation with moderate fluences is suitable to leave the diamond lattice moderately damaged [143] while the implantation of other elements should be performed remotely in a different depth than the impurity layer in order to avoid strain induced by the implantation process. Furthermore, the PECVD growth is directly compatible with growth of wafer-scale chip production as it has been shown that single crystalline diamond wafer can be grown [141].

Recapitulating the preceeding discussion, PECVD growth has major advantages in producing colour centres with litte variation in large chips, nevertheless, the scalability is strongly inhibited by the stochastical nature of the growth process.

Shifting the focus to ion implantation, we will discuss the subject in slightly more detail as the samples within this thesis are produced utilising this technique and it benefits from a higher flexibility. As a starting point, a suitable diamond substrate in which the colour centres are to be incorporated has to be chosen. Regarding the discussion on the PECVD growth, the preferrable material is a grown single crystalline diamond with a minimised amount of unwanted impurities, defects and strain. The element X of choice is typically extracted as an ion from a target cathode in a particle accelerator, accelerated until it reaches the desired implantation energy and eventually guided onto the diamond substrate. In a post-implantation step, the sample is annealed and vacancies that are created in the implantation process are captured by the impurities to form XV centres.

During the implantation process, the ion will collide with electrons and nuclei of the diamond lattice loosing kinetic energy until it stops. As it undergoes many collisions, especially upon the impact of atomic nuclei its direction will be changed. The latter effect is called straggle. A simulated distribution based on a Monte-Carlo approach (Stopping range of ions in matter, SRIM [154]) of one thousand tin ions implanted with 700 keV under zero degree angle of incidence into a (100) diamond is displayed in Fig. 2.1a). The mean implantation depth is 167.9 nm with a straggle of 29.5 nm. The lateral distribution exhibits a straggle of 20.8 nm. In terms of well defined localisation the straggling imposes

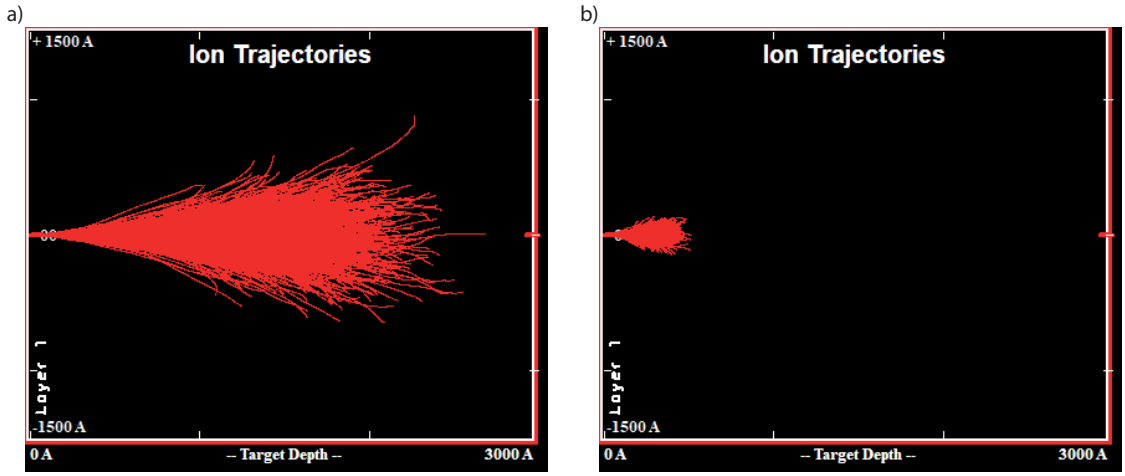

Figure 2.1: **Implantation distribution of tin ions:** SRIM simulations reveal the ion trajectories and thus the depth and lateral distribution of group IV elements being implanted into the diamond target material. The implantation is simulated for a (100) diamond substrate under perpendicular incidence of the ion beam on the target. The ion trajectories are exemplarily shown for 1000 tin ions at an implantation energy of **a)** 700 keV and **b)** 100 keV.

a first limit. By reducing the implantation energy, the ions will be implanted more shallow but with a narrower distribution as can be seen in Fig. 2.1b) again simulating tin ions but with an implantation energy of 100 keV. The simulated dependency of depth and straggle of the group IV elements on the implantation energy is displayed in Fig. 2.2a). However, even though depth and lateral distributions below 10 nm can be achieved, there remains the problem of implanting the ion exactly at the right spot. Usual particle accelerators operate at a large ion beam diameter that can be reduced using pinholes or masks. One possibility is the use of polymer masks, that are patterned by electron beam lithography. With this technique, lateral resolutions of below 100 nm can be achieved [129]. The procedure is disadvantageous, if colour centres are to be implanted into prestructured diamond devices, such as photonic crystal cavities [127, 128]. These devices tend to be fragile and are likely to be destroyed during the deposition of the photoresist on the diamond. Furthermore, the technique does not overcome the problem of the implanted ions being randomly distributed and therefore it is impossible to have exactly one ion implanted at each spot.

The mask problem can be overcome by using an AFM tip with a tiny pinhole in it which can be produced using focussed ion beam (FIB) milling. Exploiting the AFM scan mode suits to find the right structure in the diamond and position the pinhole relative to it. The tip itself serves as mask and ion implantation will only occur through the pinhole. With this technique, lateral positioning accuracies of 25 nm have been achieved [155]. Another possibility is to use a FIB for the implantation itself which yields positioning accuracies of below 50 nm relative to a target structure [156]. While these accuracies are satisfying for most device requirements, the problem of implanting one and only one ion remains. Several approaches towards this goal were made which can be divided into two categories. The first one relies on post implantation detection of the ion by secondary processes such as electron emission from the target upon the impact of an implanted ion [157] or the detection of excited electron-hole pairs [158]. The second category of techniques relies on detecting the ion before the implantation. This can be done by using an ion trap and

implanting only a selected ion being extracted from the trap [159, 160]. This approach yields good results but at a high technical overhead and a low implantation rate. Another possibility is the proposed detection of mirror charges induced by the travelling ion which poses high technical demands in signal processing [161]. Even though, being capable of implanting exactly one ion to a designed spot still leaves the need for transforming this ion into an optically active XV centre. While the above-mentioned techniques for PECVD are still applicable, the most promising tool is the laser writing. A high intensity laser pulse inserts the energy needed for creation of a vacancy and at the same time serves as annealing mechanism by heating up the diamond and thereby enabling the vacancy to diffuse and being captured by the impurity [146]. This scheme can be implemented including an optical feedback, heralding the successful creation of the XV centre upon detection of its characteristic fluorescence [162]. This technique enables close to unity conversion yield in combination with very good spatial positioning precision. Regarding requirement three, ion implantation typically induces a lot of damage in the diamond lattice. In Fig. 2.2b) the number of vacancies created by implantation of a single group IV ion is plotted against the implantation energy. This damage will only multiply in usual implantation schemes as more ions than necessary have to be implemented due to low conversion yields. For the single ion implantation scheme, the preselected diamond substrate is disturbed as marginally as possible since only one ion is implanted and the laser writing itself is a gentle technique coming along with mitigation of introduced damage by thermal annealing. It might be that an additional annealing step is necessary to overcome the damage induced when implanting heavier ions such as tin and lead, compared to the lighter group IV elements silicon and germanium. The comparison of vacancy creation in Fig. 2.2b) shows that the overall damage to the diamond lattive increases massively when implanting elements heavier than silicon. Overall, requirements 1 to 3 can be rightly fulfilled by combination of the above-mentioned schemes and the industrial production is mainly limited by the still significant technical overhead that needs to be reduced in the future.
We would like to mention a very recent ion implantation scheme potentially useful in well-positioned G4V centre generation. It is based on recoil momentum transfer and labeled "Knock-On implantation" [163]. This indirect implantation technique relies on a few nanometer thick layer of element X being deposited on the diamond sample. Subsequently, a focused ion beam transfers its momentum on the atoms in the deposited layer pushing them inside of the diamond. This yields ultra-shallow implantation depths below 5 nm and lateral resolutions of below 50 nm [163] which could be further improved. Combining the approach with laser writing might be a valuable extension of the well-established set of techniques.

2.1.2 Structural symmetry and charge state

Being aware of the different fabricational techniques of G4V centres in diamond, it is important to elaborate on the structural symmetry of the defects inside their host matrix. Its of particular importance since the electronic level structure and furthermore the response to environmental magnetic and electric fields are consequential of it. We do already know the G4V colour centres being formed by an impurity atom X and a lattice vacancy V. However, this leaves several possibilities of the two constituents being situated within the diamond lattice. A defect structure with the impurity atom sitting in an interstitial position between two empty carbon lattice sites (Fig. 2.3) was initially proposed for the SiV^- centre by Goss et al. employing density functional theory (DFT) [164]. In order to avoid confusion, it has to be clarified that the two empty lattice sites result from the combination of the impurity atom replacing a carbon atom and an empty lattice site. It

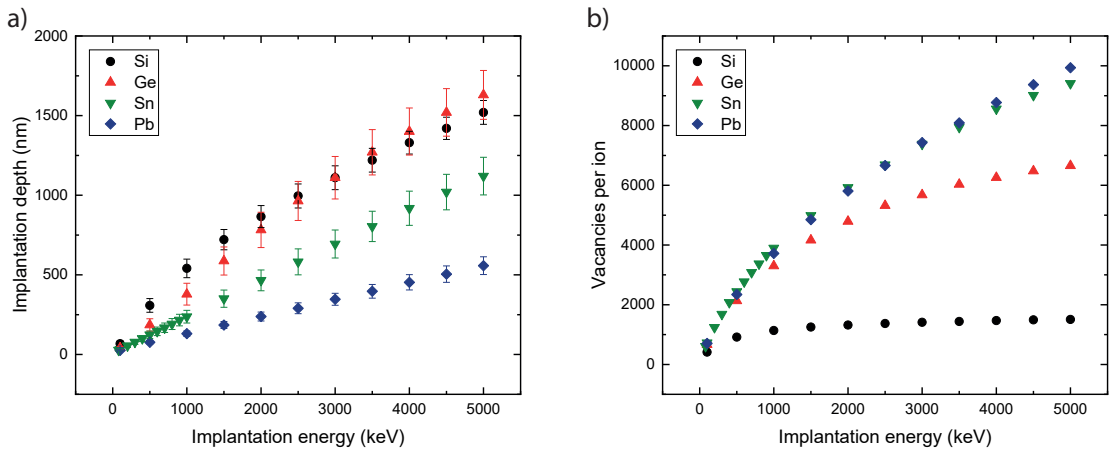

Figure 2.2: **Implantation depth and vacancy creation:** SRIM simulations for all group IV elements assuming perpendicular incidence on the diamond substrate yield **a)** the mean implantation depth for varying implantation energy with the straggle being denoted as the error bars. In **b)** the vacancies created on average by a single ion upon implantation are shown.

is thus not a divacancy but a single vacancy that contributes to the defect formation and literature refers to it as a "split-vacancy" configuration. This geometric structure implies a defect symmetry being equivalent to the point group D_{3d}. The theoretical groundwork has been further extended by DFT to cover all G4V centres [100]. To understand the working principle, we will very briefly review the theoretical foundation it is based on. In a first step, a subset of the diamond lattice containing a finite number of carbon atoms is implemented in the computation, the so-called diamond supercell. Subsequently, the impurity atom and the lattice vacancy are introduced in the centre of the super cell. The lattice will impose a force on the atom and vice versa which in reality will be minimal in order to reach its thermodynamic optimum. Therefore, the position of the atom is varied and by recording the force the adiabatic potential energy surface (APES) of the system is obtained. The global minimum of the APES relates to the expected geometry of the system yielding the interstitial position of the impurity atom and thus D_{3d} symmetry for all G4V centres [100].

Before looking further into the experimental findings on the crystallographic structure of the colour centre, we introduce the concept of different charge states as they are necessary to understand the experiments. The charge state of a G4V centre results from the electrons contributed by the unsatisfied carbon valences (dangling bonds) of the empty lattice sites, the electrons provided by the impurity atom and electrons being donated or accepted by other impurities in the diamond lattice. Each dangling bond of the carbon atoms supplies an electron and thus a total amount of six electrons results from the unoccupied carbon lattice sites. The impurity atom being part of the fourth group of the periodic table adds another four electrons. This ten electron state is called the neutral charge state of the G4V centre. The charge state of highest relevance within the thesis is the singly negative charge state for the constitution of which an additional electron is captured by the colour centre from a surrounding donor impurity. While it would be expected that the structural symmetry of the G4V centres does not depend on the charge state, theory implies that a charge state with an uneven number of electrons added to or taken from the colour centre does disturb the symmetry a little by distorting the positions of the six adjacent

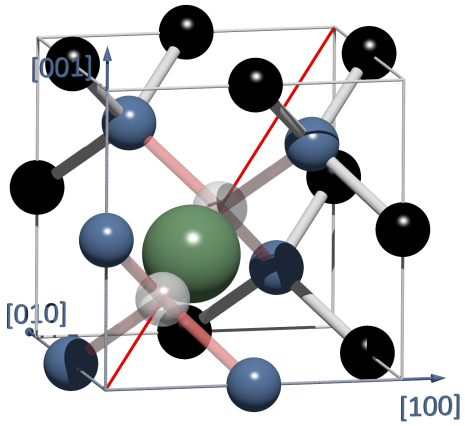

Figure 2.3: **Geometrical structure of the G4V centres:** The impurity atom (green) sits in an interstitial position between two empty (light grey) lattice sites aligned along the <111> direction. The size of the impurity atom relative to the carbon atoms is chosen to match the ratio for the SnV^- centre. The six nearest neighbour carbon atoms being important as the contribute one electron each to the defect centre are shown in blue.

carbon atoms slightly (0.03 Å (0.01 Å) in the excited (ground) state of the SnV^- centre, values obtained from T. Gergő, unpublished, private communication) compared to the G4V centres' bond length of approximately 2 Å [100]. This effect yields a lowered symmetry being described by the C_{2h} point group. For each G4V centre, three potential minima exist in which the system might relax to. As a consequence of the dynamic Jahn-Teller (JT) effect, being discussed in more detail in the following section, tunneling between all three minima occurs. Since the time scales of such tunneling rates are typically on the order of a few tens of femtoseconds [165] the effect is not observed on experimental time scales limited to the nanosecond regime within our work. The observed average of the system is effectively again of D_{3d} symmetry, however, with the position of the adjacent carbon atoms exhibiting a larger average deviation from the equilibrium position than would be expected from zero point motion of a harmonic oscillator. This effect does not influence the experiments within this thesis, however, it is nevertheless important to understand why theoreticians refer to a C_{2h} symmetry of negative charge states of the G4V centres and furthermore that the dynamic JT effect has an impact on the strength of spin-orbit coupling as will be seen in the following. Nevertheless, for the course of the thesis we will refer to the G4V centres being of D_{3d} symmetry since their properties are determined by the averaged symmetry on the time scales relevant for our experiments.

Experimentally, it is very challenging to reveal or confirm a structural symmetry of a colour centre in a direct measurement. This is the reason why all initial experiments relied on secondary confirmation mechanisms. For instance, if the singly negative charge state of a G4V centre is investigated, the optically active electron oscillates along the symmetry axis as an electric dipole and thus the polarisation of the emitted light will be perpendicular to the defect axis. Measurements on the absorption dipole gave the first indications for the G4V centres being aligned along the <111> axis [166] even though the authors interpreted the results as an alignment along <110> corresponding to the projection of the dipoles in <111> directions into the (100) observation plane in these experiments. Further insight was given by magneto-optical spectroscopy conducted by Hepp et al. in which they found the Zeeman splittings for a single SiV^- centre and an ensemble of these emitters to coincide for a magnetic field being aligned along the

[100] direction [99]. As there are four crystallographic equivalent axes to which the G4V centres can be aligned to, the magnetic field projection onto these axes will differ except for the case of an alignment along the <111> axes. This is clear evidence of the D_{3d} symmetry as well as the alignment direction in <111>. Furthermore, measurements of the electron paramagnetic resonance of the neutral charge state of the silicon vacancy centre also indicated a <111> orientation [167].
Very recently, during the experimental phase of this thesis, an experiment aiming at a direct proof of the structural symmetry of the SnV centre has been conducted by Wahl et al. [168]. They implanted the radioactive isotope ^{121}Sn into diamond and employed the concept of β^- emission channeling. This method enables a direct probe of the lattice site in which an implanted radioactive isotope is situated in a single crystal. Upon the β decay of ^{121}Sn into ^{121}Sb, the emitted electrons will be influenced by the crystal potential. Thus, depending on the initial lattice site they were emitted from their angular distribution is determined. Recording this pattern in the vicinity of the major crystallographic directions can be used to compare the characteristic pattern with simulations and thereby reveal the lattice site position of the tin atom. The results exhibit that about 40 % of the tin atoms sit within or close to an interstitial position within the diamond lattice. Upon a short ten minute thermal annealing, only atoms in a close to perfect interstitial position remain with a probability of approximately 30 %, while the remaining atoms sit at a lattice site in substitution of a carbon atom. The deviation of one third of the atoms forming SnV centres compared to the formation yields below 5 % of SnV^- centres reported in [132] is striking. Either the difference is due to a significant amount of SnV centres being in an optically dark or not detected charge state as the doubly negative or neutral one or the SnV centres are passivated by an adjacent hydrogen atom which is commonly found for nitrogen vacancy centres in PECVD grown diamond [169]. While the origin of the yield mismatch could not be resolved within the study they could nevertheless verify the D_{3d} symmetry of SnV centres resulting from the interstitial position in <111> direction. This symmetry is of particular importance regarding the coupling of G4V centres to external electric fields which will be discussed in the following section.

2.1.3 Electronic level structure

The structural symmetry of the G4V centres being revealed enables to derive their electronic structure. Since a stringent derivation delves deeply into group theoretical approaches we will only summarise the theoretical approach and the resulting findings in literature. The interested reader is redirected to the detailed analysis conducted for the SiV centre in [99, 170] and the research extending it to all G4V centres [100].
The starting point for deduction of the electronic structure is the investigation of the electrons contributing to the defect centre from different constituents. Let us therefore briefly review the concepts and notation of group theory. Using group theory on molecules relies heavily on the symmetry properties imposed by the molecular structure. Such a configuration is fully characterised by the symmetry operations acting on it, like a mirror transformation on a certain mirror plane or a rotation by a given angle. Sampling all the operations which unambiguously describe the molecule yields a point group. For each point group there exists a group formed by matrix operations that is homomorphic to it and is called a representation. Representations that can be reduced into sums of lower dimensional representations are called reducible while these of lowest dimensionality are called irreducible represenations. The latter can be used to describe quantum mechanical functions such as orbitals or eigenfunctions and label them. These labels obey a certain notation for the D_{3d} group, that is as follows:

- The main label a (e) refers to a basis function (the single electron states) with a one- (two-) dimensional representation A (E) representing the interplay of all electron states forming an electronic (multiparticle) state of the G4V centre.
- The subscript g (u) refers to a basis function with even (odd) parity under the symmetry operation of the inversion at the interstitial position where the impurity atom is situated.
- The subscript 1 (2) refers to even (odd) parity under a 180° rotation about a rotational symmetry axis being perpendicular to the symmetry axis of the G4V centre.
- The subscript x (y) is only applicable to the main label e and distinguishes between the two orthogonal basis functions of the two-dimensional representation E.

With this notation on hand and by employing the concept of symmetry-adapted linear combinations (SALCs) the final form of the electronic levels of the G4V centres is derivable. The principal level structure is shown in Fig. 2.4a) for the case of the ground state ${}^2E_\mathrm{g}$ and in b) for the first excited state ${}^2E_\mathrm{u}$ of a negatively charged G4V centre with respect to the valence band (VB) maximum and the conduction band (CB) minimum of the diamond bandgap. The superscript 2 refers to the twofold spin degeneracy of the states. The level ordering is as follows: the state $a_{1\mathrm{g}}$ lies deeply in the valence band and is fully occupied with two electrons of opposite spin. Above it lies the fully occupied state $a_{2\mathrm{u}}$ which will be of importance in sec. 4.4. Both states mix with the diamond valence band states [100, 171, 172]. The doubly degenerate e_g state lies fully occupied slightly below (SiV^-, GeV^-), coincides with (SnV^-), or slightly above (PbV^-) the valence band edge for the ground state [100]. The highest lying e_u state is filled by only three electrons in the ground state while transfer of an electron from the e_g state to the e_u state upon excitation yields a fully occupied e_u configuration in the excited state. Due to the change in electronic configuration the electron levels move up in energy with respect to the diamond VB and the lower $\mathrm{e_u}$ state pops out of the VB into the diamond band gap for all G4V centres [100]. Both ground and excited state are fourthfold degenerate, twice orbitally and twice by their spin degree of freedom. The absolute positions of the electron levels are not specified here as they differ for each G4V centre. They are well predicted for the $\mathrm{e_g}$ and $\mathrm{e_u}$ orbitals in [100], however, the values for the $\mathrm{a_{2u}}$ and $\mathrm{a_{1g}}$ orbitals are not specified.
While this energy structure gives an idea on how the electron configuration of the different states is constituted it does not fully cover the physical reality. The orbital degeneracy of the e_g and the e_u state is lifted upon the spin-orbit (SO) interaction, the Jahn-Teller effect or a crystal strain field. The mathematical description for all three effects on a G4V centre were introduced by C. Hepp and while we will write down their respective Hamiltonians here, a detailed analysis can be found in reference [170]. For the SO interaction, the Hamiltonian, including the twofold spin degeneracy, expressed in the basis $\{|\mathrm{e_{g,ux}}\uparrow\rangle, |\mathrm{e_{g,ux}}\downarrow\rangle, |\mathrm{e_{g,uy}}\uparrow\rangle, |\mathrm{e_{g,uy}}\downarrow\rangle\}$ reads

$$\mathcal{H}^{\mathrm{SO}}_{\mathrm{g,e}} = \begin{pmatrix} 0 & 0 & -i\lambda_{\mathrm{g,e}} & 0 \\ 0 & 0 & 0 & i\lambda_{\mathrm{g,e}} \\ i\lambda_{\mathrm{g,e}} & 0 & 0 & 0 \\ 0 & -i\lambda_{\mathrm{g,e}} & 0 & 0 \end{pmatrix} \tag{2.1}$$

were we distinguish between the coupling strength λ in the ground (g) and excited (e) orbital state. While the SO interaction is discussed at length in textbooks on atom physics the JT effect is less known. Its foundational hypothesis of the static effect is that a molecular structure leading to degenerate orbital states will be instable [173]. This instability

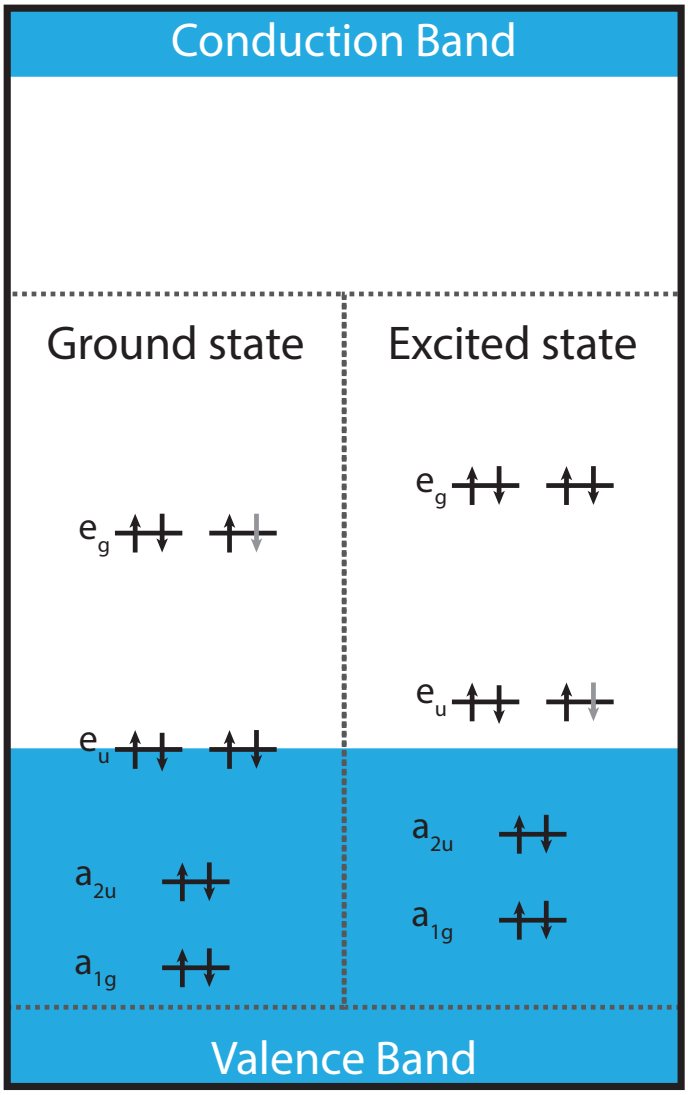

Figure 2.4: **Electronic states of a negatively charged G4V centre:** Schematic picture of the general electron state level structure of a negatively charged G4V centre within the diamond bandgap. The absolute positions of the levels differ for the four G4V centres and can be found partially in [100]. **a)** Depicted are the electron states that, in their entirety, constitue the orbital ground state of the G4V centre. The grey arrow in the highest energy e_g state indicates an unoccupied electron state, i.e. a hole. The states a_{2u} and a_{1g} lie deeply within the valence band and mix with the valence band states [100, 171, 172]. **b)** For the orbital excited state an electron from the e_u level is excited to fill the e_g level. Thus the hole is now left in the e_u state. Due to the different electronic configuration the electron states shift up with respect to the diamond band gap [100].

expresses itself in a distortion of the molecular symmetry in turn lowering the symmetry and thus lifting the degeneracy. The interaction is described as

$$\mathcal{H}_{\mathrm{g,e}}^{\mathrm{JT}} = \begin{pmatrix} \Upsilon_{\mathrm{g,ex}} & 0 & \Upsilon_{\mathrm{g,ey}} & 0 \\ 0 & \Upsilon_{\mathrm{g,ex}} & 0 & \Upsilon_{\mathrm{g,ey}} \\ \Upsilon_{\mathrm{g,ey}} & 0 & -\Upsilon_{\mathrm{g,ex}} & 0 \\ 0 & \Upsilon_{\mathrm{g,ey}} & 0 & -\Upsilon_{\mathrm{g,ex}} \end{pmatrix} \tag{2.2}$$

in the same basis states as used above. The JT coupling strengths are denoted as $\Upsilon_{\mathrm{x,y}}$, again potentially differing in ground (g) and excited state (e). The Hamiltonian of the JT effect has exactly the same shape as for describing crystal strain which reads

$$\mathcal{H}_{\mathrm{g,e}}^{\mathrm{Strain}} = \begin{pmatrix} \alpha_{\mathrm{g,e}} & 0 & \beta_{\mathrm{g,e}} & 0 \\ 0 & \alpha_{\mathrm{g,e}} & 0 & \beta_{\mathrm{g,e}} \\ \beta_{\mathrm{g,e}} & 0 & -\alpha_{\mathrm{g,e}} & 0 \\ 0 & \beta_{\mathrm{g,e}} & 0 & -\alpha_{\mathrm{g,e}} \end{pmatrix}, \tag{2.3}$$

the constants α, β denoting the response of the G4V centre to crystal strain. As a consequence, JT effect and the influence of strain cannot be distinguished in experiments on colour centres in diamond. For example, Hepp et al. introduced it to describe the level structure of the SiV^- centre in [99], however, it is not clear whether the splitting exceeding the SO coupling is due to JT effect, strain imposed by impurities or defects in the crystal matrix next to the colour centre or even by the distortion of the lattice induced by the impurity atom of the G4V centre itself. In the following, whenever we refer to the static JT effect it is important to keep the mentioned ambiguity in mind. Apart from the static JT effect a dynamic JT effect exists which occurs if more than one energy minimum for the molecular configuration exists. The molecule will tunnel between these positions, recovering the original symmetry and replacing the electronic by a vibrational degeneracy [173]. The effect is fast and will typically not be observed in experiments apart from causing a quenching of the SO interaction which is referred to as the Ham effect [174]. Therefore, the SO interaction and the static JT effect, respectively crystal strain, lift the degeneracy of the electronic orbitals while the dynamic JT effect diminishes the contribution of SO. The effects impact the e_{g} and e_{u} orbital, and thus ground $^2E_{\mathrm{g}}$ and excited state $^2E_{\mathrm{u}}$, differently.

	SiV^-	GeV^-	SnV^-	PbV^-
Δ_{gs}(theoretical) [100]	61 GHz	207 GHz	945 GHz	4385 GHz
Δ_{gs}(experimental)	46-50 GHz [99, 102, 121]	150-180 GHz [110, 175]	820-850 GHz [113, 136, 176]	3900-4230 GHz [116, 119]
Δ_{es} (theoretical) [100]	215 GHz	989 GHz	2925 GHz	6920 GHz
Δ_{es} (experimental)	250-260 GHz [99, 102, 121]	980-1120 GHz [110, 175]	≈3000 GHz [113, 136, 176]	n.a.

Table 2.1: **Orbital ground and excited state splittings for all G4V centres**

This can be explained by the fact that while the overall contribution of the impurity atoms orbitals to the wavefunction is small, it is larger in the excited state than in the ground state [100]. Since the SO interaction strength increases with the atomic number to the power of four, the SO splitting in the $^2E_{\mathrm{u}}$ excited state will be larger than in the $^2E_{\mathrm{g}}$ ground state. The effect is somewhat mitigated since the dynamic JT effect is quenching the SO interaction more heavily in the excited state [100]. The splitting in between the orbital ground, labeled Δ_{gs}, and excited states, labeled Δ_{es}, is depicted in Fig. 2.5. The transitions between the ground and excited states are optically dipole allowed since being of different parity and thus having a finite overlap when being subjected to the uneven parity electric dipole operator. Therefore, a four line fine structure spectrum as depicted in Fig. 2.11a) is the typical fingerprint of all G4V centres in diamond. In table 2.1, the

ground and excited state splittings for all G4V centres are given their theoretical values calculated in [100] and the corresponding experimentally discovered values. For the SnV^- centre [113,136,176] and the PbV^- centre [116,119] these values were only revealed during the course of this thesis. The last feature of the electronic structure to discuss is the spin degeneracy of the ground as well as the excited states. It is lifted under application of a magnetic field and leads to the Zeeman split states depicted in Fig. 2.5. The Hamiltonian of the interaction is given by the orbital (L) and spin (S) contributions to the Zeeman effect, yielding

$$\begin{aligned}\mathcal{H}^{\mathrm{Z}}_{\mathrm{g,e}} &= \mathcal{H}^{\mathrm{Z,L}}_{\mathrm{g,e}} + \mathcal{H}^{\mathrm{Z,S}}_{\mathrm{g,e}} = \mathrm{q}\gamma^{\mathrm{L}}_{\mathrm{g,e}} \begin{pmatrix} 0 & 0 & i\mathrm{B_z} & 0 \\ 0 & 0 & 0 & i\mathrm{B_z} \\ -i\mathrm{B_z} & 0 & 0 & 0 \\ 0 & -i\mathrm{B_z} & 0 & 0 \end{pmatrix} \\ &\quad + \gamma^{\mathrm{S}}_{\mathrm{g,e}} \begin{pmatrix} \mathrm{B_z} & \mathrm{B_x} - i\mathrm{B_y} & 0 & 0 \\ \mathrm{B_x} + i\mathrm{B_y} & -\mathrm{B_z} & 0 & 0 \\ 0 & 0 & \mathrm{B_z} & \mathrm{B_x} - i\mathrm{B_y} \\ 0 & 0 & \mathrm{B_x} + i\mathrm{B_y} & -\mathrm{B_z} \end{pmatrix}. \end{aligned} \tag{2.4}$$

The magnetic field $\mathbf{B}$ is expressed in the reference frame set by the internal coordinate system of the G4V centre [170] and the exact values of the gyromagnetic ratios $\gamma^{\mathrm{L,S}}_{\mathrm{g,e}} = \mathrm{g}^{\mathrm{L,S}}_{\mathrm{e,g}} \frac{\mu_{\mathrm{B}}}{\hbar}$ can differ in the ground and excited state due to variations in the Landé-factor $\mathrm{g}^{\mathrm{L,S}}$. Quenching of the orbital Zeeman effect is described by the Ham-factor q. The actual magnetic field dependence of the splittings, and therefore the spectral line positions, varies for the different G4V centres. It first of all depends on the orientation of the magnetic field with respect to the symmetry axis of the defect. Secondly, the different contributions of orbital and spin dependent Zeeman effect in ground and excited states lead to a splitting even of the transitions in between states with the same spin projection, so called spin-conserving (SC) transitions. For example transition A1 ($|1\downarrow\rangle \rightarrow |A\downarrow\rangle$) and B2 ($|2\uparrow\rangle \rightarrow |B\uparrow\rangle$) have a different transition energy, however, the extent of this effect varies among the G4V centres. A third effect occuring is the spin mixing in the presence of a magnetic field the axis of which exhibiting a finite angle with respect to the symmetry axis of the G4V centre. It manifests itself in the form of avoided crossings [99] and occurs at lower magnetic fields for the G4V centres with lower ground and excited state splittings. A simulated representative magneto-optical spectrum based on the full Hamiltonian

$$\mathcal{H}_{\mathrm{g,e}} = \mathcal{H}^{0}_{\mathrm{g,e}} + \mathcal{H}^{\mathrm{SO}}_{\mathrm{g,e}} + \mathcal{H}^{\mathrm{JT}}_{\mathrm{g,e}} + \mathcal{H}^{\mathrm{Strain}}_{\mathrm{g,e}} + \mathcal{H}^{\mathrm{Z,L}}_{\mathrm{g,e}} + \mathcal{H}^{\mathrm{Z,S}}_{\mathrm{g,e}}, \tag{2.5}$$

with $\mathcal{H}^{0}_{\mathrm{g,e}}$ representing the unpertubed system, is shown for the SnV^- centre in Fig. 2.6. The SO coupling is chosen to amount to 95 % (50 %) of the ground (excited) state splitting of 820 GHz (3030 GHz) while the static JT effect contributes 5 % (50 %). The angle in between the magnetic field and the symmetry axis of the centre is chosen to be 54.7° being representative for a SnV^- centre in a (100) oriented diamond sample while the magnetic field is pointing along the [100] axis. The four transition lines split up into sixteen transitions, among these are eight SC and eight spin-flipping (SF) transitions.

2.1.4 Phonon coupling and decoherence mechanism

The previous section assumed in most parts a perfect diamond lattice at a temperature of absolute zero. Since this is not given in experiments the impact of lattice vibration has to be taken into account. In quantum physics, diamond lattice vibrations are described by elementary excitations of these vibrations, the bosonic quasi-particles named phonons.

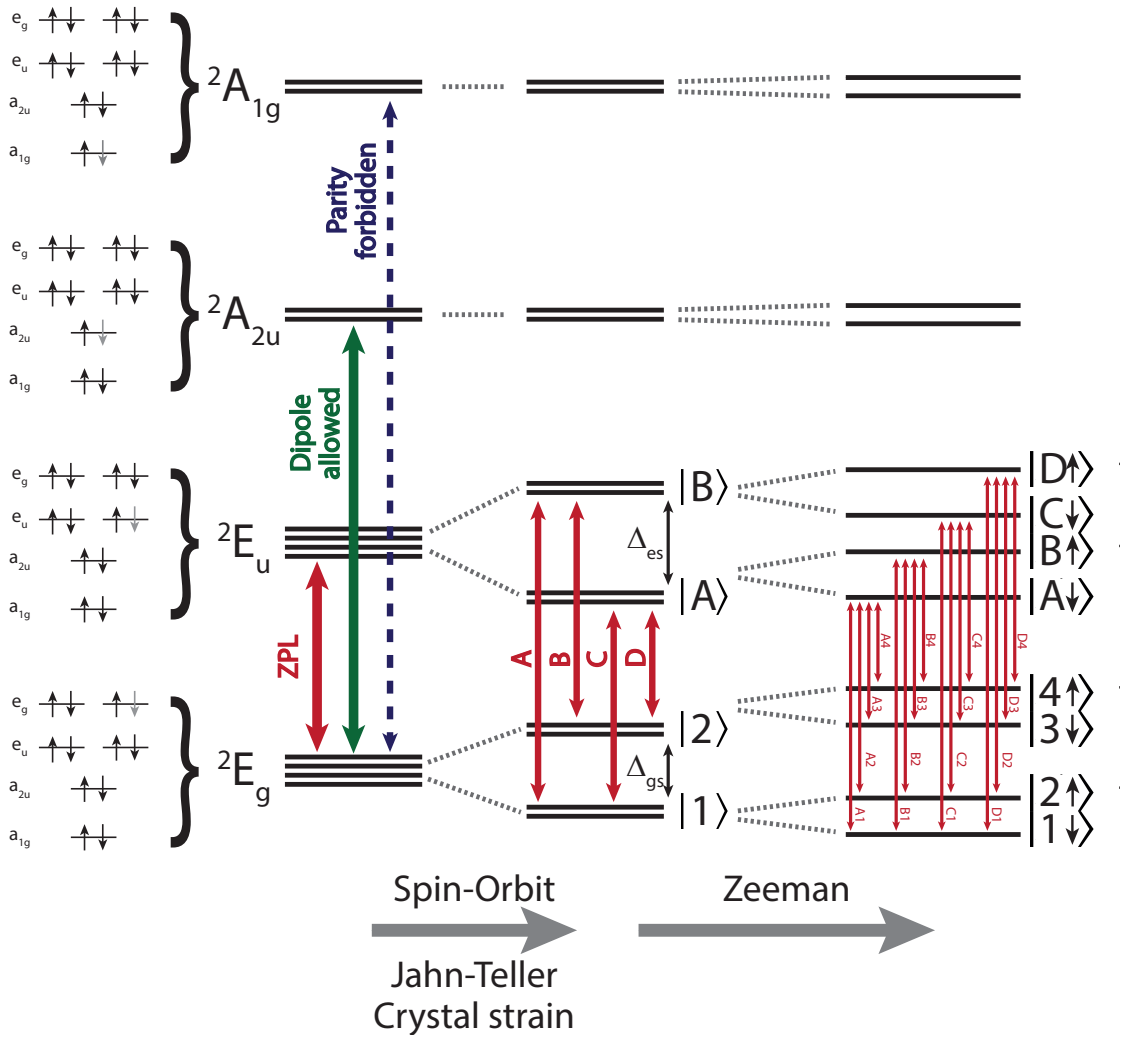

Figure 2.5: **Schematic of the electronic states of a negatively charged G4V centre:** On the left, the electronic states of the D_{3d} symmetric G4V centres resulting from group theoretical approaches are depicted. Spin-Orbit interaction, Jahn-Teller effect and crystal strain lift the orbital degeneracy. The spin degeneracy can be lifted by application of a magnetic field resulting in the Zeeman split level structure.

Their effect on colour centres in diamond is manifold, we will highlight here two important aspects. The first aspect aims at the fulfillment of the sixth and seventh criterion for QNN. Taking phonons into account has different effects on the photons being emitted by a colour centre. First of all, the emission spectrum will consist of two compositions. The ZPL comprises all photons emitted upon decay on optically allowed transitions not involving phonons. This spectral feature relates to the electronic transitions discovered in the previous section. In contrast, it is possible to fulfill the conservation of energy by emitting a lower energy photon compared to the ZPL while the excess energy is transferred to a lattice vibration. This results in a broad spectral feature red shifted to the ZPL that is called the phononic sideband (PSB). Absorption of a lattice vibration and subsequent emission of a higher energy photon is in general an allowed process but since its probability is very low the impact of this scenario on the emission spectrum is negligible. Physically, the underlying effect of the emission of lattice vibrations in the process of excited state decay

is the distortion of the diamond lattice by the change of the electron charge distribution when undergoing the transition from the excited to the ground state. Vice versa, if a lattice vibration is present the charge distribution of the electronic states will be affected und thus their overlap, giving rise to the energy of the transition between them. This can be described by a harmonic oscillator model intuitively introduced by Davies [177]. The important aspect is that colour centres exhibiting a similar charge distribution in the excited as in the ground state are emitting a larger amount of photons into their ZPL according to the Franck-Condon principle. This is favourable as only these coherently emitted photons can be used in QIP schemes where entanglement is achieved by interference of indistinguishable photons. Indistinguishability requires the same frequency and this is not guaranteed for photons emitted into the broad PSB but only for the ZPL. The spectral purity of an emitter with respect to photons being emitted without involving lattice vibrations is quantified by the Debye-Waller factor [178] at finite temperatures, respectively the Huang-Rhys factor at approximately 0 K. The Debye-Waller factor is given by the amount of photons that are emitted upon decay on the ZPL transitions I_{ZPL} divided by the overall number of photons being emitted. The latter consists of the ZPL photons as well as the photons of the PSB (I_{PSB}) and thus the definition of the Debye-Waller factor is given by

$$\mathrm{DW} = \frac{I_{\mathrm{ZPL}}}{I_{\mathrm{ZPL}} + I_{\mathrm{PSB}}} \tag{2.6}$$

This definition is universal for all temperatures, however, the density of states of phonons can be temperatur dependent and thus also the Debye-Waller factor. The Huang-Rhys factor S, defined as

$$S = -\ln(\mathrm{DW}(\mathrm{T{=}0K})), \tag{2.7}$$

is directly dependent of the Debye-Waller factor at zero Kelvin. It gives the average number of phonons being involved in an optical transition of the colour centre [173].
Having discussed the impact of phonons actually taking part in population transfers, there is a further effect caused by second-order phonon coupling [177] that only effects the phase of the excited state of the colour centre, which is called phonon broadening. It can be pictured as phonon collisions with the excited state and thereby randomly altering its phase. This dephasing leads to a homogeneous broadening of the electronic transitions at finite temperatures. It is strongly temperature dependent since its strength is determined by the lattice vibrations present in the diamond. For most applications it is thus necessary to operate G4V centres at cryogenic temperatures where the linewidth of the ZPL transitions is marginally affected by phonons and mainly determined by the time uncertainty of the decay of the excited state.
The second aspect of phonon-centre interactions apart from the optical coherence addresses the third criterion put forth by DiVincenzo. It emphasises the importance of long coherence times of the qubit system and thus the focus is upon the coherence in between quantum states rather than optical transitions. In this section we will focus on the main source of decoherence present for the G4V centres and furthermore different pathways to mitigate the effect. Therefore, it is necessary to determine the optimal choice of qubit states. Regarding the fine structure of the G4V centres it would be tempting to choose the two orbital ground states as qubit states as it has already be done in previous studies on the SiV^- centre [179]. However, transitions between orbital states can be driven by lattice vibrations. For example absorption of a phonon with an energy of $\hbar\Delta_{\mathrm{gs}}$ will transfer the G4V centre from state $|1\rangle$ to state $|2\rangle$. In the same manner, state $|2\rangle$ can decay into the lowest orbital ground state under the emission of a phonon with energy $\hbar\Delta_{\mathrm{gs}}$. At a given temperature both of these effects will take place simultaneously which is referred to as

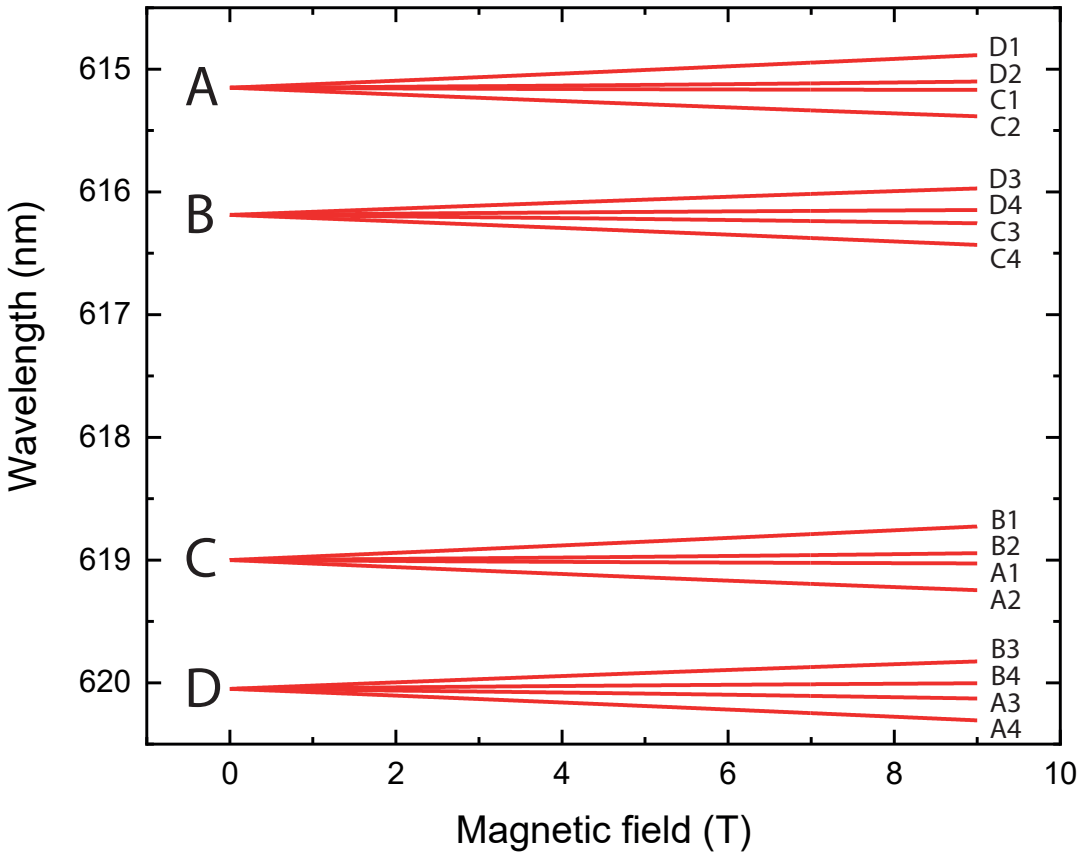

Figure 2.6: **Zeeman splitting of the transition spectrum of a SnV$^-$ centre:** Application of a magnetic field in an angle of 54.7° relative to the symmetry axis of the SnV$^-$ centre lifts the spin degeneracy of the energy levels and thus splits up the four transition lines into sixteen. In the simulation the static JT effect contributes to 5 % of the ground and 50 % of the excited state splitting.

thermalisation of the two states. The state population given by the statistical mixture in thermal equilibrium is dependent on the temperature as the occupation of the phonon modes resonant with the transition between the two orbital ground states is given by the Bose-Einstein distribution [120]

$$n(\Delta_{\mathrm{gs}}, \mathrm{T}) = \frac{1}{\exp(\frac{h\Delta_{\mathrm{gs}}}{k_{\mathrm{B}}\mathrm{T}}) - 1}. \tag{2.8}$$

This equation states that while emission of phonons is always possible the absorption of phonons is inhibited if there are no phonons present to drive the transition at temperatures $\mathrm{T} \ll \frac{\hbar\Delta_{\mathrm{gs}}}{k_{\mathrm{B}}}$. The resulting phonon absorption rate γ_+ is found [120] to amount to

$$\gamma_+ = 2\pi\chi\rho\Delta_{\mathrm{gs}}^3 n(\Delta_{\mathrm{gs}}, \mathrm{T}), \tag{2.9}$$

where χ and ρ are proportionality constants. This effect of thermalisation imposes strict boundaries on the coherence times between the orbital states as the thermalisation time scale τ_{therm} is on the order of several tens of nanoseconds for the SiV$^-$ centre at $T = 4\,\mathrm{K}$ [120, 179]. Cooling down does not diminish this decoherence mechanism for the orbital

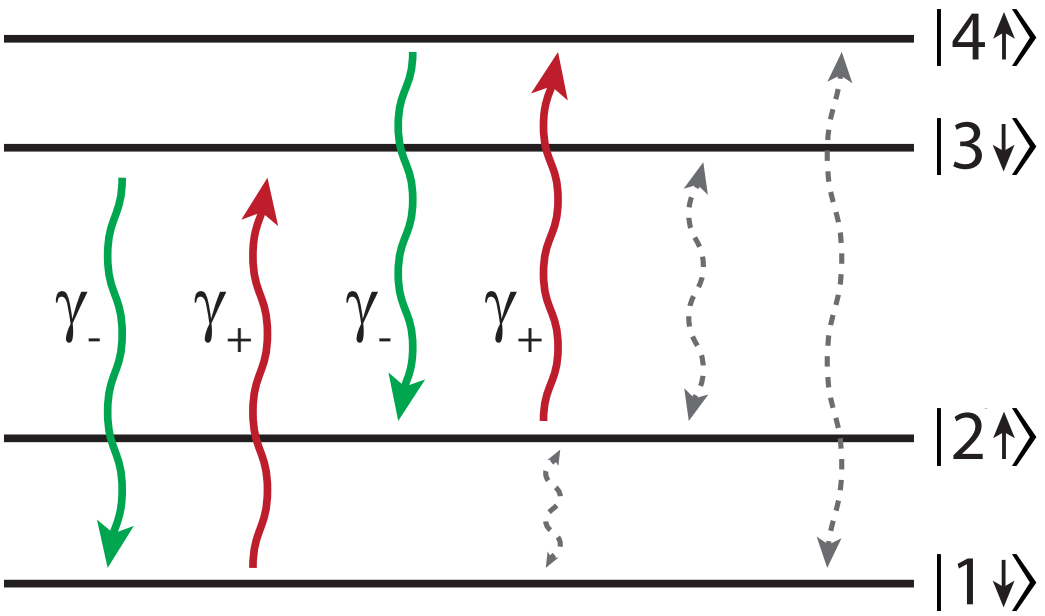

Figure 2.7: **Phonon induced decoherence processes of G4V centres:** Emission and absorption of phonons between the two orbital branches of the ground state induces decoherence. Even in the case of lifting the spin degeneracy of the lower branch in a magnetic field spin-conserving absorption of phonons can still induce significant decoherence of the qubit states. This absorption is reduced by increasing the orbital ground state splitting, reducing the temperature or incorporating the G4V centre in a phononic bandgap material.

states as state $|2\rangle$ will rapidly decay to state $|1\rangle$. Therefore, the orbital ground states cannot be used as a longtime coherent qubit, instead it is advantageous to utilise the spin degree of freedom of the lowest orbital ground state. By application of a magnetic field the degeneracy is lifted and the qubit is constituted by the states $|1\downarrow\rangle$ and $|2\uparrow\rangle$. The direct transition between these states driven by phonons is enabled only by spin mixing as phonons do not magnetically interact with their environment and thus drive exclusively transitions with an overlap between the spin wave functions of the involved states. Typically, the direct transition probability between the qubit states is thus very weak.

Having determined the qubit states of choice its coherence is nevertheless affected by phonons. While the direct transition between the two qubit states is not driven it is still possible to absorb a phonon and drive the transitions between the two orbital ground states of equal spin projection which is indicated in Fig. 2.7. This unwanted decoherence mechanism however can be mitigated as it solely relies on the absorption of phonons and therefore the occupation of the phonon mode resonant with the ground state splitting. There are three possibilities in order to minimise the latter:

1. **Temperature reduction:** The most intuitive way when evaluating equation 2.8 is to decrease the temperature until the phonon occupation becomes minimal, $n(\Delta_{gs}, T) \overset{T\to 0}{\longrightarrow} 0$. However, this comes at the price of additional technical overhead. For example, reasonable spin coherence times of a few milliseconds for the SiV^- centre, exhibiting the smallest ground state splitting of all G4V centres, have been shown to require temperatures below 400 mK [36]. These conditions are achievable by placing the sample in a helium dilution refrigerator, however, this cryostat is a

complex, large device and thus contradicts the wish for a scalable quantum processor system.

2. **Large ground state splitting:** Another pathway is to increase the ground state splitting such that $\exp(\frac{h\Delta_{gs}}{k_B T})-1 \gg \Delta_{gs}^3$ remains valid for higher temperatures, which is achievable in two ways: Firstly, application of strain increases the ground state splitting and has been used to improve the spin coherence [180]. This method has the disadvantage that strain is not only altering the ground state splitting but effects several properties of the G4V centre such as the general transition frequency [134,180] and the polarisation of the emitted light [170]. Therefore, it is not only difficult to apply strain to each qubit in a quantum processor but the strain has to have the same impact on each colour centre if the initial centres are equal in their physical properties. Elsewise, each centre has to be addressed individually and the desired ground state splitting and ZPL transition frequencies need to be fine-tuned. Both cases are challenging to achieve using common techniques for exerting strain on G4V centres. The second approach is to choose a G4V centre with an inherently large ground state splitting. The decoherence rates γ_+ for the G4V centres are depicted in Fig. 2.8 with the rates being normalised to the case of the unstrained SiV^- centre ($\Delta_{gs} = 46\,\mathrm{GHz}$) at $T = 4\,\mathrm{K}$, where the coherence time is known to be only tens of nanoseconds [120,179]. The dashed line between the green and the orange shaded area marks the decoherence rate of the strained SiV^- centre ($\Delta_{gs} = 80\,\mathrm{GHz}$) at 400 mK where millisecond coherence times were demonstrated [36]. This line is crossed for the unstrained GeV^- centre at a temperature of about 0.75 K, the SnV^- centre at 2.4 K and the PbV^- centre at about 9.8 K. Below these temperatures long spin coherence times should be achievable indicated by the green shading. For the SnV^- and the PbV^- centre these temperatures can be conveniently reached using closed-cycle helium cryostats imposing significantly less technical overhead. Additionally, a considerable effort is going on to miniaturise these devices and make them standard rack size compatible. The lightly orange shaded area indicates the transition zone where the coherence of the strained SiV^- centre dropped by about one order of magnitude when increasing the temperature from 400 to 600 mK. In the red shaded area coherence times will be severely limited by the phonon induced decoherence.

3. **Phononic bandgaps:** A further opportunity to achieve reduced phonon mode occupation is to implement phononic structures in the diamond host lattive surrounding the colour centre. For example a periodic hole pattern can induce a phononic band gap, in which phonons of a certain frequency cannot occur [181, 182]. Using nanodiamonds with sizes small enough to prevent phonon expansion presents another pathway. However, this requires the dimensions of the nanodiamonds not exceeding 100 nm for the SiV^- centre while the boundary conditions are increasing with the ground state splitting of the heavier G4V centres. As mentioned before, this will typically result in large inhomogeneities [134] and thus a proof of increasing the spin coherence time of G4V centres in these materials has not been demonstrated up until now.

In consequence of the above considerations the SnV^- centre was chosen as the most promising candidate to evaluate within this thesis. While the PbV^- centre is also an interesting candidate phonon coupling affecting the Debye-Waller factor is predicted to be significantly stronger for this colour centre [100] thus likely limiting its applicability.

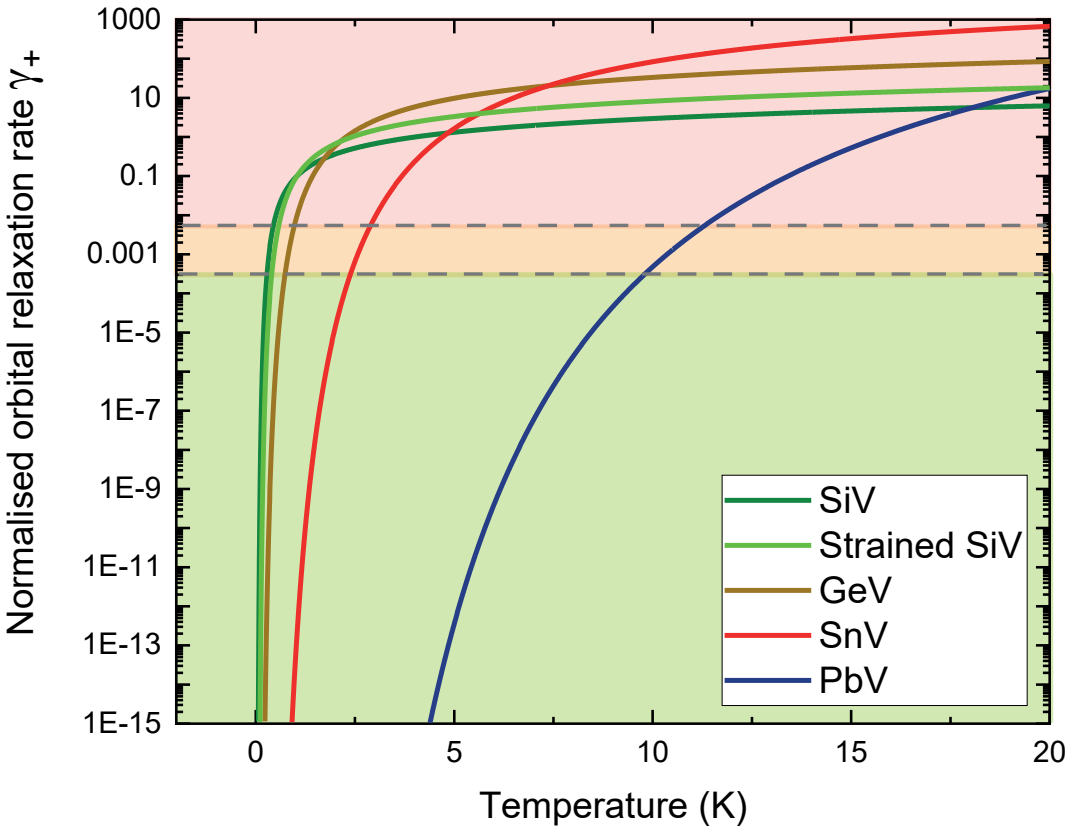

Figure 2.8: **Temperature dependence of the phonon induced decoherence rate:** Depicted is the temperature dependence of the thermalisation rate γ_+ upon phonon absorption between the lower and the upper branch of the orbital ground state for all G4V centres. The ground state splitting of the unstrained centres denoted in tab. 2.1 is assumed except for the strained SiV where $\Delta_{gs} = 80\,\mathrm{GHz}$ is extracted from ref. [36]. The green shaded area indicates long coherence times comparable to what is found in [36], in the orange area phonon coupling starts to significantly introduce decoherence, and in the red area the coherence properties are dominated by phonon decoherence.

2.1.5 Brightness of single photon emission

An important measure for application in QIP protocols is the brightness of a single photon emitter. It is determined by the following parameters:

- Quantum efficiency: The quantum efficiency η_{QE} is defined as the ratio of the radiative decay rate of a colour centre Γ_{rad} compared to the total decay rate given by the excited state lifetime Γ_{tot}. The latter includes also non-radiative decay channels ocurring for example by multi-phonon decay [122] and not producing a meaningful readout according to criterion three of DiVincenzo. The mathematical definition of the quantum efficiency is given by

$$\eta_{\mathrm{QE}} = \frac{\Gamma_{\mathrm{rad}}}{\Gamma_{\mathrm{tot}}}. \tag{2.10}$$

- Collection efficiency: The collection efficiency η_{CE} is defined as the fraction of the total radiatively emitted photon rate by a colour centre collected by an optical device Γ_{coll} such as a microscope objective. Therefore, it is strongly dependent of the numerical aperture (NA) of the device. Mathematically it can be written as

$$\eta_{\mathrm{CE}} = \frac{\Gamma_{\mathrm{coll}}}{\Gamma_{\mathrm{rad}}} \tag{2.11}$$

  and it is strongly limited for colour centres in diamond where it is well known that the difference in refractive index between diamond and air leads to total internal reflection and thus a preferential photon emission into bulk diamond, see [183] for a thorough discussion. This can be overcome by the implementation of nanophotonic structures [184, 185] such as optical antennas [186, 187], solid immersion lenses [125, 126], nanowires and -pillars [176, 188, 189], and photonic crystal cavities [128, 190, 191]. Another possibility is utilising diamond nanoparticles with the geometrical dimensions being smaller than the wavelength of the emitted light. However, while this can yield high count rates [147] colour centres in nanodiamonds are subject to large variations in strain and thus it is challenging to find several colour centres with identical properties [134].

- Charge stability: Instability of the charge state under resonant excitation is oftentimes observed for colour centres in diamond [104, 192, 193] and will play a crucial role within this thesis. For quantification we assume a charge transfer rate from the desired to an unwanted charge state Γ_{CT} and a repump rate Γ_{CR} set for example by an additional laser returning the colour centre to the desired charge state. The fraction of time that the emitter spends in the wanted charge state η_{CS} is then defined as

$$\eta_{\mathrm{CS}} = 1 - \frac{\Gamma_{\mathrm{CT}}}{\Gamma_{\mathrm{CT}} + \Gamma_{\mathrm{CR}}}. \tag{2.12}$$

  In the limits that either $\Gamma_{\mathrm{CT}} \longrightarrow 0$ or $\Gamma_{\mathrm{CT}} \ll \Gamma_{\mathrm{CR}}$ the value of η_{CS} approaches unity which is the favourable situation.

The overall detected photon rate Γ_{det} is then given by

$$\Gamma_{\mathrm{det}} = \eta_{\mathrm{det}}\eta_{\mathrm{loss}}\eta_{\mathrm{CS}}\eta_{\mathrm{CE}}\eta_{\mathrm{QE}}\Gamma_{\mathrm{tot}} \tag{2.13}$$

where we introduced η_{loss} to describe photon loss at optical components such as lenses and fibre couplings and η_{det} as the efficiency of the single photon detectors. The relative

brightness B_{rel} of the emitter can consequently be described as

$$B_{\mathrm{rel}} = \frac{\Gamma_{\mathrm{det}}}{\Gamma_{\mathrm{tot}}}. \tag{2.14}$$

We will here state the relative brightness achieved in experiments with single colour centres in bulk diamond for a fair comparison of the fundamental G4V centres' properties. The influence of coupling to nanophotonic devices and thus improved brightness is discussed in the respective section below. When considering QIP applications only the number of coherent photons emitted upon decay via ZPL transitions is of relevance and therefore we introduce the factor

$$B_{\mathrm{QIP}} = \mathrm{DW} \cdot B_{\mathrm{rel}}, \tag{2.15}$$

yielding exactly this number by multiplying the derived relative brightness B_{rel} from equation 2.14 by the Debye-Waller factor. In real world applications not only the relative factor B_{QIP} of the accessible fluorescence of a colour centre is interesting but furthermore the absolute value of the detected emission rate Γ_{det}, ultimately determined by the excited state lifetime, since it limits the repetition rate of QIP protocols. Therefore, we will always compare both of these values in order to characterise the brightness of a colour centre.

2.1.6 Spectral diffusion

A common limitation to the first criterion of DiVincenzo in the case of solid state quantum emitters is the impact of spectral diffusion on the resonance positions [129,136,194,195]. It originates from the Stark effect introduced by a fluctuating charge environment, typically created by an applied laser used for excitation of the qubit. This laser provides the energy for ionisation of surrounding defects and impurities in the diamond and thus influences the electric fields acting on the colour centre. The effect is minimised for G4V centres as their inversion symmetry protects them from first-order Stark shifts. In an inversion symmetric system no permanent dipole moment is present which could be addressed by an electric field in first order of pertubation. However, the electric field will introduce a shift in the charge distribution of the electrons breaking the inversion symmetry and inducing a dipole moment. The coupling of the electric field to this induced dipole moment is a second-order effect and thus its strength depends quadratically on the electric field strength. During the course of this thesis two experiments were performed probing the electric field dependence of the C-transition resonance line of single SnV^- centres. In both experiments a comparably small linear Stark shift and a dominant quadratic contribution was found for unstrained SnV^- centres [196,197]. The impact of strain, measured by an increase in the ground state splitting, lifts the inversion symmetry thus leading to the observation of significant linear contributions [196]. However, even in these studies of inversion symmetric, marginally strained SnV^- centres spectral diffusion was commonly observed. In Fig. 2.9, we depict the shift in the resonance position of a G4V centre using the parameters for the unstrained emitters extracted from [196, 197]. As SD originates from charges in the vicinity of the G4V centre in diamond we assume the electric field to be originating from a single charge with varyiing distance to the emitter. It can be seen that a single charge brought to a distance within 2 nm of the G4V centre can cause lineshifts of 250 MHz [196] up to about 1 GHz [197]. While the emitter in the study of Aghaeimeibodi et al. was specified to exhibit a ground state splitting of 820 GHz [196] which is attributed to the unstrained case within this thesis, the ground state splitting was not specified for the emitter under investigation by De Santis et al. [197]. Only a "typical" spectrum is depicted from which a ground state splitting of about 827 GHz can be extracted. Therefore, the larger electric

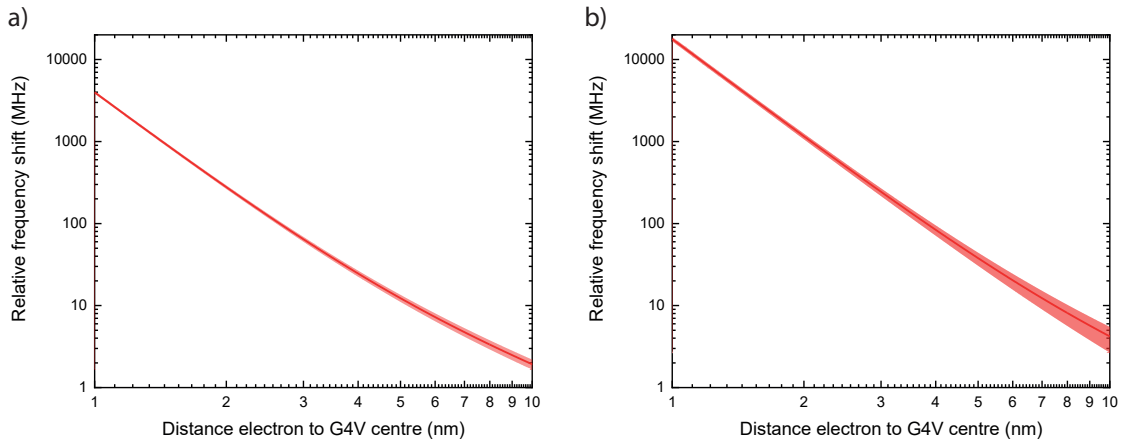

Figure 2.9: **Frequency shift of a G4V centre induced by the electric field of a single charge:** Depicted is the resonance shift of a G4V centre under the influence of an electric field imposed by a single charge at a variable distance to the colour centre. The proportionality parameters are extracted from studies conducted on the SnV^- centre by **a)** Aghaeimeibodi et al. [196] and **b)** De Santis et al. [197] with the red shading indicating the range of confindence inferred from the given error bars.

field sensitivity found in this study could be a result of slightly larger strain. Eitherway, these findings demonstrate that even few charges at moderate distances to the G4V centres can still cause significant lineshifts despite the inversion symmetry.

2.1.7 Members of the G4V-vacancy centre family

While the previous sections aim at giving an introduction to the general properties of the G4V centres, there nevertheless exist significant differences between them. We will here review the most important characteristics found in experiments and the state of the art on their applicability in QIP. An in-depth analysis of the historical findings and the discovery of the SiV^- centre as the first G4V centre however has been discussed in detail in several PhD theses [170, 198, 199] and will thus be omitted here.
As the research on G4V centres in diamond is a vividly evolving field especially since the experimental discovery of the SnV^- centre some of the findings presented here were only published throughout the course of this thesis. Therefore, there is overlap with the experimental results of this thesis and we will compare the results that we gathered to the findings summarised below.

The negatively charged silicon vacancy centre

The SiV^- centre is the most thoroughly studied of the G4V centres due to its early discovery as a silicon related defect in mid-nineties [164, 200]. We will therefore first review its properties and compare the studies on other G4V centres to it.

Spectral fingerprint and Debye-Waller factor of the SiV^- centre The fine structure described in sec. 2.1.3 gives an overview of the relative energies of the different transitions but group theory fails on assigning absolute energy values. The calculations obtained by DFT simulations put the ZPL at a wavelength (energy) of 729 nm (1.7 eV) [100]. This

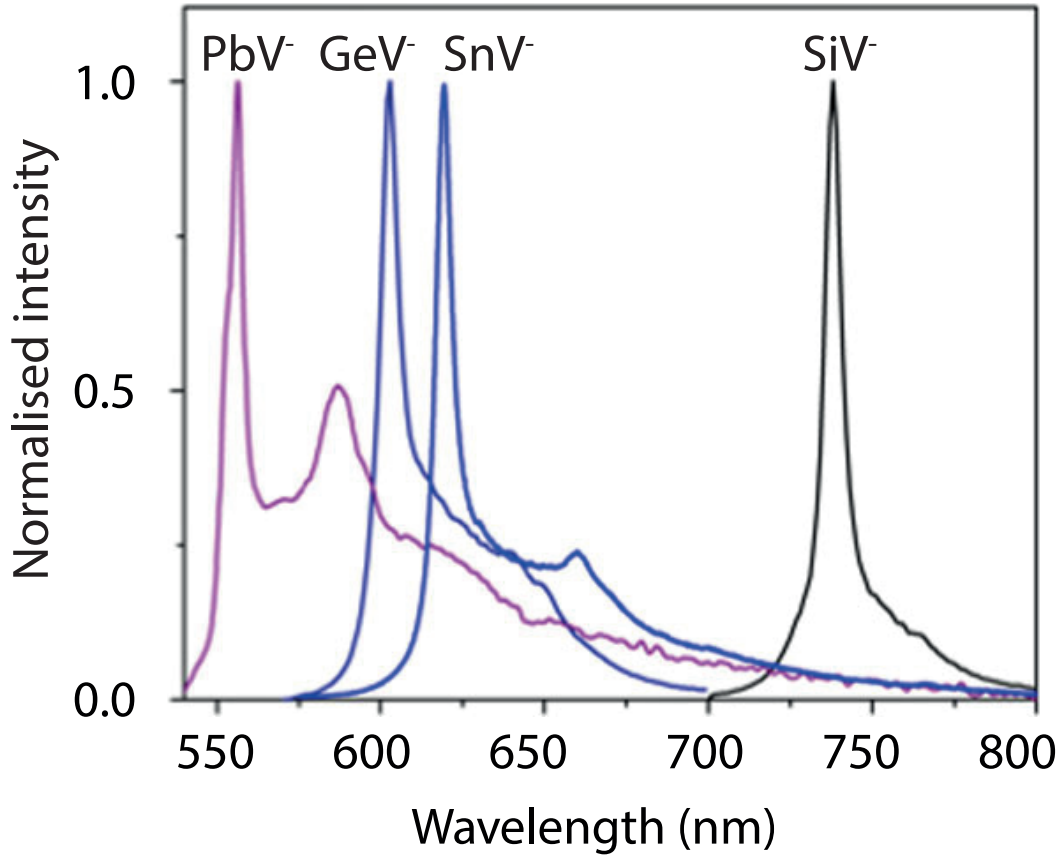

Figure 2.10: **Room temperature spectra of the G4V centres:** Comparison of typical spectra of all four G4V centres acquired at room temperature. The dominant peak corresponds to the ZPL while the PSB is constituted by the broad red shifted feature. The graph is reproduced with permission from [107].

is close to the experimentally observed 738 nm (1.68 eV) at room temperature [164, 200]. A typical spectrum taken at room temperature [107] is depicted in Fig. 2.10 with the ZPL constituting the dominant peak in the spectrum whereas the PSB is visible as the broad red shifted feature. The phonon coupling at room temperature is quantified by the DW factor and is reported in the range of $0.7 - 0.92$ [147, 201–203]. The ZPL being subject to minimised phonon broadening at a temperature of 4 K is shown in Fig. 2.11a). The now resovable optical transitions labeled A, B, C and D are revealed corresponding to the allowed finestructure transitions in between the two orbital excited and ground states, compare to Fig. 2.5. From the spectral distance between transitions A and B, respectively C and D the ground state splitting can be determined. For an unstrained SiV^- centre it corresponds to 46-50 GHz [99, 102, 121]. The distance between transitions A and C, respectively B and D corresponds to the excited state splitting being 150-180 GHz [110, 175] in a low strained diamond matrix.

Charge states of the SiV centre The previous discussion on the electronic structure assumed the negative charge state of the SiV centre being prevalent. However, there are other charge states possible and prediction of them is not straightforward. SiV^- centres

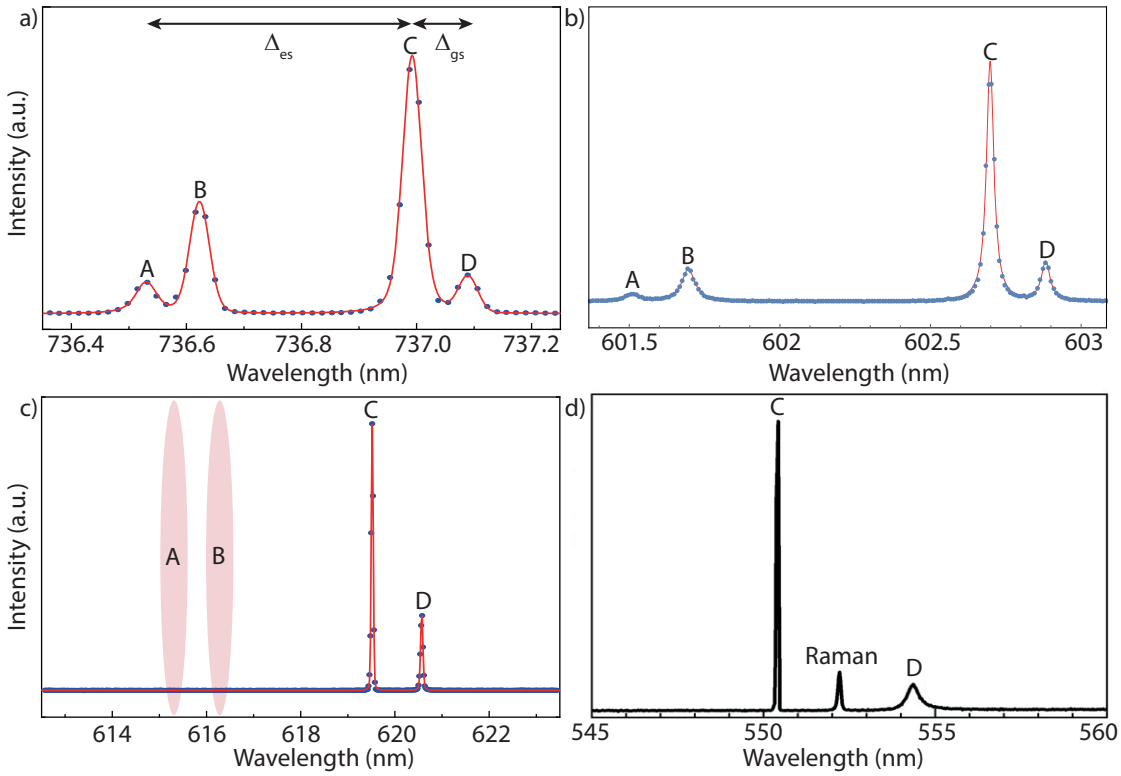

Figure 2.11: **Cryogenic temperature spectra of the G4V centres ZPL:** The fine structure of the G4V centres is revealed at cryogenic temperatures where the impact of phonon broadening is minimised. The excited state splitting corresponds to the energetic separation between peaks A-C and B-D while the ground state splitting can be extracted from the peak splitting of A-B and C-D. **a)**, **b)** Fine structures of the SiV^- at 4 K and GeV^- centre at 50 K exhibiting all four dipole allowed transitions. **c)** Fine structure of the SnV^- centre at 10 K. Only transitions C and D are visible due to the upper excited state being unoccupied at cryogenic temperatures. **d)** Similarly, for the PbV^- centre at 10 K just C and D can be resolved while the third peak is resulting from the Raman line of diamond. The plots in b) and d) are reproduced with permission from the American Physical Society from [110, 119] and [119], copyright 2022 American Chemical Society.

are typically detected by their optical signature obtained under laser excitation. However, the laser will not only excite the colour centre but also potentially ionise the G4V centre or even provide an additional electron from the valence band or an impurity atom in the vicinity of the G4V centre. Therefore, the charge state of the colour centre will be strongly dependent on the excitation conditions and the impurities and defects prevalent in the surrounding diamond matrix. The neutral charge state SiV^0 has its ZPL at 946 nm [167] but it is ionised to its negatively charged counterpart for excitation wavelengths shorter than 825 nm [204]. Thus, when exciting the SiV centre at typical excitation wavelengths shorter than the ZPL of the SiV^- the neutral charge state will hardly be detectable due to laser induced charge state conversion. Nevertheless, the SiV^0 centre is an interesting candidate for application in QIP due to promising long spin coherence times of about 250 ms [205], optically detectable magnetic resonances [206], a large Debye-Waller factor of 0.9 [205], and stable, narrow optical transitions. The complex electronic structure is not yet fully understood but can be potentially exploited for coherent control schemes [206,207].

On the down side, it suffers from rather low count rates even in material where the charge state is assumed to be stable [205].
The charge stability of the SiV^- centre is further limited as resonant optical excitation transfers the centre to its doubly negative charge state SiV^{2-} by laser induced electron capture from the valence band [137] when the centre is in its excited state. This charge state is optically inactive as all the electron orbitals are filled (compare Fig. 2.4) and it is therefore referred to as the dark state of the SiV centre. The charge transfer can be mitigated by applying green laser light to efficiently set the singly negative charge state of the SiV, an extensive characterisation of which can be found in the supplemental material of reference [104].

Brightness and quantum efficiency of the SiV^- centre The limited brightness of the SiV^- centre under resonant excitation in unstructured electronic grade diamond is oftentimes considered a major disadvantage and attributed to a low quantum efficiency on the order of $1-10\,\%$ [104,208,209]. For instance, in electronic grade bulk diamond brightnesses of about $B_{\mathrm{QIP}} \approx 10^{-5}$ and absolute count rates of about 1 kHz are reported [36,37]. There are two possible explanations for the low radiative yield: The first one is non-radiative decay mediated by several phonons or a metastable quantum state. The second possibility is that the low quantum efficiency results from the SiV^- centre residing significant amounts of time in a dark charge state. These effects are challenging to distinguish as their impact on the fluorescence is the same. Efficient charge state initialisation in combination with impressive light extraction by a nanophotonic cavity structure enabled the measurement of an excellent brightness of $B_{\mathrm{QIP}} \approx 0.14$ and a single photon detection rate of 31 kHz [191]. Without technical imperfections this brightness could have reached about 60 % approaching deterministic photon extraction. However, it is unclear whether the efficient charge state initialisation or the lifetime reduction due to Purcell enhancement improved the quantum efficiency. The latter would mean that the significant cavity enhancement sped up radiative processes such that they outperformed non-radiative ones. Without the application of a charge stabilising laser, the brightness of SiV^- centres is significantly higher in materials with a certain nitrogen content [37, 210, 211] in comparison to electronic grade diamond. This is again most likely due to a charge conversion from dark to bright state eased by the presence of interstitial nitrogen in the vicinity of the SiV centre and points towards the charge stability posing a significant limitation to the quantum efficiency.
Instead of using a nanophotonic crystal cavity, light extraction can be further enhanced when utilising nanodiamonds [212]. While the brightness in studies on nanodiamonds was still limited to below $B_{\mathrm{QIP}} \approx 10^{-3}$ absolute count rates of up to 4.5 MHz were measured [147]. Combining nanodiamonds with fibre-based micro resonators improved the brightness by about a factor of two, however, the absolute measured count rate was below 2 MHz.
In summary, the SiV^- centre is a relatively dim colour centre in diamond but its limitation can be overcome employing sophisticated nanofabrication and efficient charge state stabilisation.

Optical and spin coherence of the SiV^- centre For application in QIP the optical and spin coherence of a colour centre are of major importance. As mentioned above, the G4V centres benefit from their inversion symmetry and thus from a reduced influence of fluctuating electric fields in their vicinity on the position of optical resonances. It was therefore possible to demonstrate resonance linewidths broadened predominantly by the uncertainty of the radiative decay of the excited state [102]. Additionally, the line position seemed to be stable for several hours and the width of inhomogeneous broadening

affecting the line positions of several emitters observed in the study was on the same order of magnitude as the lifetime limited linewidth. These are remarkable results in terms of fulfilling the first criterion of DiVincenzo in being able to fabricate emitters with very similar properties. However, spectral diffusion does occur also for the SiV^- centre especially in nanofabricated structures and nanodiamonds [129, 213, 214]. These effects limit the applicability of the SiV^- centre and need to be overcome for QIP applications.
The second important coherence aspect concerns the dephasing of the lowest ground state spin qubit of the SiV^- centre. The effect of phonon induced decoherence was discussed in 2.1.4 and in accordance with it Sukachev et al. found long spin coherence times for the SiV^- centre being observable exclusively at millikelvin temperatures [36]. In their study they investigated two samples: sample 1 contained a natural abundance of ^{13}C nuclear spins (1.1 %), while sample 2 was isotopically purified to a concentration lower than 10^{-3} %. The spin dephasing time T_2^* was found to be 300 ns in sample 1 and up to 12 µs long in sample 2 at 100 mK. However, in both samples dynamical decoupling of environmental fluctuations yielded 1− 13 ms of spin coherence times $T^{2,dd}$ for four to thirtytwo decoupling pulses. The origin of the spin bath leading to the reduced spin dephasing time is unclear, since linear scaling of $T^{2,dd}$ with the number of applied decoupling pulses is counter to the expected scaling proportional to $N^{2/3}$ for dipolar interactions with nuclear spins [215, 216]. The authors explain the scaling by the presence of a fast and a slow noise source, where the first limits the spin dephasing time while the second is the origin of the reduced $T^{2,dd}$. Nevertheless, these spin coherence times meet the requirements for demonstration of memory enhanced quantum communication [101]. They can be further extended by transferring the coherence to a long-lived nuclear spin such as a neighbouring ^{13}C atom is carrying. This was achieved for the SiV^- centre, however, the coupling strength and protocol fidelities were moderate [105, 106].

Coupling to nanophotonic devices and application in QIP of the SiV^- centre
In order to strongly enhance light-matter interactions and the extraction of light from the diamond host matrix it is mandatory to couple G4V centres to nanophotonic devices. A broad review of the state of the art of quantum nanophotonics with G4V centres is given in [107]. We will here summarise the most recent achievements made on coupling the SiV^- centre to nanophotonic crystal cavities and the resulting applicability in QIP. In 2019, Nguyen et al. demonstrated the foundation for realisation of a quantum repeater with SiV^- centres by fabricating a one dimensional nanobeam structure coupled to a single SiV^- centre with a cooperativity of $C \approx 38$ [105, 129]. The latter is an important figure of merit as a cooperativity significantly exceeding one indicates working in the strong coupling regime where cavity-emitter interactions become deterministic. The system was addressed in a fibre based fashion by adiabatically coupling a tapered fibre to the nanobeam. Storage of a photonic qubit in a heralded fashion in the spin states of the SiV^- centre in the nanophotonic device was demonstrated making use of highly spin state dependent reflections of weak coherent pulses at the cavity. Furthermore, Nguyen et al. extended the possible storage time and implemented the option of quantum error correction by entangling the spin state of the SiV^- centre with a weakly coupled nearby ^{13}C nuclear spin. In a follow-up paper, Bhaskar et al. used an even stronger coupled cavity ($C \approx 100$) demonstrating memory enhanced quantum communication in an asynchronous Bell-state measurement [101]. The latter means, that the photonic qubit state of one of two communicating parties was stored in the SiV^- centre's spin qubit until the photon from the second party arrived and a Bell-state measurement could be performed. In order to achieve this, a time-bin encoded photonic qubit state was sent onto the cavity in

which the SiV^- centre spin qubit resided in a coherent 50:50 superposition. In between the two time bins the spin state was fully rotated such that if the early time-bin was not reflected (leaving the system in the non-reflecting spin state), the late time-bin would be reflected. The reflected photon heralded the storage of the photonic qubit state and thus the spin qubit quantum memory being prepared for the Bell-state measurement with the photonic qubit sent by the second party. This possibility of asynchronous measurement greatly enhances the speed of operation in systems with transmission losses (optical fibres, absorption in the atmosphere) compared to the case of utilising only linear optics, where it is necessary to rely on both photons arriving at the same time at a beam splitter (BS). Since the beforementioned achievements depend strongly on the fabrication of nanophotonic structures it is encouraging to see that even large scale implementation of hybrid photonic circuits with 128 integrated SiV^- and GeV^- centres have been realised [133].
The experiments summarised here demonstrate the greatly advanced applicability of the SiV^- centre in QIP protocols. Finally, an interesting new approach for addressing the SiV^- centre's spin qubit by surface acoustic waves lead recently to demonstration of coherent control [217] and even to efficiently coupling to a near ^{13}C nuclear spin [218]. While this design has not yet been used in QIP protocols it might turn out to be useful in future experiments.

The negatively charged germanium vacancy centre

Spectral fingerprint and Debye-Waller factor of the GeV^- centre The next heavier element in the periodic table is germanium and DFT simulations place the ZPL of the GeV^- centre at a wavelength (energy) of 585 nm (2.12 eV) [100]. This is again closely matching the experimentally observed 602 nm (2.06 eV) at room temperature [135, 175, 219, 220]. The room temperature spectrum is depicted in Fig. 2.10 [107] in which the dominant peak corresponds again to the ZPL. The PSB is more pronounced than for the SiV^- centre and the DW factor is reported to be $0.45 - 0.7$ [112, 219, 221]. It has to be noted that the ZPL's of single GeV^- centres created by ion implantation or knock-on doping exhibit a significantly larger spread ($\approx 1-4$ nm) than SiV^- centres after annealing at $800-950$ °C (supplemental [135], [163]). The ZPL at a temperature of 50 K is shown in Fig. 2.11b) [110]. At this temperature all four allowed transitions in between the two orbital excited and ground states are still visible in photoluminescence. At lower temperatures the upper orbital excited state is rapidly depopulated by fast phononic decay into the lower orbital excited state and thus the transitions A and B are hardly visible [219]. This is due to the larger orbital excited state splitting compared to the SiV^- centre. All splittings can be extracted in the same way as for the SiV^- centre and are stated in tab. 2.1.

Charge states of the GeV centre The GeV centre can reside in the same charge states as the SiV centre, however, up to now no signature of the neutral charge state could be found which is theoretically expected to have its ZPL at a wavelength (energy) of 689 nm (1.8 eV) [222]. This could be due to an even lower quantum efficiency of the defect compared to the SiV^0 centre or by an energetically unfavourable placement within the diamond bandgap requiring careful codoping for stabilisation. Chen et al. report the presence of a dark state of the GeV^- centre occuring under resonant excitation [193]. Since they employ the same 532 nm laser induced mitigation of the fluorescence termination as for the SiV^- centre it is most likely that this dark state again corresponds to the doubly negatively charged GeV centre. They also find a two step process being the reason for

the termination when the GeV^- centre is in its excited state, being in agreement with the electron capture process found for the SiV^- centre [137].

Brightness and quantum efficiency of the GeV^- centre The GeV^- centre faces similar limitations to its quantum efficiency and in turn brightness as the SiV^- centre. The quantum efficiency has been estimated to range between 3– 40 % [109–112] despite utilising 532 nm radiation for excitation which is claimed to mitigate the charge transfer to the dark state as stated in [193]. It is nevertheless very unlikely that multi-phonon induced decay for the significantly higher energy of the GeV^- centre's ZPL should be of comparable strength as for the SiV^- since the more phonons being involved in such a transition the unlikelier its probability [122]. This is further confirmed by the lifetime being independent of the temperature up to 450 K [110]. As it will be discussed within this thesis, the charge transfer to the dark state could still be a limiting factor since the charge dynamics of the GeV^- centre are not well understood. The brightness of single GeV^- centres in electronic grade bulk diamond reached up to $B_{\mathrm{QIP}} \approx 10^{-3}$ which is significantly larger than for the SiV^- centre and an absolute count rate of about 170 kHz was emitted into the ZPL. This increased brightness for high excitation powers of a 532 nm laser would again hint at improving the quantum efficiency by stabilising the charge state of the GeV^- centre. In nanodiamonds the brightness could be boosted due to more efficient light extraction by about one order of magnitude, approaching $B_{\mathrm{QIP}} \approx 10^{-2}$ [109] for count rates up to 750 kHz.

Optical and spin coherence of the GeV^- centre The GeV^- centre benefits from the same inversion symmetry as the other G4V centres, however, to the best of our knowledge the narrowest linewidths measured still exceed the lifetime limit by a factor of about two to three [108, 110] while others report more than one order of magnitude difference [193]. Furthermore, at powers exceeding the saturation value significantly spectral diffusion about one order of magnitude larger than the Fourier limited linewidth and blinking was observed [108,110]. Siyushev et al. measured the spin dephasing time at 2 K using coherent population trapping (CPT) and direct microwave driving yielding $T_2^* = 19$ ns [108]. This value is even shorter compared to the SiV^- centre at 4 K, seemingly counter to Fig. 2.8 as the orbital relaxation rate should be slightly lower. However, already at an increase in temperature of 0.8 K, the orbital relaxation rate for the GeV^- centre exceeds the value for the SiV^- centre by a factor of two. Thus, it has to be suspected that microwave or optical field induced heating in combination with non-optimal thermal anchoring caused the increase in the relaxation rate. Moreover, to the best of our knowledge the limited coherence time hindered the transfer of coherence to a neighbouring nuclear spin.

Coupling of the GeV^- centre to nanophotonic devices Coupling of the GeV^- centre to a waveguide including a bragg mirror has been achieved, however, the cooperativity of the device was limited to $C \approx 0.1$ [110] falling short of the values needed for application in QIP [101, 105]. An attempt at enhancing the fluorescence of a GeV^- centre in a fibre-based micro cavity succeeded in increasing the peak spectral density [111]. The actual retrieved count rate was unfortunately about an order of magnitude lower than without application of the cavity. Utilising a circular plasmonic Bragg cavity instead and coupling a GeV^- centre situated in a nanodiamond to the device resulted in a significant shortening of the radiative lifetime (factor 2-5) but also introduced a large background fluorescence, strongly diminishing the single photon character of the emitter [223]. To the best of our knowledge, no results approaching applicability of the GeV^- centre in QIP have been ob-

tained. Due to the combination of millikelvin temperatures for reaching long coherence times being required while suffering more strongly from environmental influences such as strain and charge fluctuations it is unlikely that the GeV^- centre will ever reach this point. Nevertheless, also GeV^- centres were integrated in the large scale hybrid photonic circuit mentioned in the section on the SiV^- centre [133].

The negatively charged tin vacancy centre

This part of the thesis overlaps partially with its experimental findings as most of the discoveries on the SnV^- centre were made during the conduct of our work. It is thus unavoidable to have some redundancy between the discoveries of other groups working on this subject and the results obtained by us. However, only the combination of both gives an overview as complete as possible on the SnV^- centre.

Spectral fingerprint and Debye-Waller factor of the SnV^- centre The ZPL as spectral fingerprint of the SnV^- centre in diamond was calculated to lie at a wavelength (energy) of 593 nm (2.09 eV) [100]. Experimentally it was found to lie close by at 620 nm (2.0 eV) at room temperature [113, 132]. The room temperature spectrum is depicted in Fig. 2.10 [107] with the ZPL dominating the spectrum. The PSB for this centre is again slightly more pronounced than for the SiV^- centre, however, the precise determination of the DW factor is addressed within this thesis. A first indicator that the significantly larger amount of lattice damage introduced by the implantation of the heavy tin ions (compare Fig. 2.2b)) needs to be lessened was revealed by the annealing study conducted in [113]. It was discovered that the room temperature line width of the ZPL of an ensemble of SnV^- centres narrowed by a factor of two when utilising annealing at 2100 °C and 7.7 GPa instead of 850 °C. The reached ensemble linewidth of about 6 nm is in agreement with single emitter linewidths in diamond of SiV^- and GeV^- centres. Furthermore, different defect centres of unknown origin showing photoluminescence were destroyed due to the high-pressure-high-temperature (HPHT) annealing. In a different study relying on annealing at a temperature of 950 °C, one of these remaining spectral peaks (centered at 631 nm) even led to confusing it with the local oscillator phonon mode resulting from the motion of the tin atom itself [132]. This is not the case as in the studies conducted in our work a significant amount of single emitters with a ZPL at this wavelength were found in low-temperature annealed samples, which is contradicting the local oscillator mode theory. Upon cooling down, the SnV^- ZPL splits up into its four transitions, however, at cryogenic temperatures of 10 K only transitions C and D are visible, see Fig. 2.11b). This is due to the even larger excited state splitting of about 3000 GHz resulting in a negligible population in the upper excited state at cryogenic temperatures [113]. The ground state splitting in the same study was found to be about 850 GHz large, however, the value for the unstrained SnV^- centre is revisited within this thesis.

Charge states of the SnV centre The different charge states of the SnV centre and especially the preparation of the negatively charged one are a main topic of this thesis. Different studies commented little on it but observed blinking and termination of fluorescence under resonant excitation [114, 132, 176, 195]. We leave the thorough discussion of this subject to chapter 5, however, it is noteworthy that an electronic transition centered at 645 nm was suspected to be the neutral charge state of the tin. This was refuted by its spectral dependence on the application of electric fields ([224], supplemental [197]).

Brightness and quantum efficiency of the SnV^- centre The first study conducted on the SnV^- centre estimated an astonishingly large quantum efficiency of $0.76 - 0.82$ for emitters in electronic grade bulk diamond [113]. The missing efficiency to unity has to be suspected to be again the result of improper charge state initialisation. The brightness of single SnV^- centres investigated in this and an accompanying study reached values of $B_{\mathrm{QIP}} \approx 10^{-3} - 5 \cdot 10^{-3}$ in electronic grade bulk diamond [113, 132]. The absolute count rate measured with a high NA objective yielded 1.37 MHz for the full spectrum being comparable with values obtained from nanodiamonds for the SiV^- and GeV^- centre. The incorporation of SnV^- centres into nanodiamonds succeeded, however, the colour centres seemed to be rather dim and no absolute value of the count rate was specified [149].

Optical and spin coherence of the SnV^- centre The optical coherence of the SnV^- centre is naturally a highly important property and thus was investigated by several groups in differently prepared samples. For implanted samples annealed at 1200 °C and subsequent fabrication of micro pillars as well as SnV^- centres fabricated by low energy implantation, subsequent diamond overgrowth and waveguide etching, resonance linewidths approaching the Fourier limit were found [176, 195]. Unfortunately, these emitters tend to exhibit pronounced spectral diffusion limiting their applicability [195,197]. We will show in chapter 6 that these properties can be further improved. The spin dephasing time was addressed in [114, 176] and found to be $0.5 - 1.3\,\mu s$. Dynamically decoupling the SnV^- centre's spin qubit from the environment resulted in an improved spin coherence time of $T^{2,\mathrm{dd}} \approx 300\,\mu s$. This brings the spin coherence of the SnV^- centre at a temperature of 2 K within reach of the SiV^- centre at millikelvin temperatures as expected from Fig. 2.8 owing to its larger ground state splitting. Additionally, first signs of coupling to a neighbouring ^{13}C nuclear spins have been detected [114].

Coupling of the SnV^- centre to nanophotonic devices Even though the SnV^- centre was discovered only in the recent past there has been serious effort to incorporate it into nanophotonic structures. Rugar, Aghaeimeibodi, Riedel et al. demonstrated a Purcell factor of about 24 for a SnV^- centre in a nanobeam structure [225]. The lifetime reduction was accompanied with a 40-fold increase of the emission intensity which unfortunately was still significantly lower than the emission in pure bulk material. An additional attempt to enhance the fluorescence emitted by single SnV^- centres utilised a monolithic cavity-based optical antenna structure designed by Fuchs et al. [186]. The device enabled larger than five-fold enhancements of the actually collected count rate compared to the bare diamond. This enhancement was accompanied by a reduction of the saturation power by a comparable factor as the excitation light enters the antenna more efficiently. The latter is of particular interest when working at cryogenic temperatures since it reduces heating effects by the excitation laser. Despite these impressive achievements we are not aware of any application of the SnV^- centre in QIP applications yet.

The negatively charged lead vacancy centre

The PbV^- centre was only discovered very recently and thus its characterisation is mainly limited to its luminescence properties that we will review in the following.

Spectral fingerprint and Debye-Waller factor of the PbV^- centre The large lattice damage introduced by implantation of lead ions into the diamond host matrix has hindered the straight away determination of its ZPL which was theoretically calculated to

lie at a wavelength (energy) of 517 nm (2.4 eV) [100]. A large variety of photoluminescence features occured in samples annealed at moderate temperatures up to 1200 °C leading to possibly wrong assignment of the ZPL doublet [115–118] observable at cryogenic temperatures. The conduction of a study on a HPHT annealed sample found most likely the correct assignment of photoluminescence features and ZPL transitions with the ZPL at room temperature lying at about 552 nm (2.25 eV) [119], see Fig. 2.10d). The Debye-Waller factor was not determined and remains subject for future studies.

2.2 Light - matter interactions in a three level system

The interaction of light and matter is the foundation of optical control of any form of qubit. Throughout the course of this thesis, a multitude of optical control and manipulation techniques such as qubit spin state initialisation and readout, Rabi oscillations and coherent population trapping are employed. The aim of this section is therefore to give an understanding of the underlying dynamics imposed by quantum mechanics and to apply them to the special case of the SnV^- centre. The section is set up in a way to explain the modelling of experimental findings and to highlight the extraction of important parameters from conducted measurements.

2.2.1 Level scheme & Master equation

Modelling the full fine structure of the SnV^- centre in the presence of a magnetic field which lifts the spin degeneracy, would require to take into account eight electronic levels. While this is possible and poses no major limitation, the description is lengthy, complex and the computational effort of simulating the quantum system is considerable. However, within the course of this thesis, all conducted experiments can be described by a simplified model that consists only of three electronic levels. In it we neglect the highest energy obital branch of the excited state, as it is far off detuned (about 3000 GHz) and any popolution quickly thermalises to the lower orbital branch at the low temperatures of typically 2 K used in the experiments.. Furthermore, in the presence of a magnetic field, the higher energy spin state in the lower orbital branch of the excited state is still far off detuned (>5 GHz) at typical magnetic field strengths and hardly affecting the population dynamics. Thus, all conducted experiments in our work can be described by a well known three-level Lambda system that consists of two ground states which are coupled via two light fields to the common excited state (see Fig. 2.12a)). In the following sections the three electronic levels can represent orbital states, when no magnetic field is applied, as well as spin states in the presence of a magnetic field. The respective sublevels being taken into account from the overall level structure depicted in Fig. 2.5 are highlighted in red in Fig. 2.12b),c). As there is mathematically no fundamental difference between the two situations, we describe the interaction Hamiltonian $\mathcal{H}$ of this driven Lambda system in a general notation and specify it when needed.
The ground states are energetically split up by $\hbar\Delta_{12}$, either due to the impact of SO and JT effect in the case of orbital states or due to the Zeeman effect for an applied magnetic field. Transitions between the ground and excited states can be driven by laser fields. The strength of the interactions between the Lambda system and the two light fields are described by their respective Rabi frequencies

$$\Omega_i = \frac{\vec{\mu}_i \vec{E}_i}{\hbar}. \tag{2.16}$$

The dipole moment of the given transition is denoted as $\vec{\mu}_i$, whereas $\vec{E}_i$ is the electric field of the incident laser radiation. The Hamiltonian of such a driven Lambda system under the rotating wave approximation is well known and its derivation can be found in various textbooks [226]. Its matrix form is given by

$$\mathcal{H} = \hbar \begin{pmatrix} 0 & 0 & \frac{\Omega_1}{2} \\ 0 & \Delta_1 - \Delta_2 & \frac{\Omega_2}{2} \\ \frac{\Omega_1}{2} & \frac{\Omega_2}{2} & \Delta_1 \end{pmatrix}, \tag{2.17}$$

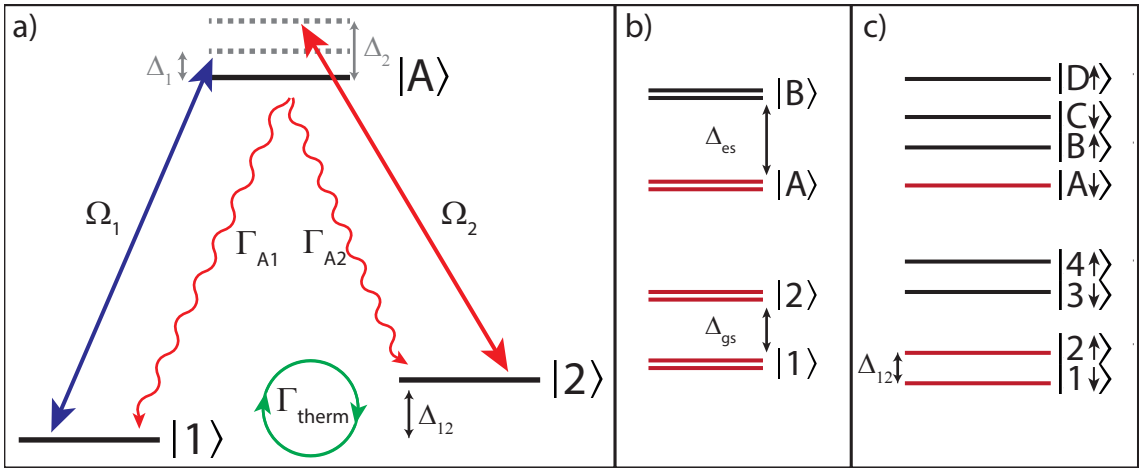

Figure 2.12: **Level scheme: a)** Generic scheme of a three level Lambda system with the states being either orbital or Zeeman split spin states. The spontaneous decay rates from state i to j are labeled Γ_{ij}, while Γ_{therm} labels the rate of thermalisation between the ground states. The interaction of the light fields with the quantum system is given by their Rabi frequency Ω_i, which can be energetically detuned from the excited state by Δ_i. The energetic splitting between the ground states is denoted as Δ_{12}. Sublevels constituting the Lambda scheme which are taken into account in the modelling are highlighted in red for **b)** the orbital and **c)** in the case of Zeeman split states.

where we introduced the detunings $\Delta_i = \omega_i - \omega_{iA}$ of the laser frequency ω_i with respect to the molecular transition frequency ω_{iA}. The Hamiltonian in its present form covers all coherent interactions and transitions from pure states to other pure states. In reality, not only mixed states need to be taken into account but also incoherent processes that diminish the coherence of quantum superposition states. Consequently we do not model our system using Schrödinger's equation but rather describe it employing a density matrix formalism and the master equation [226], which are suitable to cover statistical mixtures as well as decoherence. Within this formalism, the density matrix ρ describes the full state of the quantum system. The master equation itself is a differential equation for deriving the time evolution of the quantum system, which can be written down in its matrix representation as

$$\dot{\rho}(t) = -\frac{i}{\hbar}[\mathcal{H}, \rho] + \mathcal{L} + \mathcal{D}. \tag{2.18}$$

The brackets $[\mathcal{H}, \rho]$ denote the anticommutator of the Hamiltonian and the density matrix. This part of the equation covers all the coherent processes of the evolution in time. The sum of all Lindblad operators $\mathcal{L}_{ij}$ is given as the Lindblad superoperator $\mathcal{L}$ and describes the incoherent spontaneous decay of electronic states, while $\mathcal{D}$ implements pure dephasing of a quantum state without transfer of population. For the case of $\mathcal{L}$ and $\mathcal{D}$ being equal to zero, the equation is called von-Neumann equation, which is capable of describing the coherent evolution of a mixed state but fails to implement incoherent processes.
The spontaneous decay of an electronic state $|i\rangle$ into another electronic state $|j\rangle$ with a rate Γ_{ij} can be mathematically described employing the Lindblad operator

$$\mathcal{L}_{ij} = C_{ij}\rho C_{ij}^{\dagger} - \frac{1}{2}(C_{ij}^{\dagger}C_{ij}\rho^{\dagger} + \rho C_{ij}^{\dagger}C_{ij}) \tag{2.19}$$

where we introduced the collapse operators

$$C_{ij} = \sqrt{\Gamma_{ij}}\,|j\rangle\langle i|\,. \tag{2.20}$$

The Lindblad superoperator is then constructed as the sum of all Lindblad operators, namely

$$\mathcal{L} = \sum_{\substack{i,j \\ i \neq j}} \mathcal{L}_{ij}. \tag{2.21}$$

Pure dephasing with a rate d_i, which only randomises the phase of a quantum state $|i\rangle$ but does not induce transfer of population, is described in a very similar way by the dephasing operators

$$\mathcal{D}_i = d_i(\rho_{ii} |i\rangle \langle i| - \frac{1}{2}\{|i\rangle \langle i| \rho + \rho |i\rangle \langle i|\}), \tag{2.22}$$

which again sum up to

$$\mathcal{D} = \sum_i \mathcal{D}_i. \tag{2.23}$$

The mathematical concept derived so far is sufficient to govern the full evolution of the density matrix and thereby the quantum system. Since equation 2.18 is linear in ρ, it is possible to find a map $\mathscr{L}$, which is called the Liouville super operator, satisfying

$$\dot{\vec{\rho}} = \mathscr{L}\vec{\rho}. \tag{2.24}$$

It is important to note, that the density 3x3 matrix is now written down as a 9 dimensional vector. Therefore the matrix entries have simply been rearranged and put in order in the following way:

$$\begin{pmatrix} \rho_{11} & \rho_{12} & \rho_{13} \\ \rho_{21} & \rho_{22} & \rho_{23} \\ \rho_{31} & \rho_{32} & \rho_{33} \end{pmatrix} \longrightarrow \begin{pmatrix} \rho_{11} \\ \rho_{12} \\ \vdots \\ \rho_{32} \\ \rho_{33} \end{pmatrix}. \tag{2.25}$$

For the explicit expression of the operator $\mathscr{L}$, it is useful to define an effective Hamiltonian as

$$\mathcal{H}_{\text{eff}} = \mathcal{H} - \frac{i\hbar}{2}\left(\sum_{\substack{i,j \\ i \neq j}} C_{ij}^\dagger C_{ij} + \sum_i \mathcal{D}_i^\dagger \mathcal{D}_i\right). \tag{2.26}$$

Utilising the effective Hamiltonian we can calculate $\mathscr{L}$ according to [227] as

$$\mathscr{L} = i(\mathbb{1}_3 \otimes \mathcal{H}_{\text{eff}}^\dagger - \mathcal{H}_{\text{eff}} \otimes \mathbb{1}_3) + \sum_{\substack{i,j \\ i \neq j}} C_{ij} \otimes C_{ij}^\dagger + \sum_i \mathcal{D}_i \otimes \mathcal{D}_i^\dagger. \tag{2.27}$$

The advantage of this representation is that the solution of equation 2.24 can be calculated in a straightforward manner as

$$\vec{\rho} = \exp(2\pi\mathscr{L}t)\vec{\rho}_0, \tag{2.28}$$

where $\vec{\rho}_0$ describes the initial state of the quantum system. It is important to note, that this solution is only valid for the operator $\mathscr{L}$ being time invariant. While decay and dephasing rates are typically constant, the formalism is not suitable to describe series of laser pulses that are not rectangular or modulations of the laser detuning with time. We also explicitly wrote the factor 2π in front of $\mathscr{L}$, as it oftentimes leads to confusion whether technical or angular frequencies have to be entered in the model. In our model, all frequencies are **technical** frequencies and the factor 2π is taken care of in the last step of the computation.

The major advantage of the formalism overall in its present form is that it can be computed without the necessity of numerical solvers of differential equations, which tend to be needing excessive computational resources. Calculating the exponential function of a matrix is a computationally less resourceful approach and therefore speeds up simulations dramatically. In the following sections, we will start using this formalism by highlighting the decoherence mechanisms that are present for the SnV^- centre and continue by using the derived model for understanding and simulating a variety of important light-matter interactions encountered in the experimental part of this thesis.

2.2.2 Spontaneous decay induced decoherence of the orbital states of the SnV^- centre

Even for the subset of levels that we investigate with our model, there are a variety of decoherence processes present. In this section, we will explore the effects on the orbital states. First of all, the excited state will decay into the ground states. For the orbital states $|1\rangle, |2\rangle$ and $|A\rangle$ (see Fig. 2.12b)) the decay from level $|A\rangle$ into both ground states is allowed with equal probability. Therefore, the decay can be modelled using one single decay rate Γ, which enters into the two collapse operators as

$$C_{A1} = \sqrt{\frac{\Gamma}{2}} |A\rangle \langle 1| \tag{2.29}$$

$$C_{A2} = \sqrt{\frac{\Gamma}{2}} |A\rangle \langle 2| . \tag{2.30}$$

Both decays contribute equally to the radiative excited state lifetime τ_r, which is therefore inversely proportional to the decay rate via the relation

$$\Gamma = \frac{1}{2\pi\tau_\mathrm{r}}. \tag{2.31}$$

The transition between the two ground states can be driven by phonons as the constituents of the thermally induced diamond lattice and molecular vibrations [120]. However, these decay rates are strongly temperature dependent, as going from $|1\rangle$ to $|2\rangle$ requires the absorption of a phonon described by the rate Γ_abs, while the inverse process is a decay with rate Γ_em that emits a phonon. The latter is therefore possible at any temperature, while the absorption does only occur if the phonon mode with the energy corresponding to the ground state splitting is thermally occupied. In thermal equilibrium the population within the two ground states is Boltzmann distributed and the rates that lead to the equilibrium are mathematically described as

$$\Gamma_\mathrm{abs} = \Gamma_\mathrm{therm}\alpha_\mathrm{therm} \exp(-\frac{\hbar\Delta_{12}}{2k_\mathrm{B}\mathrm{T}}) \tag{2.32}$$

$$\Gamma_\mathrm{em} = \Gamma_\mathrm{therm}\alpha_\mathrm{therm} \exp(\frac{\hbar\Delta_{12}}{2k_\mathrm{B}\mathrm{T}}), \tag{2.33}$$

with

$$\alpha_\mathrm{therm} = \frac{1}{\exp(\frac{\hbar\Delta_{12}}{2k_\mathrm{B}\mathrm{T}}) + \exp(-\frac{\hbar\Delta_{12}}{2k_\mathrm{B}\mathrm{T}})}. \tag{2.34}$$

Γ_therm denotes the shared thermalisation rate, the Boltzmann factor is given by k_B and the temperature as T. In the experiment, only the effective rate $\Gamma_\mathrm{therm} = \frac{1}{2\pi\tau_\mathrm{therm}}$ can be measured for the given temperature, which is defined by the time scale τ_therm of the exponential law with which the system returns to the thermal equilibrium population after

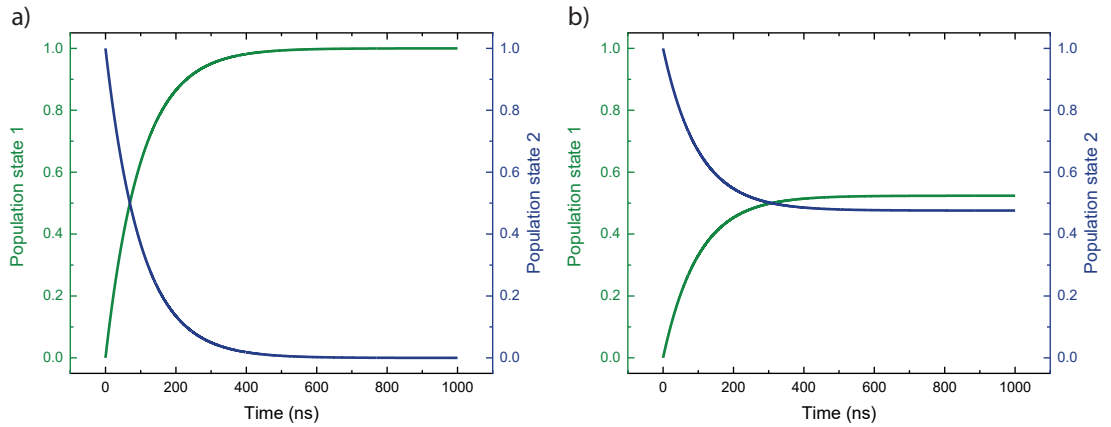

Figure 2.13: **Thermalisation within the ground states of the SnV$^-$ centre: a)** Simulated time evolution of the ground states after preparing the population in state $|2\rangle$ and letting the system thermalise. The ratio between the equilibrium populations depends on the ground state splitting set to 820 GHz and the temperature of 2 K. The thermalisation time scale is artificially set to 100 ns. **b)** Simulation with the same parameters, except the ground state splitting being reduced to a typical Zeeman splitting of 4 GHz observed within this thesis. In this case the equilibrium population is close to 50 % in each of the ground states.

being disturbed from it. Fig. 2.13a) displays this case for the system being prepared in state $|2\rangle$ at a temperature of 2 K, a fictional thermalisation time scale of $\tau_{\text{therm}} = 100$ ns and the orbital ground state splitting of the SnV$^-$ centre $\Delta_{12} = 820$ GHz. It can be seen that with the time constant of 100 ns the population prepared in state $|2\rangle$ decays almost completely (less than 10^{-6} % remains) into the lower state $|1\rangle$ until the ratio between the populations equals the ratio between the rates of the absorption and emission rate, which is

$$\frac{\Gamma_{\text{abs}}}{\Gamma_{\text{em}}} = \exp(-\frac{\hbar\Delta_{12}}{k_{\text{B}}\text{T}}). \tag{2.35}$$

For comparison, we plot the same graph for a reduced ground state splitting of $\Delta_{12} = 4$ GHz, which is a typical Zeeman splitting at a magnetic field of 200 mT applied with an angle of 54.7° with respect to the symmetry axis of the SnV$^-$ centre. In this case, the ratio between the populations approaches almost 50 % in each of the two states. We would like to emphasise that the timescale of the process simulated here is only for instructive purposes and does not resemble the experimental values found within our work.

2.2.3 Rabi oscillations between orbital states

Rabi oscillations have been observed in many experiments and are the most popular coherent process in quantum mechanics. They occur when a transition between two quantum states is coherently driven, for example by a laser, and are observable as an interchange of population between the two quantum states. The population dynamics follow a sinusoidal time dependence with the frequency of the oscillations being given by the Rabi-frequency of the applied laser field. There are two factors that can only be explained when taking into account coherence in the system: First of all, the oscillation can lead to a complete population inversion, which is called a $\pi-$rotation. This is not achievable with incoherent

light sources, which can at maximum transfer the system into a 50:50 mixed state. The second aspect is visible when using laser pulses. If a laser pulse is applied that transfers the system into a coherent 50:50 superposition of ground and excited state, a so called $\frac{\pi}{2}-$pulse, the system ends up in a state

$$|\psi_\pi\rangle = \frac{1}{\sqrt{2}}(|1\rangle + |A\rangle). \tag{2.36}$$

In contrast to classical analogues, the oscillation can be continued from this point on as long as the coherence is preserved and the phase relation between the two states stays the same. This means that application of two subsequent phase-coherent $\frac{\pi}{2}-$pulses is equivalent to one $\pi-$pulse. These two features are very important in many QIP protocols, for example retrival of a photon with maximum probability from the system is achievable by applying a resonant $\pi-$pulse in between a ground and excited state. Furthermore, it is used to generate superposition states with different population contributions of the involved states. These operations are a subset of the single qubit gates specified in the fourth DiVincenzo criterion. In Fig. 2.14, Rabi oscillations between ground state $|2\rangle$ and excited state $|A\rangle$ for Rabi frequencies of 100 MHz and 200 MHz are depicted. In a) no damping due to spontaneous decay is assumed for giving an intuition of perfectly coherent interactions of laser fields with quantum systems. However, in reality the excited state lifetime imposes a limitation on this coherent population transfer. It can be seen in Fig. 2.14b) how the oscillations are damped due to the decay of the excited state with a time constant of $\tau_\mathrm{r} = 7$ ns. However, it is noteworthy that the time scale of the enveloppe of the exponentially damped Rabi oscillations is equal to $\frac{4}{3}\tau_\mathrm{r}$. This result was analytically derived in [228] and confirmed in our simulations. We do point this out, as it is in many textbooks confused to be twice the radiative lifetime. The decay channel from the excited state to the ground state $|1\rangle$ is neglected in the simulations for simplicity reasons. The relationship between laser power and Rabi frequency becomes clear from equation 2.16. The laser power is proportional to the square of the electric field and thus the square root of the laser power P is directly proportional to the Rabi frequency

$$\sqrt{P} \propto \Omega. \tag{2.37}$$

We will use the proportionality later to convert laser power to Rabi-frequency and thereby enabling adequate theoretical modelling.

2.2.4 Decoherence processes of the spin states of the SnV^- centre

The decoherence properties differ for the case of using spin states in the presence of a magnetic field. In this section we will focus on the main spin states that are utilised within this thesis. The spin qubit is formed by the Zeeman split levels of the lowest orbital state ($|1\downarrow\rangle, |2\uparrow\rangle$), see Fig. 2.5. As excited state, we choose the spin down state of the lower excited orbital state, $|A\downarrow\rangle$. It is straighforward to adapt the theory within this section to the excited state $|B\uparrow\rangle$, while the spin states of the higher excited orbital state cannot be used due to a very rapid phononic decay to the lower excited state at typical temperatures of about 2 K. The same holds true for the higher orbital ground state, which exhibits no significant thermal population at $T = 2$ K due to a very fast phononic decay channel into the lower orbital ground state.
For the excited state $|A\downarrow\rangle$ the decay rates into the two ground states do now significantly differ from each other. The decay into state $|1\downarrow\rangle$, which preserves the spin state, is allowed due to the transition being spin-conserving and the corresponding rate is labeled Γ_SC. On

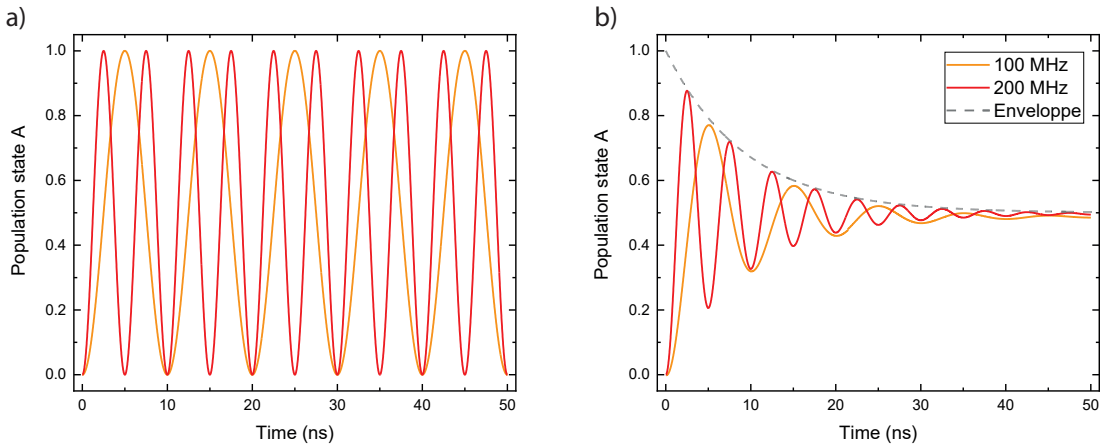

Figure 2.14: **Rabi oscillations: a)** Laser induced Rabi oscillations indicated by coherent population transfer from the ground state $|2\rangle$ to the excited state $|A\rangle$. The Rabi frequency imposed by the laser is set either to 100 MHz or to 200 MHz. The excited state lifetime is assumed to be infinite and thus no decoherence is induced by it. **b)** Simulation of the realistic scenario of an excited state lifetime $\tau_r = 7$ ns. The oscillations are damped due to the decoherence induced by the spontaneous decay. The decay channel into state $|1\rangle$ is neglected for the sake of simplicity. The enveloppe of the Rabi oscillations decays with a time constant equal to $\frac{4}{3}\tau_r$.

the contrary, the decay from the excited state $|A\downarrow\rangle$ into the ground state $|2\uparrow\rangle$, which is of orthogonal spin projection, is forbidden by spin selection rules. These selection rules are only slightly weakened due to the SnV^- centre not being an isolated atom but within the diamond lattice that is subject to strain and JT effect. They can be additionally lowered by spin mixing in the case of an magnetic field being applied with a relative angle to the symmetry axis of the defect [36, 114]. Debroux et al. find that the strength of the SF transition of an unstrained SnV^- centre (see supplemental material of reference [114]) can be approximated to be proportional to

$$\frac{\gamma_e^2 B_\perp^2}{2\lambda_{SO}^2}. \tag{2.38}$$

Here, $\gamma_e = \frac{2\mu_B}{\hbar}$ denotes the gyromagnetic ratio, $B_\perp$ the strength of the magnetic field perpendicular to the defect axis and λ_{SO} the strength of the SO interaction in the ground state manifold. The transition is nevertheless labeled a spin flipping transition and the decay rate satisfies $\Gamma_{SF} \ll \Gamma_{SC}$. Therefore, in good approximation, the spontaneous decay of the excited state is largely dominated by the decay on the SC transition and thus

$$\Gamma_{SC} \approx \frac{1}{2\pi\tau_r}. \tag{2.39}$$

In reality the decay into the second orbital ground state does take place but the population rapidly decays ($\gg \Gamma_{SC}$) into the lowest ground state. This is equivalent to modelling it as direct decay into the lowest orbital ground state as the decoherence induced by the excited state lifetime is captured and the population transfer into the lowest orbital ground state with time constant τ_r as well. The relative strength of the two transitions is described by the branching ratio

$$\eta_{\text{cyling}} = \frac{\Gamma_{SC}}{\Gamma_{SF}}. \tag{2.40}$$

As we will find in chapter 6, both rates differ about 3 orders of magnitude even for a large angle between the magnetic field axis and the symmetry axis of the SnV^- centre. The corresponding collapse operators are therefore given by

$$C_{A1} = \sqrt{\Gamma_{\mathrm{SC}}}\,|A\downarrow\rangle\langle 1\downarrow| \tag{2.41}$$

$$C_{A2} = \sqrt{\Gamma_{\mathrm{SF}}}\,|A\downarrow\rangle\langle 2\uparrow|\,. \tag{2.42}$$

The transition between the two ground states is also a SF transition and therefore cannot be driven by phonons, which do not carry a magnetic moment. Again, this selection rule is slightly weakened due to spin mixing. It will turn out in chapter 6 that the spin states return to a thermal equilibrium population even after being properly initialised in either one of the states, but the time constant $T_{1,\mathrm{spin}}$ of this process is comparably slow and happens on the order of milliseconds. The corresponding decay rate at a given temperature is $\Gamma_{\mathrm{spin}} = \frac{1}{2\pi T_{1,\mathrm{spin}}}$ and the decay rates leading to the thermal equilibrium are given by

$$\Gamma_{\mathrm{abs,spin}} = \Gamma_{\mathrm{spin}}\alpha_{\mathrm{therm}}\exp(-\frac{\hbar\Delta_{12}}{2k_{\mathrm{B}}\mathrm{T}}) \tag{2.43}$$

$$\Gamma_{\mathrm{em,spin}} = \Gamma_{\mathrm{spin}}\alpha_{\mathrm{therm}}\exp(\frac{\hbar\Delta_{12}}{2k_{\mathrm{B}}\mathrm{T}}), \tag{2.44}$$

where the ground state splitting Δ_{12} is now depending on the strength of the magnetic field, which splits up the spin states.

2.2.5 Optical pumping & Single-shot readout of the spin states of the SnV^- centre

For every starting point of a QIP protocol with a qubit, it is necessary to initialise the qubit in a well defined state according to the second DiVincenzo criterion. Therefore, it is usually required to have all the population of the qubit transferred to one particular quantum state. Consequently, one needs to bring the qubit from a mixed thermal equilibrium state into a well defined pure state. This can be done by optical pumping. Recalling the spin selection rules and the slow thermalisation rate of the spin qubit from the previous section, one can drive the SC transition with a laser and while the population will cycle numerous times on this SC transition, at some point the spin state will be flipped to state $|2\uparrow\rangle$. In this state it will remain for time scales given by the spin lifetime $T_{1,\mathrm{spin}}$. In Fig. 2.15a) the effect of optical pumping on the spin state populations is depicted for a lifetime of $\tau_{\mathrm{r}} = 7\,\mathrm{ns}$, a branching ratio of $\eta_{\mathrm{cycling}} = 1000$ and a pump Rabi frequency of 100 MHz. When applying the laser, the population in state $|1\downarrow\rangle$ is transferred partially to the excited state. As soon as the decoherence imposed by the radiative lifetime of the excited state has unfolded, the system is in a mixed state with 50 % of the population cycling between state $|1\downarrow\rangle$ and $|A\downarrow\rangle$ and 50 % in state $|2\uparrow\rangle$. The cycling population slowly decays in a mono-exponential way into state $|2\uparrow\rangle$, where it resides. At sufficiently long pump times, the system is initialised in state $|2\uparrow\rangle$. As an important figure of merit, the initialisation efficiency η_{eff} of the protocol is directly related to the fraction of the remaining population ϵ_{rem} in state $|1\downarrow\rangle$ via the relation

$$\eta_{\mathrm{eff}} = 1 - \epsilon_{\mathrm{rem}}. \tag{2.45}$$

Apart from the efficiency of the initialisation, also the time scale on which it can be achieved is of interest. For laser powers that do not saturate the SC transition, the speed increases with increasing laser power. In contrast to this finding, in the case of laser

powers significantly larger than the saturation power, the time scale τ_{pump} approaches its maximum given by the spin flipping rate Γ_{SF} as

$$\tau_{\text{pump}} = \frac{2}{\Gamma_{\text{SF}}}. \tag{2.46}$$

The factor two results from the fact that incoherent pumping will only populate the excited state with half of the population residing in state $|1\downarrow\rangle$ and thus it takes twice the time compared to direct decay from state $|A\downarrow\rangle$ to state $|2\uparrow\rangle$. By taking the inverse of the pumping time the pumping rate $\gamma_{\text{pump}} = \frac{1}{\tau_{\text{pump}}}$ is defined. This rate saturates with laser power P according to the formula

$$\gamma_{\text{pump}} = \frac{\Gamma_{\text{SC}}}{2\eta_{\text{cycling}}} \frac{P}{P + P_{\text{sat}}}, \tag{2.47}$$

in analogy to what is derived in [229] (p.142-143). P_{sat} denotes the saturation power of the SC transition. Consequently, the speed of an initialisation pulse is ultimately limited by the intrinsic dynamics of the SnV^- centre. These dynamics can be modified by the use of cavities or application of strain, however, this imposes further technical difficulties. The saturation of the pumping rate gives a direct measurement tool of the branching ratio $\eta_{\text{cycling}}$when the excited state lifetime and thus Γ_{SC} is known. Faster initialisation speed can be reached by pumping on the SF transition, as the speed is now only limited by Γ_{SC} and the available laser power.

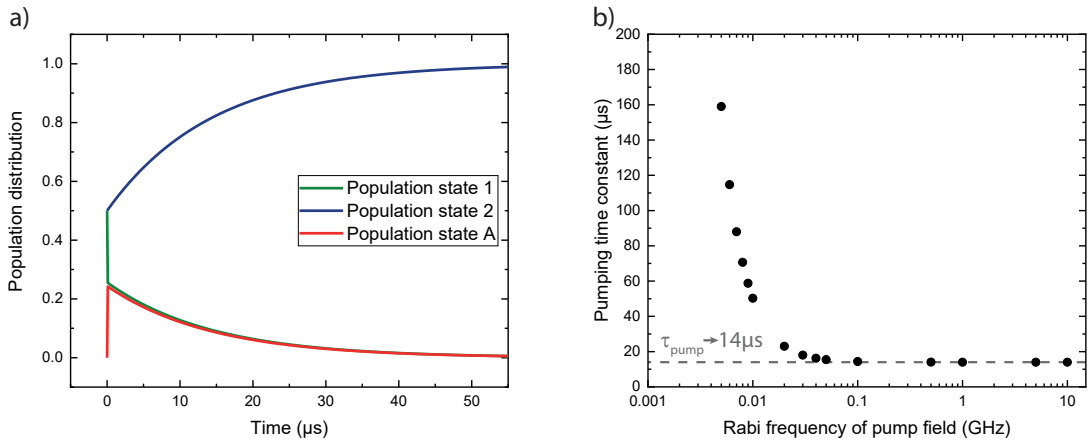

Figure 2.15: **Simulation of optical pumping: a)** The system starts in thermal equilibrium in which about 50 % of the population resides in each of the ground state spin states while the excited state is not populated. Application of a pump laser on the SC transition with a Rabi frequency of 100 MHz induces cycling of the population between state $|1\downarrow\rangle$ and $|A\downarrow\rangle$. Due to the short radiative lifetime of the excited state of $\tau_{\text{r}} = 7$ ns the population transfer quickly becomes incoherent, see Fig. 2.14b), and creates a mixed state with about 25 % in state $|1\downarrow\rangle$ and $|A\downarrow\rangle$ each. The SF transition, which is set to be a factor of 1000 weaker than the SC transition, enables flipping of the spin state and thus the population is initialised in state $|2\uparrow\rangle$ after sufficiently long pumping time. **b)** The time constant τ_{pump} of the pump process is plotted against the Rabi frequency of the pump laser. For large Rabi frequencies on the order of the excited state decay $\Gamma_{\text{SC}} = \frac{1}{7}$GHz, the time scale saturates and approaches the limit of $\tau_{\text{pump}} = \frac{2}{\Gamma_{\text{SF}}} = 14\,\mu$s imposed by the strength of the SF transition.

A large value of the branching ratio opens up the way for efficient state readout, which corresponds to the fifth criterion of DiVincenzo. A perfect state readout consists of only one optical pulse, which generates a sufficiently high photon response to be distinguished from the background fluorescence of the sample or the noise of the single photon detector. This is only possible in the presence of strongly cycling transitions as on these transitions a large number of photons can be scattered without alteration of the spin state. For example the branching ratio describing the relative strength of SC and SF transition gives the average number of scattered photons on the cycling transition before a spin flip occurs. Consequently, a SF transition that is three orders of magnitude weaker than the corresponding SC transition enables a single-shot readout in which 1000 photons are scattered on average until the spin state is flipped. If the majority of these photons can be detected, the signal can be clearly distinguished from any possible background or noise and therefore a single pulse is sufficient to read out the spin state. The quality of such a readout scheme can be defined via the fidelity $\mathcal{F}$ as reported in [68]. To understand the definition of the fidelity, we introduce here the notion of "dark" and "bright" events. Lets assume that we implemented the state initialisation scheme in a highly efficient way and all the population is now in state $|2\uparrow\rangle$. Hence, the single-shot readout on the SC transition will produce no photon response and thus remain dark. On the contrary, if the population is prepared in state $|1\downarrow\rangle$ consequently a fluorescence response of scattered photons would be produced, labelling the state as being bright. These two cases serve as the calibration of the single-shot readout. In Fig. 2.16 the histogram of fictive fluorescence responses for both cases is depicted and we set, for illustrative purposes, a threshold of three photons as the detection of a bright event. It is obvious that the two cases do have a certain overlap, which defines the error ϵ_{B} as the probability with which a bright event is detected as dark and the error ϵ_{D} for a dark event to be detected as bright. In the depicted scenario the probability for a bright state preparation yielding less than three photons is relatively small and adds up to $\epsilon_{\mathrm{B}} = 0.016$, while for the dark state preparation the sum over all probabilities of detecting more than three photons is significant, yielding $\epsilon_{\mathrm{D}} = 0.174$. The total error of the protocol is then given as the average of both values, yielding

$$\epsilon = \frac{\epsilon_{\mathrm{B}} + \epsilon_{\mathrm{D}}}{2}, \tag{2.48}$$

in our scenario $\epsilon = 0.095$. The state readout fidelity as a measure of the reliability of the readout scheme is defined as

$$\mathcal{F} = 1 - \epsilon, \tag{2.49}$$

which amounts to $\mathcal{F} = 0.905$ for the model calculation. While the readout starts to be meaningful for $\mathcal{F} > 0.5$, a high fidelity approaching unity is needed for actual implementation in QIP protocols with a suitably low readout error rate. The major advantage of the single-shot readout scheme is that it enables real time decisions. A completed protocol run does not have to be repeated a large number of times with postselection of the data but as soon as an erroneous state preparation or protocol error is detected with a single readout pulse, a reset can be initialised and the protocol be started again.

2.2.6 Coherent population trapping

The previous sections mainly focused on the incoherent processes that are necessary to initialise and readout the qubit formed by the spin states of the lowest orbital ground state. In this part, we will introduce coherent population trapping as means to coherently address the spin qubit and extract information on the spin dephasing time of the qubit.

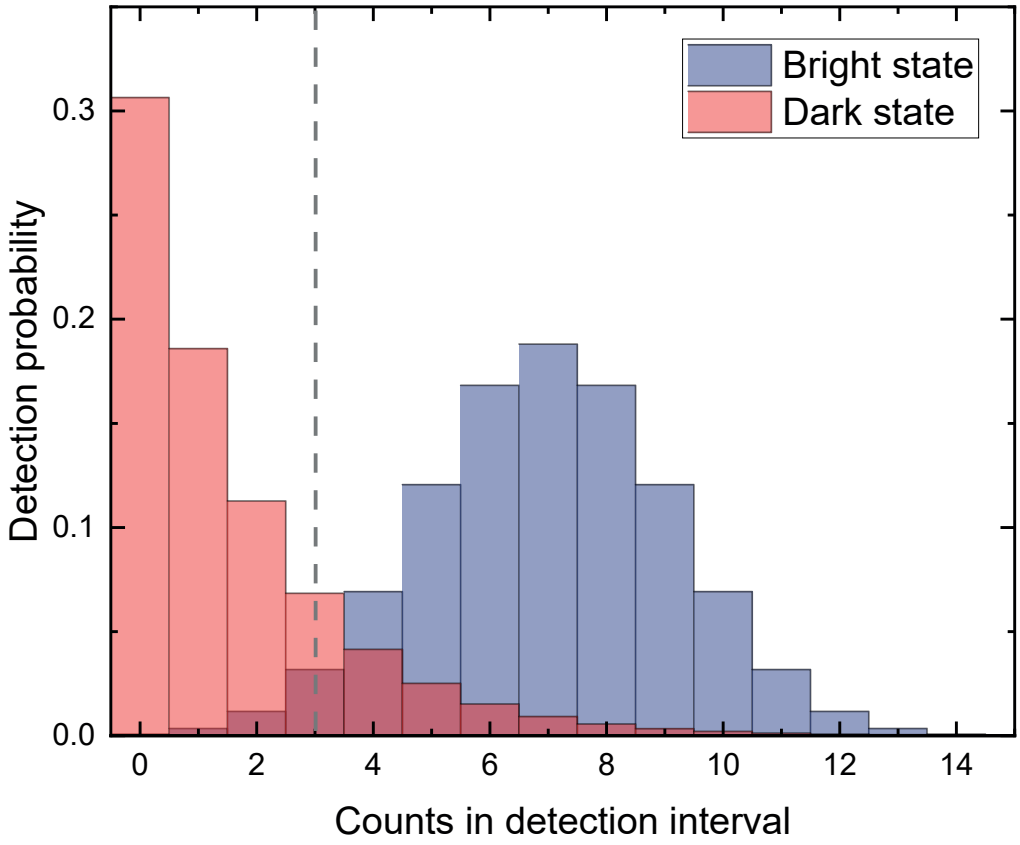

Figure 2.16: **Histogram of single-shot readout calibration:** Histogram of a fictive single-shot readout calibration, in which the probability of the number of photon counts in a read interval is depicted for the system being either prepared in the dark or the bright state. It can be seen that both probability distributions have significant overlap, which induces state readout errors. These errors depend on the threshold on the photon number that has to be detected in a read interval for attributing a state as bright. In the illustration, this threshold is set to three photons and is indicated by the dashed grey line.

The latter is a very important number concerning the third DiVincenzo criterion. CPT is a quantum mechanical phenomenon occuring when adressing a three level system simultaneously with two lasers. In this thesis we focus on the so-called $\Lambda-$scheme (see Fig. 2.12), in which the spin states of the lowest orbital branch ($|1\downarrow\rangle, |2\uparrow\rangle$) are brought into two-photon resonance utilising lasers on the transitions A1 (SC) and A2 (SF) to the excited state $|A\downarrow\rangle$. Two-photon resonance means that both lasers exhibit the same detuning from the excited state, namely $\Delta_1 = \Delta_2$. For the two-photon resonance condition being fulfilled in a three level system it can be easily shown [226], that the system is transferred into a dark state

$$|\Psi_{\text{dark}}\rangle = \frac{1}{\sqrt{2}}(\cos(\theta)\,|1\downarrow\rangle - \sin(\theta)\,|2\uparrow\rangle). \tag{2.50}$$

The mixing angle θ is directly related to the Rabi frequencies of the lasers by the relations

$$\cos(\theta) = \frac{\Omega_{\mathrm{SF}}}{\sqrt{\Omega_{\mathrm{SF}}^2 + \Omega_{\mathrm{SC}}^2}} \tag{2.51}$$

$$\sin(\theta) = \frac{\Omega_{\mathrm{SC}}}{\sqrt{\Omega_{\mathrm{SF}}^2 + \Omega_{\mathrm{SC}}^2}}. \tag{2.52}$$

The state written down in equation 2.50 is referred to as being dark, since it has no contribution of the excited state $|A\downarrow\rangle$ and thus no spontaneous decay is detectable. It is noteworthy that this is true even for the case that both lasers are in resonance with the atomic transition frequencies (e.g. $\Delta_1 = 0 = \Delta_2$). The state Ψ_{dark} corresponds to an energy eigenvalue of zero of the Hamiltonian denoted in equation 2.17, when fulfilling the two-photon resonance condition. This dark state is useful in gaining insight into the coherence of the system: Since the transition that leads to the generation of $|\Psi_{\mathrm{dark}}\rangle$ is of two-photon nature and furthermore the excited state does plays no role in it, the width of this transition is governed by the coherence of the two laser fields with respect to each other and, most important for our work, the coherence of the ground states. That means, in the limit of the relative laser coherence significantly exceeding the coherence of the ground states one can derive the spin dephasing time T_2^* from the full-width-half-maximum $\Delta\nu_{\mathrm{spin}}$ of the transition as

$$\Delta\nu_{\mathrm{spin}} = \gamma_{22} = \frac{1}{\pi T_2^*}. \tag{2.53}$$

The spin dephasing rate γ_{22} defines the relative decoherence of the spin states by a pure dephasing of $|2\uparrow\rangle$. There are several important points to note:

1. The definition of the spin coherence in equation 2.53 by acting only on state $|2\uparrow\rangle$ rather than on both ground states is justified by the fact that coherence is always a relative and no absolute value. Furthermore, as can be seen in Fig. 2.17a), the imaginary part of the off-diagonal elements of the density matrix that describe the coherence between the spin states decays with the time constant T_2^*, which is here set to 5 µs. This is exactly what is expected as the effect of the spin dephasing. It has to be further emphasised that only a factor of π is contributing in eq. 2.53 while in literature a factor of 2π is oftentimes erroneously introduced.

2. In reality, the width of the dark resonance can only be measured as a pure Lorentzian in a certain power regime. This is due to the fact that one of the lasers needs to be scanned across the transition to probe it. Assuming that the laser adressing the SF transition is scanned, then it will probe the dressed states generated by the laser adressing the SC transition. These two states are the bright eigenstates of the three level system that, in contrast to the dark state, contain the excited state $|A\downarrow\rangle$ and correspond to the energy eigenvalues

$$\lambda_{\pm} = \frac{\hbar}{2}(\Delta \pm \sqrt{\Delta^2 + \Omega_{\mathrm{SF}}^2 + \Omega_{\mathrm{SC}}^2}) \tag{2.54}$$

of the Hamiltonian derived in eq. 2.17. The absolute detuning of the lasers being in two-photon resonance is here denoted as Δ. From this equation it can be seen that the dressed states are symetrically shifted around the energy of the dark state for working in resonance with $\Delta = 0$. Furthermore, the splitting between the two states is given as $\hbar\Omega_{\mathrm{SC}}$ in the case that the scanned laser is significantly weaker, e.g. $\frac{\Omega_{\mathrm{SF}}}{\Omega_{\mathrm{SC}}} \ll 1$. This case is depicted for Rabi frequencies $\Omega_{\mathrm{SC}} = 200\,\mathrm{MHz}$ and $\Omega_{\mathrm{SF}} = 0.1\,\mathrm{MHz}$ in Fig.

2.17b). In this scan, the laser addressing the SC transition is kept fixed, while the other one is scanned. For resolving the dark resonance, both Rabi frequencies need to be sufficiently small, as will be explained in the following remarks.

3. It is important to note that for Γ_{SF} and Γ_{SC} differing significantly, the lineshape of the CPT measurement will be different for the case that the laser addressing the SF transition is kept at a fixed frequency and the laser on the SC transition is scanned or vice versa. This is true even for $\Omega_{\mathrm{SF}} = \Omega_{\mathrm{SC}}$ and is again a result from the peculiarities that arise when working with a level system that exhibits a large branching ratio η_{cycling}. It can be understood by taking into account the different optical pumping rates. As explained in sec. 2.2.5, when a laser addresses the SC transition, the population will cycle on average η_{cycling}(set to 1000 in the simulations) times until the spin state is flipped. On the contrary, as soon as a laser excites the SnV^- centre on the SF transition, with almost unity probability the spin state will flip in the subsequent decay on the SC transition. Thus pumping on the SF transition can be very rapid and efficient. We will now discuss the two cases of CPT: When the SC transition is addressed resonantly and constantly by one laser, the population will at some point be flipped over to $|2\uparrow\rangle$. There it will reside until either thermalisation happens, which is typically on the timescale of several milliseconds, or pumping on the SF transition brings it back to state $|1\downarrow\rangle$. The latter is 1000 times more efficient than pumping on the SC transition and thus even if the SF laser is detuned far off resonance, it will start to repopulate state $|1\downarrow\rangle$. This population is again cycling between $|1\downarrow\rangle$ and $|A\downarrow\rangle$ due to the fixed laser addressing the SC transition. In the experiment this is detected as fluorescence. In Fig. 2.18a) the population of all three states is depicted for different detunings of the SF laser. It yields a broad feature, due to the efficient backpumping in state $|1\downarrow\rangle$ and the characteristic dark resonance at zero detuning. The width of this peak narrows strongly, when decreasing the ratio of $\frac{\Omega_{\mathrm{SF}}}{\Omega_{\mathrm{SC}}}$. The height of the sidepeaks next to the dark resonance can reach a maximum of 50 % of the overall population, which is the limit of incoherent pumping. On the contrary, when keeping the laser addressing the SF transition fixed and scanning the laser addressing the SC transition (2.18b)), the SF laser will pump all population into $|1\downarrow\rangle$. However, due to the inefficient repumping on the SC transition, even for comparably small detunings of the SC laser the population will reside in $|1\downarrow\rangle$ and no fluorescence can be detected. Only when the SC laser addresses resonantly the Autler-Townes split dressed states fluorescence will be detected. Thus the overall feature is rather narrow, though the dark resonance is still observed in the same manner at zero detuning. The peak height is reduced to a maximum of only 25 % of the population. The reason lies again in the inefficient pumping of the SC transition, as now the population dynamics are dominated by the SF laser. It splits the excited state up into the two dressed states, in which 50 % of the population will be pumped. As the SC laser addresses only one of the two transitions efficiently at a time, it reaches the incoherent limit of pumping to the excited state again, but this time starting with only half the population, which yields only 25 % in the excited state.

4. Taking care when extracting the width $\Delta\nu_{\mathrm{spin}}$ from a measurement is necessary as a consequence of the last two remarks. In order to ensure that the transition is not power broadened, it is necessary to work in a regime with both Rabi frequencies ensuring $\frac{\Omega_{\mathrm{SF}}}{\Gamma_{\mathrm{SC}}}, \frac{\Omega_{\mathrm{SC}}}{\Gamma_{\mathrm{SC}}} \ll 1$. These criteria follow directly from the theory of power broadening of optical transitions derived in [229] (p.142), with the saturation laser

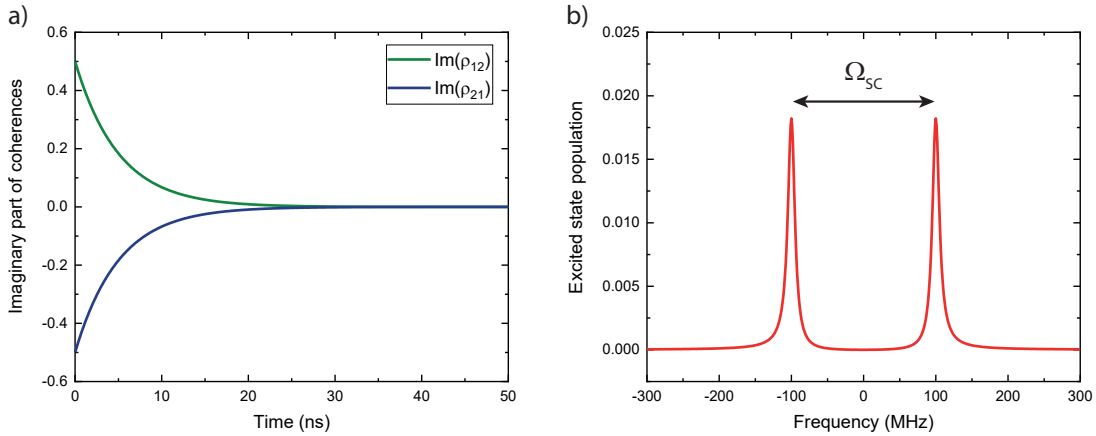

Figure 2.17: **Decay of coherence and Autler-Townes-Splitting: a)** When preparing the spin ground states in a coherent superposition, the coherence between the states is set by the relative off-diagonal elements of the density matrix. In the simulation, the decoherence is chosen to $\gamma_{22} = \frac{1}{\pi T_2^*}$, with $T_2^* = 5\,\mu s$, which is the time constant of the decay of coherence depicted. When all coherence decayed for times $\gg T_2^*$, the system is in a mixed state with 50 % classical probability to be in each state. **b)** Autler-Townes splitting of the dressed states, which is revealed in the excited state population when scanning the weak SF laser ($\Omega_{SF} = 0.1\,MHz$) across the dressed states generated by the strong SC laser ($\Omega_{SC} = 200\,MHz$).

power being

$$\frac{P}{P_{sat,SC/SF}} = \frac{2\Omega_{SC/SF}^2}{\Gamma_{SC/SF}^2}. \tag{2.55}$$

It is important to be aware that the saturation power $P_{sat,SC/SF}$ is directly proportional to the decay rate of the transition $\Gamma_{SC/SF}$. Thus to reach the same Rabi frequency on the SF transition, the excitation power needs to be increased by a factor $\eta_{cycling}$ and not by the square of it. One might think that the boundary condition for Ω_{SF} thus has to be related to Γ_{SF} and not to Γ_{SC}. However, we are adressing the dressed states that are an admixture of both spin levels and therefore the restriction is set by the dominant decay path, which is the SC transition in our system. Simulation of the CPT resonance in the low power regime and its power broadening are depicted in Fig. 2.19a). The most reliable way to extract $\Delta\nu_{spin}$ is to use the model presented in this section to fit experimental data. However, typically an estimation of the linewidth is performed by fitting it with a Lorentzian. This is generally valid, however, in the case of extreme branching ratios, the dark resonance shape can be strongly affected by the pumping effects highlighted above (Fig. 2.19b)). For example it overlaps with the dressed states in the case that the SC laser is scanned. Therefore, a proper fit can only be obtained by fitting the lower part of the dip. The fit is more reliable when the SF laser is scanned, as the broadening of the dressed states leads to a better baseline for a Lorentzian fit and thus the fitting error is minimised.

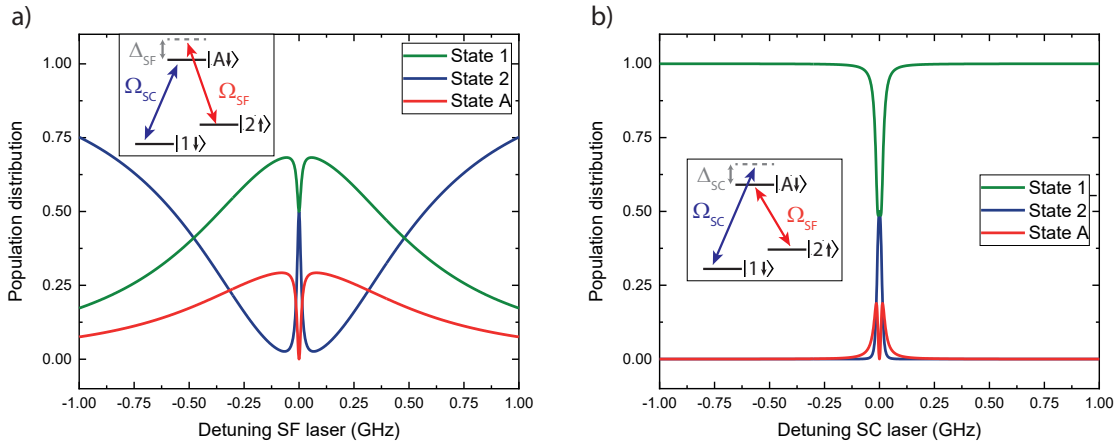

Figure 2.18: **Comparison of scanning SF or SC laser: a)** The SC laser is kept fixed to the resonance of the SC transition ($\Omega_{\mathrm{SC}} = 20\,\mathrm{MHz}$), while the SF laser ($\Omega_{\mathrm{SF}} = 20\,\mathrm{MHz}$) is scanned. Due to the very effective pumping of the SF laser even for large detunings from resonance, population is transferred to state $|1\downarrow\rangle$ from which the SC laser excites it to $|A\downarrow\rangle$. For zero detuning, the characteristic CPT dark resonance can be seen, in which the system is in a coherent 50:50 superposition of $|1\downarrow\rangle$ and $|2\uparrow\rangle$ that is decoupled from the excited state. **b)** Same process with the roles of SC and SF laser being interchanged. The population dynamics are dominated by the effective population pumping of the SF laser and thus the excited state is not populated for large detunings. Only when approaching the dressed states generated by the SF laser, the characteristic CPT feature is observed in the excited state. Again at zero detuning the dark state is prepared.

2.3 Hong-Ou-Mandel interference

This section is dedicated to the derivation and description of the theory necessary to model and analyse the experiments on two-photon interference (TPI) of consecutively emitted photons from single SnV^- centres. The derivation follows the theory derived by Benjamin Kambs in [230,231], which we adapt in order to cover all experimental boundary conditions within this thesis. Parts of the modifications were already implemented in the course of Robert Morsch's Master thesis [232] and are integrated, reevaluated and extended within this section.

2.3.1 Two-photon interference at a beam splitter

The theoretical description of interference of only two photons at a 50:50 beamsplitter becomes rapidly complicated as soon as real photons and experimental boundary conditions are taken into account. To give the interested reader an intuition of the process, we will start this section by considering a commonly used thought experiment [233] and extend this model stepwise in order to approach the theoretical grade of complexity necessary to describe the physical reality observed in the laboratory. Therefore, we consider two photons with no temporal width, but rather being described by a delta peak in time. These photons may exhibit different features such as their spatial mode or their polarisation state, with the resulting quantum state being completely captured by the labelling i, respectively j. The corresponding Fock state of the photons can be mathematically implemented by the creation $\hat{a}_i^\dagger$ ($\hat{a}_j^\dagger$) and annihilation operators $\hat{a}_i$ ($\hat{a}_j$). These operators obey the well known

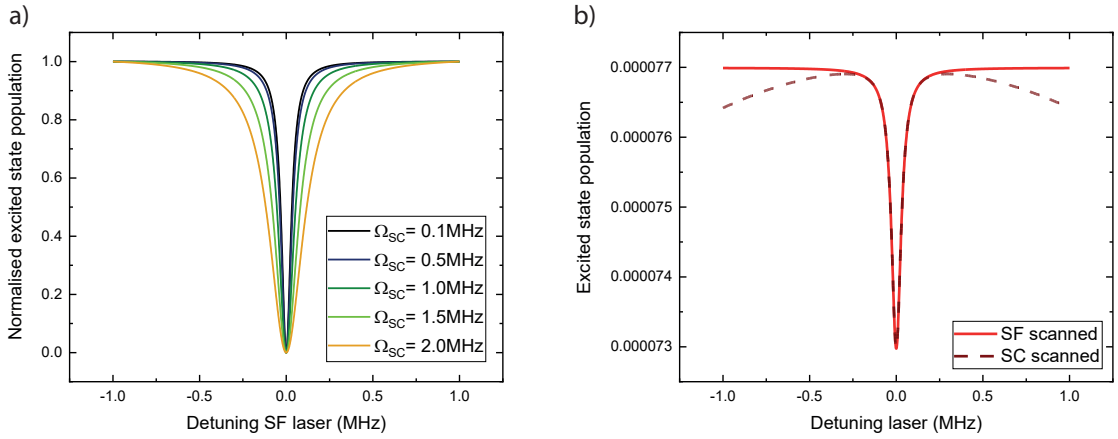

Figure 2.19: **Power broadening of CPT resonance and extraction of $\Delta\nu_{\mathrm{spin}}$: a)** Depicted is the power broadening of the CPT resonance for different Rabi frequency strengths Ω_{SC}, while Ω_{SF} is set to 0.2 MHz and is scanned across the transition. The spin dephasing time is set to $T_2^* = 5\,\mu\mathrm{s}$. The excited state population is normalised to its maximum value after substracting the minima imposed by the dip in order to make the graphs comparable and to visualise the broadening of the dip with increasing Rabi frequency. **b)** Dependence of the CPT dark resonance feature for $\Omega_{\mathrm{SC}} = \Omega_{\mathrm{SC}} = 0.2\,\mathrm{MHz}$ on the scanning laser field. When the SF laser is scanned, the CPT feature can be fitted perfectly by a Lorentzian. However, when scanning the SC laser, the distortion of the dark resonance hinders reliable fitting. The width $\Delta\nu_{\mathrm{spin}}$ is determined correctly only when restricting the Lorentzian fit to the lower half of the resonance dip.

anticommutation relations

$$[\hat{a}_i, \hat{a}_j] = 0 \tag{2.56}$$

$$[\hat{a}_i^\dagger, \hat{a}_j^\dagger] = 0 \tag{2.57}$$

$$[\hat{a}_i, \hat{a}_j^\dagger] = \delta_{ij}, \tag{2.58}$$

with δ_{ij} being the Kronecker delta. The principal experiment in which quantum interference of such two photons at a ideal, lossless fibre based BS (FBS) occurs is schematically depicted in Fig. 2.20. A photon in input mode 1 (I1) of the FBS with quantum state i and a second photon in input mode 2 (I2) with quantum state j, impinge simultaneously on the FBS. This input state can thus be written as

$$|\Psi_{\mathrm{in}}\rangle = \hat{a}_{1,i}^\dagger \hat{a}_{2,j}^\dagger |0\rangle .$$

However, before a measurement, in whichever form, on the output ports of the FBS can be performed, the effect of the FBS on the two photons must be taken into account. It can be mathematically described by the unitary transformation $\hat{U}$ in the following way

$$\hat{a}_{1,i}^\dagger \xrightarrow{\hat{U}} \frac{1}{\sqrt{2}}(\hat{a}_{3,i}^\dagger + \hat{a}_{4,i}^\dagger) \tag{2.59}$$

$$\hat{a}_{2,j}^\dagger \xrightarrow{\hat{U}} \frac{1}{\sqrt{2}}(\hat{a}_{3,j}^\dagger - \hat{a}_{4,j}^\dagger) \tag{2.60}$$

The transformation represents the 50 % probability of a photon being reflected, respectively transmitted, as well as the phase change of π resulting from the reflection at an optically

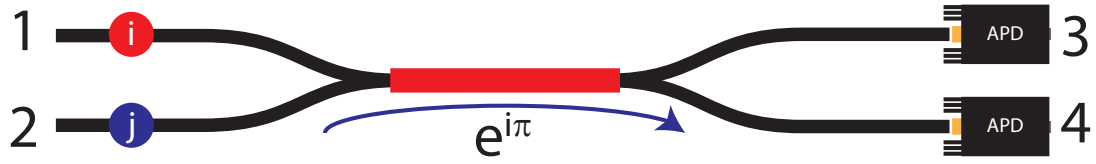

Figure 2.20: **Schematic of TPI at a 50:50 FBS:** Two photons, one in input mode 1 with its quantum state being described by the label i, and another in input mode 2 with quantum state j, impinge on a 50:50 FBS. Reflection of the blue photon in input port 2 implies a phase shift of π. At the output ports 3 and 4, single photon detectors, namely avalanche photo diodes (APD) are utilised to measure the coincidences of one photon ending up in channel 3 while the other one is detected in channel 4.

dense medium. The latter occurs for the photon in mode 2 by definition in our thought experiment. The output state $|\Psi_{\text{out}}\rangle$ thus can be calculated as

$$\begin{aligned} |\Psi_{\text{out}}\rangle &= \hat{U}\,|\Psi_{\text{in}}\rangle \\ &= \frac{1}{2}(\hat{a}^\dagger_{3,i} + \hat{a}^\dagger_{4,i}) \cdot (\hat{a}^\dagger_{3,j} - \hat{a}^\dagger_{4,j})\,|0\rangle \\ &= \frac{1}{2}(\hat{a}^\dagger_{3,i}\hat{a}^\dagger_{3,j} - \hat{a}^\dagger_{3,i}\hat{a}^\dagger_{4,j} + \hat{a}^\dagger_{4,i}\hat{a}^\dagger_{3,j} - \hat{a}^\dagger_{4,i}\hat{a}^\dagger_{4,j})\,|0\rangle \end{aligned} \tag{2.61}$$

As a photon in output mode 3 (O3) results with equal probability from the photon in I1 being reflected or the photon in I2 being transmitted at the FBS and in an analogous way for output mode 4 (O4), there are four possible outcomes of such an interference experiment corresponding to the four summands in the output states:

1. The photon in I1 is reflected into O3, the photon in I2 is transmitted into O3.
2. The photon in I1 is reflected into O3, the photon in I2 is reflected into O4. A relative phase change of π is introduced, resulting in a sign flip.
3. The photon in I1 is transmitted into O4, the photon in I2 is transmitted into O3.
4. The photon in I1 is transmitted into O4, the photon in I2 is reflected into O4. A relative phase change of π is introduced, resulting in a sign flip.

A graphical illustration of the scenario is shown in Fig. 2.21. Now let's consider two cases, which we label distinguishable and indistinguishable. In the distinguishable case the input photons exhibit at least one feature of their quantum state that renders its state orthogonal to the other photon's quantum state, for example horizontal and vertical polarisation degrees of freedom. Therefore, it is straightforward to determine a photon's origin by measuring its polarisation at the FBS output. The four different experiment outcomes mentioned above are all equally probable and thus we can set up a coincidence measurement at the FBS output ports by placing a detector in each ouput and measure in which cases both of them detect a photon. As equation 2.61 exhibits two possibilities for one photon being in output 3 and one photon being in output 4, the overall coincidence probability amounts to $\text{p}_{\text{coinc}} = \frac{1}{2}$ in the distinguishable scenario. In the indistinguishable case, the quantum state of both photons is equal in all respects with $i \equiv j$. Therefore, the terms corresponding to the possibilities 2 and 3 are equal but of opposite sign and

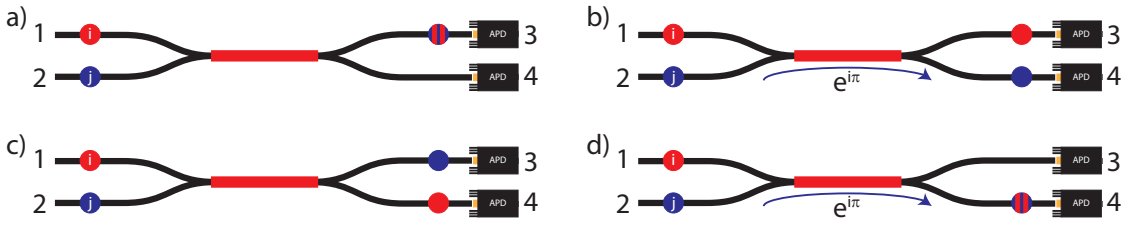

Figure 2.21: **Possible pathways of TPI at a 50:50 FBS:** The photons in the input channels can take four possible pathways: **a)** Photon i is reflected while photon j is transmitted. **b)** Photon i and photon j are both reflected, which yields a phase shift of π and thus a sign flip in the overall wavefunction. **c)** Both photons are transmitted. **d)** Photon i is transmitted, while photon j is reflected and again a phase shift of π is introduced. For the case of indistinguishable photons, the cases **b)** and **c)** cannot be distinguished but are of opposite sign and therefore cancel each other out. As a result, all coincidences vanish, which is the measurement indicator of two photons being indistinguishable.

consequently cancel each other out, leading to the output state

$$|\Psi_{\text{out,indist}}\rangle = \frac{1}{2}((\hat{a}_3^\dagger)^2 - (\hat{a}_4^\dagger)^2)\,|0\rangle\,, \tag{2.62}$$

where the label of the quantum state is omitted, as they are equal. This means, that both photons always take the same path of O3 or of O4, but never different ones. As a result, the coincidence probability for indistinguishable photons is equal to zero, $\mathrm{p}_{\text{coinc}} = 0$.
The consequences of these two cases are manifold: First of all, it yields a straightforward way to tell whether two photons are indistinguishable or not. While it is usually very effortful to fully characterise a quantum state of a photon, a simple coincidence measurement can reveal whether two complex quantum states are equal. Furthermore, even though photons do not interact with each other by collisions, electromagnetic or any other known force, the indistinguishability of the photons at the FBS decides which paths they can take. The output state is therefore called a path entangled number state [234] and the interference at a 50:50 FBS an effective photon-photon interaction, which is of great importance in quantum computation using linear optics [50, 235].
While the thought experiment described in this section illustrates the most important effects and consequences of TPI at a 50:50 FBS, it is not suitable to model the interference of realistic photons with a temporal shape and quantum degrees of freedom, which might not only be parallel or orthogonal to each other but also somewhere in between. As a consequence, indistinguishability is not a binary feature but can can be quantified in a degree ranging from 0% (fully distinguishable) to 100% (fully indistinguishable). The following section is thus dedicated to implement a full theoretical model of the experimentally observed TPI in this thesis.

2.3.2 TPI of consecutively emitted real photons

Single photons generated by the excitation of a single quantum emitter result from the radiative decay of an excited electronic quantum state. The nature of this decay is probabilistic and exhibits a characteristic time constant, which we label τ_r throughout the course of this thesis. As a consequence, an emitted photon exhibits a temporal shape corresponding to the decay probability of the excited state. This is also called the wave function $\zeta(t)$ which we use to describe the full quantum state of a photon. The wave function $\zeta(t)$ is

normalised in a way that $\int \zeta(t)\zeta^*(t)\mathrm{d}t = 1$. The mathematical description of a photon in input mode n, which can be either 1 or 2, of the 50:50 FBS can therefore be modeled by introduction of the field operators [236]

$$\hat{E}_n^+(t) = \zeta_n(t)\hat{a}_n \tag{2.63}$$

$$\hat{E}_n^-(t) = \zeta_n^*(t)\hat{a}_n^\dagger. \tag{2.64}$$

$\hat{E}_n^+(t)$ and $\hat{E}_n^-(t)$ are complex conjugates of each other and obey the relations 2.56, 2.57 and 2.58 in the fashion

$$[\hat{E}_n^+(t), \hat{E}_m^+(t)] = 0 \tag{2.65}$$

$$[\hat{E}_n^-(t), \hat{E}_m^-(t)] = 0 \tag{2.66}$$

$$[\hat{E}_n^+(t), \hat{E}_m^-(t)] = \zeta_n(t)\zeta_n^*(t)\delta_{nm}. \tag{2.67}$$

Since in our work we investigate photons being emitted consecutively from one single photon source under pulsed excitation, it is necessary to somehow overlap two individual photons at the FBS. The latter is achieved employing an imbalanced MZI as sketched in Fig. 2.22. The interferometer imposes a time delay τ_{mzi}, which needs to compensate for the delay τ_{exc} in between two excitation pulses or an integer multiple N of it. For a proper compensation of the excitation delay, in one fourth of all possible cases two photons will impinge at the same time at the FBS. This is the case where the early arriving photon takes the long path in the imbalanced MZI, while the photon that arrives $\mathrm{N}\tau_{\mathrm{exc}}$ later takes the short path. For that situation, we can implement the FBS transformation in a fashion analogue to the previous section and find field operators, which describe the photons in output modes 3 and 4, namely

$$\hat{E}_3^+(t) = \frac{1}{\sqrt{2}}\left(\zeta_1(t)\hat{a}_1 + \zeta_2(t)\hat{a}_2\right) \tag{2.68}$$

$$\hat{E}_4^+(t) = \frac{1}{\sqrt{2}}\left(\zeta_1(t)\hat{a}_1 - \zeta_2(t)\hat{a}_2\right). \tag{2.69}$$

Also these field operators obey the relations 2.65 - 2.67 in a similar fashion.
As we do now have the means to describe the photons in the output modes resulting from reflection or transmission of the photons impinging on the FBS, we can implement a formalism for the probability of detecting a coincidence between the output modes, ie. having one photon in each output modes 3 and 4, respectively. This is called the joint detection probability $\mathrm{P}_{\mathrm{joint}}$ and its derivation follows the concept reported in [237]. We start with the detection of a single photon on a usual single photon detector, whose working principle is based on the absorption of the arriving photon at a time t_0. That means that the field annihilation operator $\hat{E_n}^+(t_0)$ annihilates a photon of the initial state of the electric field, which we describe as before by $|\Psi_{\mathrm{in}}\rangle$. The electric field is now left in a final state $|f\rangle$. There are a variety of final states and they can be described without any loss of generality by a complete orthonormal basis, obeying the well known relation $\sum_f |f\rangle\langle f| = 1$. The probability of a photon absorption per time unit is therefore the sum of each absorption probability over all final states, resulting in

$$\begin{aligned}\mathrm{P}_{\mathrm{single}}(t_0) &= \sum_f |\langle f|\hat{E}_n^+(t_0)|\Psi_{\mathrm{in}}\rangle|^2 \\ &= \langle\Psi_{\mathrm{in}}|\hat{E}_n^-(t_0)\hat{E}_n^+(t_0)|\Psi_{\mathrm{in}}\rangle.\end{aligned} \tag{2.70}$$

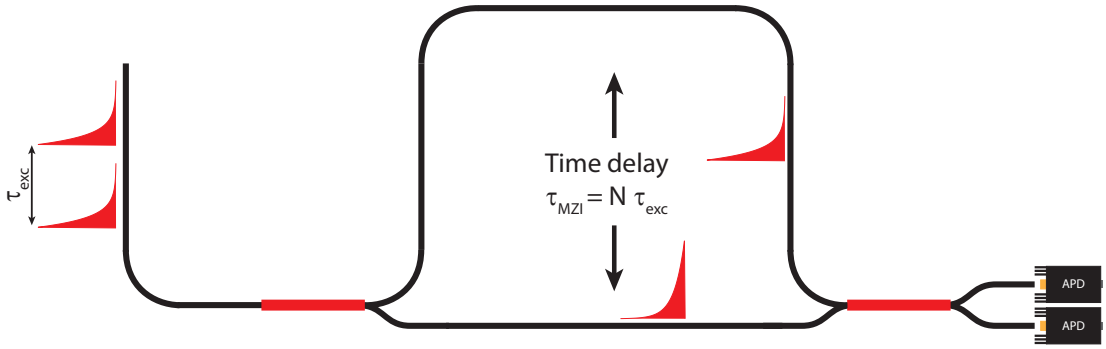

Figure 2.22: **Schematic of the imbalanced MZI:** In order to overlap photons emitted by one quantum emitter at a 50:50 FBS, the quantum emitter is excited with laser pulses that exhibit an excitation delay of τ_{exc}. An integer number N of this delay is compensated in a fibre based imbalanced MZI for the case that an early arriving photon takes the long path and a subsequent late photon (arriving $\mathrm{N}\tau_{\mathrm{exc}}$ later) takes the short path. When they reach the FBS, TPI occurs in the case of the photons being at least partially indistinguishable.

The result is very intuitive as the number operator $\hat{E}_n^-(t_0)\hat{E}_n^+(t_0)$ of a photon in mode n, counts the number of photons being present in the initial state of the electric field $|\Psi_{\mathrm{in}}\rangle$ and this is exactly what we expect from a (number resolving) single photon detector. In the case of only one photon impinging on a detector at a time, it is equivalent to a not number resolving single photon detector. Now we can extend this to the case of the joint detection of photons in the output modes 3 and 4 of the FBS at which TPI takes place. This is now described by the annihilation operators $\hat{E_3}^+(t_0)$ and $\hat{E_4}^+(t_0+\tau)$, where τ denotes a possible time difference in the detection times of the photon in mode 4 with respect to the arrival of the photon in mode 3. The joint detection probability is then given by

$$\begin{aligned} \mathrm{P}_{\mathrm{joint}}(t_0,\tau) &= \sum_f |\langle f|\, \hat{E_4}^+(t_0+\tau)\hat{E_3}^+(t_0)\,|\Psi_{\mathrm{in}}\rangle\,|^2 \\ &= \langle\Psi_{\mathrm{in}}|\, \hat{E_3}^-(t_0)\hat{E_4}^-(t_0+\tau)\hat{E_4}^+(t_0+\tau)\hat{E_3}^+(t_0)\,|\Psi_{\mathrm{in}}\rangle\,. \end{aligned} \tag{2.71}$$

Using the relations 2.65, 2.66, we find

$$\mathrm{P}_{\mathrm{joint}}(t_0,\tau) = \langle\Psi_{\mathrm{in}}|\, \hat{E_3}^-(t_0)\hat{E_3}^+(t_0)\hat{E_4}^-(t_0+\tau)\hat{E_4}^+(t_0+\tau)\,|\Psi_{\mathrm{in}}\rangle\,, \tag{2.72}$$

which is again the intuitive result of the expectation value of the number operators for a photon in mode 3 at a time t_0 and a photon in mode 4 at a time $t_0+\tau$. However, evaluation of $\mathrm{P}_{\mathrm{joint}}(t_0,\tau)$ is easier employing the less intuitive relation 2.71 and making use of the fact that $\hat{a}_i\,|0\rangle = 0$. This leads to the simplified expression

$$\mathrm{P}_{\mathrm{joint}}(t_0,\tau) = \frac{1}{4}|\zeta_1(t_0+\tau)\zeta_2(t_0) - \zeta_2(t_0+\tau)\zeta_1(t_0)|^2, \tag{2.73}$$

that depends only on the wave functions of the input photons and their detection time, assuming that the detectors are placed at equal distance from the FBS. This expression can be separated into one term P_0 that results purely from incoherent contributions and describes the case of completely distinguishable photons and a second term $\mathrm{P}_{\mathrm{int}}$, which describes the quantum interference of two photons being indistinguishable to a certain

degree, impinging on the FBS. The two terms read

$$\mathrm{P}_0(t_0,\tau) = \frac{1}{4}(|\zeta_1(t_0+\tau)\zeta_2(t_0)|^2 + |\zeta_2(t_0+\tau)\zeta_1(t_0)|^2) \tag{2.74}$$

$$\mathrm{P}_{\mathrm{int}}(t_0,\tau) = -\frac{1}{2}\mathcal{R}\{\zeta_1(t_0)\zeta_2^*(t_0)\zeta_2(t_0+\tau)\zeta_1^*(t_0+\tau)\}, \tag{2.75}$$

with $\mathcal{R}$ taking the real part of the expression in braces. With these general results on hand, we can proceed to the description of TPI with real photons consecutively emitted by the same quantum emitter. We will therefore now derive the mathematical description of the photon wave function resulting from the decay of an excited quantum state. This function has to describe photons emitted under the influence of spectral diffusion and pure dephasing that are impacting the quantum emitter. Furthermore, we have to take into account a temporal separation of the photons arriving at the FBS, which can originate from an excitation jitter induced by internal dynamics of the excitation process of the quantum emitter or the finite pulse width of the excitation pulse as well as a fixed delay mismatch due to experimental imperfections.
As the decay of a quantum state is usually of mono-exponential nature, we can describe the temporal shape of the photon wave package by the product of the Heavyside function $\Theta(t)$ and an exponential decay with time constant τ_r. As we only investigate consecutive photons emitted by the same quantum emitter in this thesis, we implement the same radiative lifetime for both photons, which simplifies the calculations. The difference in the arrival time at the beamsplitter can be implemented by a relative time shift of $\Delta\tau$. As a result of spectral diffusion (SD, see sec. 2.1.6), the carrier frequency ν_n and consequently the resulting phase accumulated over time of the two photons can differ. Furthermore, pure dephasing (PD) due to collisions of phonons with the quantum emitter can introduce an additonal time dependent randomised phase $\phi_n(t)$ that needs to be taken into account. The mathematical derivation of the description of SD and PD are not carried out within this thesis but can be found elsewhere [230,231]. The resulting wave function of the electric field of a photon in I1 or I2 of the beamsplitter can be written as

$$\zeta_{1,2}(t) = \frac{1}{\sqrt{\tau_\mathrm{r}}}\Theta(t \pm \frac{\Delta\tau}{2}) \exp(-\frac{t \pm \frac{\Delta\tau}{2}}{2\tau_\mathrm{r}}) \exp(-2\pi i\nu_{1,2}t + i\phi_{1,2}(t)). \tag{2.76}$$

Plugging these expressions into equation 2.74 and 2.75, we find

$$\begin{aligned} \mathrm{P}_0(t_0,\tau) &= \frac{1}{4\tau_\mathrm{r}^2}\{\Theta(t_0+\tau+\frac{\Delta\tau}{2})\Theta(t_0-\frac{\Delta\tau}{2}) + \Theta(t_0+\tau-\frac{\Delta\tau}{2})\Theta(t_0+\frac{\Delta\tau}{2})\} \\ &\quad \cdot \exp(-\frac{2t_0+\tau}{\tau_\mathrm{r}}) \end{aligned} \tag{2.77}$$

$$\begin{aligned} \mathrm{P}_{\mathrm{int}}(t_0,\tau) &= -\frac{1}{2\tau_\mathrm{r}^2}\Theta(t_0+\frac{\Delta\tau}{2})\Theta(t_0-\frac{\Delta\tau}{2})\Theta(t_0+\tau-\frac{\Delta\tau}{2})\Theta(t_0+\tau+\frac{\Delta\tau}{2}) \\ &\quad \cdot \exp(-\frac{2t_0+\tau}{\tau_\mathrm{r}}) \cos(2\pi\Delta\nu\tau + \Delta\phi_1 - \Delta\phi_2). \end{aligned} \tag{2.78}$$

The dependencies of P_0 on $\Delta\tau$ and $\mathrm{P}_{\mathrm{int}}$ on $\Delta\tau$, $\Delta\nu = \nu_1 - \nu_2$ and $\Delta\phi_n = \phi_n(t_0 + \tau) - \phi_n(t_0)$ are omitted for the sake of readability. For a sufficiently large number of repetitions in the experiment, the cross-correlation function $g^{(2)}(\tau)$, constituted by the coincidences measured on the detectors, equals the probability $\mathrm{P}_{\mathrm{joint}}$ integrated over all possible detection times t_0 at the BS. We proceed further by evaluating $\mathrm{P}_0(t_0,\tau)$ and $\mathrm{P}_{\mathrm{int}}(t_0,\tau)$ separately. It is straightforward to find

$$
\begin{aligned}
g_0^{(2)}(\tau,\Delta\tau) &= \int_{-\infty}^{\infty} \mathrm{P}_0(t_0,\tau)\mathrm{d}t_0 \\
&= \frac{1}{8\tau_\mathrm{r}}\{\Theta(\tau+\Delta\tau)\exp(-\frac{\tau+\Delta\tau}{\tau_\mathrm{r}}) + \Theta(-\tau-\Delta\tau)\exp(\frac{\tau+\Delta\tau}{\tau_\mathrm{r}}) \\
&\quad +\Theta(\tau-\Delta\tau)\exp(-\frac{\tau-\Delta\tau}{\tau_\mathrm{r}}) + \Theta(-\tau+\Delta\tau)\exp(\frac{\tau-\Delta\tau}{\tau_\mathrm{r}})\}. \quad (2.79)
\end{aligned}
$$

The evaluation of $\mathrm{P}_{\mathrm{int}}(t_0,\tau)$ is comparably more difficult. However, up to now, we did only take into account a static frequency difference between the two emitters upon SD and a set phase due to PD. This obviously does not display reality in which both of these effects have to be modelled by stochaistic ergodic processes [230, 238] and thus we need to take the average of these fluctuations on $g_{\mathrm{int}}^{(2)}(\tau)$, yielding $G_{\mathrm{int}}^{(2)}(\tau) = \ll g_{\mathrm{int}}^{(2)}(\tau) \gg$. We denote here the average of both SD and PD by $\ll . \gg$, while averaging over one of the two is denoted as $< . >_{\mathrm{SD/PD}}$. Since the processes are ergodic, every possible phase or frequency displacement will occur with certainty when measuring for sufficiently long observation times. Thus it is possible to interchange the integration over t_0 with the averaging and we find

$$
\begin{aligned}
G_{\mathrm{int}}^{(2)}(\tau) &= \ll g_{\mathrm{int}}^{(2)}(\tau) \gg \\
&= \int_{-\infty}^{\infty} \ll \mathrm{P}_{\mathrm{int}}(t_0,\tau) \gg \mathrm{d}t_0.
\end{aligned}
$$

Since the cosine in equation 2.78 is the only part of $\mathrm{P}_{\mathrm{int}}(t_0,\tau)$ that is sensitive on phase and frequency fluctuations, we need only evaluate its average, which yields

$$
\begin{aligned}
&\ll \cos(2\pi\Delta\nu\tau + \Delta\phi_1 - \Delta\phi_2) \gg \; = \\
&\frac{1}{2}\{< \exp(2\pi i\Delta\nu\tau) >_{\mathrm{SD}} < \exp(i\Delta\phi_1) >_{\mathrm{PD}} < \exp(-i\Delta\phi_2) >_{\mathrm{PD}} \\
&+ < \exp(-2\pi i\Delta\nu\tau) >_{\mathrm{SD}} < \exp(-i\Delta\phi_1) >_{\mathrm{PD}} < \exp(i\Delta\phi_2) >_{\mathrm{PD}}\} \; = \\
&\frac{\exp(-2\Gamma|\tau|)}{2}\{< \exp(2\pi i\Delta\nu\tau) >_{\mathrm{SD}} + < \exp(-2\pi i\Delta\nu\tau) >_{\mathrm{SD}}\}.
\end{aligned}
$$

In the last step, we used the equality $< \exp(i\Delta\phi_n) >_{\mathrm{PD}} = \exp(-\Gamma|\tau|)$, which is derived in [239]. The PD rate Γ is the same for both $\Delta\phi_{1,2}$, since the photons are emitted by one emitter, which is permanently subject to PD. It is also assumed that PD occurs instantaneously, which is justified by its time scale being typically much faster than the excited state lifetime. For the evaluation of the SD, we assume that its impact over sufficiently long observation times yields a Gaussian distribution of emission frequencies ν_n. In this case the distribution of finding the first photon at a frequency ν_1 is given by the SD distribution in the equilibrium state

$$
p_1(\nu_1) = \frac{1}{\sqrt{2\pi\sigma_0^2}}\exp(-\frac{(\nu_1-\nu_0)^2}{2\sigma_0^2}). \quad (2.80)
$$

The central frequency of the distribution is ν_0 and its width is given by σ_0. However, since the two photons can possibly be retrieved from the quantum emitter much faster than the time scale on which SD typically happens, their emission frequencies can be dependent on

each other. The probability of finding the second photon at a frequency shifted by $\Delta\nu$ with respect to the frequency ν_1 of the first photon according to [230, 231] is given by

$$p_2(\nu_1+\Delta\nu) = \frac{1}{\sqrt{2\pi\sigma^2(\tau_{\mathrm{mzi}})}}\exp(-\frac{(\nu_1+\Delta\nu-\nu_c(\tau_{\mathrm{mzi}}))^2}{2\sigma^2(\tau_{\mathrm{mzi}})}) \tag{2.81}$$

$$\sigma^2(\tau_{\mathrm{mzi}}) = \sigma_0^2\{1-\exp(-\frac{2\tau_{\mathrm{mzi}}}{\tau_{\mathrm{SD}}})\} \tag{2.82}$$

$$\nu_c(\tau_{\mathrm{mzi}}) = \nu_0 + (\nu_1-\nu_0)\exp(-\frac{\tau_{\mathrm{mzi}}}{\tau_{\mathrm{SD}}}). \tag{2.83}$$

The timescale on which frequency fluctuations are correlated to each other is given by τ_{SD} and is generally not known for a quantum emitter under investigation. However, as we will find within this section, varying the timescale τ_{mzi} of the imbalanced MZI and measuring the coincidence probability of the interfering photons can be used to determine τ_{SD}. It is worthy to note that the case of photons being uncorrelated to each other is equal to the fact $\tau_{\mathrm{MZI}} \gg \tau_{\mathrm{SD}}$ and thus $\sigma \longrightarrow \sigma_0, \nu_c \longrightarrow \nu_0$, yielding the same distribution of SD for both photons as expected save the relative frequency difference $\Delta\nu$.
Since we are not interested in absolute frequency positions but only in relative frequency fluctuations between the two interfering photons as only this affects their wavefunction overlap, we calculate the probability distribution $\rho_\nu(\Delta\nu)$ describing two photons being separated exactly by a frequency difference $\Delta\nu$. This distribution is simply given by the cross-correlation of $p_1(\nu_1)$ and $p_2(\nu_1+\Delta\nu)$, yielding

$$\begin{aligned}\rho_\nu(\Delta\nu) &= \int_{-\infty}^{\infty} p_1(\nu_1)p_2(\nu_1+\Delta\nu)\mathrm{d}\nu_1 \\ &= \frac{1}{\sqrt{2\pi\Sigma^2}}\exp(-\frac{\Delta\nu^2}{2\Sigma^2}),\end{aligned} \tag{2.84}$$

with

$$\Sigma = 2\sigma_0^2\{1-\exp(-\frac{\tau_{\mathrm{mzi}}}{\tau_{\mathrm{SD}}})\}. \tag{2.85}$$

Having the right distribution on hand, we can calculate the average of the SD using

$$\begin{aligned}< \exp(\pm 2\pi i\Delta\nu\tau) >_{\mathrm{SD}} &= \int_{-\infty}^{\infty}\rho_\nu(\Delta\nu)\exp(\pm 2\pi i\Delta\nu\tau)\mathrm{d}\Delta\nu \\ &= \exp(-2\pi^2\Sigma^2\tau^2).\end{aligned} \tag{2.86}$$

It is worth noting, that Σ depends on the delay τ_{mzi}, which should be firmly kept in mind, however, we omit the dependency for the sake of readability. As a result of the evaluation of the SD and PD, we can write down the average of $\mathrm{P}_{\mathrm{int}}(t_0,\tau)$, which is given by

$$\begin{aligned}\ll \mathrm{P}_{\mathrm{int}}(t_0,\tau) \gg \;=\; & -\frac{1}{2\tau_{\mathrm{r}}^2}\Theta(t_0+\frac{\Delta\tau}{2})\Theta(t_0-\frac{\Delta\tau}{2})\Theta(t_0+\tau-\frac{\Delta\tau}{2})\Theta(t_0+\tau+\frac{\Delta\tau}{2}) \\ & \cdot\exp(-\frac{2t_0+\tau}{\tau_{\mathrm{r}}})\exp(-2\pi^2\Sigma^2\tau^2)\exp(-2\Gamma|\tau|).\end{aligned} \tag{2.87}$$

The cross-correlation function $G^{(2)}(\tau)$ can be obtained by integration of $\mathrm{P}_{\mathrm{joint}}(t_0,\tau)$ over all possible arrival times t_0 at the FBS. For a more convenient display of the result, we

define the following functions

$$f_0(\tau,\Delta\tau) = \frac{1}{2}\{\exp(-\frac{|\tau+\Delta\tau|}{\tau_\mathrm{r}}) + \exp(-\frac{|\tau-\Delta\tau|}{\tau_\mathrm{r}})\} \tag{2.88}$$

$$f_\mathrm{int}(\tau,\Delta\tau) = h_\mathrm{int}(\tau)\exp(-\frac{|\tau|+|\Delta\tau|}{\tau_\mathrm{r}}) \tag{2.89}$$

$$h_\mathrm{int}(\tau) = \exp(-2\pi^2\Sigma^2\tau^2)\exp(-2\Gamma|\tau|), \tag{2.90}$$

which enable us to write down the cross-correlation function in a compact way as

$$G^{(2)}_{\Delta\tau}(\tau,\Delta\tau) = \frac{1}{4\tau_\mathrm{r}}(f_0(\tau,\Delta\tau) - f_\mathrm{int}(\tau,\Delta\tau)), \tag{2.91}$$

with the label $\Delta\tau$ stating that the time averaging discussed below was not yet performed. Before the average can be calculated a secondary effect needs to be introduced: Throughout the course of the TPI measurements of photons emitted by SnV^- centres in sec. 7.1.2, it will become clear that excitation at a wavelength of about 530 nm populates a higher lying excited state. The decay into the lower excited state exhibits a significant time constant, with the meaning of its label τ_AE being explained in the experimental part on the TPI. The amount of τ_AE can be typically on the order of about 20 % of the excited state lifetime visible in time correlated single photon counting (TCSPC) measurements as a rising edge. This leads to an exponential excitation jitter, that we need to take into account in our model. Furthermore, a fixed timing delay δt between the photons arriving at the FBS results from imperfect length matching of the fibres in the imbalanced MZI. While the mismatch is small, it is still significantly contributing to the results and thus needs to be covered by the theoretical description. We take both of these effects into account by calculating a similar average over the time delay $\Delta\tau$, resulting from the excitation jitter, as for the description of the SD. The probability functions of finding one photon at a fixed time t_1 and a second photon at a relative time distance of $\Delta\tau + \delta t$ are given by

$$p_1(t_1) = \frac{\Theta(t_1)}{\tau_\mathrm{AE}}\exp(-\frac{t_1}{\tau_\mathrm{AE}}) \tag{2.92}$$

$$p_2(t_1,\Delta\tau,\delta t) = \frac{\Theta(t_1+\Delta\tau+\delta t)}{\tau_\mathrm{AE}}\exp(-\frac{t_1+\Delta\tau+\delta t}{\tau_\mathrm{AE}}). \tag{2.93}$$

We calculate the probability distribution describing the relative time distance between two photons being emitted again by the cross-correlation of $p_1(t_1,\Delta\tau,\delta t)$ and $p_2(t_1,\Delta\tau,\delta t)$, which yields

$$\rho_{\Delta\tau}(\Delta\tau,\delta t) = \frac{1}{2\tau_\mathrm{AE}}\exp(-\frac{|\Delta\tau+\delta t|}{\tau_\mathrm{AE}}). \tag{2.94}$$

Since the integrals that were solved on the way of deriving $G^{(2)}_{\Delta\tau}(\tau,\Delta\tau)$ do interchange with an integration over all time delays $\Delta\tau$, we can directly calculate the average

$$\begin{aligned} G^{(2)}(\tau) &= < G^{(2)}_{\Delta\tau}(\tau,\Delta\tau) >_t \\ &= \int_{-\infty}^{\infty}\rho_{\Delta\tau}(\Delta\tau,\delta t)G^{(2)}_{\Delta\tau}(\tau,\Delta\tau)\mathrm{d}\Delta\tau \\ &= \frac{g(\tau,\tau_\mathrm{r},\delta t) - g(\tau,\tau_\mathrm{AE},\delta t) - h_\mathrm{int}(\tau)(g(0,\tau_\mathrm{r},\delta t) - g(0,\tau_\mathrm{AE},\delta t))}{4(\tau_\mathrm{r}^2-\tau_\mathrm{AE}^2)}, \end{aligned} \tag{2.95}$$

with

$$g(\tau,\tau_i,\delta t) = \frac{\tau_i}{2}(\exp(-\frac{|\tau-\delta t|}{\tau_i}) + \exp(-\frac{|\tau+\delta t|}{\tau_i})). \tag{2.96}$$

With this we can directly evaluate TPI experiments conducted with consecutively emitted photons by a single quantum emitter. In Fig. 2.23, the solution of equation 2.95 for certain parameter sets is depicted in red as well as the constituting parts $G_0^{(2)}(\tau)$ (green) and $G_{\mathrm{int}}^{(2)}(\tau)$ (purple). For the case of no imperfections being present, those two parts add up to zero and we end up in the case of perfectly indistinguishable photons shown in Fig. 2.23a) for a radiative lifetime of $\tau_{\mathrm{r}} = 5\,\mathrm{ns}$. In b) an excitation jitter of $\tau_{\mathrm{AE}} = 1\,\mathrm{ns}$ is assumed, which leads to $G_{\mathrm{int}}^{(2)}(\tau)$ no longer fully compensating $G_0^{(2)}(\tau)$. Furthermore, the timing jitter leads to a smoothening of the peak of $G_0^{(2)}(\tau)$. The case of a fixed arrival time mismatch $\delta t = 1\,\mathrm{ns}$ illustrates a similar reduction of compensation in c) but with a different shape, while the time offset is visible in the double peak structure of $G_0^{(2)}(\tau)$. The influence of PD in d) with $\Gamma = 100\,\mathrm{MHz}$ and SD in e) with a width of $\sigma_0 = 100\,\mathrm{MHz}$ and a time delay of the imbalanced MZI of $\tau_{\mathrm{MZI}} = 10\,\mathrm{ns}$, while τ_{SD} is set to 100 ns, again reduces the compensation of $G_0^{(2)}(\tau)$ by $G_{\mathrm{int}}^{(2)}(\tau)$. However, the different shape of the dip in $G^{(2)}(\tau)$ makes it possible in principal to tell the two effects in measurements apart. Finally, all beforementioned imperfections contribute to the cross-correlation function depicted in f) and furthermore reduce the contrast between $G_0^{(2)}(\tau)$ and $G^{(2)}(\tau)$. It is interesting as well as expected from the theoretical description of $G^{(2)}(\tau)$, that no matter the effect of imperfections, for a time delay of exact $\tau = 0$, the cross-correlation function is equal to zero. In the presented graphs this is visible as the dip at $\tau = 0$, which only gets narrower for increasing contributions of decoherence but does not vanish. In the experiment however, resolving this dip can be obstructed for the case of nearly distinguishable photons when the dip width approaches the timing resolution of the detectors and electronics.
As the final value of interest, the visibility of the TPI can be extracted using the theoretical model described above. This is achieved by calculating the total probability of coincidences $\mathrm{p_{coinc}}$ by simply integrating $G^{(2)}(\tau)$ over all time delays τ between coincidence events. We find it to amount to

$$\begin{aligned}\mathrm{p_{coinc}} &= \int_{-\infty}^{\infty} G^{(2)}(\tau)\mathrm{d}\tau \\ &= \frac{1}{2}\Big(1 - \frac{\mathrm{erfc}(\frac{\gamma}{2\sqrt{2}\pi\Sigma})\exp(\frac{\gamma^2}{8\pi^2\Sigma^2})}{\sqrt{2\pi}\Sigma(\tau_{\mathrm{r}}^2 - \tau_{\mathrm{AE}}^2)}\{\tau_r \exp(-\frac{|\delta t|}{\tau_{\mathrm{r}}}) - \tau_{\mathrm{AE}}\exp(-\frac{|\delta t|}{\tau_{\mathrm{AE}}})\}\Big),\end{aligned}$$

where we introduced the abbreviation $\gamma = 2\Gamma + \frac{1}{\tau_{\mathrm{r}}}$. The visibility V of the interference is defined in accordance with literature [230] as

$$V = 1 - 2\mathrm{p_{coinc}},$$

which yields zero in the classical limit of totally distinguishable photons ($\mathrm{p_{coinc}} = \frac{1}{2}$) and one for fully indistinguishable photons ($\mathrm{p_{coinc}} = 0$). The exact degree of indistinguishability in between these limits is given by the result

$$V = \frac{\mathrm{erfc}(\frac{\gamma}{2\sqrt{2}\pi\Sigma})\exp(\frac{\gamma^2}{8\pi^2\Sigma^2})}{\sqrt{2\pi}\Sigma(\tau_{\mathrm{r}}^2 - \tau_{\mathrm{AE}}^2)}\{\tau_{\mathrm{r}}\exp(-\frac{|\delta t|}{\tau_{\mathrm{r}}}) - \tau_{\mathrm{AE}}\exp(-\frac{|\delta t|}{\tau_{\mathrm{AE}}})\}). \tag{2.97}$$

The dependence of the visibility on its individual constituents is shown in Fig. 2.24. In part a), the decrease of visibility with increasing excitation jitter compared to the excited state lifetime is depicted for photons emitted by a quantum emitter. The biexpontential decrease of the visibility with the fixed time delay δt in the arrival time shown in part b)

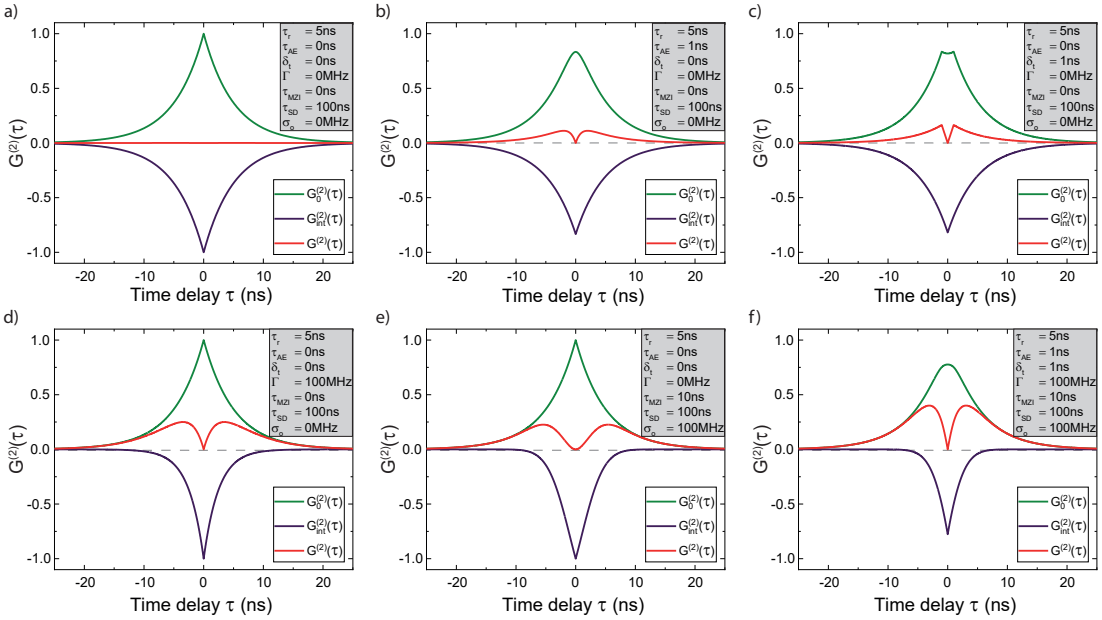

Figure 2.23: **Dependence of the cross-correlation function on imperfections:** Illustration of the dependence of the cross-correlation function $G^{(2)}(\tau)$ and its constituting parts $G_0^{(2)}(\tau)$ and $G_{\mathrm{int}}^{(2)}(\tau)$ of photons being emitted by a quantum emitter with a radiative lifetime $\tau_{\mathrm{r}} = 5\,\mathrm{ns}$ and a timescale of SD of $\tau_{\mathrm{SD}} = 100\,\mathrm{ns}$. The emitter is subject to either **a)** no other influences, **b)** an excitation jitter with $\tau_{\mathrm{AE}} = 1\,\mathrm{ns}$, **c)** a fixed timing offset between the arriving photons of $\delta t = 1\,\mathrm{ns}$, **d)** PD with a width of $\Gamma = 100\,\mathrm{MHz}$, **e)** SD with a width of $\sigma_0 = 100\,\mathrm{MHz}$ and a time delay of the imbalanced MZI of $\tau_{\mathrm{MZI}} = 10\,\mathrm{ns}$ or **e)** all beforementioned imperfections acting together.

of the figure is to be expected from the namely dependence in equation 2.97. However, more surprising is the comparison to the comined effects of excitation jitter and fixed time delays contributing to the visibility in part c). While the maximum of V at $\delta t = 0$ is reduced for an excitation jitter of $\tau_{\mathrm{AE}} = 0.8\tau_{\mathrm{r}}$, the visibility surpasses the one derived for $\tau_{\mathrm{AE}} = 0$ for larger values of δt. The reason for this is, that the excitation jitter for photons arriving with a relatively large fixed time separation at the FBS enhances the overlap of the photon ensemble wave package and thus leads to an increase in visibility. In the last part of the figure, the impact of PD and SD on the visibility are depicted for widths of $\Gamma \cdot \tau_{\mathrm{r}} = 0.5$ and $\sigma_0 \cdot \tau_{\mathrm{r}} = 0.5$ while the MZI delay τ_{MZI} is varied with respect to the SD time scale τ_{SD}. For small values of τ_{MZI}, PD is the dominating factor limiting the visibility, while for larger values SD becomes relevant and its effect fully unfolds for $\tau_{\mathrm{MZI}} \gg \tau_{\mathrm{SD}}$.

2.3.3 Timing pattern of TPI measurements with consecutive photons

The previous section describes the effect of TPI on the coincidence pattern of two photons interfering at a FBS. In a real measurement, this interference pattern is obtained by acquiring large statistics of coincidences in a correlation measurement as described above. As the photons are consecutively retrieved from a single quantum emitter, the imbalanced MZI (Fig. 2.22) is used to overlap them at the FBS. This leads to an overall coincidence pattern in time that is more complex than only the interference peak shown in Fig. 2.23, which the theoretical description was focussed on in the previous section. For the derivation of the pattern it is helpful to regard the following thought experiment: Consider a stream of

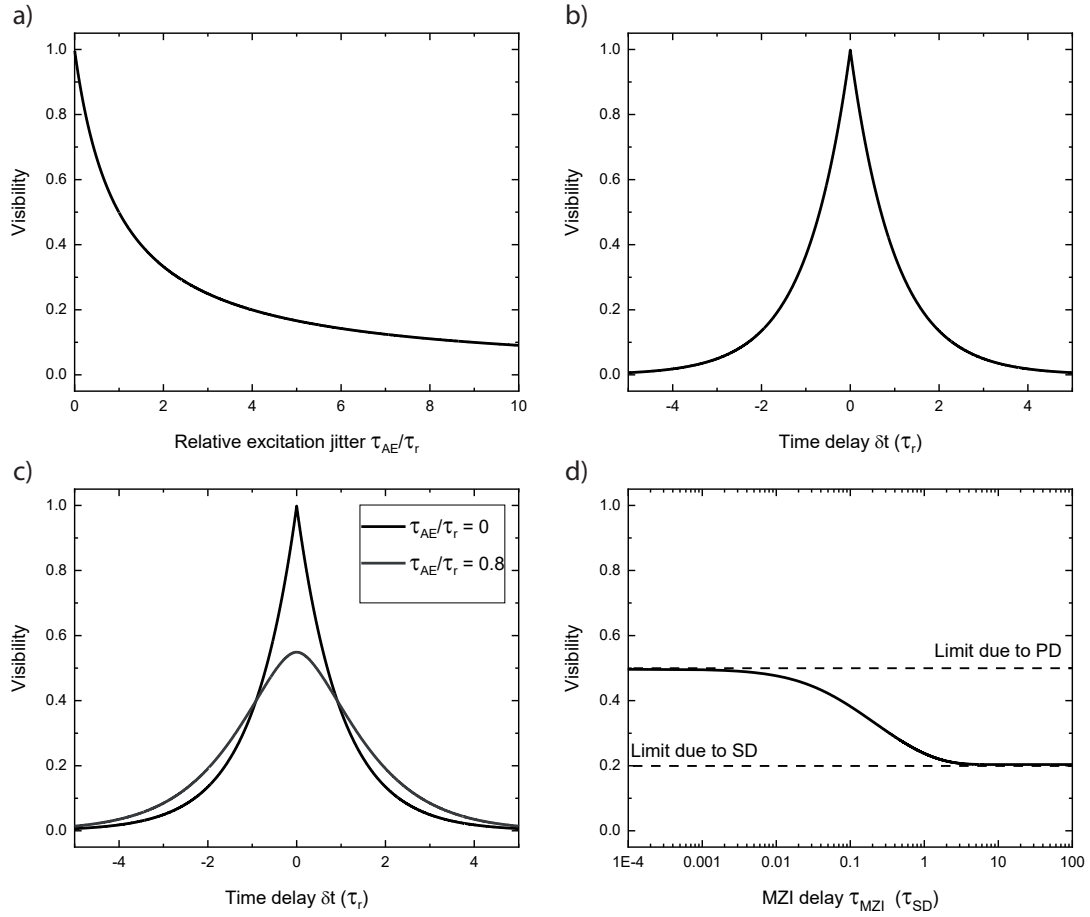

Figure 2.24: **Dependence of the visibility on imperfections:** According to equation 2.97, the visibility of TPI for a quantum emitter is derived in dependence of an influential factor such as **a)** the excitation jitter τ_{AE}, **b)** the fixed time delay δt in between the arrival of the photons at the FBS and **c)** the combined effect of the previous two factors. Depicted is the case for no excitation jitter (black) in comparison to $\tau_{\mathrm{AE}} = 0.8\tau_{\mathrm{r}}$ (brown) in dependence of the time delay δt. It is worth noting that while the maximum visibility for the case of a significant excitation jitter is lowered, V surpasses the visibility of no excitation jitter being present for larger time delays δt. In this case the excitation jitter leads to a larger photon wave package overlap compared to photons arriving only with a fixed arrival time delay. In **d)** the effects of PD and SD are depicted for $\Gamma \cdot \tau_{\mathrm{r}} = 0.5$ and $\sigma_0 \cdot \tau_{\mathrm{r}} = 0.5$ and variation of the MZI delay τ_{MZI} with respect to the SD time scale τ_{SD}. The limited visibility for small values of τ_{MZI} is caused by the fast process of PD, while the effect of SD only fully unfolds for $\tau_{\mathrm{MZI}} \gg \tau_{\mathrm{SD}}$.

entirely distinguishable photons with no temporal width (delta-pulse) and separated by a time delay τ_{exc}. The MZI interferometer is set to exactly compensate for the excitation delay, i.e. $\tau_{\mathrm{MZI}} = \tau_{\mathrm{exc}}$ (N=1). We will now pick out one photon i within this stream of photons and evaluate how many possibilities and at which time delays exist for yielding a detectable coincidence. We only consider the options of arrivals with a certain delay at the FBS, which for distinguishable photons can then lead to a coincidence in one half of the cases. As this is valid for all possibilities, the scaling factor of $\frac{1}{2}$ is omitted. The time delay τ is set negative if a photon arrives in advance of photon i at the FBS and thus at an APD, while its sign is set positive for a photon arriving later than photon i. This leads

to the following possibilities:

1. For a coincidence, where both photons arrive at the same time ($\tau = 0$) at the FBS, there are two possibilities:
   (a) Photon $i-1$ preceeding photon i takes the long interferometer path and photon i takes the short path
   (b) Photon i takes the long path and the following photon $i+1$ takes the short path.
2. For a coincidence, where both photons arrive separated by a time delay of $\tau = -\tau_{\text{exc}}$ at the FBS, there exist three possibilities:
   (a) Photon $i-1$ and photon i both take the short path
   (b) Photon $i-1$ and photon i both take the long path
   (c) Photon $i-2$ takes the long path, while photon i takes the short path
3. For a coincidence, where both photons arrive separated by a time delay of $\tau = \tau_{\text{exc}}$ at the FBS, there exist three possibilities:
   (a) Photon $i+1$ and photon i both take the short path
   (b) Photon $i+1$ and photon i both take the long path
   (c) Photon $i+2$ takes the short path, while photon i takes the long path
4. For a coincidence, where both photons arrive separated by a time delay $\tau = -\text{k}\tau_{\text{exc}}$ (k>1) at the FBS, there exist four possibilities:
   (a) Photon $i-k$ and photon i both take the short path
   (b) Photon $i-k$ and photon i both take the long path
   (c) Photon $i-k-1$ takes the long path and photon i takes the short path
   (d) Photon $i-k+1$ takes the short path and photon i takes the long path
5. For a coincidence, where both photons arrive separated by a time delay $\tau = \text{k}\tau_{\text{exc}}$ (k>1) at the FBS, there exist four possibilities:
   (a) Photon $i+k$ and photon i both take the short path
   (b) Photon $i+k$ and photon i both take the long path
   (c) Photon $i+k-1$ takes the long path and photon i takes the short path
   (d) Photon $i+k+1$ takes the short path and photon i takes the long path

These probabilities result in a coincidence pattern, which consists of a middlepeak at $\tau = 0$ with a relative height of 2, two neighbouring peaks at $\tau = \pm\tau_{\text{exc}}$ with a relative height of 3 and an infinite number of peaks at $\tau = \pm\text{k}\tau_{\text{exc}}$ (k>1) with a relative heigth of 4. The scheme can be directly converted to the situation of $\tau_{\text{MZI}} = \text{N}\tau_{\text{exc}}$, with the difference now that all peaks are at a relative height of 4, while the middle peak stays at two and the peaks at $\tau = \pm\text{N}\tau_{\text{exc}}$ are diminished to a relative height of 3. Translating the thought experiment to the use of real photons with a temporal shape and the possibility of TPI, the pattern stays the same but the peaks are now described by copies of the incoherent contribution $G_0^{(2)}(\tau)$ of the cross-correlation function $G^{(2)}(\tau)$ derived in the previous section, weighed by their relative peak height. The only exception is the middle peak for which TPI can

occur. In general, also the photons resulting from the overlap of the neighbouring peaks at zero delay are influenced by TPI, however, as their wavefunction overlap is negligible it is neglected here. In consequence, the middle peak is weighed by the relative peak height of 2, but described by the full cross-correlation function $G^{(2)}(\tau)$. In conclusion, the summed pattern can be written as

$$G^{(2)}_{\sum}(\tau) = 2G^{(2)}(\tau) + 3G^{(2)}_0(\tau \pm \mathrm{N}\tau_{\mathrm{exc}}) + 4 \sum_{\mathrm{k}\neq \mathrm{N},0} G^{(2)}_0(\tau \pm \mathrm{k}\tau_{\mathrm{exc}}). \tag{2.98}$$

Multiplying this theoretical function with an amplitude factor A and thereby accounting for the experimentally obtained unnormalised statistics and furthermore adding a uniform background contribution bg, which might result from APD dark counts or background fluorescence from the sample under investigation, leads to the fitting function

$$G^{(2)}_{\mathrm{fit}}(\tau) = \mathrm{A}G^{(2)}_{\sum}(\tau) + \mathrm{bg}. \tag{2.99}$$

This function is now the final instrument for fitting the measurement data obtained in a TPI experiment. For illustration, Fig. 2.25a) shows a simulated coincidence measurement

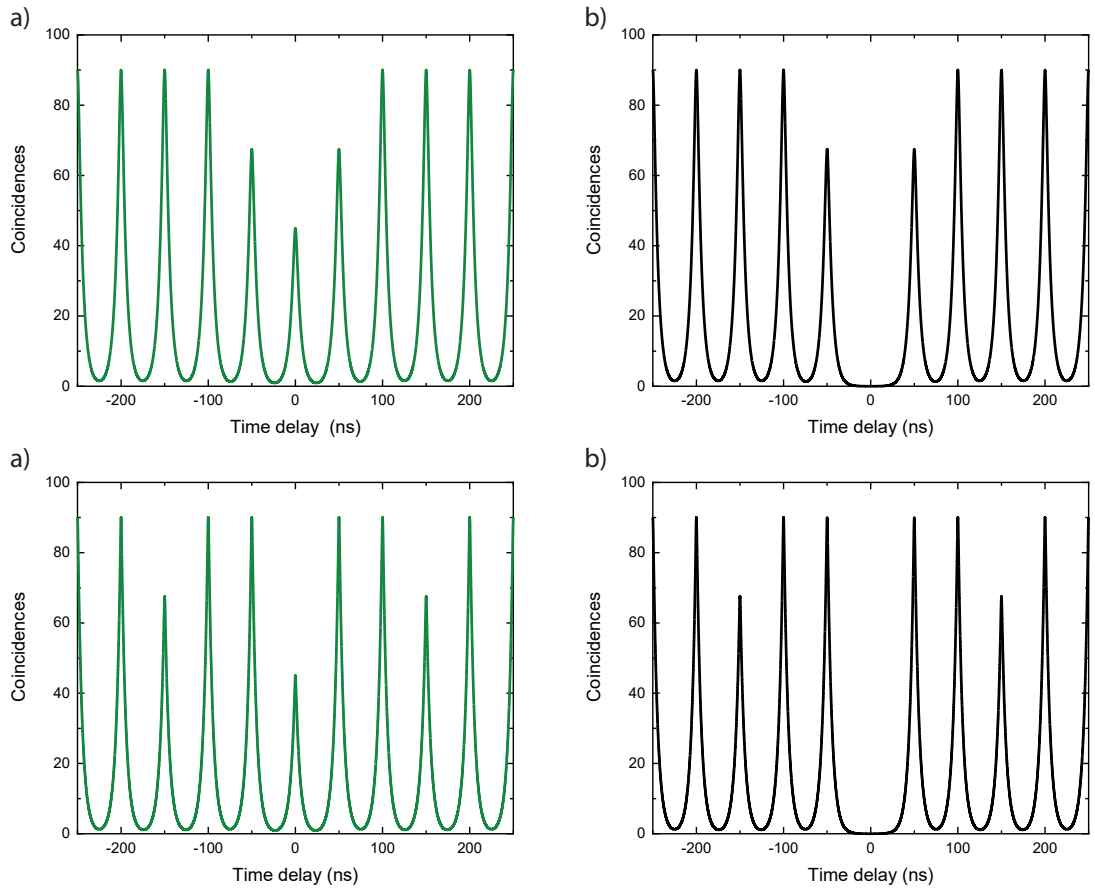

Figure 2.25: **Simulated coincidence measurement:** The simulation displays a fictional coincidence measurement with $\tau_{\mathrm{MZI}} = \tau_{\mathrm{exc}} = 50\,\mathrm{ns}$ and $\tau_{\mathrm{r}} = 5\,\mathrm{ns}$ following equation 2.99 for **a)** fully distinguishable and **b)** completely indistinguishable photons. The same pattern for $\tau_{\mathrm{MZI}} = 3\tau_{\mathrm{exc}}$ are displayed in **c)** and **d)** where the reduced peak height of the third neighbouring peak discussed in the main text becomes obvious.

for $\tau_{\mathrm{MZI}} = \tau_{\mathrm{exc}} = 50\,\mathrm{ns}$ in the case of fully distinguishable photons with $\tau_{\mathrm{r}} = 5\,\mathrm{ns}$. The relative peak height as derived in this section is clearly visible. For the case of completely indistinguishable photons, which is depicted in Fig. 2.25b), the middle peak vanishes due to the occuring TPI.

Chapter 3

Sample preparation & optical setups

3.1 Samples

3.1.1 Fabrication of SnV HPHT samples

Within this thesis, we investigate two different HPHT annealed samples, which are named NI58 and BOJO_001. Both samples are fabricated in a similar fashion, starting off with an electronic grade (001) diamond sample. The latter is specified to contain less than 5 ppb (typically 0.1- 1 ppb) of substitutional nitrogen ($[N]_s^0$) and less than 1 ppb of substitutional boron ([B]).

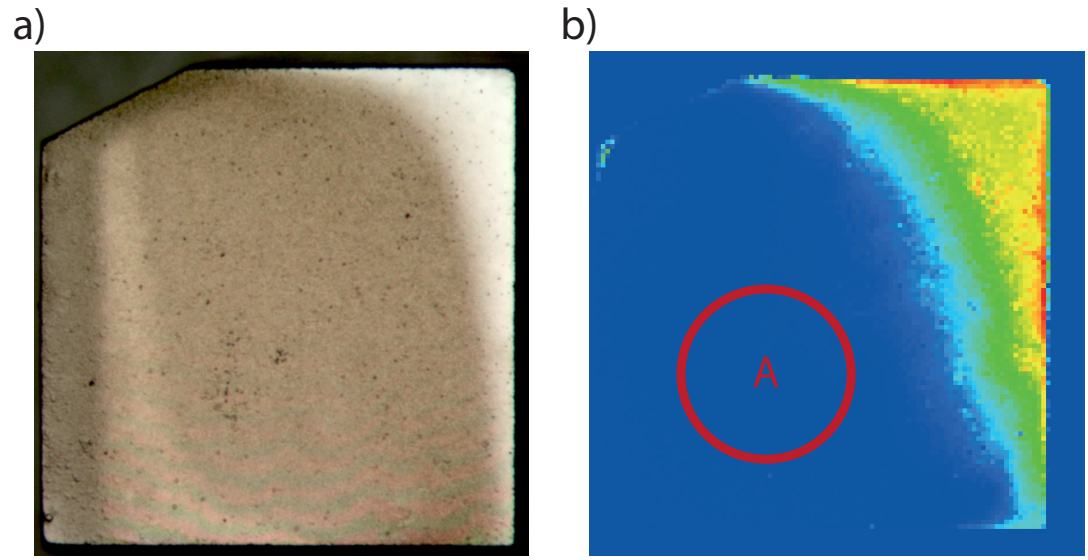

Figure 3.1: **Microscope and fluorescence image of sample NI58: a)** Light microscope picture of sample NI58. In the upper right corner, no removal of diamond during the HPHT annealing was induced. In the other parts of the sample, the graphitisation of diamond is obvious by brown residues. **b)** Fluorescence image taken in a confocal microscope scan under 532 nm illumination and detection with a 600LP filter. In the upper right corner, the implanted ensemble is fully resolved, while the fluorescence intensity decreases where diamond and the incorporated SnV^- centres were removed. This yields a smooth transition from dense ensembles to region A, in which single SnV^- centres can be resolved.

The clean diamond environment leads to the reduction of charge traps and donors as well as the content of NV^- centres. Reducing the NV^- centre concentration is crucial, as the emission spectrum overlaps strongly with the one of the investigated SnV^- centres.
Tin is introduced into the samples by ion implantation, in which the ions are accelerated to an energy of 700 keV and subsequently focussed onto the diamond samples. The resulting implantation depth of the tin ions, estimated by Monte-Carlo simulations (SRIM), amounts to 168(30) nm. For NI58, the sample is homogeneously implantated with a fluence of $8\text{x}10^{13}\,\frac{\text{Ions}}{\text{cm}^2}$, where the lateral homogeneity is achieved by repeatedly scanning the ion beam with a diameter of $1\,\text{cm}^2$ across the diamond. The implantation of BOJO_001 is carried out with four different fluences of $1\text{x}10^{9}\,\frac{\text{Ions}}{\text{cm}^2}$, $1\text{x}10^{10}\,\frac{\text{Ions}}{\text{cm}^2}$, $1\text{x}10^{11}\,\frac{\text{Ions}}{\text{cm}^2}$ and $1\text{x}10^{12}\,\frac{\text{Ions}}{\text{cm}^2}$, which are guided to distinct spots on the sample via stainless steel pinholes mounted on top of the diamond. For this sample, the tin isotope ^{119}Sn is chosen, which exhibits a nuclear spin of $I = \frac{1}{2}$.

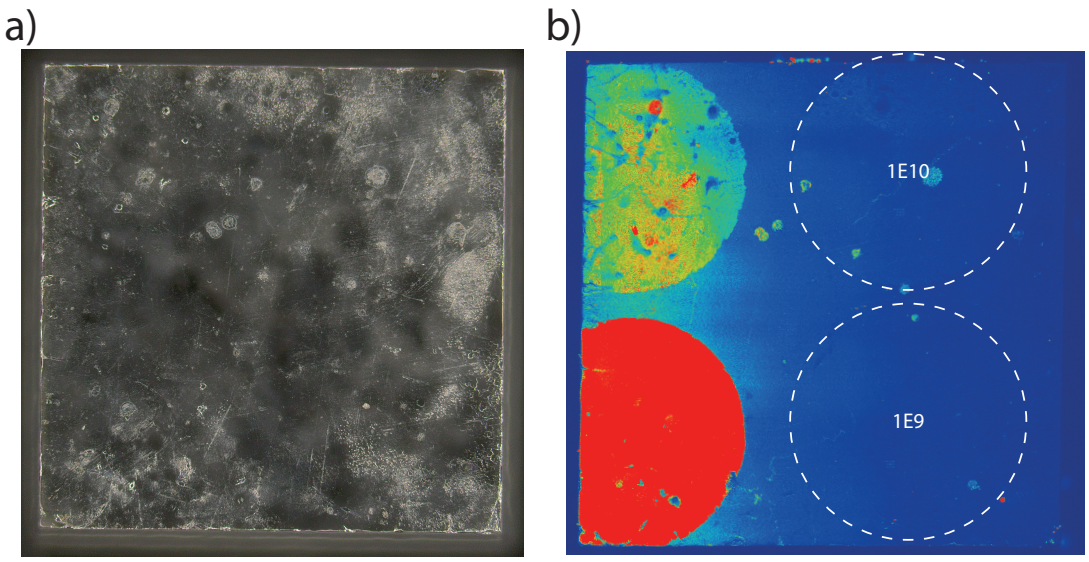

Figure 3.2: **Microscope and fluorescence image of sample BOJO_001: a)** Dark field microscope picture of sample BOJO_001. The cracks induced by the HPHT treatment are visible as bright regions. **b)** Fluorescence image taken in a confocal microscope scan under 532 nm illumination and detection with a 600LP filter. In the lower and upper left corner, the ensembles implanted with the highest fluences ($1\text{x}10^{12}\,\frac{\text{Ions}}{\text{cm}^2}$,$1\text{x}10^{11}\,\frac{\text{Ions}}{\text{cm}^2}$) are visible. While for the implantation fluence of $1\text{x}10^{10}\,\frac{\text{Ions}}{\text{cm}^2}$ a slightly brighter area can be distinguished, for the lowest fluence region the fluorescence response is too weak to resolve it in the image. However, only in the latter, clearly spatially separated single SnV^- centres can be resolved.

As the implantation process with heavy tin ions induces massive damage in the diamond lattice (see sec. 2.1.1), both samples are subsequently subjected to a HPHT annealing. This is carried out at a temperature of T = 2100 °C. As this temperature is sufficient to massively graphitise diamond, a pressure of 7.7 GPa (8 GPa) for sample NI58 (BOJO_001) is applied to stabilise the diamond phase. The annealing is conducted for 20 min (120 min) on sample NI58 (BOJO_001). Fig. 3.1 shows the comparison of a picture of sample NI58 obtained in an optical microscope (a) to a fluorescence scan (b) of SnV^- centre emission. The crescent-shaped fluorescence pattern of SnV^- centres translates directly to regions of

the sample where no diamond was removed during the annealing, i.e. regions of the sample purely transparent in the optical image. This inhomogeneous removal is induced during the annealing process unintentionally, however, it provides a smooth transition from dense ensembles of SnV^- centres to low density ensembles. In region A in Fig. 3.1 even single emitters can be resolved. The brown graphite residues visible in the regions of the diamond where diamond was graphitised, could not be removed by several cleaning steps in boiling tri-acid (1:1:1 mixture of sulfuric, perchloric and nitric acid, 500 °C). Fig. 3.2 shows the same comparison for sample BOJO_001, where the two spots containing SnV^- centres resulting from the highest implantation fluences can be resolved in the fluorescence scan. The lower fluence implantation spots are highlighted by the dashed white circles. Only in the lowest fluence spot, clearly spatially separated single emitter can be resolved. In the optical dark field image, impact of the HPHT annealing can be seen on the surface, resulting in cracks and scratches. None of these were removable by the tri-acid cleaning.

3.1.2 Fabrication of SnV LPLT sample

The sample SC500_01 is the result of tin ion implantation at an energy of 80 keV and varying fluences into an electronic grade (001) diamond. The resulting depth of the tin ions obtained by SRIM simulations is 26 nm. The annealing process for this sample in the following is labeled as low-pressure-low-temperature (LPLT), as it is conducted at a temperature of 1200 °C in vaccuum for 4 h. After the annealing the same tri-acid clean is applied, followed by an additional oxidisation at 450 °C in an air atmosphere.

3.2 Optical setups

This section is dedicated to give a detailed overview and understanding of the experimental setups that are the foundation of this thesis. Since there were used two main setups that consist of similar components, the section starts by introducing different modules such as excitation sources or laser modulation. The complete setups will then be explained by combining the modules introduced before.

3.2.1 Excitation sources

A set of different excitation sources is necessary to conduct the experiments described in this thesis as the excitation of SnV^- centres can be achieved through resonant excitation, off-resonant excitation via the phononic ladder of the excited state or via a quasi-resonant excitation into higher lying excited states, which strongly couple to the valence band. Furthermore, a main finding of our work is the necessity to implement a charge stabilisation when resonantly exciting the SnV^- centre, which is introduced utilising a second light field. For these reasons, we use the following laser sources:

1. Quasi-resonant laser: Linos Nano-532-100 (Qioptiq Photonics, 532 nm, continuous wave)
   This laser is used for quasi-resonant excitation and is of major importance through the course of chapter 4. It is furthermore needed as a weak repump laser of spin state populations for the photoluminescence excitation spectroscopy under application of magnetic fields.

2. Supercontinuum laser source: SuperK Extreme and SuperK Fianium (NKT Photonics, tunable wavelength, pulsed, variable repetition rate and bandwidth)
   The two lasers will be addressed in the following as “Supercontinuum laser source”

as their main difference is the achievable output power. These lasers are used for a variety of measurements including PLE on higher lying excited states, the fluorescence enhancement under two colour excitation, lifetime measurements and the pulsed HOM interference.

3. Dye laser: Matisse 2DS (Sirah, tunable wavelength, continuous wave)
   Resonant excitation of SnV^- centres is achieved with a tunable dye laser. It offers a modehop free tuning range of 60 GHz while preserving a linewidth of below 200 kHz in a time interval of 100 ms. Active stabilisation is obtained by a low Finesse ($\mathcal{F} \approx 50$) reference cavity in a side of fringe scheme. The absolute wavelength can be stabilised on a wavemeter feedback signal.

4. Charge stabilisation laser: (Hübner Photonics, 445 nm, continuous wave)
   Active charge stabilisation of the negative charge state of SnV^- centres is achieved with a 445 nm continuous wave diode laser.

3.2.2 Laser modulation

Amplitude modulation Many of the experiments conducted within this thesis rely on the application of laser pulses. Since three of the above-mentioned excitation sources are continuous wave lasers, it is necessary to carve out pulses. This amplitude modulation is achieved using acousto-optical modulators (AOM, AOMO 3200-146, Crystal Technology). The basic working principle is that an acoustic wave is applied to a transparent crystal, creating a periodic modulation of the refractive index. This effectively constitutes an optical grating and leads to diffraction of the laser light. The devices used in our work are optimised for maximal diffraction into the first diffractive order. The zeroth order and the first order are separated in space. We filter the first order spatially by coupling it into a single mode fibre, with the fibre core acting as pinhole. This leads to transmission of the first and extinction of the zeroth order light. By switching the acoustic wave on and off, amplitude modulation is achieved. In order to achieve this, the driver of the AOM which provides the acoustic wave, is controlled by TTL pulses, which we deliver using a digital delay generator (DDG, DG645, Stanford Research Systems). Since the rise time of the optical pulses is limited by the travelling time of the acoustic wave through the laser spot in the crystal, we focus our laser to about 50 µm diameter using optical lenses with a focal length of 50 mm. Two AOMs of the same type are used, one for carving pulses from the resonant light ("Red AOM") and the other chopping the 445 nm charge initialisation light ("Blue AOM"). The achieved rise time of the red AOM for the intensity increasing from 10 % to 90 % is 7.3(1) ns while the fall time amounts to 9.6(1) ns, see Fig. 3.3. This is ultimately limited by the rise and fall time of the TTL pulse applied, being about 4 ns. The same measurement for the blue AOM yields a rise time of 8.0(1) ns and a fall time of 9.9(1) ns. The second important characteristic of an AOM is the extinction ratio, which gives information about the ratio between the transmitted intensity when the TTL pulse is or is not applied. Both AOMs show a trailing edge that is depicted in Fig. 3.3b), which limits the extinction ratio to about 1:650 for both AOMs after the pulse is switched off for 500 ns. This is most likely induced by a trailing edge of the voltage pulse generated by the DDG and can be optimised in future experiments.

Phase modulation The coherent manipulation of SnV^- centres, which is discussed in sec. 2.2, requires the use of two laser fields. We generate the second light field by using one laser and employing an electro optical phase modulator (EOPM, WPM-K0620,

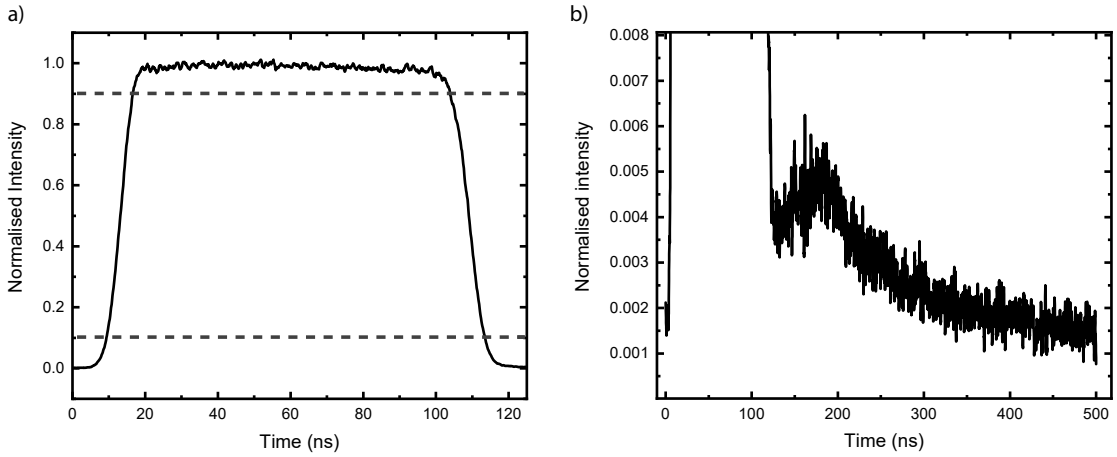

Figure 3.3: **AOM characterisation: a)** Application of a 100 ns long TTL pulse to the red AOM results in the displayed optical pulse carved out of the cw dye laser. The rise (fall) time of the pulse amounts to 7.3(1) ns (9.6(1) ns). **b)** The extinction ratio is limited by the trailing edge of the AOM and reaches about 1:650 after switching the TTL pulse off for 500 ns.

AdvR). Within this modulator, light is send through an in-diffused non-linear crystal waveguide made of KTP. Application of a strong microwave field introduces a change in the refractive index due to the electro-optic effect. This effect leads to the creation of optical sidebands at the difference and sum of the laser carrier and the microwave frequency. An exemplary sideband spectrum created with the EOPM used is depicted in Fig. 3.4a). The characteristic two first and second order sidebands are separated symmetrically around the carrier frequency by the applied microwave frequency of 2.5 GHz. Since the spectrum is measured using a scanning FPI (Toptica Photonics) with a free spectral range (FSR) of 2 GHz, the replicas of the carrier and their respective sidebands are omitted for the sake of clarity. The strength of the microwave field determines the amount of laser power being emitted into the sidebands and the suppression of the light at the carrier frequency. The intensity emitted into the sidebands and carrier as function of the voltage induced by the applied microwave is depicted in Fig. 3.4b). The power dependent intensities are fitted well by the expected squared Bessel functions of zeroth, first and second order. We extract a $\pi-$ voltage of $V_\pi = 3.5\,V$ and a carrier extinction of 1:60. In most experiments the microwave is provided by the microwave generator mg3692c (Anritsu). For the single-shot readout, two sidebands at different microwave frequencies are necessary and the second field is retrieved from the microwave generator SG384 (Stanford Research Systems). In the experiments where the sidebands need to be switched on and off, the microwave fields are modulated using microwave switches (ZASW-2-50DRA+, Mini-Circuits). Before being applied to the EOPM, the microwave is amplified (ZHL-42+, Mini-Circuits) by about 32 dBm.

3.2.3 Hong-Ou-Mandel interferometry setup

This section is dedicated to the different components of the setup, which are employed for the TPI experiments.

Filter setup The visibility of TPI relies strongly on the spectral indistinguishability of the interfering photons. This means that a narrow spectral filtering of one fine structure

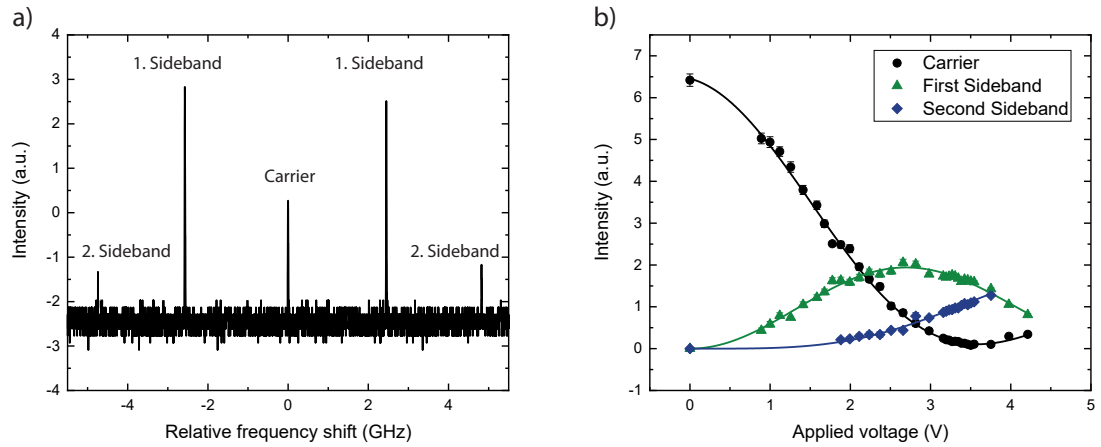

Figure 3.4: **Sideband spectra and microwave power dependent sideband modulation: a)** Characteristic spectrum of the EOPM driven with a microwave frequency of 2.5 GHz and an applied voltage of 2.5 V taken with a scanning FPI. Adjacent carrier signals and their respective sidebands overlapping due to the FSR of 2 GHz of the FPI are omitted for the sake of clarity. **b)** The intensity of the carrier and the first two sidebands as function of the voltage applied to the EOPM is well described by the expected squared Bessel functions of zeroth, first and second order (for carrier, first and second sideband). The modulator characteristics are extracted to be $V_\pi = 3.5\,V$ and an extinction of the carrier at this voltage of 1:60.

line of the SnV^- centre is necessary in order to achieve spectral purity. In the present case, the spectral selectivity is achieved using a specifically designed plano-convex filter lens (r = 250 mm). The optic is made of NBK-7, which is coated such, that the reflectivity amounts to R = 98.5 % at a wavelength of 620 nm (Coating done by Laseroptik). The system constitutes a monolithic Fabry-Perot interferometer and thus an optical resonator, which periodically transmits longitudinal and transversal modes. The working principle is to tune the temperature stabilised filter lens into resonance with one of the optical transitions of the SnV^- centre, while the other transitions and potential background are not transmitted through the cavity and therefore suppressed. This functionality is characterised in detail in the following.

Since the filter lens acts as a cavity, it is important to achieve mode matching of the incoupling light to the TEM_{00} mode of the lens (see. Fig. 3.5 for design of the optical setup). To this end, an uncoated plano-convex coupling lens ($f = 250\,mm$) is employed, which is mounted on a linear positioning stage to achieve optimal coupling. We measure the divergence of the Gaussian mode utilising a beam profiler (BeamScope-P8, Soliton GmbH) that we position at variable distances behind the filter lens. The extracted $\frac{1}{e^2}$ beam radius $r_{\frac{1}{e^2}}$ obeys the theoretically expected

$$r_{\frac{1}{e^2}}(z) = r_0\sqrt{1+\left(\frac{z}{z_0}\right)^2} \tag{3.1}$$

divergence law [240], with the Rayleigh length $z_0 = \frac{\pi r_0^2}{\lambda}$. The data is reproduced well using r_0 as fit parameter and the result is depicted in Fig. 3.6. For x- and y- direction, we extract a beam waist of $r_{0,x} = 289(75)\,\mu m$ and $r_{0,y} = 268(64)\,\mu m$, which emphasises that the resonator TEM_{00} mode is addressed. With the used optics, we achieve a coupling

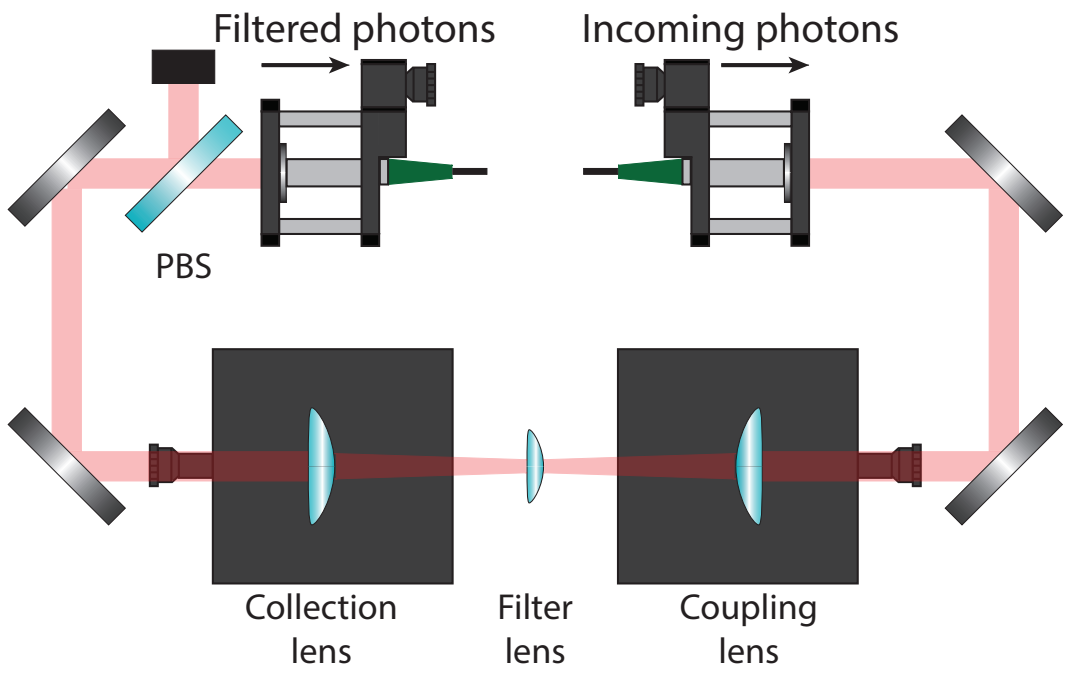

Figure 3.5: **Optical filter lens setup:** The photons are coupled out of an optical fibre and focussed via a collection lens into the filter lens. Transmitted photons through the filter lens are collimated by a subsequent collection lens. The distance of the two collection lenses relativ to the filter lens can be adjusted by the linear stages the lenses are mounted on. The outgoing photons from the filter lens are passing through a PBS, which fixes their polarisation axis, and coupled into an optical fibre.

efficiency to the filter lens of $\eta_{\mathrm{FL}} = 65\,\%$. This efficiency is limited by losses during the numerous round trips in the cavity due to absorption in the coating and mode mismatch. In combination with the subsequent fibre coupling efficiency of $\eta_{\mathrm{FC}} = 90\,\%$ and the transmission efficiency of an employed polarising beam splitter (PBS) $\eta_{\mathrm{PBS}} = 89\,\%$, we reach an overall filter setup efficiency of $\eta_{\mathrm{FS}} = \eta_{\mathrm{FL}} \cdot \eta_{\mathrm{FC}} \cdot \eta_{\mathrm{PBS}} = 52\,\%$. The PBS is necessary since the input polarisation of the subsequent interferometer needs to be well defined.
Having implemented efficient coupling to the filter lens, we evaluate the width ν_{FL} of the transmission peaks and the free spectral range (FSR) of the resonator. To this end, we scan the narrowband dye laser and record the transmitted laser power after the filter setup. In Fig. 3.7a) the scan over one resonance is depicted and fitted by a Lorentzian. The extracted FWHM yields $\nu_{\mathrm{FL}} = 354(1)\,\mathrm{MHz}$, which is about an order of magnitude larger than typical linewidths of single SnV^- centres. In Fig. 3.7b) we scan the laser over a large range in order to measure the distance between different transmission peaks. This yields a free spectral range of FSR = 93.8(5) GHz, i.e. at a typical ground state splitting of 820 GHz the cavity is only resonant with one of the transitions C and D, since 820 GHz modulo FSR equals to 69 GHz. The transmission resonance closest to the other transition lies at 820 GHz +FSR− 69 GHz = 845 GHz, corresponding to a detuning of about 30 % of the FSR. The Finesse extracted from the FSR and the FWHM of the transmission maximum yields $\mathcal{F} = 265$. We quantify the extinction at the second transition by scanning the laser over a frequency distance of up to 40 GHz relative to a transmission peak and record the transmitted power. The resulting transmission, which is corrected by the variation of laser power during the scan, is shown in Fig. 3.8a). The extinction exceeds four orders of

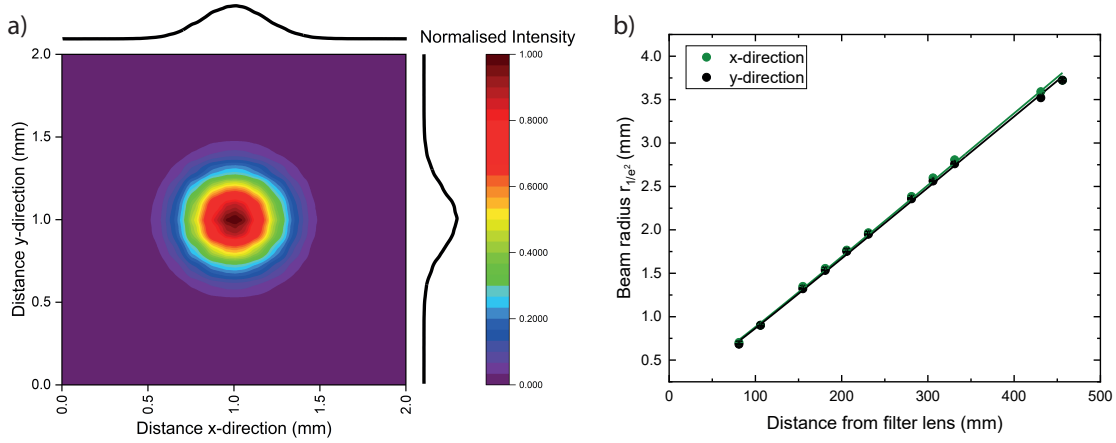

Figure 3.6: **Divergence of TEM_{00} mode: a)** Exemplary measurement of the diverging TEM_{00} mode of the filter lens at a distance of 81 cm. The black curves on the side are the cuts through the x- respectively y- direction of the profile. A Gaussian fit yields the beam diameter. **b)** Evolution of the beam diameter r_{1/e^2} for x- and y- direction of the Gaussian mode with increasing distance between the filter lens and the beam profiler. The data is fitted using equation 3.1, yielding a beam radius of $r_{0,x} = 289(75)\,\mu m$ and $r_{0,y} = 268(64)\,\mu m$. Within the error bars, this shows the near perfect Gaussian profile of the TEM_{00} mode of the filter lens.

magnitude corresponding to the situation of the filter lens being resonant with either C- or D- transition and suppressing the other one by a factor of 12000.

In a last step, we characterise the temperature dependent tuning of the filter setup. The tuning results from the thermal expansion of the NBK-7, which induces a change in the resonator length. The temperature is stabilised using a Peltier element, which is controlled by an Arduino Uno. For each temperature, we scan across one designated filter lens resonance and determine its central frequency by a Lorentzian fit. The resulting temperature tuning is depicted in Fig. 3.8b) and we find a temperature coefficient of $\lambda_{FL} = 4.046(4)\,GHz/°C$. This coefficient can be used to calculate temperature changes necessary for tuning the filter lens into resonance with the optical transition of a SnV^- centre. Furthermore, we will employ it for calibration in the measurements of the spectral diffusion of single emitters, in which we scan the filter lens across the emitted photon spectrum via temperature tuning.

Fibre-based Mach-Zehnder interferometer The measurement of the HOM visibility of consecutively emitted photons from a SnV^- centre is based on an imbalanced Mach-Zehnder interferometer (MZI). The aim is to delay the early photon that enters the MZI by the time separation until the late photon arrives (see sec. 2.3) and to achieve perfect temporal overlap between the two photons at the output fibre-based beam splitter of the interferometer. This procedure is designed to guarantee the indistinguishability of the photons with respect to the arrival time at the FBS where TPI occurs.

The technical realisation of this MZI in a complete fibre-based fashion is sketched in Fig. 3.9. The polarisation of the incoming photons, after passing through the filter setup, is controlled by the application of specifically designed polarisation paddles that are fabricated by the precision mechanics workshop of our faculty. In the following, they are split up at the first 50:50 FBS (TW670R5A2, Thorlabs), from which on each photon has two possible pathways: The upper arm (labeled “long arm”) of the interferometer, con-

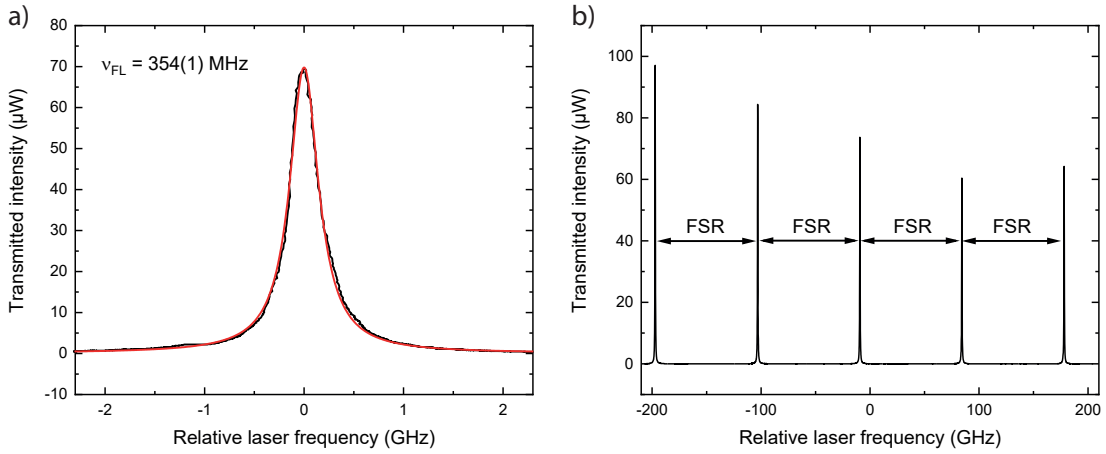

Figure 3.7: **FWHM and FSR of the filter lens: a)** Transmission spectrum of a single resonance of the filter lens. The linewidth of the almost perfect Lorentzian shaped peak amounts to 354(1) MHz, about an order of magnitude larger than the typical lifetime limited linewidth of single SnV^- centres. **b)** Multiple transmission peaks of the filter lens separated by the FSR of 93.8(5) GHz.

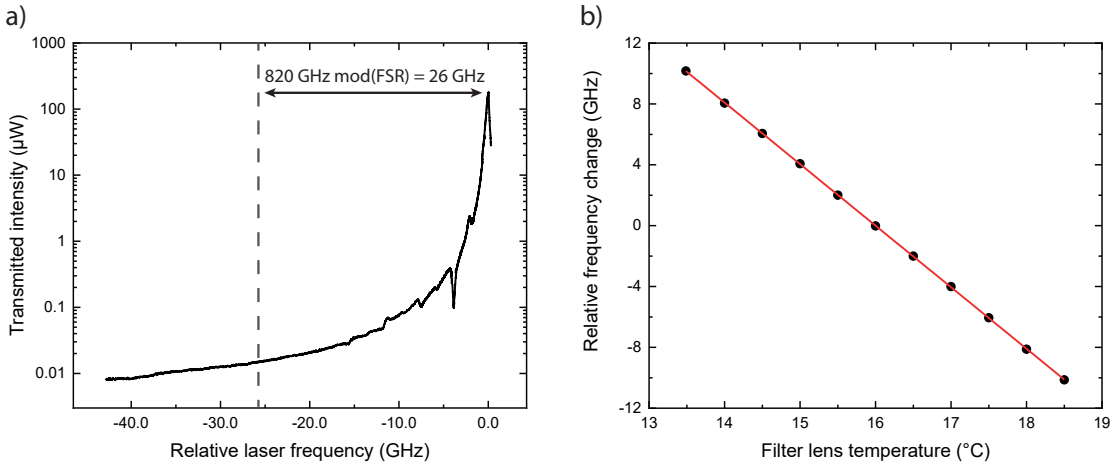

Figure 3.8: **Extinction measurement and temperature tuning of the filter lens: a)** Transmission spectrum of the filter lens next to a transmission peak. The grey line indicates the spectral position of the D (C) fine-structure line, when the filter lens is tuned into resonance with the C (D) transition for an unstrained emitter with about 820 GHz ground state splitting. The extinction of the second transition is larger than four orders of magnitude. **b)** Temperature tuning of the filter lens. The frequency of a transmission peak follows a linear temperature dependence and shifts with a temperature coefficient of $\lambda_{FL} = 4.046(4)$ GHz/°C.

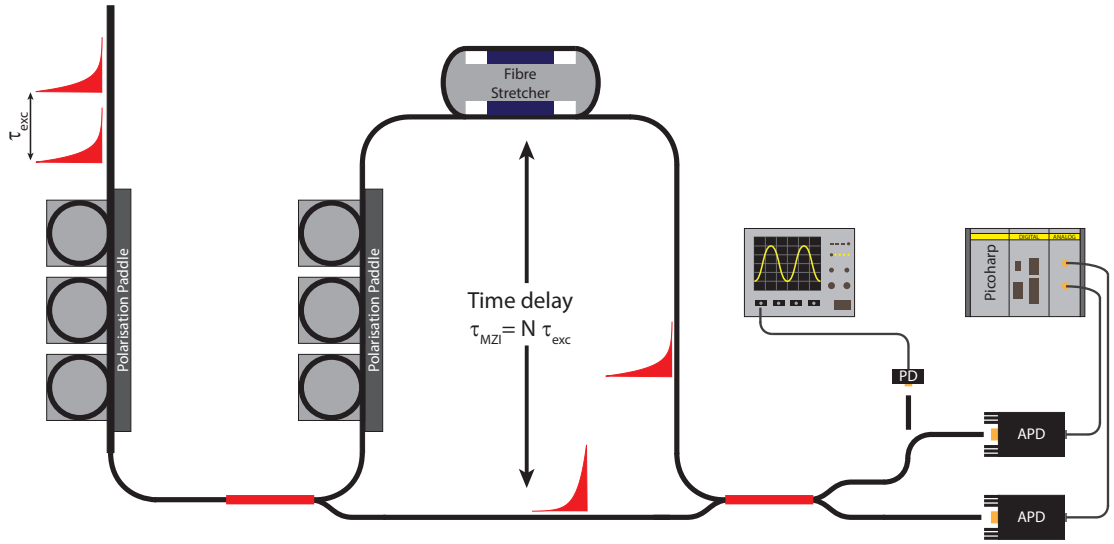

Figure 3.9: **Fibre-based Mach-Zehnder interferometer:** Fibre-based, imbalanced MZI for overlapping consecutive photon wave packages in time. The first polarisation paddle sets the overall input polarisation for the MZI. The photons are then split up at a 50:50 FBS and undergo a second polarisation control in the longer arm for setting the relative polarisation between photons travelling through both interferometer arms. The fibre stretcher in the long arm can introduce a length shift resulting in a different phase between the two arms. This is necessary for measuring the classical visibility of the interferometer with laser light. The photons are overlapped at a second FBS. Either the HOM interference can be measured using APDs or the classical visibility can be monitored on a PD.

sisting of a fibre with an increased length or the lower arm ("short arm"). The length difference is matched by careful fibre splicing to compensate an integer multiple N of the time separation τ_{exc}, imposed by the excitation laser, between consecutively emitted single photons. In the longer arm, an additional polarisation control is implemented, which can be used to set the polarisation state of the early photon parallel or orthogonal to the late photon's polarisation. Furthermore, a fibre stretcher (915B, Evanescent Optics) with 38 wraps ($\approx$8.4 m) is part of the longer arm. This device is not necessary for the HOM measurements, but is only used for inducing a phase difference between the two arms and thereby enabling measurement of the classical visibility of the MZI using laser light. The phase difference results from piezo plates (blue bars in Fig. 3.9) pushing on the fibre wraps and thereby effectively changing the fibre length by up to 19 µm. After the fibre stretcher, the photons passing through both arms are overlapped at the second 50:50 FBS at which the two-photon interference occurs. The FBS guarantees an almost perfect spatial mode overlap. The output can be either detected on a standard photodiode in order to measure the classical visibility or by APD's for every two-photon interference measurement.

We characterise the MZI employing the classical visibility as a measure for the achieved polarisation and spatial mode matching and furthermore the intensity balance of the photons passing through the longer/shorter arm. We use coherent light retrieved from the actively stabilised Dye laser for the interference, as its coherence length is about 3 km and thus significantly larger than the several meter long fibre delay. The fibre stretcher is driven with a sine wave voltage, thereby introducing a periodic phase variation between the two arms. The interference is then monitored on a PD in one of the output arms of the second FBS.

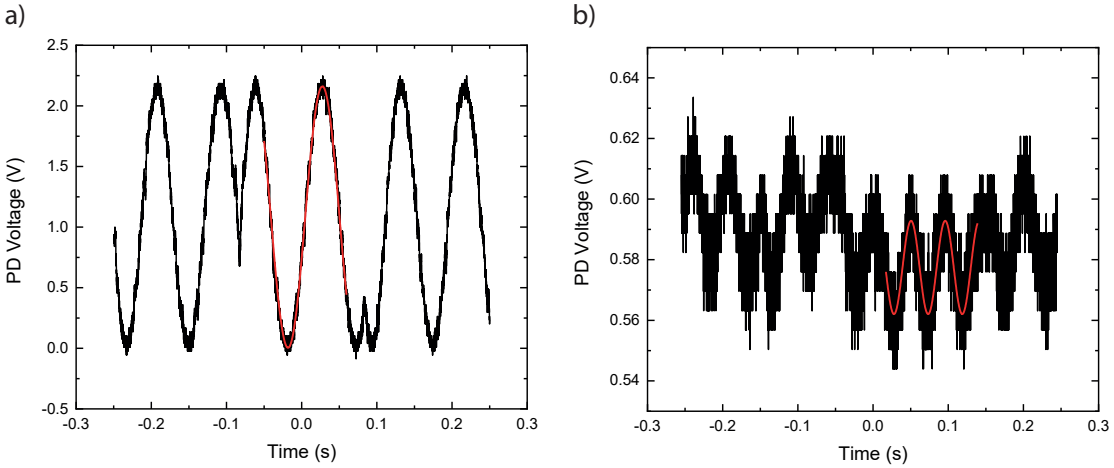

Figure 3.10: **Classical visibility of the fibre-based MZI: a)** Classical visibility for the case of the polarisation state in the two arms of the MZI being set parallel to each other. The achieved visibility of V = 99.6(3) % proofs accurate polarisation overlap, spatial mode matching and photon intensity balance for the incoming arms of the second FBS. **b)** Measurement for the polarisation state being set orthogonal for longer and shorter arm of the MZI. The visibility is strongly reduced to V = 2.7(4) %, indicating almost perfect orthogonal polarisation of the two interfering light fields.

A characteristic signal for the polarisation state of the two arms being aligned in parallel is displayed in Fig. 3.10a), where a visibility of V = 99.6(3) % is achieved. The visibility approaching unity is a clear sign of very accurate polarisation overlap, spatial mode matching and photon intensity balance in the input arms of the FBS. For verifying HOM interference, it is interesting to also measure the TPI for the case of orthogonal polarisation states of the incoming photons. In this case, no HOM interference can be observed. The classical visibility for this case is displayed in Fig. 3.10b), where the orthogonal polarisation of the two interfering light fields leads to a reduced visibility of V = 2.7(4) %. The low visibility of the remaining oscillations indicates almost perfect orthogonal polarisation states in the two arms of the MZI. These results render the fibre-based MZI perfectly suitable for the observation of HOM interference of single photons from SnV^- centres. We would like to emphasise that the setup being fibre-based strongly reduces the complexity in terms of alignment drifts, modularity and compactness in comparison to free-space interferometers. Changing the delay length requires only to add a different fibre in one of the arms and realigning the polarisation state, which enables quick and easy modifications on the MZI.

3.2.4 Detection

The photons emitted by SnV^- centres are subject to a variety of different analyses through the course of this thesis. However, the last part of the implemented setups is a simple detection of photons on a detector. In this section we characterise the employed single photon detectors and introduce the Hanbury-Brown-Twiss setup for measuring photon autocorrelation as well as the grating spectrometer.
The detection process of a single photon is rather challenging given the low energy deposited onto the detector by a single photon and the lab environment providing a large photon rate background even under dim illumination. The devices of choice within our work are avalanche photodiodes (APDs, SPCM-AQRH-14, Excelitas Technologies) in which a single

photon is absorbed by a semiconductor chip and creates a free electron in the conduction band via the inner photoelectric effect. This electron is accellerated by an applied voltage into the multiplication zone of the chip. There the electron is multiplied by a large factor, creating a charge avalanche. This electrical pulse can now easily be detected and yields a detection efficiency of single photons of about 65 % at 620 nm. The amplification between the impact of the photon and the detection of the electrical pulse leads to an uncertainty in time, the so called jitter. We measure the jitter of the utilised APDs by sending a weak laser pulse of about 60 ps duration, retrieved from the supercontinuum source at 532(1) nm, onto the detector and measure its response. This is depicted in Fig. 3.11 and yields a Gaussian timing jitter with a FWHM of 589(3) ps for APD1 and 486(2) ps for APD2. While it is possible to fit the jitter response more accurately by a convolution of a Gaussian peak and a mono exponential decay, in the models evaluating HOM and autocorrelation measurements the jitter is implemented as a Gaussian response function in order to reduce the computational overhead. Another measure of interest of the single photon detectors are the dark counts, when not being subject to any photon retrieved from the experiment, as these result in a uniformly distributed background contribution in any coincidence measurement. For the given set of APDs, the dark counts are $d_1 = 114\,\mathrm{cts/s}$ for APD1 and $d_2 = 156\,\mathrm{cts/s}$ for APD2.
These detectors can be used to measure the autocorrelation function of a stream of photons emitted by a SnV^- centre. To this end, we split the photons up at a 50:50 BS and detect the photon arrival in each output with an APD. The resulting electrical pulses are sent to a time-correlating-single-photon-counting system (TCSPC, PicoHarp300, PicoQuant), which assigns a time stamp to each detection event from an APD. These time stamps can be processed and correlated, yielding the autocorrelation function of the stream of photons. In the case of single photons being emitted from an isolated SnV^- centre, this leads to the characteristic vanishing signal of the autocorrelation at zero time delay between detection events of the two APDs, commonly known as antibunching, as a single photon will only be detectable in either one of the output arms of the BS. The schematic design of the HBT setup used within this thesis is displayed in Fig. 3.12. We apply a free space setup as well as a fibre based version of the HBT throughout the course of this thesis, but as there is no significant difference only the free space setup is sketched.
When being not only interested in the fact whether a photon is there or not but rather about its wavelength, we apply a grating spectrometer (iHR550, Horiba). Within this spectrometer, the photons are send on one of three possible gratings ($600\frac{\mathrm{Lines}}{\mathrm{mm}}$, $1200\frac{\mathrm{Lines}}{\mathrm{mm}}$ or $1800\frac{\mathrm{Lines}}{\mathrm{mm}}$) depending on the required resolution. The grating translates different frequencies into a spatial separation, which is detected on a CCD camera chip. This enables us for example to measure the spectral separation between the fine-structure lines resulting from the C- and D-transition of the SnV^- centres as the width of the spectrometer response function for $1800\frac{\mathrm{Lines}}{\mathrm{mm}}$ approximated by a Gaussian is about 20 GHz.

3.2.5 Flow cryostat setup

Interactions between phonons present in the crystal lattice and the colour centre under investigation play an important role in terms of optical as well as spin coherence (see sec. 2.1.4). The presence of phonons can be strongly reduced upon cooling the diamond sample to liquid helium temperatures. The easiest way to achieve this is within a liquid helium flow cryostat (Janis Research ST-500LN). A helium nozzle connected to a liquid helium storage is inserted into the cryostat and an underpressure leads to a flow of liquid helium passing the cold-finger of the cryostat. The cold-finger made of copper is thereby cooled down to about 4 K and in turn cools the sample glued to its top by a drop of silver

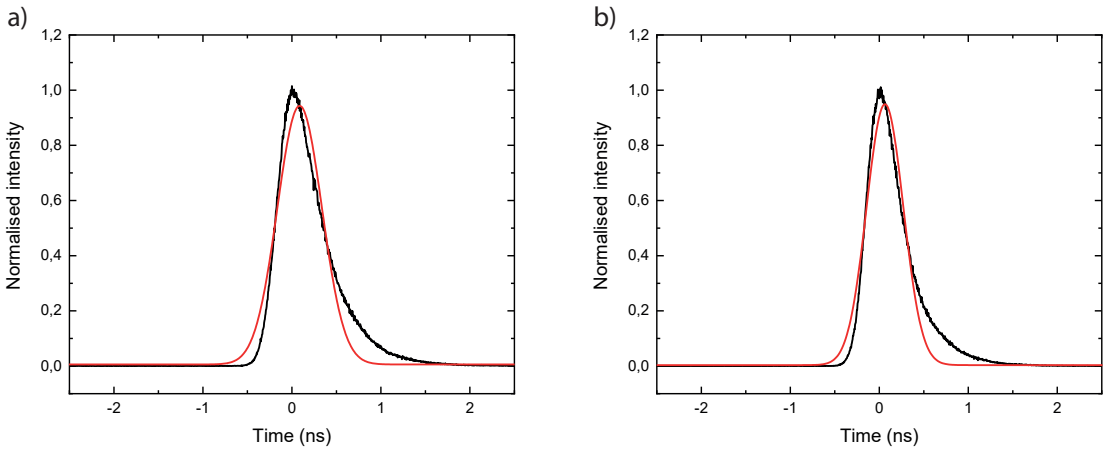

Figure 3.11: **Timing jitter of the applied APDs:** The response function of the used APDs to a detected weak laser pulse with a duration of about 60 ps at a wavelength of 532(1) nm is characterised. The jitter response (black solid line) is approximated by a Gaussian (red solid line) and yields a FWHM of **a)** 589(3) ps for APD1 and **b)** 486(2) ps for APD2.

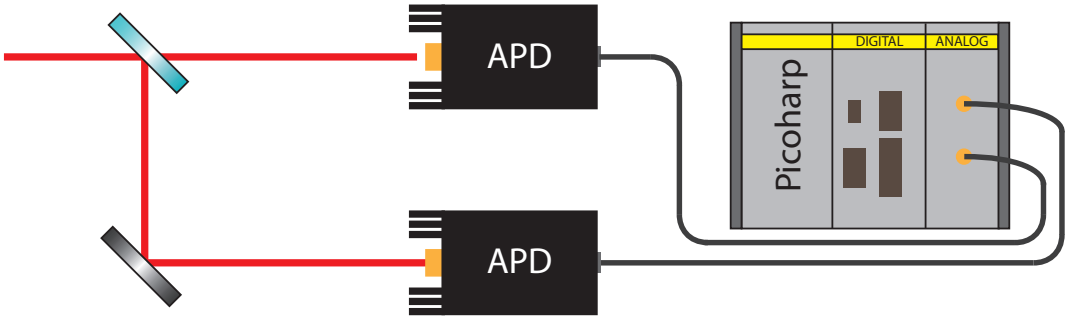

Figure 3.12: **HBT setup:** The setup is used for autocorrelation measurements on the stream of photons emitted by a single SnV^- centre. The photons are split up at a 50:50 BS and detected on APDs. If a photon is detected on one APD, the generated output pulse is send to correlation electronics, which assign a timestamp to the event. The arrival times of photons on the two APDs can furthermore be compared and yield the autocorrelation function.

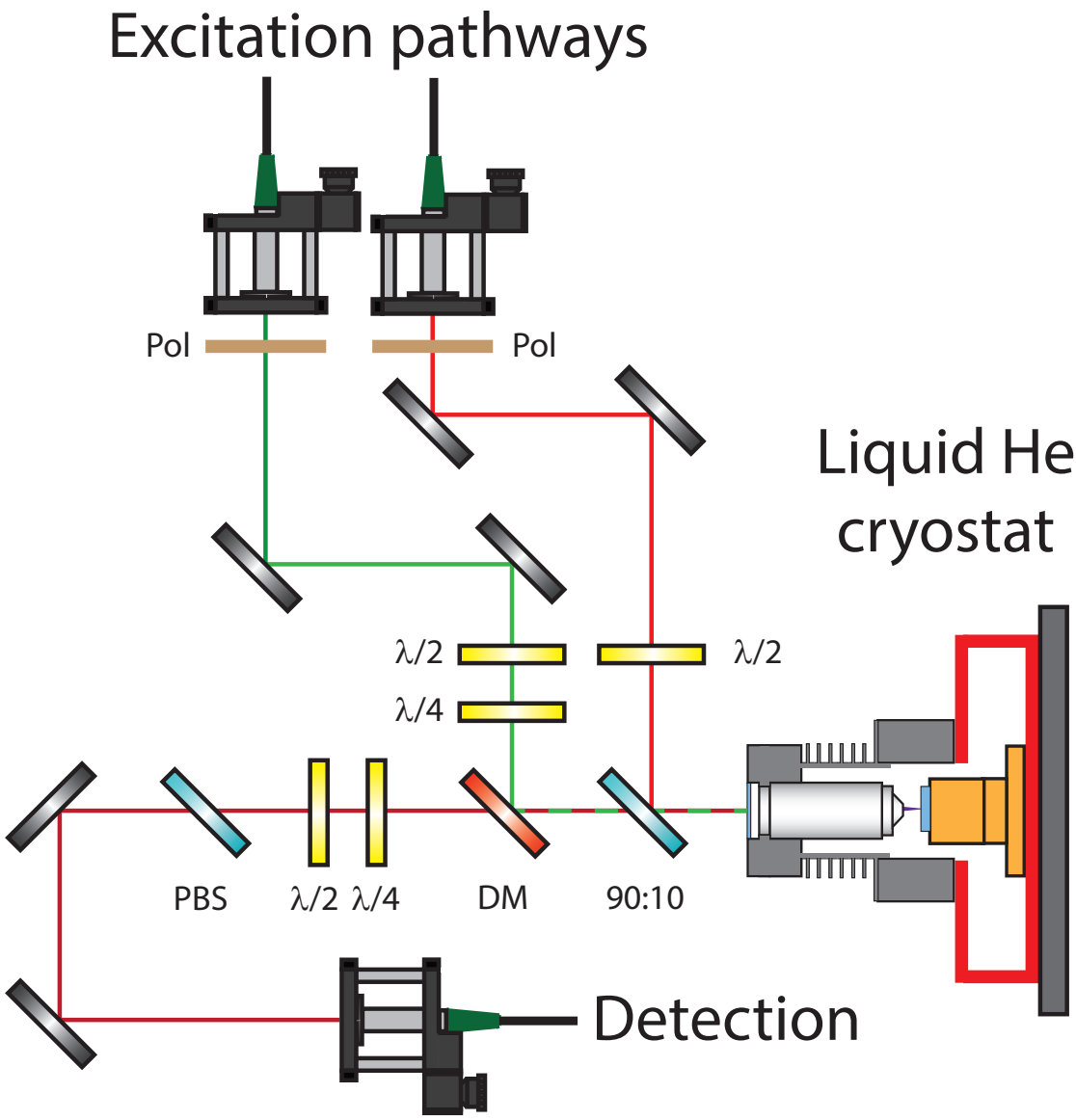

Figure 3.13: **Schematic flow cryostat setup:** The excitation light fields are passing through a polariser and subsequently the linear polarisation state can be rotated by a half-wave plate. For the quasi resonant excitation / charge stabilisation path (green), an additional quater-wave plate is inserted at a fixed rotation angle to compensate for the phase shift induced by the DM. The light fields are overlapped with the resonant excitation path (red) at a 90:10 BS and guided onto the sample. The fluorescence emitted by the SnV^- centres is transmitted through the DM and the induced phase shift is again compensated by a quater-wave plate. The subsequent half-wave plate and the polarising BS are used for polarisation analysis of the fluorescence. The light is coupled into a single mode optical fibre and transferred to the various detection systems.

conductive paste. Above the sample, an objective (MPLFLN100x, Olympus) is mounted on a motorised linear translation stage used for focussing the excitation light onto the sample and collection of the emitted photons. The objective and the sample are within an evacuated sample chamber, which guarantees that the objective itself stays at room temperature while the sample is at cryogenic temperatures.

The back plate of the cryostat, on which the cold-finger is attached, is mounted on two orthogonal linear positioning stages, which can be employed for scanning the sample. The relative positioning of the sample with respect to the objective while maintaining the vacuum is made possible by a flexible steel bellow. The advantage of the system is the very short cool-down and warm-up time of about half an hour each, yielding the flexibility to possibly investigate more than one sample a day. This flexibility is payed for by sample drifts induced by the flow of the liquid helium as well as the weight of the helium nozzle and increased vibrations due to the induced mechanical connection to the floor. Furthermore, since liquid helium grows ever more expensive its excessive use becomes increasingly uneconomic. Finally, the helium can storage capacity is finite and furthermore tends to build up unwanted pressure, thus the uninterrupted measurement time is limited to a user being present. In summary, it is a very flexible tool for preliminary characterisation of samples at liquid helium temperatures, but not designed for time excessive long term measurements on a specific single emitter of interest. Furthermore, the base temperature of 4 K is not suitable to reach long coherence times of SnV^- centres as it is derived in sec. 2.1.4.

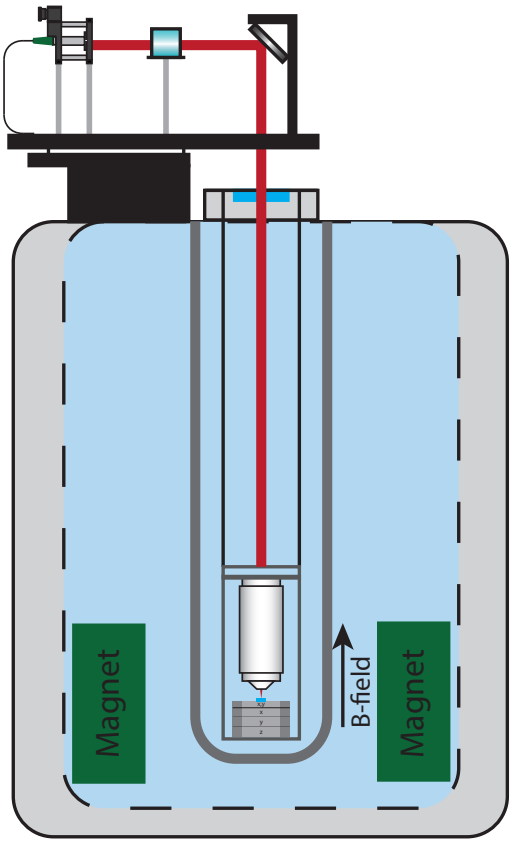

Figure 3.14: **Schematic of the attodry2100:** The confocal microscope is set up on a breadboard on top of the cryostat. It can be retracted for taking out the VTI. Optical access to the cryostat is achieved free space through a window. On the bottom of the VTI, the laser is focussed onto the sample, which itself is mounted on top of a three axis piezo stack for coarse and a two axes piezo scanner unit for fine positioning. A superconducting magnet provides a uniaxial magnetic field along the optical axis of the VTI with up to 9 T.

The colour centres within the sample chamber are addressed by a home-built confocal microscope. The basic properties of such a device are discussed at length in [170] and are directly applicable to our setup. The noteworthy differences that can be seen in the schematic picture of the setup in Fig. 3.13 are as follows: We employ a dichroic mirror (DM) that reflects light for wavelengths shorter than 550 nm and transmits it for wavelengths larger than this threshold. This DM is followed by a subsequent 90:10 BS and the combination of both allows us to overlapp resonant, quasi-resonant and charge

stabilising light fields (see sec. 3.2.1 for definition) in the excitation path and still being able to separate them from the colour centre fluorescence, e.g. by optical filters, in the detection path. Furthermore, a polarisation control is implemented in each excitation pathway by adding a nanofilm polariser (LPVIS050-MP2, Thorlabs) defining a linear axis of the light followed by a half-wave plate (HWP) that is employed for rotations of the polarisation state. In the quasi-resonant excitation path a quater-wave plate (QWP) is added before and in the detection path after the DM to compensate for the phase shift induced by the DM itself. The polarisation state of the colour centres can be investigated by adding a HWP and a polariser in the detection pathway. The fluorescence in the detection path is coupled into a single mode optical fibre and can be send to any of the previously mentioned detection setups.

3.2.6 Closed cycle cryostat

Overcoming the limits in terms of long-term stability and base temperature of the flow cryostat described above is crucial for the experiments performed within this thesis. Therefore, a second cryostat setup is implemented by employing a closed-cycle helium cryostat (attodry2100, attocube systems AG). In the following, we will briefly sketch the working principle of such a cryostat. A first cooling step is implemented by using a standard pulse-tube cooler (PT410-RM, Cryomech), which principle of action is very similar to the well-known Stirling motor. The cooling medium is the helium gas, which is periodically expanded and compressed by a compressor (CPA289C, Cryomech). By a moving piston, the compression and the expansion regions are spatially separated and thus a directed transfer of heat is implemented. With this precooling, sample temperatures of about 3 K are achievable. An additional helium cycle is utilised as a second cooling stage. This part of the cryostat is referred to as "condensing cycle", since a scroll pump pushes the helium into a reservoir, where it condenses into its liquid state. At the outlet of the reservoir is a needle valve through which the liquid helium flows and after passing, it expands rapidly. This expansion is accompanied by the transition to its gaseous state, in which heat from the environment is taken up and cooling of the sample is achieved. This process is called the Joule-Thomson effect and within our system the base temperature of the sample can be reduced by this additional cooling mechanism to about 1.7 K. While the whole cryostat, including a solenoid magnet capable of reaching uniaxial (along the optical axis) magnetic fields up to 9 T, typically remains at the precooled temperature of 3 K, the sample can be exchanged without warming up the whole cryostat. Instead it is mounted on a vertical temperature insert (VTI), which is inserted into a metal tube in the cryostat (see Fig. 3.14) that can be heated up separately. The heat exchange between the tube and the sample is performed using helium exchange gas. This setting enables sample warm-up and cool-down times of about half a day each, compared to about three days warming up and two days cooling down of the whole cryostat system.
Optical access to the sample is enabled in free space by a wedged window on top of the VTI. Above the sample, a high NA objective (0.82 for LT-APO/VISIR/0.82, attocube systems AG; 0.9 for MPLN100x, Olympus) is mounted, which focusses the light onto the sample. Coarse positioning of the sample relative to the objective is achieved by a three axis piezo positioner stack (ANPxyz51, attocube systems AG). For fine spatial resolution, two axis piezo scanners (ANSxy50, attocube systems AG) are employed. The confocal microscope is mounted on a breadboard on top of the cryostat, which can be retracted for taking out the sample. The confocal microscope setup itself is the same as for the flow cryostat setup, except the QWPs being not necessary due to using an optimised DM (DMLP567, Thorlabs) which does not introduce a significant phase shift. The full setup,

consisting of the excitation sources, the confocal microscope, the detection using the HBT interferometer or grating spectrometer and the HOM filter setup in combination with the imbalanced MZI is depicted in Fig. 3.15. If a fibre splits into two paths without a FBS it means that a connection can be achieved to either one of the paths.

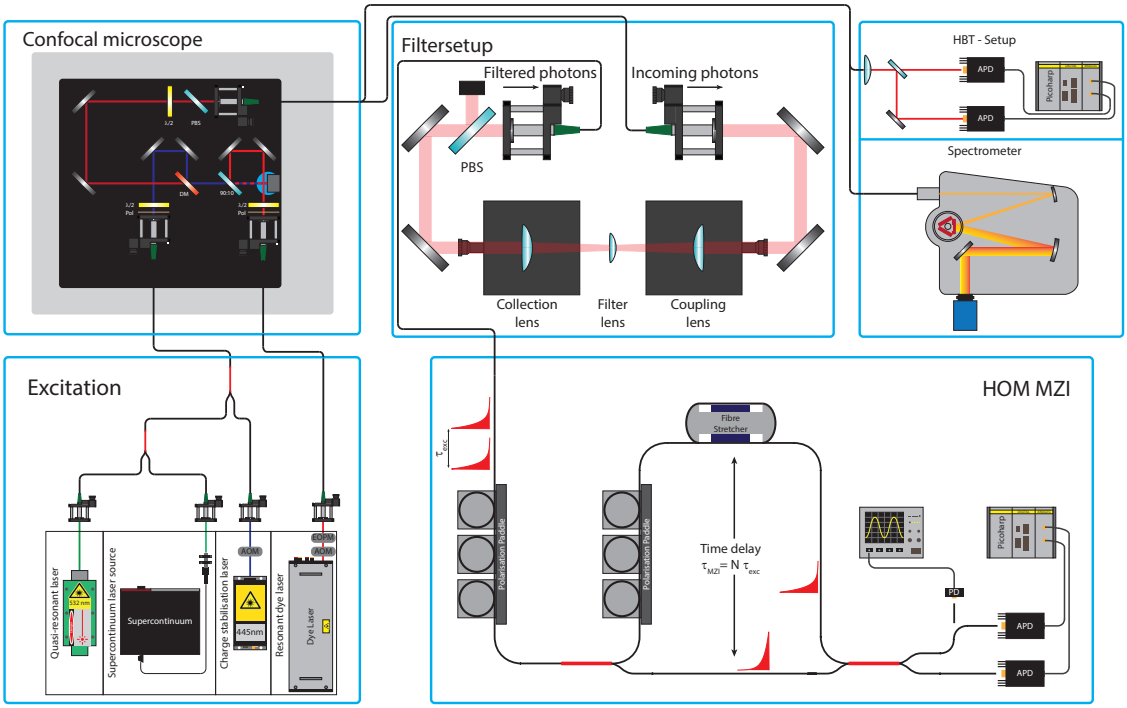

Figure 3.15: **Schematic of the full attodry2100 setup:** The excitation laser sources are modulated by AOMs or EOPMs and then guided to their respective excitation path in the confocal microscope. After setting the polarisation state the light fields are combined on a 90:10 BS and enter the cryostat vertically (out of the picture plane). The fluorescence leaves the cryostat on the same way and is separated from the laser light on a DM and subsequent optical filters. Investigation of the polarisation state of the emitted photons can be done by adding a HWP and a polarising BS in the detection path. Subsequently, the photons are coupled into an optical fibre and can be directed to the desired detection setup, e.g. the detection in the HBT setup or the grating spectrometer. For the HOM measurements, the photons pass through the filter setup and enter the imbalanced MZI. The HOM interference pattern is finally detected on APDs and recorded by the time correlating electronics.

Chapter 4

Spectroscopic investigations of the SnV

Contributions and copyright notice

The experiments conducted in this chapter were carried out under the supervision of Christoph Becher (C.B.). The investigated HPHT sample NI58 was fabricated by ion implantation by Takayuki Iwasaki (T.I.) under supervision of Mutsuko Hatano (M.H.) in the Tokyo institute of technology in Japan. The subsequent HPHT annealing was implemented by Takashi Taniguchi (T.T.) in the national institute for material science in Namiki, Japan. The sample SC500_01 was implanted with tin ions by Michael Kieschnick (M.K.) and Philipp Fuchs (P.F.) under supervision of Jan Meijer (J.M.) at the facilities of the Felix Bloch institute for solid state physics in Leipzig. The annealing and cleaning of the sample was conducted by P.F.. The optical setup was designed and set up by Johannes Görlitz (J.G.) and Dennis Herrmann (D.He.). J.G. and D.He. carried out the measurements and the analysis of the data with input from P.F. and Morgane Gandil. Helpful information was obtained from Elke Neu (E.N.) and Richard Nelz (R.N.). Gergő Thiering (G.T.) and Adam Gali (A.G.) provided theoretical information about the phonon coupling of G4V vacancy centres and the extended electronic structure of the SnV^- centre.

This chapter outlines the results of detailed spectroscopic investigations of the SnV^- centre in diamond. These studies encompass the pure and bright single photon emission and its polarisation properties as well as the dependence of emission spectra on the temperature. We investigate the fabricational requirements of SnV^- centres by comparing the spectra of HPHT and LPLT annealed samples at cryogenic temperatures and find the HPHT annealing to provide a significant advantage in terms of inhomogeneous broadening of the optical transitions. The investigations are completed by an in-depth analysis of the PSB and the Debye-Waller factor revealing a large fraction of coherent photons being emitted into the ZPL. Throughout the whole chapter sample NI58 is investigated if not stated differently.

4.1 Single photon emission and fluorescence lifetime

4.1.1 Photon correlation and saturation measurements

The aim of this chapter is to reveal the foundational spectroscopic properties of the SnV^- centre and thus the majority of experiments is carried out on single emitters. This is crucial in order to eliminate effects caused by different strain or charge interactions in ensembles of SnV^- centres, which can impact their characteristics. Due to the limited resolution of our confocal microscope, it is impossible to directly resolve single atoms. Therefore, we first identify a SnV^- centre by its spectral fingerprint (see sec. 3.1.1) and subsequently employ intensity autocorrelation measurements of the emitted photons in a HBT setup (see sec. 3.2.4). The outcome for a representative emitter is shown in Fig. 4.1a), where we extract $g^{(2)}(0) = 0.05$ at vanishing time delay from a fit according to the derived formula in reference [198]. The remaining disparity from zero of the autocorrelation at simultaneous arrival times of the photons at the single photon detectors can be fully explained by the significant impact of the dark counts of the APDs specified in sec. 3.2.4. We conclude that the investigated SnV^- centre is a pure single photon emitter and therefore the emission must result from a single centre. All emitters investigated in this chapter, if not stated elsewise, exhibit close to perfect single photon character, which means that we can explain the autocorrelation measurement by the measured background, the jitter and the dark counts of the APDs.
In order to fortify the advantage achieved by exploiting quantum mechanics in QIP protocols over the classical equivalents in communication, computation or simulation, the achievable protocol repetition rate is crucial. Its value depends directly on the brightness of a quantum emitter, which can be limited by the radiative lifetime, non radiative decays and charge instabilities (the quantum efficiency). Furthermore, a poor collection efficiency of photons and setup losses set another limitation. For the set of investigated single SnV^- centres, we measure photon countrates in saturation including the full emission spectrum (LP600 filter) ranging from 80-150 $\frac{\text{kcts}}{\text{s}}$ corresponding to $B_{\text{QIP}} = 10^{-4} - 10^{-3}$, while the saturation intensities range from 200-600 µW under off-resonant excitation with 532 nm excitation (see Fig. 4.1b)). The saturation curve is fitted by the equation

$$\text{CR(P)} = \frac{\text{CR}^{\infty} \cdot I}{I + I_{\text{sat}}} + d, \tag{4.1}$$

where CR^{∞} denotes the saturation count rate, I (I_{sat}) the excitation laser (saturation) intensity and d the dark counts of the APD. The extracted values include all before mentioned limiting factors and are in agreement with what is found in comparable studies [113, 132]. In comparison to studies on other G4V centres in unstructured electronic grade bulk diamond using similar collection optics, the count rates are between one and two orders of magnitudes larger than for SiV^- centres, while they are of the same order of magnitude as observed for GeV^- centres, see sec. 2.1.7.
Furthermore, we contrast these values with the largest values of NV^- centre in bulk diamond [241], as it is up to now predominantly used in fundamental QIP protocols with colour centres in diamond. For a fair comparison it is necessary to take into account the difference of the Debye-Waller factors of 4 % for the NV^- centre and 60 % for the SnV^- centre (see sec. 4.3 below) and the collection efficiencies present in the studies. We find that the photon count rate of photons emitted into the ZPL is about one order of magnitude larger than for the NV^- centre. Since QIP requires coherent photons emitted, which result solely from decays of ZPL transitions, we find the SnV^- centre potentially enabling higher repetition rates than lately used colour centres in diamond.

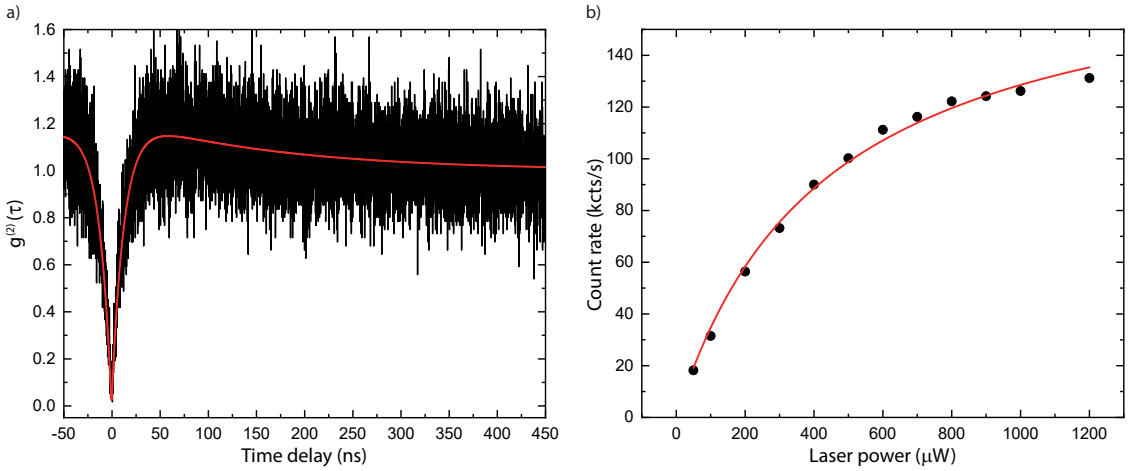

Figure 4.1: **Autocorrelation and saturation measurement: a)** Autocorrelation measurement of photons emitted by a single SnV^- centre exhibiting a $g^{(2)}(0) = 0.05$. The displayed data is raw data without any post processing and the residual deviation of $g^{(2)}(0)$ from zero is fully explained by the dark counts of the APDs. **b)** Exemplary saturation measurement when recording the count rates of the full spectrum of a single SnV^- centre. Saturation count rates between 80-150 $\frac{\text{kcts}}{\text{s}}$ are reached for saturation intensities in the range of 200-600 µW. Typically, no linear background contribution is discernible in the HPHT samples. The wavelength of the excitation laser source for both depicted measurements is 532 nm.

4.1.2 Radiative lifetime of single emitters

It is possible to infer the radiative lifetime of the excited state of single SnV^- centres by power dependent autocorrelation measurements. However, the results need to be extrapolated to zero excitation power which leads to a significant error bar. Therefore, it is more precise and with less experimental effort to measure the excited state lifetime employing TCSPC. To this end, we employ short laser pulses at a wavelength of 532(10) nm retrieved from the supercontinuum laser source and record the fluorescence response of the single SnV^- centre. A representative result from such an experiment is depicted in Fig. 4.2a), yielding a lifetime of the excited state of $\tau_r = 25.4(1)$ ns. Surprisingly, we find a variety of lifetimes with the majority between 5 - 10 ns but some even exceeding 25 ns. The histogram of fourteen emitters under investigations in sample NI58 is displayed in Fig. 4.2b). The maximum of this distribution is in agreement with the findings in other reports [100,113,132,176,242], however, none have observed the broad lifetime distribution between 10 and 30 ns. In sample BOJO_001 the distribution of lifetimes seems also to be much narrower, centered around 6 ns. We therefore attribute the spread to the fact that the removal of diamond due to the HPHT annealing in sample NI58 results in single emitters being situated directly at the surface. This vicinity to the surface and thus an altered photon density of states might be the cause of the diverse lifetimes measured.

4.1.3 Radiative lifetime of ensembles of SnV^- centres

Due to the non-conclusive results of the fluorescence lifetime of single emitters, we additionaly evaluate the excited state lifetime for ensembles of different densities, again by employing TCSPC. According to sec. 3.1, the inhomogeneous removal of diamond during the sample preparation leads to a direct correlation between the density and the depth of

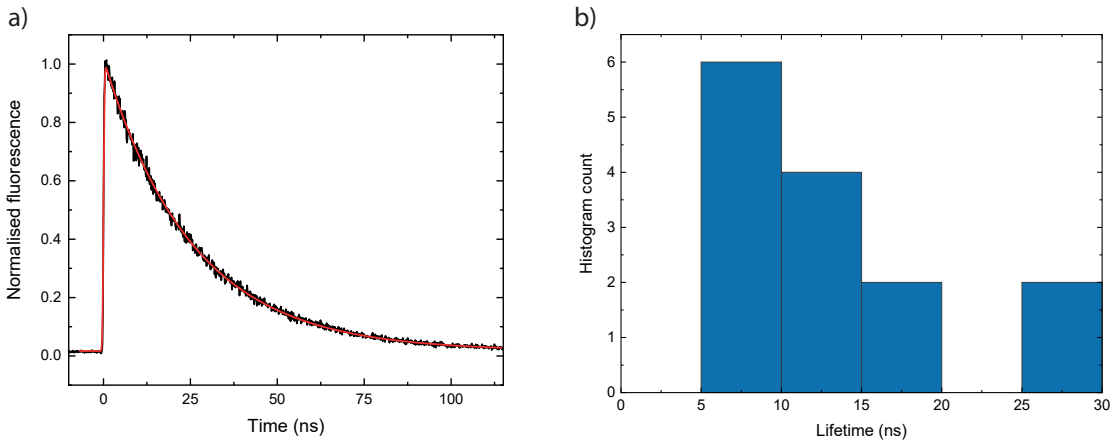

Figure 4.2: **Lifetime statistics on single emitters: a)** Exemplary TCSPC measurement of a single SnV^- centre with a long-lived excited state. The radiative decay constant amounts to $\tau_r = 25.4(1)$ ns. This lifetime is on the long-lived side of the histogram of lifetimes depicted in **b)** obtained from fourteen single emitters under investigation. The majority of the excited state lifetimes is in the range between 5 - 10 ns. The inhomogeneity of this distribution is most likely a result of the close vicinity of the single SnV^- centres to the diamond surface.

an ensemble with respect to the diamond surface. The definition and measurement of the ensemble depth, which will be used throughout the rest of this secion, results from the following considerations:

- Implantation of ions yields a Gaussian depth distribution, which we obtain by Monte-Carlo simulations (SRIM).
- The ensemble depth for a given part of the sample is defined as the distance from the surface at which the implantation probability has dropped to approximately one percent of the distribution maximum, lying 168 nm deep within the diamond if no diamond is removed. An illustration of this definition is depicted in Fig. 4.3a) and b) for the values of 200 nm respectively 140 nm ensemble depth.
- The ensemble depth in the experiment is evaluated by recording the count rate of a given ensemble for a fixed excitation intensity, which is way below the saturation intensity to ensure working in a regime where the count rate depends linearly on the excitation power. This count rate can then be compared to the count rate obtained in the high density region of the sample, where almost no diamond was removed during sample preparation.

The choice of low excitation intensities is furthermore important in order to ensure that the differing lifetimes of the ensembles are not significantly influencing the count rates. The correlation between the lifetime and the ensemble depth is shown in Fig. 4.3c). In the regions of the sample where 0 - 100 nm diamond were removed (ensemble depth 100 - 200 nm), the ensemble excited state lifetime is around 5 ns, which is in agreement with theoretical predictions and experimental findings in previous studies [100,113,132,176,242]. For an ensemble depth of 100 - 40 nm the lifetime increases and reaches a maximum of 7.5 ns. We attribute this increase in lifetime to a reduction of the photonic local density of states as a result of the proximity of the ensemble to the surface. A similar effect is already

reported for NV^- centres [243]. When further approaching the diamond surface (ensemble depth of 40 -0 nm), the lifetime decreases rapidly which is most likely the result of non radiative decay processes caused by defects on the diamond surface. Again, comparable effects are observed for NV^- centres in nanodiamonds upon reduction of the size of their host material [244].

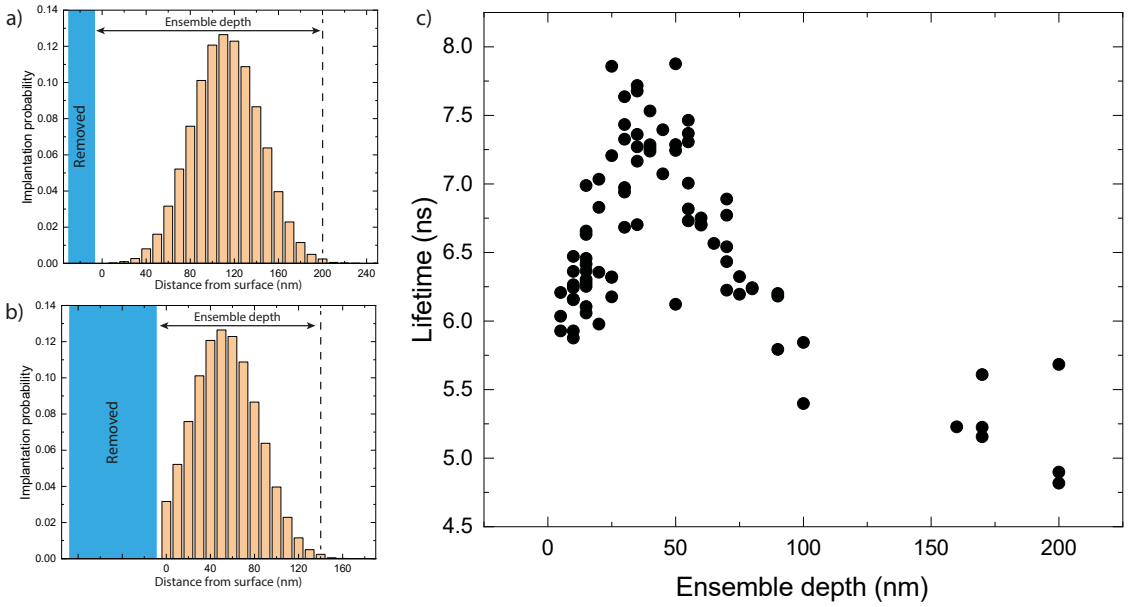

Figure 4.3: **Lifetime dependence on ensemble depth:** We define the depth of a certain ensemble within our diamond sample as the distance from the surface (blue shaded area) to the depth in which the original Gaussian implantation depth distribution (simulated by using SRIM Monte-Carlo simulations) has dropped to about one percent of it's maximum height. In the main text, a detailed description on the determination of this depth in the experiment is given. In **a)** 200 nm and **b)** 140 nm of ensemble depth and the corresponding depth distributions are sketched. **c)** The variation of the ensemble lifetime in dependence of the ensemble depth is shown. Reduction of the photonic local density of states, when approaching the surface, causes the increase in lifetime visible from 100-40 nm ensemble depth. The steep decrease in lifetime for ensembles very close to the surface is likely caused by non-radiative decay channels in the vicinity of surface defects as it is also reported in [244]. The lifetime measurements are conducted using pulsed 532(10) nm excitation provided by the supercontinuum laser source.

4.2 Zero phonon line emission

4.2.1 Temperature dependence of optical transitions

The existence and occupation of vibrational modes within the diamond lattice is strongly dependent on the temperature. Therefore, it is possible to characterise the electron-phonon interaction of the SnV^- centre by the means of temperature dependent spectroscopy.
For a single defect, the evolution of the ZPL emission upon excitation with the quasi-resonant laser source emitting at 532 nm is shown within a temperature range in between 10 -250 K in Fig. 4.4. At elevated temperatures only a single broad feature can be observed, which splits into four transitions at temperatures around 100 K, representing the typical fingerprint of the D_{3d} symmetric G4V vacancy centers [100]. These transitions A,B (C,D)

correspond to the decay from the upper (lower)orbital excited state into the two orbital ground states. Upon further reduction of the temperature, the transitions A and B vanish due to a fast, non radiative relaxation process from the upper excited state into the lower excited state, resulting from the reduced phonon occupation of the energy mode corresponding to the excited state splitting. This effect is also observed in [113]. The excited state splitting in the investigated sample NI58 amounts to an averaged 3030(100) GHz over several emitters, while the ground state splitting ranges from 820 -840 GHz. These measurements imply that a ground state splitting of 820 GHz corresponds to the unstrained case, which is further narrowed down by measurements in the HPHT sample BOJO_001, where all emitters under investigation exhibit a ground state splitting of 818(5) GHz. Due to the sixfold longer annealing time of the latter sample, it is most likely that this value is more accurate.

The evaluation of the temperature dependent photoluminescence spectra yields an increasing linewidth, which follows a $A + BT^3$ power law (Fig. 4.5a)). The cubic dependence was theoretically proposed and experimentally confirmed for SiV^- centres and interpreted as an indication of a low strain host material [120, 245]. Its origin is suspected to lie in a single phonon absorption and the thereby induced Raman scattering between sublevels of orbital ground and excited states. In contrast, the lineshift of the C-transition is following a $A + BT^2 + CT^4$ correlation, with a vanishing quadratic contribution in the measurement of the single emitter. A cubic power law, which was derived as a consequence of linear e-symmetric phonon coupling for the SiV^- centre [120], is reproducing the data less adequately. Theoretically, Hizhnyakov et al. [246–248] predict a T^4 dependence in the case of dominant quadratic electron-phonon coupling of a_{1g} phonons, which was also confirmed for SiV^- centres [245].

Further confirmation of the results is given by the temperature evolution of the photoluminescence emission of ensembles of SnV^- centres in Fig. 4.6. The measurements are conducted in a low density region of the sample in order to provide high spectral resolution. We cannot distinguish a significant contribution of the ensemble linewidth to the spectrometer response function, which is about 16 GHz broad, while at the same time being unable to saturate the ensemble with 532 nm laser intensities up to 10 mW.

The ensemble linewidth broadens according to the same cubic power law as in the single emitter case, which confirms the possibility of fabricating dense ensembles of SnV^- centres, while preserving narrow inhomogeneous broadening. The line position of C- and D-transition are both precisely reproduced by the $A + BT^2 + CT^4$ power law. The non-vanishing T^2 contribution is most likely associated with inhomogeneous broadening and was also observed for ensembles of SiV^- centres [245].

The accurate relation between linewidth respectively line position and temperature renders the SnV^- centre a potential candidate for thermometry on nanoscale. The necessary measurements are easily calibrated, integration time for ensemble measurements can be fast (on the order of milliseconds) and cover a temperature range from 0-75 K with high resolution. Above that temperature, the merging of peaks requires slightly advanced calibration, but for the C-transition data can be acquired up to room temperature, which was also demonstrated by Alkahtani et al. in the temperature range 120-295 K [249].

4.2.2 Comparison of photoluminescence spectra for different annealing temperatures

The first published experimental study conducted on SnV^- centres in diamond investigates the effect of annealing temperature on the room temperature linewidth of ensembles [113].

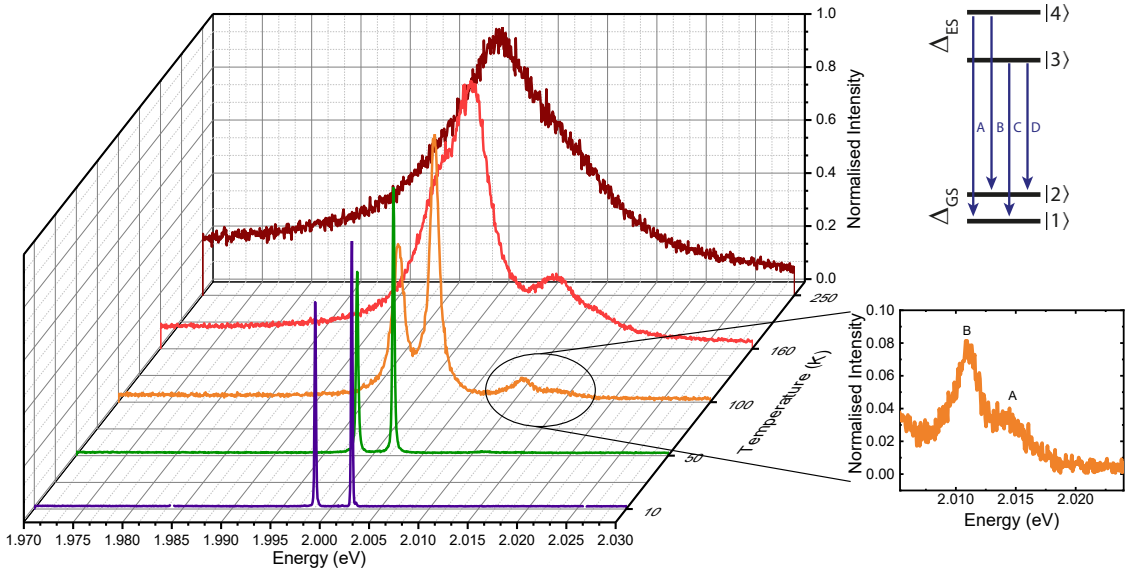

Figure 4.4: **Temperature dependent spectra:** Temperature variation of the spectrum of a single SnV^- centre in the range between 10-250 K. For decreasing temperatures, the ZPL splits up into the characteristic four line fine-structure that is inherent to G4V centres. Upon further temperature reduction below 75 K, the transition lines A and B, which result from the decay of the upper excited state, vanish due to the reduction of the thermal population in this state. It is furthermore observed, that line shifts and line narrowing are induced by approaching 10 K. The excitation source in this experiment is the 532 nm quasi-resonant laser.

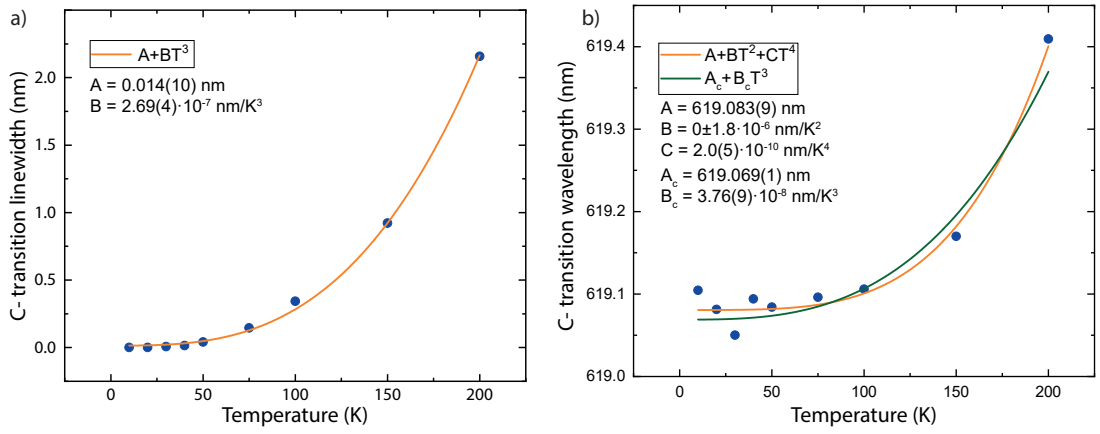

Figure 4.5: **Temperature dependence of line shift and line broadening of a single emitter: a)** Evolution of the C-transition linewidth with temperature for a single SnV^- centre. The data is well described by a cubic power law (solid line). **b)** Temperature dependence of the resonance wavelength of the C-transition, which is more accurately fitted by a power law with T^2 and T^4 contributions than a simple cubic formula. The measurement is conducted using the quasi-resonant laser at 532 nm for optical excitation.

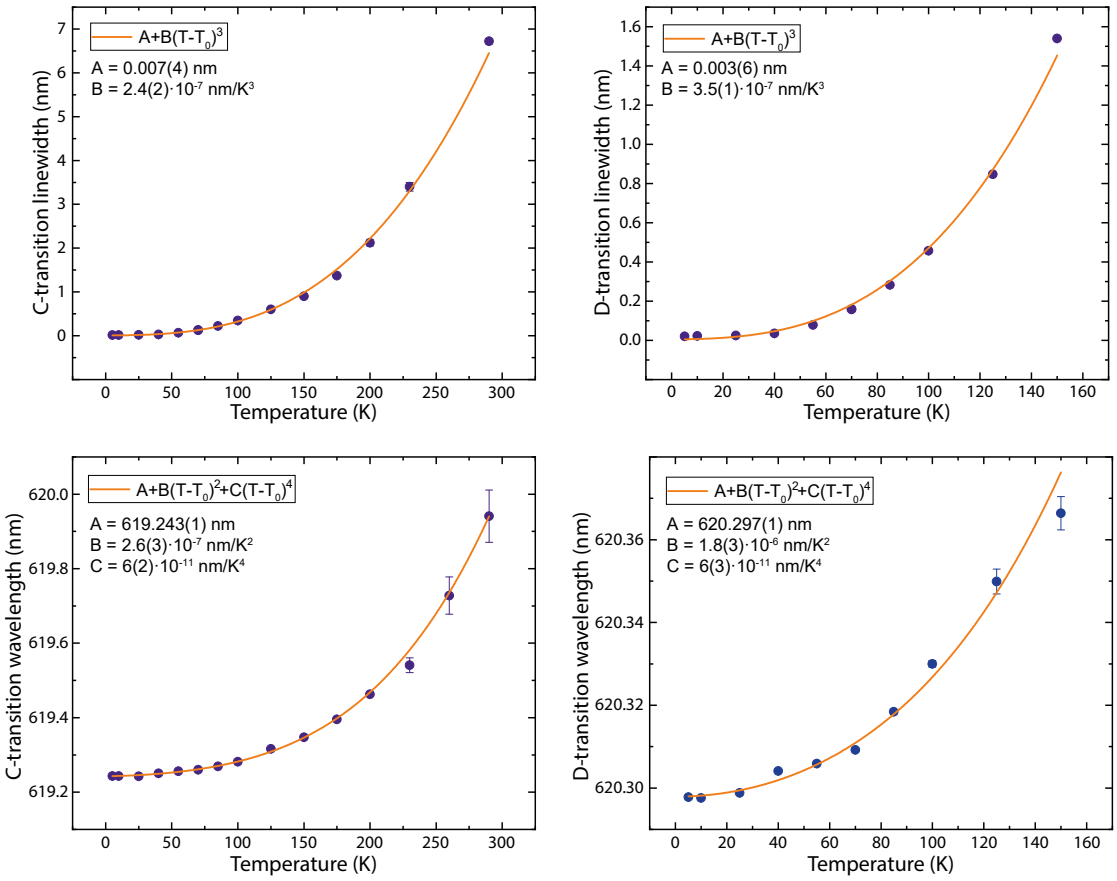

Figure 4.6: **Temperature dependence of line shift and line broadening of an ensemble of SnV^- centres:** Depicted are the evolution of the linewidth and the resonance frequency of C- and D-transition of a spectrally narrow ensemble of SnV^- centres. The solid lines are fits to the data according to a power law with cubic temperature dependence for the linewidths and with T^2 and T^4 contributions for the line shifts. The measurements are carried out utilising a light field at 532 nm for excitation.

They report a steady decrease and attribute it to the reduction of damage induced by the ion implantation of the heavy tion ions.
We expand this study and compare the inhomogeneous distribution of ZPLs at cryogenic temperatures for the HPHT annealed sample NI58 and the LPLT annealed sample SC500_01. The result of the HPHT annealing on sample NI58 is obvious when contrasting the clear two line fine-structure at 10 K with the broad forest of lines that is found in sample SC500_01 for an ensemble of similar density (see Fig. 4.7). The ZPL linewidth yields 15 GHz in sample NI58 and the absolute line positions exhibit a spread within a 150 GHz (0.19 nm) margin for ensembles (measured as FWHM in the most dense ensemble region) as well as single emitters (measured as a range of spread ZPL positions). On the contrary, the widths of individual lines in sample SC500_01 range from 10-50 GHz and are spread over more than 7800 GHz (10 nm). This is a clear distinction to the production of ensembles of SiV^- centres with little inhomogeneous broadening, which only require annealing temperatures of 1100 °C after ion implantation [214]. For the SnV^- centre, annealing temperatures of 2100 °C are mandatory in order to sufficiently reduce the strain induced by the ion implantation. We emphasize that also in sample BOJO_001, we clearly see the impact of the HPHT annealing resulting in the same quality as for sample NI58.

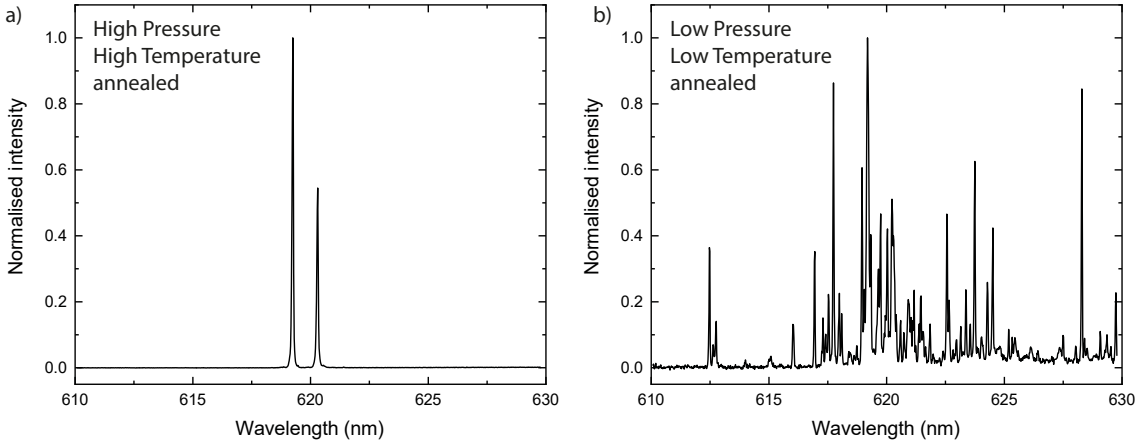

Figure 4.7: **Comparison of ensemble spectra in HPHT and LPLT samples:** The spectra of two SnV^- centre ensembles of similar density in sample **a)** NI58 and **b)** SC500_01 are depicted. The HPHT annealing conducted on sample NI58 leads to a tremendous narrowing of the inhomogeneous distribution that is prevalent in the LPLT annealed sample SC500_01 due to reduction of the lattice damage that is induced by the implantation process.

We also investigate the effect of annealing temperature on the room temperature emission of single emitters. For the HPHT samples, a very narrow and homogeneous distribution of the ZPL line positions spreads around 619.6 nm. As expected from the low temperature measurements, the LPLT sample exhibits a large distribution of ZPL central wavelengths ranging from 610 - 630 nm. Surprisingly, we find a secondary effect on the room temperature linewidth of single emitters in the LPLT sample. While emitters with a ZPL centered around 619.6 nm exhibit the same 5 - 6.5 nm linewidth as found in sample NI58, emitters shifted by more than one nanometer in central ZPL position show a considerably narrower linewidth of 2 - 3 nm, as it is depicted in Fig. 4.8b). Furthermore, the photon emission into the PSB for these SnV^- centres is reduced. Since the main difference between the samples is the strongly differing strain and homogeneity within the surrounding diamond lattice, these effects are most likely the result of different phonon coupling in high strain samples, which effects the phonon broadening of the ZPL line at room temperature. A previous study on SiV^- centres in nanodiamonds reported similar distributions of ZPL linewidths and line positions [134]. This is in agreement with our findings, since it is common that nanodiamonds can exert large amounts of strain on incorporated colour centres [134, 147].

4.2.3 Polarisation of single SnV^- centres

In the previous sections, we discover that the SnV^- centre exhibits the characteristic fine-structure of G4V centres. It is therefore very likely, that the orientation within the crystal lattice is in the <111> direction, as it is reported for the SiV^- centre [99]. While it is difficult to measure the orientation directly, we examine the polarisation of the absorption and emission dipole of single SnV^- centres, as it reveals the orientation of the electrical dipoles within the diamond lattice. The absorption dipole is measured by rotating the linearly polarised 532 nm excitation light with a HWP and recording the count rate for each incident polarisation state. For determining the polarisation of the emitted photons, we rotate the photon polarisation state in the detection path by utilising a HWP before sending it through a fixed linear polariser. In both measurements, it is necessary to introduce a

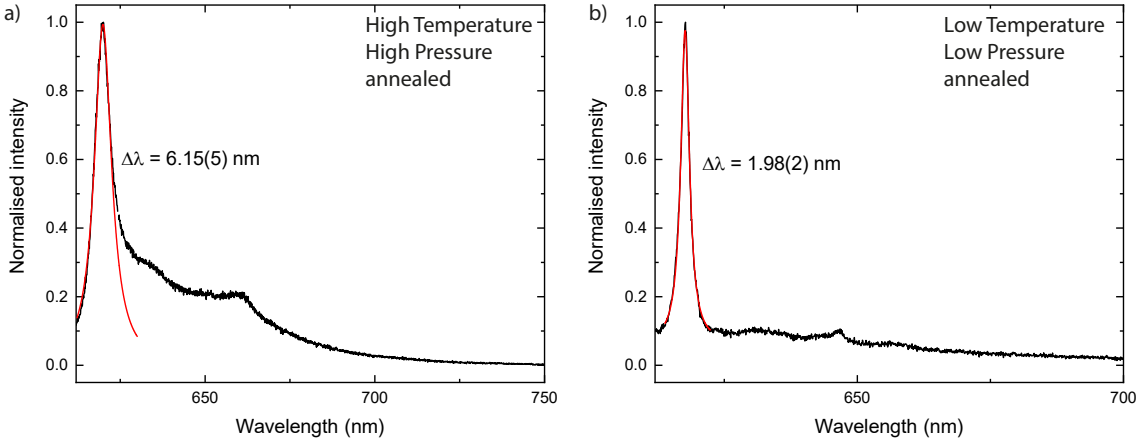

Figure 4.8: **Comparison of single emitters spectra in HPHT and LPLT samples: a)** Representative spectra of a single emitter in sample NI58, which was HPHT annealed. The emitter exhibits a typical room temperature linewidth of about 6 nm centered around 620 nm. In comparison, the spectrum of a single emitter in the LPLT sample SC500_01 is depicted in **b)**, which has a significantly narrower linewidth of about 2 nm and its centre wavelength is shifted to 618 nm.

QWP at a fixed position in front and after the dichroic mirror in order to correct for a phase shift caused by the optics. In Fig. 4.9, the projection into the measurement plane ((001) plane of the diamond sample) of the emission (in green) and absorption (in red) dipole at room temperature are depicted. The plotted angle is relative to the crystal axes with the x-axis (y-axis) corresponding to the [010] ([100]) surface edge of the diamond sample. Both projected dipoles exhibit an angle of about 45° with respect to the surface edges. This is to be expected for the high symmetry axis of the SnV^- centre being aligned with the <111> direction, which is reported for the SiV^- centre [99]. Additional emitters under investigation reveal the same or a perpendicular pattern, which is a result of the four possible directions being contained in the <111> group. This is in contrast to the findings in [132], where the absorption polarisation is almost perpendicular to the <100> axis, which might be a result of the high strain present in the sample investigated in the study. However, it is in good agreement with the direct investigation of the inversion symmetric alignment of the SnV^- centre along <111> measured using β^- emission channeling of implanted radioactive Sn isotopes [168]. For the investigated set of emitters, we find maximum visibilities of 85 % for the emission dipole and 87 % for the excitation dipole. It is important to note, that the recorded count rate results from the full spectrum, including the ZPL and the PSB. In order to distinguish the contributions of the constituents of the full spectrum, we repeat the investigation of the emitted photons, but instead of recording the count rate, we record the respective spectra. It has to be emphasised that for this emitter no autocorrelation is recorded due to technical reasons and it has to be suspected that the spectral contribution results from two emitters. In Fig. 4.10a) a subset of the measured spectra is plotted, where the polarisation dependence of the ZPL, but also of a phonon mode at about 50 meV and 110 meV are visible. The polarisation of the full spectrum, the ZPL and the 50 meV are shown in Fig. 4.10b). While the visibility of the oscillations is not very high, it becomes clear that the emission dipole of the ZPL and the phonon mode are exhibiting a relative angle of about 35°. This fact and also the unpolarised regions of the spectrum are the likely cause for limited visibilities in the emission dipole when recording the full spectrum of a SnV^- centre.

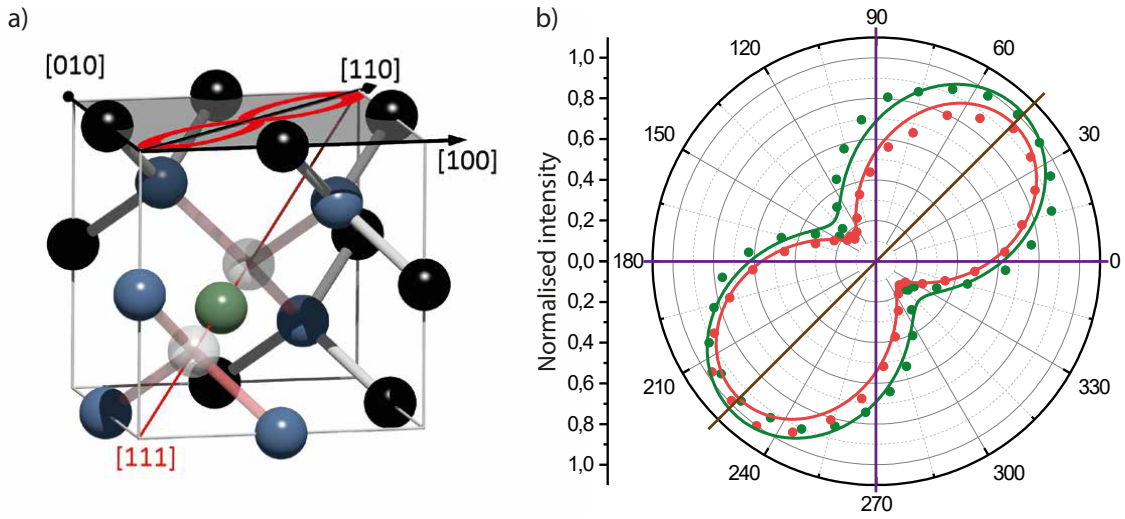

Figure 4.9: **Polarisation of single SnV^- centres: a)** Visualisation of the polarisation dipole being projected into the (001) measurement plane of the diamond sample. **b)** Exemplary measurement of the absorption (green) and emission (red) dipole for a single emitter under excitation with linearly polarised laser light at 532 nm. Both dipole axis overlap within the margin of error induced by the employed HWP and are in agreement with an alignment along the predicted <111> axis as the high symmetry axis of the SnV^- centre. The purple axes are an indication for the [100] and [010] edges of the diamond sample.

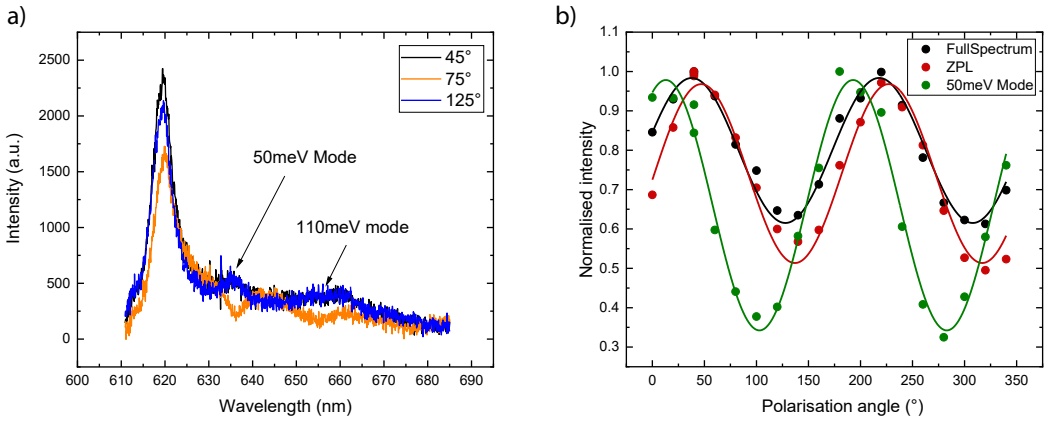

Figure 4.10: **Polarisation of the full room temperature spectrum: a)** Polarisation dependency of the full spectrum of at least two emitters for three different settings of the HWP. Two phonon modes at 50 meV and 110 meV as well as the ZPL exhibit a preferential polarisation dipole axis. **b)** The intensity of the 50 meV mode and the ZPL is depicted as a function of the rotation angle of the HWP, yielding oscillations with moderate visibilities most likely limited by two emitters with orthogonal polarisation of the ZPL being present.

4.3 Analysis of the phonon sideband and Debye-Waller factor

The SnV^- centre is, in contrast to trapped single atoms or ions, strongly influenced by the surrounding diamond matrix. In particular it is subject to interactions with lattice vibrations, which impact a key factor in QIP: the spectral purity of the photon emission of the defect. Therefore, this section addresses an in-depth investigation of the PSB of single SnV^- centres. An exemplary spectrum of the PSB at 30 K is depicted in Fig. 4.11a) and can be fitted by six lorentzians with peaks shifted relative to the ZPL by 46 meV, 76 meV, 109 meV, 122 meV, 148 meV and 181 meV. The modes at 46 meV and 109 meV are in agreement with the polarisation dependent modes found at room temperature in sec. 4.2.3. The overall structure of the PSB is in astonishing agreement with the calculated sideband spectrum by G. Thiering and A. Gali (extracted from [100]), for the case of exclusively a_{1g} symmetric phonons taking part in the centre-phonon interactions. The peak positions are also reproduced well for the combined coupling of a_{1g} and e_g symmetric phonons, but there is a significant mismatch between the predicted relative peak height and the measured data. In order to compare the spectra and the simulation data, we normalise the calculated dataset to the dominant sideband peak at 660 nm in the measured spectrum. It is noteworthy that no quasi-local mode, which should be shifted by 29 meV relative to the ZPL [132], can be distinguished. This so called local-oscillator transition corresponds to the eigenmotion of the tin-atom and results from a coupling to e_u symmetric phonons [250]. For this reason it is symmetry forbidden and the transition rules can only be lessened by the influence of crystal strain. In conclusion, the abscence of the transition is another strong indicator for the emitters in the HPHT sample NI58 being situated in a low strain crystal environment. For SiV^- and GeV^- centres, the local oscillator mode could be observed in material with residual strain [175, 202].
Apart from the knowledge of the exact phononic modes taking part in the emitter-phonon coupling, the strength of optical transitions without phonons being involved (i.e. the ZPL) in relation to the PSB is of great interest. Since only the ZPL transitions can be used in most QIP protocols, we explore the Debye-Waller (DW) factor, which is defined in equation 2.6. The value $I_{\mathrm{ZPL/PSB}}$ describes the emitted intensity into the ZPL respectively the PSB. As this ratio can be temperature dependent, we investigate it in a temperature regime ranging from 5 K up to 300 K. We determine the different intensities by fitting the whole spectra with Voigt profiles. The latter takes into account the spectrometer response function which is convoluted with the Lorentzian emission profile resulting from the emitter. The obtained data is shown in Fig. 4.11b) and exhibits a clear increase of the DW factor with decreasing temperature. We fit the data according to the model derived in [251], which predicts a theoretical temperature dependence of the DW factor of

$$\mathrm{DW(T)} = \exp(-\mathrm{S}(1 + \frac{2\pi^2}{3}\frac{\mathrm{T}^2}{\mathrm{T}^2_{\mathrm{cutoff}}})).$$

S stands for the Huang-Rhys factor, which is a measure of the phonon-emitter interaction and its value gives the average number of phonons being emitted during an electronic transition [173]. The temperature $\mathrm{T_{cutoff}}$ denotes an equivalent of the Debye temperature [252] and yields the cutoff temperature of the subset of phonons that are actually involved in the interaction between phonons and the SnV^- centre. The fit to the data yields a Huang-Rhys factor of $\mathrm{S} = 0.57(2)$, which translates into a DW factor of $\mathrm{DW(0\ K)} = 0.57(1)$ corresponding to 57 % of the total photons being emitted into the ZPL. The latter is furthermore matching closely to the theoretically calculated $\mathrm{DW_{a_{1g}}(0\ K)} = 0.63$ in the case of only a_{1g} symmetric phonons interacting with the SnV^- centre [100]. Again, the

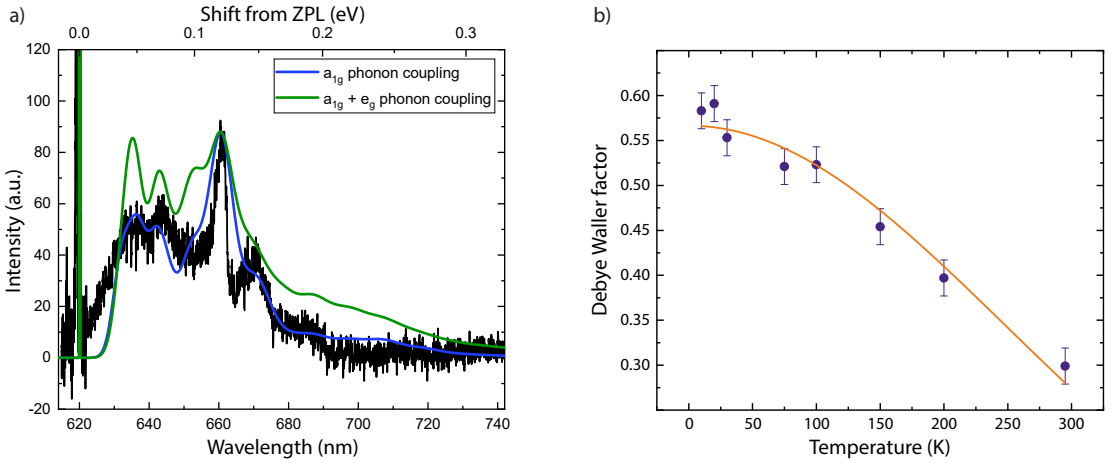

Figure 4.11: **PSB and temperature dependence of the Debye-Waller factor: a)** Exemplary spectrum of the PSB of a single emitter at 30 K. The black measurement data is overlapped with the theoretical spectrum predicted in [100]. The blue curve corresponds to the case of phonons with a_{1g} symmetry coupling to the SnV^- centre. The peak height as well as the peak positions are remarkedly well reproduced. The green line, taking into account phonons of both a_{1g} and e_g symmetry, also predicts the peak positions accurately but the peak height matches to a lesser extent. Both theoretical curves are normalised to the highest sideband peak at about 660 nm. **b)** Temperature dependency of the Debye-Waller factor of the same single SnV^- centre. For each temperature a spectrum is taken and the comparison of the fraction of photons emitted into the ZPL to the total number of photons yields the Debye-Waller factor. The fit to the data is according to the model derived in [252] and yields a Huang-Rhys factor of $S = 0.57(2)$ and a phonon cutoff temperature of 680(40) K. Both measurements are carried out using the quasi-resonant excitation light source emitting at 532 nm.

value for both a_{1g} and e_g symmetric phonons contributing to the phonon-centre interaction of $DW_{a_{1g}+e_g}(0\ K) = 0.41$ agrees to a lesser extent with our experimental findings. For the cutoff temperature, we extract $T_{cutoff} = 680(40)$ K, corresponding to an averaged effective phonon frequency of 59(4) meV. The theoretical simulations narrow down the frequency of the acoustical a_{1g} symmetric phonons to be contained in an interval from 60 meV up to 100 meV, with the lower edge being in agreement with our measured value. On the other hand, the frequency of e_g symmetric phonons is calculated to an exact value of 75.6 meV exhibiting a significant difference with our experimental evaluation. Due to the three indicators presented in the course of this section, we conclude that a_{1g} symmetric phonons are the predominant contributor in phonon-centre interactions for the SnV^- centre.

4.4 Excited state spectroscopy

The expectation that the molecular structure of the SnV^- centre can be described as the inversion symmetric D_{3d} point group is supported by the findings in this thesis, several indirect measurements in literature [113,132,176,242] and a direct measurement [168]. Accordingly, the electronic structure of the SnV^- centre is believed to be closely related to the ones of the other G4V vacancy centres. While the existence of E_g and E_u symmetric ground and excited states are evident from the PL measurements in Fig. 4.4 and the magnetic field dependent Zeeman splittings characterised in sec. 6.2.1 and reported in [176,242], the

nature of the commonly termed "off-resonant" excitation at around 532 nm is not revealed. We therefore present PLE measurements on an ensemble of SnV^- centres, in which we scan the excitation radiation retrieved from the supercontinuum laser source at constant power and a fixed bandwidth of 5 nm over the spectral range from 480 nm up to 595 nm. We conduct this measurement at room temperature and repeat it at cryogenic temperatures of 2 K. For each excitation wavelength in the room temperature measurement, we take a spectrum and extract the number of photons constituting the ZPL via a Voigt fit, which is depicted in Fig. 4.12a). We find a dominant broad resonance that is fitted accurately by a Lorentzian and lies centered around 2.348(4) eV (528 nm) with a width of 190(12) meV. A second resonance lies at 2.12 eV (585 nm) and overlaps well with the most prominent sideband peak of the mirror image of the PL spectrum of the SnV^- centres with respect to the ZPL.

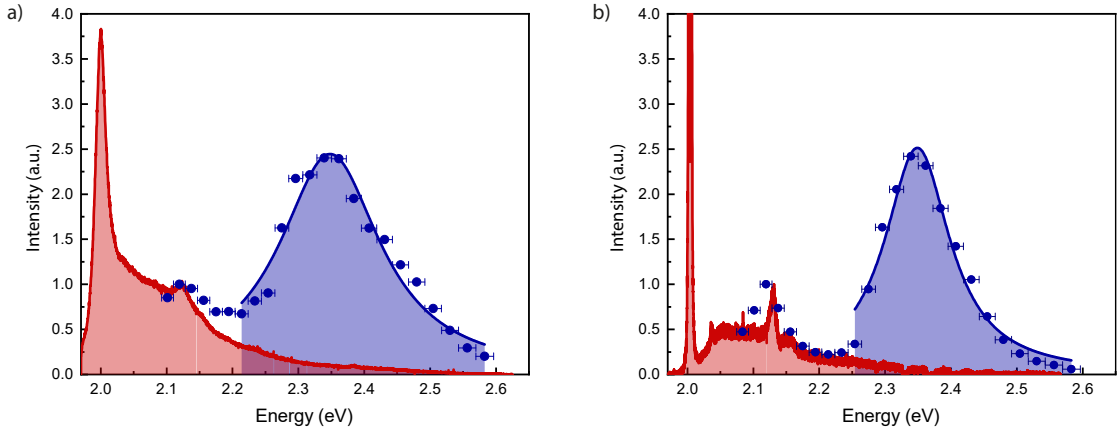

Figure 4.12: **PLE of higher lying excited states: a)** Room temperature measurement: Excitation of an ensemble of SnV^- centres resulting from an a_{2u} state in the valence band leads to a broad resonance (blue shaded) centered at 2.348(4) eV with a FWHM of 190(12) meV. The peak at 2.12 eV coincides with the prominent sideband peak of the mirrored (red image) PL spectrum with respect to the ZPL. **b)** Cryogenic measurement (1.6 K): The FWHM of the broad resonance narrows down to 120(8) meV as a result of reduced homogeneous phonon broadening. The resonance remains centered around 2.349(3) eV. The second peak observed in excitation overlaps furthermore with the sideband peak of the mirrored PL spectrum.

The same two peaks dominate the PLE measurement at 2 K, which is measured in a slightly different way by simply recording the ZPL count rates in a filter window of 620(10) nm on an APD for each excitation wavelength (see Fig. 4.12b)). The dominant resonance lies still centered around 2.349(3) eV but narrows down to a width of 120(8) meV. This narrowing is a strong indicator of a direct electronic transition being involved which narrows down at low temperatures upon reduced homogeneous phonon broadening. We attribute it to an excitation of a higher lying excited state with A_{2u} symmetry upon excitation of an electron from a broad a_{2u} band. The latter one is a result of an a_{2u} defect level, that is lying within the valence band of diamond and broadens due to mixing with the diamond band. While similar results were reported on the SiV^- centre with a 400 meV broad resonance at room temperature [172], that was confirmed independently in our group (see sec. 5.4 below), the observed narrower width of 190 meV for the SnV^- centre points toward the absolute energy position of the a_{2u} level being closer to the valence band edge. The latter finding agrees well with the theoretical predictions in [100]. While the excitation is resonant with the

higher lying excited state, the coherence of this state is massively limited by the mixing with the diamond band so that no coherent effects of this excitation could be observed throughout the course of this thesis. Consequently the 532 nm excitation light, which is usually termed "off-resonant" excitation of the SnV^- centre, is labeled "quasi-resonant" excitation in this thesis.
The peak at 2.12 eV occurs also in the low temperature measurement and overlaps again with the most dominant sideband peak in the mirrored PL spectrum. This peak results from excitation of the population within the fine-structure ground states into the higher lying vibrational ladder of the excited state. As the peak coincides well with the mirrored PL spectrum, it indicates a similar ground and excited state vibronic structure, due to the overlap of emission and absorption measurements.

Chapter 5

Charge cycle of the SnV

Contributions and copyright notice

The experiments conducted in this chapter were carried out under the supervision of C.B. Two HPHT samples are investigated: NI58 was fabricated as stated in the previous chapter. The second HPHT sample, BOJO_001, was fabricated employing ion implantation by Detlef Rogalla (D.R.), J.G. and D.He. at RUBION at the university of Bochum. The HPHT annealing was implemented by David Hardeman (D.H.) and Pierre-Olivier Colard (P.-O. C.) under supervision of Matthew Markham (M.M.) at the Element Six Global Innovation Centre in Oxford, UK. Post-annealing cleaning of the sample was conducted by P.F.. The optical setup was designed and set up by J.G. and D.He.. J.G. and D.He. conceived the measurements and the analysis of the data with input from P.F.. J.G., D.He., P.F. and C.B. discussed and designed the charge cycle model. The measurement on the ensemble of SiV^- centres was carried out in an optical setup implemented by Anna Maria Fuchs (A.M.F.) and the experiment and analysis of the data were carried out by J.G. and A.M.F.. A.G. and Jero Maze (J.M.) contributed valuable discussions and theoretical insights on the charge cycle of colour centres in diamond.
The main results of this chapter were originally published in [136] and [138] and are reproduced with permission according to Attribution 4.0 International (CC BY 4.0).

The chapter is dedicated to revealing and mitigating the charge mechanism leading to the termination of SnV^- centre fluorescence under resonant excitation. In a first step, the enhancement of fluorescence of an ensemble of SnV^- centres, resonantly excited on the C-transition, under addition of a second lightfield is explored. In the following, we experimentally study the number of photons contributing to the fluorescence termination process and the possibility of charge state initialisation. Based on these findings, we derive a complete charge cycle model of the SnV^- centre. The validity of this model for further G4V centres is explored in the last section by investigating an ensemble of SiV^- centres.

5.1 Termination of fluorescence under resonant excitation

Resonant optical excitation is a crucial prerequisite for initialisation, readout and all-optical coherent control of the SnV^- centre. Monitoring of successful resonant excitation is in the following implemented by recording the emitted photons into the PSB, while scanning the dye laser across electronic transitions. For single emitters in sample NI58 and BOJO_001, the fluorescence is reproducibly terminated under resonant excitation,

which is consistent with the findings reported in [114, 176]. An exemplary measurement is depicted in Fig. 5.1a), where the abrupt termination of fluorescence, when approaching the resonance maximum, is indicated by the dashed red line. In order to exclude a simple spectral shift of the resonance line, we perform large spectral scans over several GHz and find the termination to be permanent. While waiting times without application of laser radiation are not sufficient to recover the fluorescence even after several hours, introduction of a laser pulse at 532 nm leads to the retrival of the fluorescence signal. At the same time, the fluorescence line shifts up to several hundred MHz, as it can be seen in the PLE scan in Fig. 5.1b), where the 532 nm laser is continuously applied. Similar findings for GeV^- centres are reported in [193].These shifts, which far exceed the lifetime-limited linewidths of about 25 MHz, render any meaningful application of the SnV^- centre in QIP impossible. We attribute the termination of fluorescence under resonant excitation to an alteration of the charge state, while the spectral shifts caused by the 532 nm radiation field result most likely from a changed charge environment. The latter has to result from second-order Stark effects, as they were reported in [196, 197], since the symmetry of the SnV^- centre is protecting the emitter against the first-order Stark effect. The hypothesis of a charge transfer being the cause for the termination of fluorescence will be further explored in the following sections.

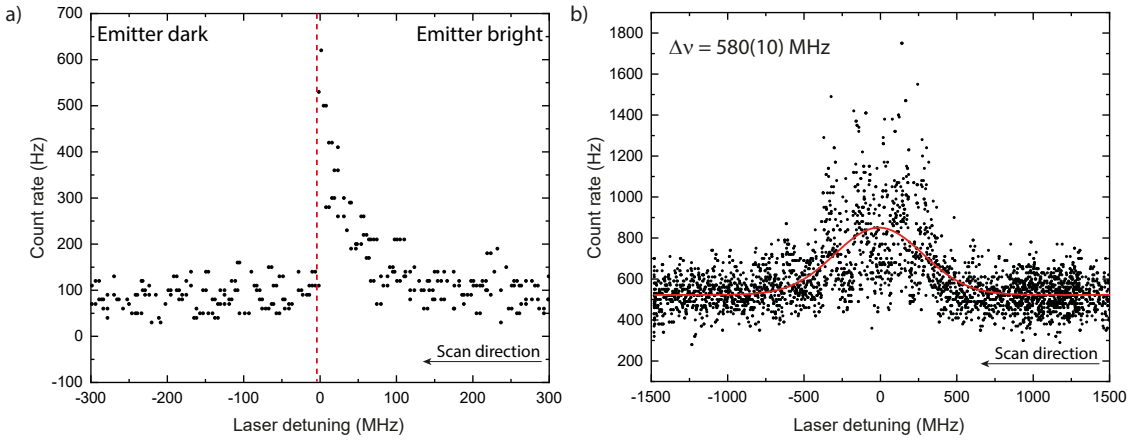

Figure 5.1: **Termination of fluorescence of single SnV^- centres: a)** Exemplary scan of the excitation laser over the resonance of the C-transition of a single SnV^- centre. The emitter remains bright until charge transfer terminates the fluorescence when approaching the resonance maximum, which is visible as a sharp drop of the fluorescence. **b)** Recovery of the fluorescence can be induced by application of an additional weak light field at 532 nm. However, this leads to spectral diffusion and spectral jumps, broadening the lifetime limited linewidth by more than a factor of 20 to 580(10) MHz.

5.2 Electron capture and charge stabilisation

A common technique to mitigate the transfer to a colour centre into its dark state is the application of an additional laser, oftentimes termed "repump" laser without specification of the pumping process itself. Due to reasons of availability, the wavelength of the repump laser is typically chosen to be 532 nm. However, systematic investigations of the underlying physical processes and the effectiveness of the repumping are rarely conducted. In this section, we want to reveal the mechanisms leading to the transfer of the SnV^- centre into its dark state and the efficient mitigation of it. We thus conduct an experiment at 1.7 K in

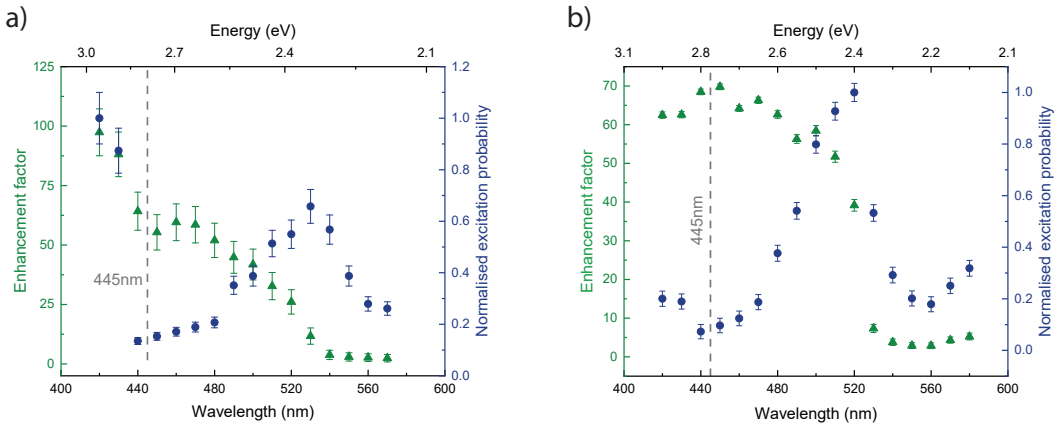

Figure 5.2: **Fluorescence enhancement measurement on ensembles of SnV^- centres:** Measurement of the enhancement of fluorescence factor of an ensemble of SnV^- centres in sample **a)** NI58 and **b)** BOJO_001. The ensemble is excited resonantly on the C-transition and a second light field is added. Non-linear enhancement of the fluorescence is observed and the enhancement factor is shown as green triangles. The normalised direct excitation probability by the second light field only is plotted in blue. The enhancement increases strongly for wavelengths (energies) of the second light field shorter (larger) than 520 nm (2.4 eV), which we attribute to a stabilisation of the negative charge state of the SnV^- centre. The peak of the direct excitation probability at 520 nm (2.4 eV) is the same as found in sec. 4.4 i.e. excitation to the A_{2u} state, while we find an indicator for a higher lying state at photon energies exceeding 2.8 eV. The origin of the latter is most likely the parity forbidden transition from state a_{1g} to e_g (Fig. 2.4). Since the parity selection rule is lowered by strain, it is consistent with the finding that the transition is more likely in sample NI58, which was six times shorter HPHT annealed than sample BOJO_001.

which we continuously excite ensembles of SnV^- centres on resonance with the C-transition in sample NI58 as well as BOJO_001 while systematically varying the wavelength of an additional laser field that we introduce. The stabilisation radiation is retrieved from the supercontinuum laser source (see sec. 3.2.1) at a fixed repetition rate of 78 MHz and a bandwidth of 10 nm. The count rate is monitored on the PSB with a 655(47) nm bandpass filter. For each wavelength of the second light field, we define the fluorescence enhancement factor $\beta = \frac{CR_w}{CR_{wo}}$ as the ratio of the fluorescence count rate CR_w with both laser fields applied (while substracting the count rate caused by the second light field alone) to the count rate obtained by only shining in the resonant laser radiation (CR_{wo}). In Fig. 5.2, the result of this measurement for a wavelength (energy) variation of the second light field in between 420 nm (2.95 eV) and 580 nm (2.15 eV) is depicted for both HPHT samples as green triangles. While radiation with wavelengths (energies) longer (shorter) than 520 nm (2.4 eV) does not cause significant changes in the count rate and the fluorescence remains weak, we observe a fluorescence enhancement for wavelengths (energies) below (above) that threshold. The enhancement factor reaches even values exceeding 50, strongly indicating an efficient stabilisation of the negative charge state. The

optimum between maximum fluorescence enhancement and minimised direct excitation probability (measured by evaluating the count rate upon purely shining in the second light field, blue dots in Fig. 5.2) lies at 445 nm. Termination of the fluorescence is only observed when the SnV^- centre is in its excited state (see Fig. 5.1), thus the charge stabilisation light

field should have a minimised direct excitation probability in order to avoid subsequent termination induced by a second charge stabilisation photon, as will become clear in the following. We therefore continue by evaluating the charge dynamics of single SnV^- centres, for which we choose 445 nm as the charge initialisation wavelength supplied by the charge stabilisation laser (see sec. 3.2.1).

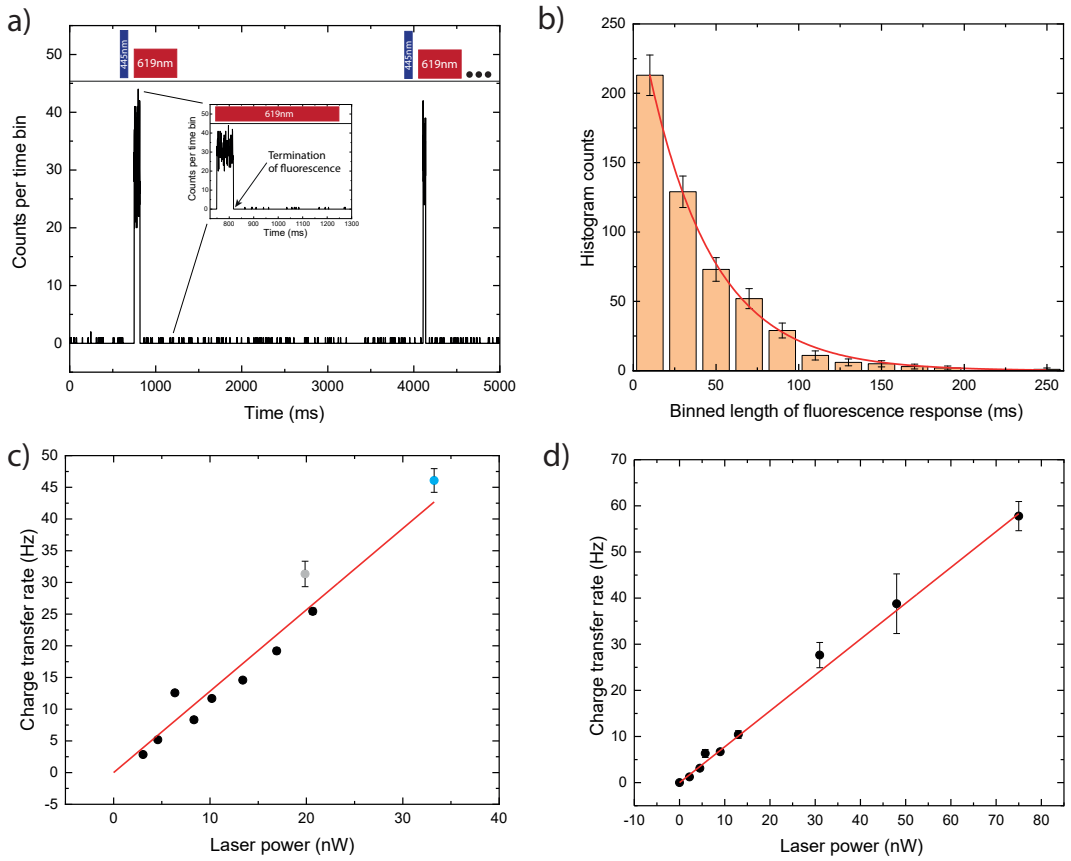

Figure 5.3: **Charge transfer of single SnV^- centres: a)** An exemplary excerpt of the time trace in an charge transfer experiment. After initialisation of the negative charge state due to the 445 nm laser pulse, a fluorescence response is created by the laser pulse resonant with the C-transition until charge transfer occurs and terminates the fluorescence. **b)** The lengths of the fluorescence responses are binned for a laser power of 20.7 nW and plotted in a histogram. The lifetime of the charge state is extracted by the time constant of the exponential fit and translated into a charge transfer rate by taking the inverse of the charge lifetime. This rate is evaluated for different resonant laser powers and increases linearly with power for **c)** EA27 and **d)** EA13, indicating a single photon process being responsible for the charge transfer. The blue data point in **c)** corresponds to the laser power that is chosen in the subsequent charge initialisation measurement for EA27, while the grey data point is the result of a measurement that was aborted slightly earlier than the others.

Another interesting feature becomes visible in the measurement when evaluating the direct excitation probability. The latter does not only peak at the excitation to the A_{2u} state found in sec. 4.4, but we find an additional indication of an even higher lying excited state at about 2.8 eV. Its origin could be the parity forbidden excitation to the A_{1g} state

indicated in Fig. 2.5, which is in agreement with the transition being more pronounced in the higher density ensemble in sample NI58. In this region, lowering of the parity selection rule by strain will be more prevalent compared to sample BOJO_001 due to the larger amount of impurities being implanted and the six fold shorter annealing time.

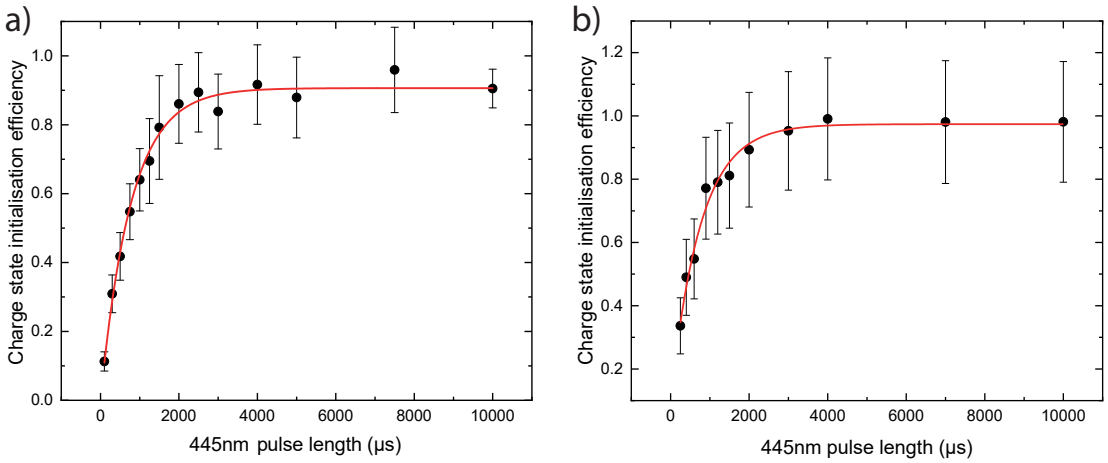

Figure 5.4: **Charge initialisation of single SnV$^-$ centres:** The negative charge state of single SnV$^-$ centres is initialised by a 445 nm pulse with variable length and is read out as well as terminated by a subsequent laser pulse resonant with the C-transition. For EA27 in **a)** (EA13 in **b)**) the resonant laser pulse is 0.5 s (1 s) long and the power chosen such that charge transfer occurs with a probability close to unity. For each blue pulse length, the number of resonant laser pulses creating a fluorescence response is divided by the total number of pulses used, yielding the charge initialisation efficiency. This efficiency increases with the initialisation pulse length following a mono-exponential growth law. It saturates with a time constant of $\tau_{\mathrm{CI}} = 780(27)$ µs ($\tau_{\mathrm{CI}} = 657(43)$ µs) at a value of 91(1) % (97(2) %).

Coming back to the charge processes, in a first step, we measure the number of photons causing the termination of fluorescence under resonant excitation. Experimentally, we employ a 445 nm laser pulse to initialise the negative charge state, followed by a long laser pulse of duration $\Delta\tau_{\mathrm{res}}$ resonant with the C-transition. The fluorescence resulting from this pulse is recorded on the PSB until it is terminated. The power and duration of the pulse $\Delta\tau_{\mathrm{res}}$ is chosen such that charge transfer will occur with a probability close to unity. This is visible in Fig. 5.3a) in the detailed time trace of such an experiment, where the charge transfer occurs long before the end of the optical pulse. We conduct this measurement for two single emitters (EA27 and EA13, autocorrelation measurements are evaluated in sec. 6.1.1) with slightly different parameters (EA27: 10 ms 445 nm pulse length, 1 s resonant laser pulse length, about 500 repetitions; EA13: 0.5 ms 445 nm pulse length, 6 s resonant laser pulse length, about 230 repetitions). We define the charge lifetime as the time until the fluorescence is terminated under resonant excitation. Thus we can extract the average τ_{charge} of it as the time constant of a mono-exponential decay fit to the histogram of duration of fluorescence before termination (see Fig. 5.3b)). This charge lifetime is measured for different resonant laser powers and we extract the charge transfer rate, defined as the inverse of the charge lifetime. This rate increases linearly with the resonant laser power, exhibiting a slope of 1.28(5) Hz/nW (0.8(1) Hz/nW) for EA27 (EA13). The underlying charge transfer therefore has to result from a single photon process, when the SnV$^-$ centre is in the excited state. The latter must be the case, since termination of fluorescence occurs only when approaching the resonance maximum (see

sec. 5.1) and not while the laser is off-resonance. Naively, a two-photon process would be expected as the first photon excites the SnV^- centre and the second photon induces the charge transfer. However, the lifetime of the excited state is about 7 ns while the charge lifetime, even for the highest resonant laser power used, exceeds 10 ms. For resonant excitation laser powers larger than the saturation power, the charge transfer thus starts from a 50 % steady state population of the excited state and consequently involves only one photon.

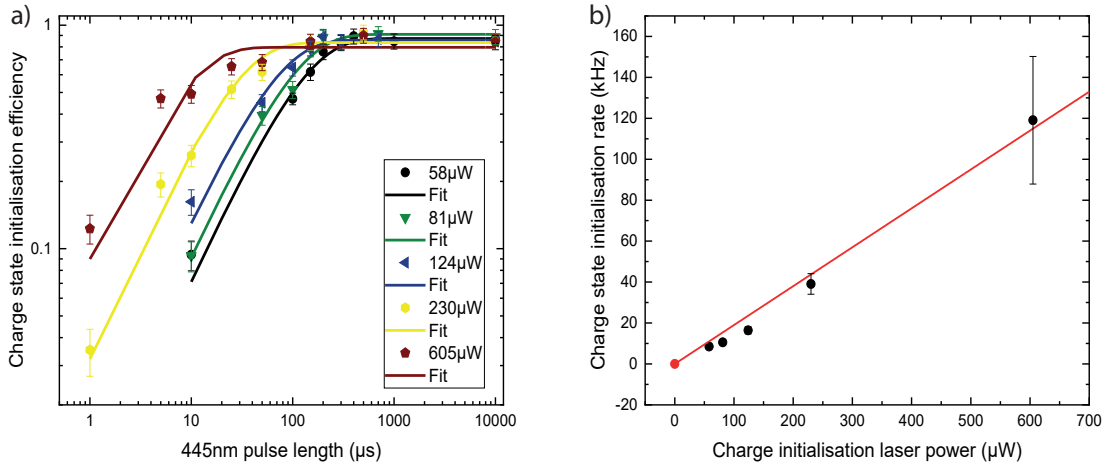

Figure 5.5: **Power dependence of the charge initialisation of a single SnV^- centre: a)** Repetition of the charge initialisation measurement on emitter E1NI58 for varying 445 nm laser powers. The charge initialisation process is sped up with higher laser power. **b)** From the measurements in **a)**, the charge state initialisation rate is extracted and plotted against the applied 445 nm laser power. It increases linearly and thus indicates a single photon process being responsible for the charge state initialisation.

In a second step, we explore the efficiency of charge state initialisation with 445 nm radiation. To this end, an initialisation pulse of variable duration, corresponding to a cw power of 50 µW (90 µW) for EA27 (EA13), is followed by a subsequent resonant laser pulse that causes a fluorescence response as well as ensures ionisation with a probability close to unity. The error of the dark state preparation is given by $1 - \exp(-\Delta\tau_{\mathrm{res}}/\tau_{\mathrm{charge}})$ and is below 10^{-10} $(2 \cdot 10^{-2})$ given the following numbers: For EA27, the resonant laser pulse length is 0.5 s and the chosen power of 33 nW corresponds to an ionisation rate of 46 Hz (blue dot in Fig. 5.3c). For EA13, the pulse length is 1 s and the ionisation rate amounts to 5 Hz. The initialisation efficiency is defined as the number of fluorescence responses that we observe divided by the number of pulses send to the emitter. The efficiency of the charge initialisation increases with the duration of the initialisation pulse, as it can be seen in Fig. 5.4. Following a mono-exponential growth law $(1 - \exp(-t/\tau_{\mathrm{CI}}))$ with the charge initialisation time constant τ_{CI}, it saturates at a value of 91(1) % (97(2) %) for EA27 (EA13). In the case of EA27, 4(1) % missing to unity charge initialisation can be explained by the number of pulses in which charge transfer occurs on time scales too short to create a detectable fluorescence response. Spurious charge transfer induced by the blue laser alone is a possible explanation of the further few percent missing to perfect charge initialisation. This is a result of the non-zero direct excitation probability, since after excitation a second 445 nm photon can induce the charge transfer. This is discussed below in detail. We furthermore

explore the power dependence of τ_{CI} and the resulting charge initialisation rate $\gamma_{\mathrm{CI}} = \frac{1}{\tau_{\mathrm{CI}}}$ on a further emitter, labeled E1NI58. This is done by conducting the same charge initialisation measurement as before, but for different 445 nm laser powers. The result is depicted in Fig. 5.5 and shows that γ_{CI} increases linearly with the charge-initialisation-laser power (slope 190(8) Hz/µW). This means that also the charge initialisation is based on a single photon process. Moreover, we demonstrate that the charge initialisation can be efficiently set within 10 µs at the highest laser power of 605 µW. As we do not see any changes of saturation in the linear increase of γ_{CI}, this time scale could be even further reduced.
It is noteworthy to comment on the time scale over which the charge state of the SnV^- centre is conserved, when it is not subject to a resonant laser. When kept in the dark (no charge stabilisation, no resonant laser), the charge state maintains up to days until being subject to resonant excitation. When addressing the SnV^- centre resonantly with pulsed excitation in an ultralow duty cycle (about 0.2 ‰) and a power far below saturation, the charge state is maintained for more than an hour after being once initialised by the 445 nm laser. We suspect that ultimately fluorescence termination was induced by the resonant laser and claim that the charge state stability is mainly limited by the application of resonant laser light.

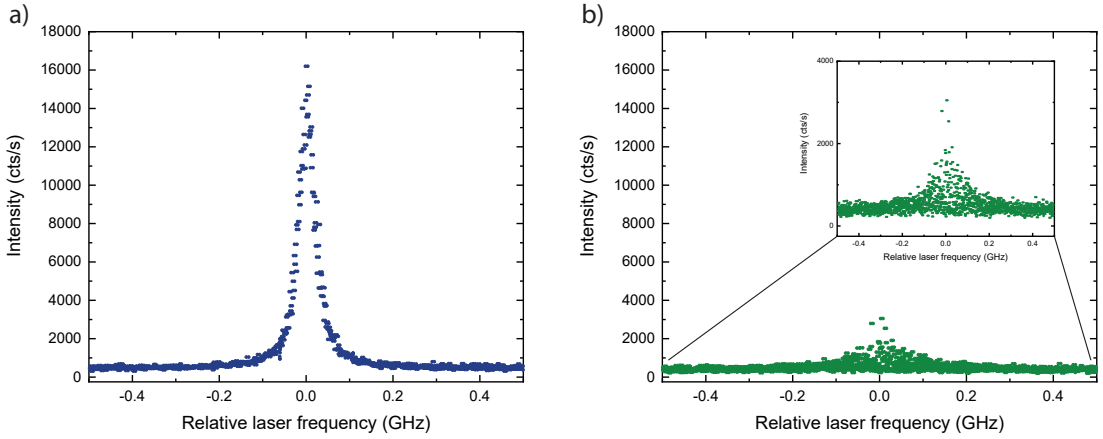

Figure 5.6: **Comparison of charge stabilisation with 445 nm and 532 nm:** We scan a 1 nW resonant laser across the C-transition of emitter E1NI58 and detect the photons emitted into the PSB. The charge stabilisation laser is applied with a laser power of 10 µW. **a)** Using 445 nm laser light for charge stabilisation leads to a stable and bright resonance transition. **b)** In comparison, when using 532 nm light, the resonance line is washed-out, dim and unstable.

We would like to compare our developed charge stabilisation technique with the commonly used 532 nm light for charge initialisation of colour centres in diamond ([114, 176, 192, 193, 195], supplemental material [104]), which is shown in Fig. 5.6 for emitter E1NI58. The utilised charge stabilisation laser power is 10 µW in both cases and the resonant excitation power is set to 1 nW (saturation power: 2.5 nW). While the 445 nm laser leads to a stable and bright resonance line, the 532 nm laser somewhat mitigates the fluorescence termination effect, but the resonance line is unstable, washed-out and dim in a comparable way as presented in Fig. 5.1b). Thus the 445 nm laser light is far more suitable for charge stabilisation of the SnV^- centre. For use in any future application, proper charge state initialisation can be induced by employing a 445 nm laser pulse with a power and duration corresponding to a high initialisation efficiency. The repetition rate with which the charge

state needs to be reset then has to be higher than the charge termination rate set by the laser power and duration of the resonant excitation. In this context, it is worth noting that for large resonant laser powers (exceeding 100 microwatts, $\sim 10^5 P_{sat}$) without application of the charge stabilisation laser the fluorescence is recovered, however, resulting in similarly washed-out and dim resonance features as for 532 nm. We suspect that the origin of the recovery is a two-photon process driving the charge transition of the divacancy, which is why it occurs only in the high power regime.
As the properties of qubits in the solid state tend to be strongly dependent on the strain and charge environment in their near vicinity, we would like to emphasise that charge initialisation in the HPHT samples worked on every emitter investigated. In very few cases, blinking of the fluorescence was still evident in the case of the charge stabilisation laser being present, which we attribute to imperfect alignment of the 445 nm radiation. This alignment is crucial for perfect charge stabilisation and another strong indicator for the termination of fluorescence as well as the recovery by the initialisation laser being due to charge effects and not caused by very long-lived metastable quantum states.

5.3 Derivation of the charge cycle of the SnV

This section is dedicated to the development of a charge cycle model of the SnV centre, which explains the experimental findings in the previous sections. We start with the termination of the fluorescence under resonant excitation and therefore consider the absolute position of the energy levels of the SnV centre within the diamond band gap. These values are extracted from the calculations performed in [100] and depicted in Fig. 5.7. A charge transfer process due to photo-ionisation by the photons constituting the resonant excitation can be excluded, since the highest lying energy levels of the SnV^- centre are situated at $E_{exc} = 2.6\,eV$ above the valence band edge. Therefore, the energy to enable photo-ionisation with a single photon would be required to exceed 2.87 eV, which is the difference between $E_{gap} = 5.47\,eV$ of the diamond band gap and $E_{exc} = 2.6\,eV$ of the highest energy levels. Since the energy of a photon resonant with the ZPL of the SnV^- centre is about 2 eV, direct ionisation would require two photons, which is in contrast to our findings of a single photon induced charge transfer process. Furthermore, such an ionisation process would transform the negative charge state of the SnV into its neutral state SnV^0. The neutral charge state of the SnV is believed to be optically active, with a ZPL that is theoretically predicted to be centered at 680(40) nm [222]. However, while exciting an ensemble of SnV^- centres resonantly on the C-transition and thereby actively driving the charge transfer, no sign of SnV^0 centre could be observed in the spectral region from $620-900\,nm$, even for integration times exceeding 10 min. Since the ladder of vibrational states in the excited state of the SnV^0 centre is expected to be similar to the SnV^- centre as they share the same structural geometry, its range should cover about 100 nm. Therefore, the 620 nm laser light should not only induce charge transfer but also excite the SnV^0 centre. Even if this excitation probability is weak, in a dense ensemble it should nevertheless create a sufficiently strong fluorescence response for detection.
Consequently, the transfer of only one charge leaves only the possibility of transforming the SnV^- centre into its doubly negative charge state SnV^{2-}. For the SnV^{2-} centre, all electron states are fully occupied with electrons, which prohibits any electronic transitions. This means that the SnV^{2-} centre is optically inactive and cannot be investigated via spectroscopic means. Also in electron-spin resonance measurements it is impossible to trace as its spin sums up to net zero. However, as explained above, our observations only leave the conclusion that the SnV^{2-} centre is the dark state of the SnV^- centre. Our

findings agree well with the recently reported experiments on the SiV^- centre, in which

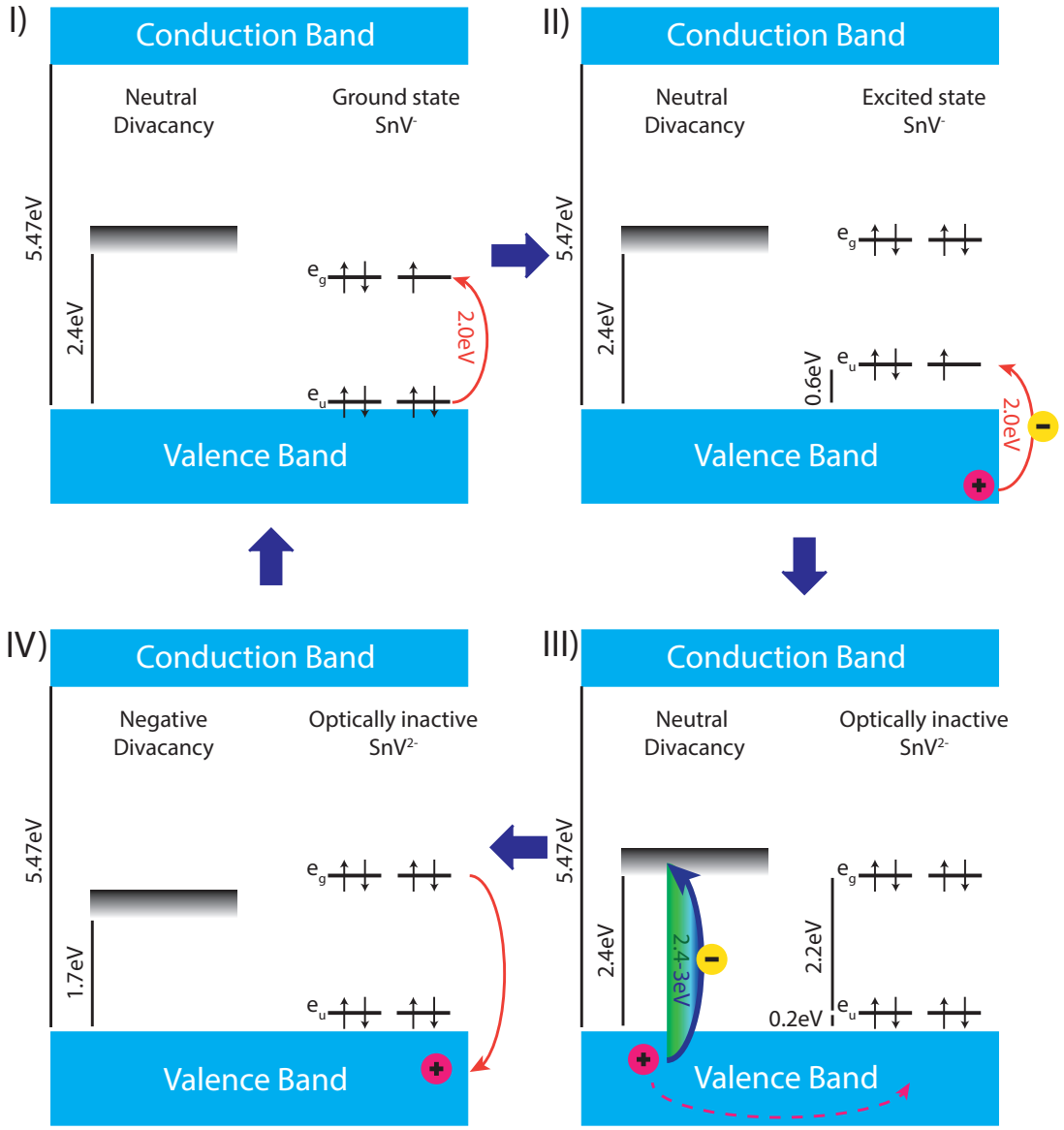

Figure 5.7: **Charge cycle of the SnV^- centre:** I) Excitation of the SnV^- centre with a resonant 2 eV photon. II) A subsequent resonant 2 eV photon transfers a photon from the valence band to the vacant site in the lower electronic orbital. This transforms the charge state of the SnV into the doubly negative SnV^{2-} centre. III) The charge transition of the neutral divacancy in diamond to its negative charge state is driven by a photon with an energy of 2.4 - 3 eV. This process leaves a hole in the valence band, which diffuses towards the SnV^{2-} centre where in IV) recombination of an electron of the SnV^{2-} centre and the hole occurs. This transforms the SnV^{2-} again into the SnV^- centre and the charge cycle is closed.

the authors also identify the SiV^{2-} centre as the dark state of the SiV^- centre [137]. The process of charge conversion from bright to dark state that Gardill et al. propose [137] is the capture of an electron in the valence band, and in turn release of an electron from

the centre to the valence band (capture of a hole) leads to recovery of the SiV^- centre fluorescence. While the capture of an electron requires a photon energy larger than 0.6 eV when the

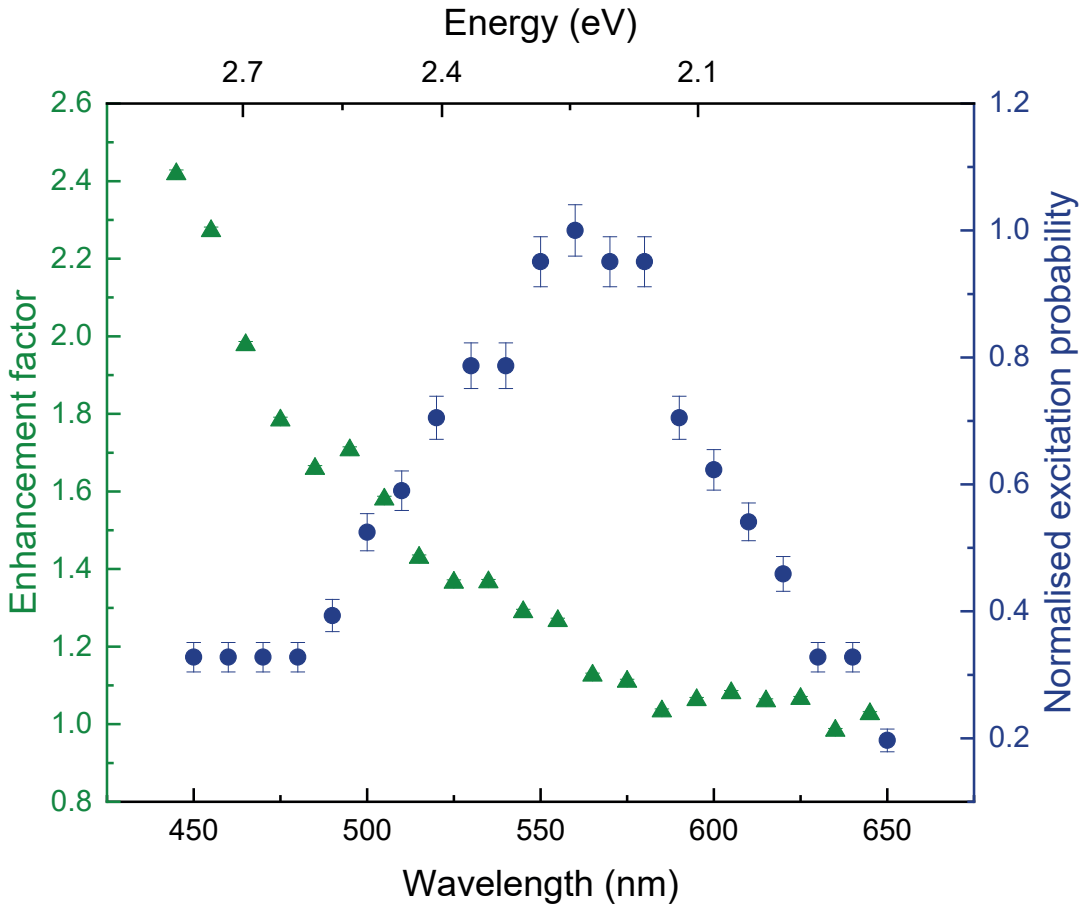

Figure 5.8: **Fluorescence enhancement measurement on ensembles of SiV^- centres:** Measurement of the enhancement of fluorescence factor of an ensemble of SiV^- centres. The ensemble is excited resonantly on the C-transition and a second light field is added. The enhancement factor is defined as in the case for the SnV^- centre measurement. The normalised excitation probability, measured by the count rate resulting from the second light field alone, is plotted in blue. The enhancement increases strongly for energies of the second light field larger than about 2.4 eV, which we attribute to the same charge stabilisation mechanism as for the SnV^- centre. The peak of the excitation probability at 2.25(1) eV is the result of exciting the a_{2u} defect level lying within the valence band, which is also reported in [172].

SnV^- centre is in the excited state, the subsequent release is only possible if there is a hole present in the valence band. Such a hole can be created by photo-excitation of another defect in the vicinity of the SnV centre. This defect can be identified by the fluorescence enhancement measurements in Fig. 5.2, where the steep rise of the enhancement factor for energies of the second light field exceeding 2.4 eV as well as the shape of the curve are in very good agreement with the charge transition of the neutral divacancy in diamond. This charge transition is theoretically predicted [253] and experimentally confirmed [254] to lie above a threshold of 2.4 eV and reaching a saturation regime at photon enegies above

3 eV. It occurs upon the transfer of an electron within the valence band to the neutral divacancy, thereby leaving a hole in the valence band. This light induced charge transition is reported to be highly efficient, where unity charge conversion can be reached for photon energies larger than 3 eV. It is furthermore very likely that the investigated HPHT samples contain a significant amount of divacancies, as each tin ion creates about 3000 vacancies at an implantation energy of 700 keV (see Fig. 2.2). These single vacancies become mobile in the annealing process and as the formation of divacancies is an exothermic reaction [255], many of them will be transformed into divacancies. This is especially true since the number of isolated vacancies generated decreases as the vacancy concentration and thus cluster formation overall increases the heavier the implanted ion is [256]. Long-term annealing at temperatures around 2100 °C will reduce the amount of divacancies, but within the time scale used in our sample preparation a significant amount will remain within the diamond lattice [257]. It is likely that other defects and impurities are also present in a certain concentration and thus we briefly discuss while we do not take them into account as candidates for the hole donor. The most simple defect is the single vacancy. While the majority of defects and impurities in diamond exhibit very low diffusion constants [257], the neutral single vacancy becomes mobile at temperatures exceeding the activation temperature of 600- 900 °C [173, 258, 259]. The negatively charged single vacancies is more stable, but has been shown to anneal out completely at temperatures above 1900 °C [260]. Under HPHT annealing both charge states are either diffusing to the surface and anneal out or they form complexes such as the divcacancy in an exothermic reaction. Therefore, it is very unlikely that neutral single vacancies are still present in significant concentrations in the investigated samples. The next common defect is the interstitial nitrogen (P1 centre), which survives HPHT treatment [260]. In the substrate samples used, nitrogen is specified to be present in concentrations of less than 5 ppb (typically 0.1- 1 ppb). However, their ionisation energy threshold lies at 1.7 eV [261], which, first of all, is not in agreement with the enhancement starting at 2.4 eV and furthermore would promote an electron to the conduction band, while a mobile hole in the valence band is needed for transforming the defect centre from SnV^{2-} back to SnV^{-}. Boron is another impurity in the diamond that occurs in small but still significant concentrations (below 1 ppb) in the investigated samples. However, the absorption of interstitial boron is within a very low energetic range (0.3-0.4 eV) and thus not in agreement with the observed enhancement measurement. We therefore conclude that the divacancy is the most likely candidate donating a hole in the valence band upon excitation with energies exceeding 2.4 eV.
Putting together the considerations discussed above, we propose the following model, depicted in Fig. 5.7, of the full charge cycle of SnV centres in diamond:

I A photon resonant to the ZPL at 620 nm (2 eV) excites the SnV^{-} centre to a now fully occupied e_g state.

II Subsequently, another 2 eV photon transforms the SnV^{-} centre into its doubly negative charge state SnV^{2-} centre by promoting an electron from the valence band to the empty site in the lower e_u orbital. The hole created in this process is captured by another defect in the vicinity of the SnV centre.

III The charge transition of the neutral divacancy to its negative charge state is induced upon an inciding photon with a wavelength (energy) shorter (larger) than 520 nm (2.4 eV). Within this process, a hole is left in the valence band, which diffuses towards the SnV^{2-} centre.

IV Recombination of an electron within the SnV^{2-} centre's e_g or e_u orbitals and the hole

in the valence band leaves the SnV centre in its singly negative charge state, which closes the charge cycle.

If a SnV^- centre undergoes this charge cycle for the first time, the hole created in step II must be captured by another defect, else there would be a dynamic equilibrium of the charge oscillating between the SnV^- and SnV^2 states and the fluorescence would not be terminated. After undergoing the full cycle for the second time, the created hole can be captured by the negative divacancy created in the first cycle. This means from this point on, the hole can be transferred back and forth between the divacancies in the vicinity and the SnV^- centre, the speed and efficiency of which is dependent on the power and wavelength of the charge initialisation radiation. For instance, the phenomenon that 532 nm radiation recovers the fluorescence after electron capture but leads to large spectral shifts, can be explained by the energy of the light being insufficient for efficient conversion of the manifold of divacancies surrounding the centre to their negative charge state. The charge environment will be fluctuating and introduce spectral diffusion due to second-order Stark effects. In contrast to this, the 445 nm radiation efficiently converts the divacancies to their negative charge state and will furthermore provide sufficiently high-energetic radiation for ionisation of most of the common other impurities being present in low concentrations such as boron and nitrogen. Therefore, the charge environment will be in the same state after each application of the initialisation laser. The cycle model explains furthermore the exponential growth law of the charge initialisation with 445 nm pulse length. If the charge-initialisation-laser would drive a direct transfer of charge to the centre, the effect would follow a saturation law, as only two electronical levels would be involved. However, in the present case the 445 nm radiation promotes the charge state of the divacancy from neutral to negative and the hole state decays exponentially due to the recombination with the electron from the SnV^{2-} centre. This is similar to the situation of optical pumping below saturation presented in sec. 2.2.

5.4 Extension of the charge cycle to other G4V centres

The charge cycle model that is derived in the last section should be generally valid for all G4V centres, since they share the same basic level structure and differ only in the absolute position within the diamond band gap [100]. It is also consistent with blinking and spectral jumps reported for SiV^- centres and GeV^- centres [129, 193]. We therefore repeat the fluorescence enhancement measurement on a PECVD grown sample containing ensembles of SiV^- centres at a temperature of 3.3 K. We resonantly excite the dense ensemble of SiV^- centres on the C-transition with a cw tunable TiSa laser and add the second light field retrieved from the super continuum laser source (Fig. 5.8). As expected, the enhancement of fluorescence follows a very similar shape as for the ensemble of SnV^- centres and increases strongly for photon energies of the second radiation field in excess of 2.4 eV. The region above 2.8 eV cannot be accessed in this experiment due to the employed optics, since it is conducted in a different optical setup. Comparing the measurement for SiV^- centres and SnV^- centres, it is striking that the enhancement factor for SiV^- centres seems to be lower. This is caused by a higher resonant laser power being used, which we anticipate to be sufficiently high for driving the (0/-) divacancy charge transition in a two-photon absorption process as mentioned also for the SnV^- centre. However, we reliably observe enhancement factors larger than 10 in the case of lower resonant power and a 445 nm charge stabilisation laser being applied. In contrast to the SnV^- centre, the fluorescence of the SiV^- centre is usually not completely terminated when being resonantly

excited. Nevertheless, the count rate of single SiV^- centres especially in pure crystal environments such as electronic grade diamond is typically very low and requires a charge repump laser [36, 104], which is consistent with residing considerable amounts of time in the SiV^{2-} dark state. A possible reason for the weak but remaining fluorescence is that the lowest energy state of the SiV^{2-} centre is situated in the valence band [100], where, in contrast to the case of the SnV centre, a dynamic electron capture and release can occur. In the same measurement conducted above, we confirm the presence of the higher lying excited state of the SiV^- centre, which was reported in [172] and is a result of excitation from a defect level with a_{2u} symmetry lying within the valence band. This is the equivalent for the SiV^- centre of the higher lying excited state that we observe for the SnV^- centre in sec. 4.4. In the measurement conducted here, the resonance lies centered around 551(3) nm (2.25(1) eV) with a FWHM of 69(7) nm (280(30) meV). The central peak position agrees resonably well with the findings in [172], while the FWHM is narrower due to homogeneous phonon broadening beeing reduced in the cryogenic regime the measurement in our work is conducted in. This linewidth reduction by a factor of 1.43 is of similar strength as the factor 1.58 observed for the SnV^- centre in sec. 4.4.

Chapter 6

Optical and spin coherence of charge stabilised SnV^- centres

Contributions and copyright notice

The experiments conducted in this chapter were carried out under the supervision of C.B.. The same HPHT samples as in the previous chapters are investigated in the same optical setup. J.G. and D.He. conceived the measurements and the analysis of the data with input from P.F.. The theoretical model used for simulation of the population dynamics of the SnV^- centre was implemented by J.G. and A.M.F..

Within the first section of this chapter, the optical coherence of charge stabilised SnV^- centres is explored. This includes resonant autocorrelation measurements, revealing the single photon emission character as well as the decay of coherence visible in Rabi oscillations between orbital ground and excited states. The polarisation state of the absorption dipole of the C-transition is investigated by resonant polarisation dependent absorption spectroscopy. The optical coherence of this transition is probed by measuring the linewidth of the transition in a low power regime and compared to the lifetime limit. This measurement is complemented by long term PLE scans, revealing the stability of the resonance over time with and without electron capture occuring. The section finishes with pulsed Rabi measurements in between the orbital ground and excited state.

The second section is dedicated to the spin coherence and spin state readout of charge stabilised SnV^- centres. In a first step a magnetic field is applied in order to lift the spin degeneracy and the Zeeman splitting is extracted in magnetic field dependent PLE and CPT scans. Building on these results, the influence of decoherence by population decay is quantified in spin lifetime measurements and the cyclicity of the spin-conserving transitions is exploited for implementation of a single-shot spin state readout. Finally, the coherence of the lowest energy ground state spins is probed and quantified using the means of CPT. All experiments throughout this chapter are conducted at a temperature of 1.7 K, if not stated elsewise.

6.1 Single photon emission, optical coherence and excitation dipole

6.1.1 Single photon emission and resonant autocorrelation measurements

The main goal of this chapter is to reveal fundamental properties of charge stabilised SnV^- centres such as e.g. optical coherence between ground and excited states and spin coherence between the spin states of the lowest orbital ground state. A study revealing these figures of merit can thus only be conducted on isolated single SnV^- centres to ensure that any effects resulting from the investigated centres being situated in an ensemble can be excluded. The most simple way of proving that the investigated emitter is a single colour centre, is to excite the SnV^- centre and employ autocorrelation measurements of the stream of emitted photons (see sec. 3.2.4 for details on the employed setup). In this section, we characterise the single photon emission properties of the different emitters that contribute to the manifold characterisation methods used within this chapter. Since the majority of the investigated SnV^- centres are investigated in more than one experiment, we refer to the emitters by the name that occurs in the lab book documentation and data files. This enables the interested reader to refer to specific datasets, which we value higher than the small loss in readability that comes along with it.

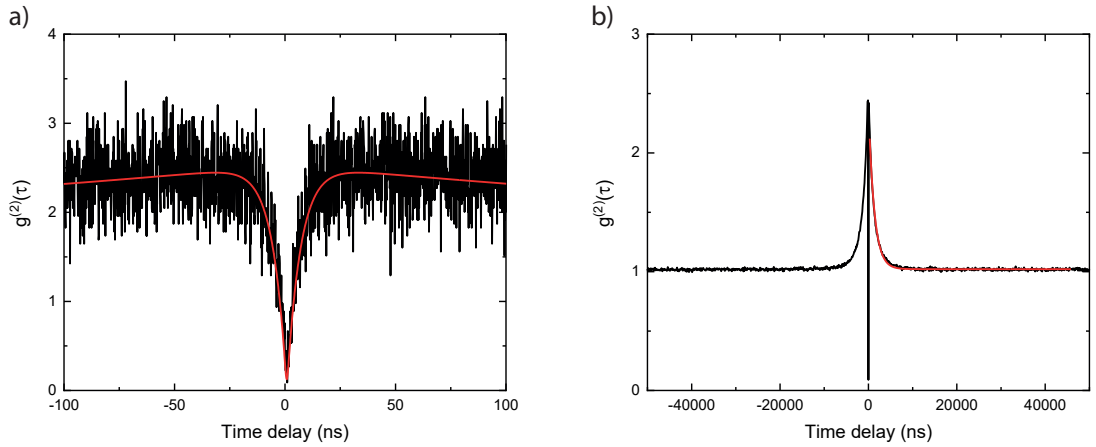

Figure 6.1: **Autocorrelation measurement under off-resonant excitation of emitter EA4: a)** Autocorrelation measurement of the photons of the full spectrum of emitter EA4 under off-resonant excitation at a wavelength of 595 nm and an excitation power of 1.3 mW. The characteristic signature of a single photon emitter is observed as the anti-bunching at zero time delay between the two APDs. The raw data value of $g^{(2)}(0) = 0.13(2)$ demonstrates pure single photon emission as the deviation from zero can be fully explained by the timing jitter of the APDs. **b)** The emitted photons exhibit clear bunching which decays with a time constant of 899(7) ns. The bunching is a result of electron capture and subsequent charge initialisation.

The photons emitted by emitter EA4 under excitation into the phononic ladder states of the excited state with a wavelength of 595 nm, retrieved from the dye laser, show clear antibunching at zero time delay visible as absence of coincidences between the two APDs used in the HBT setup as is displayed in Fig. 6.1. The raw data can be fitted assuming only the timing jitter of the APDs and no additional background, yielding $g^{(2)}(0) = 0.13(2)$. The characteristic bunching, that is a result of the charge dynamics explained in chap. 5

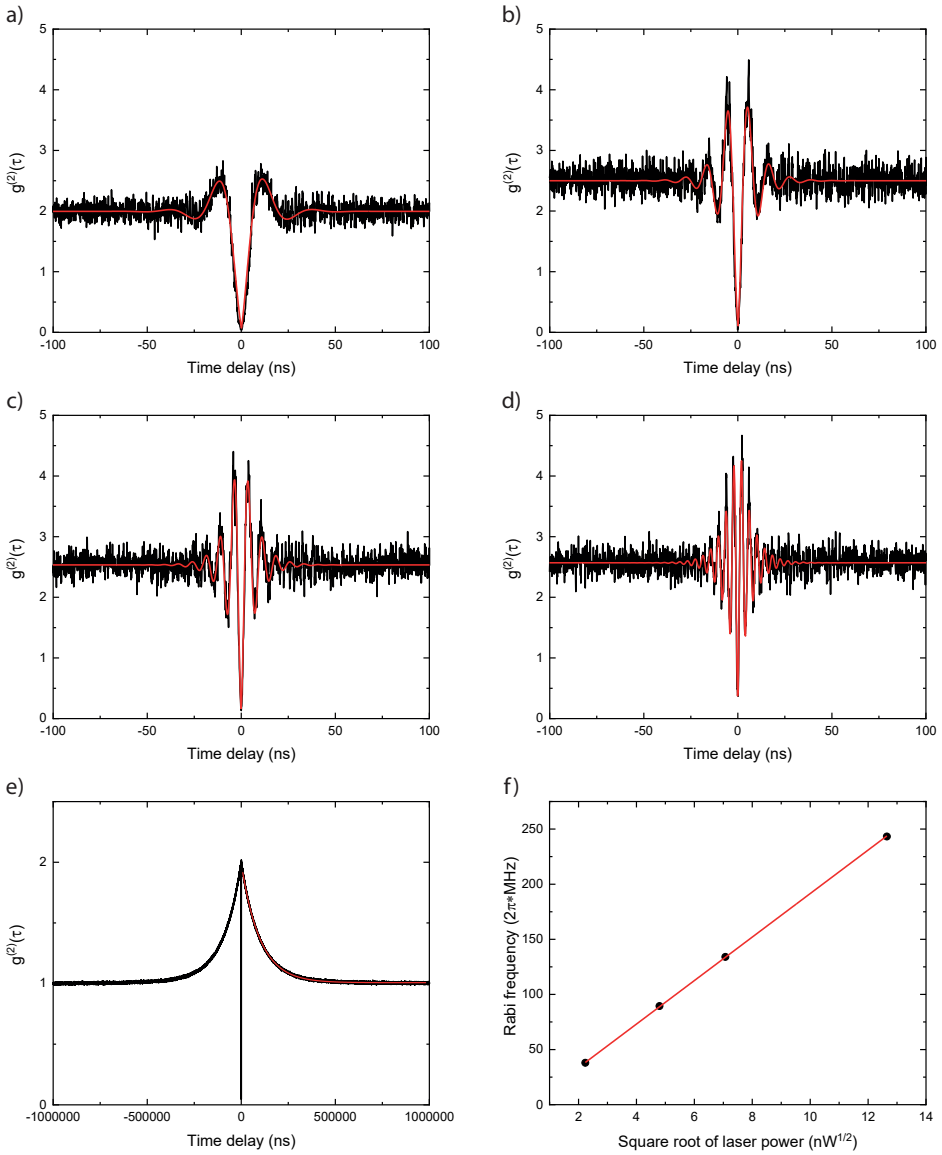

Figure 6.2: **Power dependent resonant autocorrelation measurements:** Autocorrelation of the photons emitted into the PSB by EA27 under resonant excitation (C-transition) for **a)** 5 nW, **b)** 23 nW, **c)** 50 nW, **d)** 160 nW. All graphs correspond to raw data and no background correction is applied. Pure single photon emission is emphasised by the value of $g^{(2)}(0) = 0.06(1)$ for the measurement presented in **a)**. The oscillations that are visible in all graphs are the result of Rabi oscillations between ground and excited state, which are damped by the decay of the coherence induced by the finite excited state lifetime. **e)** Typical bunching for the measurement in **a)**, as a result of the charge stabilisation. The decay time of the bunching for a charge initialisation power of 105 µW amounts to 99.58(6) µs **f)** The Rabi frequency extracted from the resonant autocorrelation measurements obeys the expected linear dependence on the square root of the laser power with a slope of $19.73(9)\,2\pi\,\mathrm{MHz/nW^{0.5}}$.

decays with a time constant of 899(7) ns. The charge initialisation is here resulting from the driving of the divacancy's charge transition in a two-photon process, which is possible below the threshold of 2.4 eV for the 1.3 mW of laser power being used.

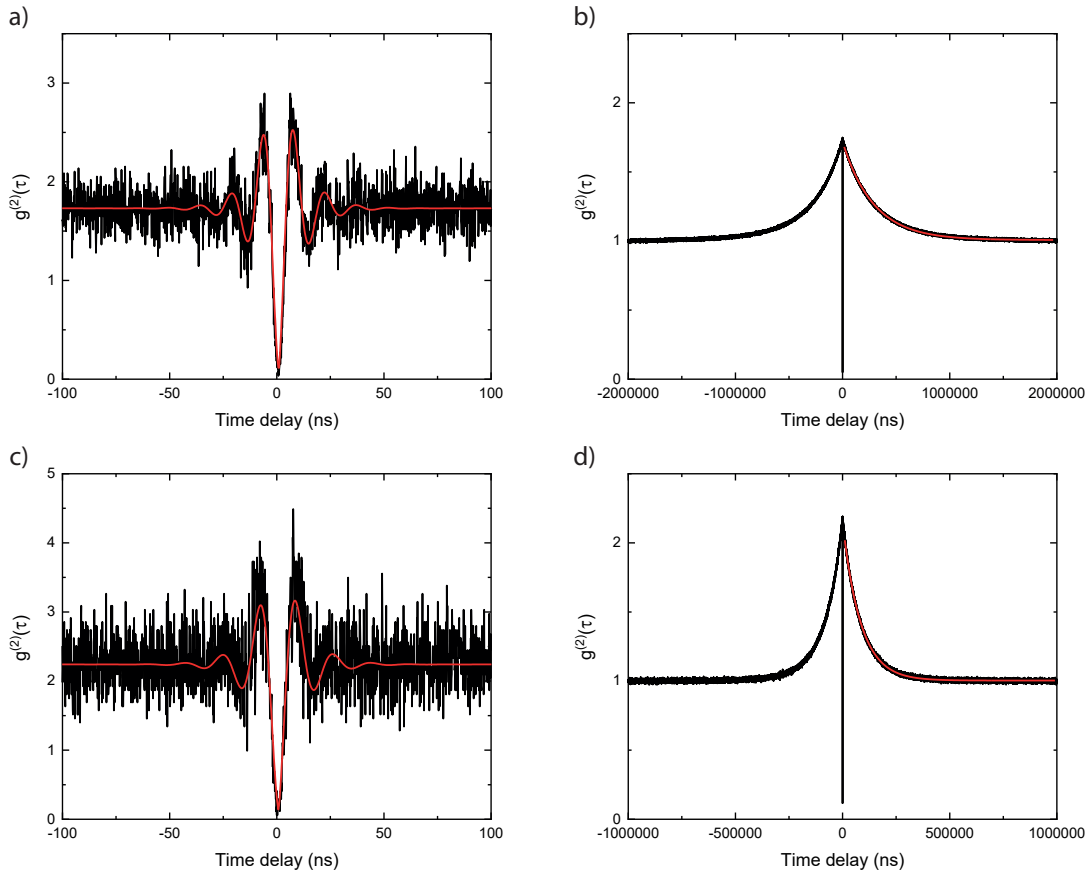

Figure 6.3: **Autocorrelation measurement under resonant excitation of EA11 and EA13: a)** Autocorrelation measurement of emitter EA11 under resonant excitation on the C-transition with a power of 80 nW. Photons emitted into the PSB are correlated and yield $g^{(2)}(0) = 0.08(2)$, which is an indicator of pure single photon emission. Rabi oscillations emphasise the underlying coherent excitation process between ground and excited state. **b)** Bunching of the photon emission decays with a time constant of 290.3(2) µs. The bunching is a result of the charge stabilisation with 60 µW of power. **c)** and **d)** depict the repetition of the measurement for emitter EA13 with a resonant laser power of 100 nW yielding $g^{(2)}(0) = 0.11(4)$. The time constant of the bunching amounts to 84.04(8) µs for a charge stabilisation power of 70 µW.

Since emitter EA4 was characterised before the charge stabilisation mechanism was discovered, the autocorrelation measurement had to be conducted using off-resonant or quasi-resonant excitation. In contrary, the following emitters are characterised using excitation resonant with the C-transition and correlation of the photons emitted into the PSB is used to retrive the autocorrelation function. For emitter EA27, we measure the autocorrelation function for different resonant laser powers, while the charge-initialisation-laser is constantly applied with a laser power of 105 µW. The lowest power experiment (5 nW, Fig. 6.2a)), yields $g^{(2)}(0) = 0.06(1)$, which is indicating very pure single photon emission. The deviation from absolute zero can be explained by the dark counts and the jitter of the APDs. Also in the case of resonant excitation, the autocorrelation data on larger timescales depicted in Fig. 6.2e) demonstrates strong bunching of the photon emission. This effect is again resulting from the electron capture and the subsequent dynamics induced by the

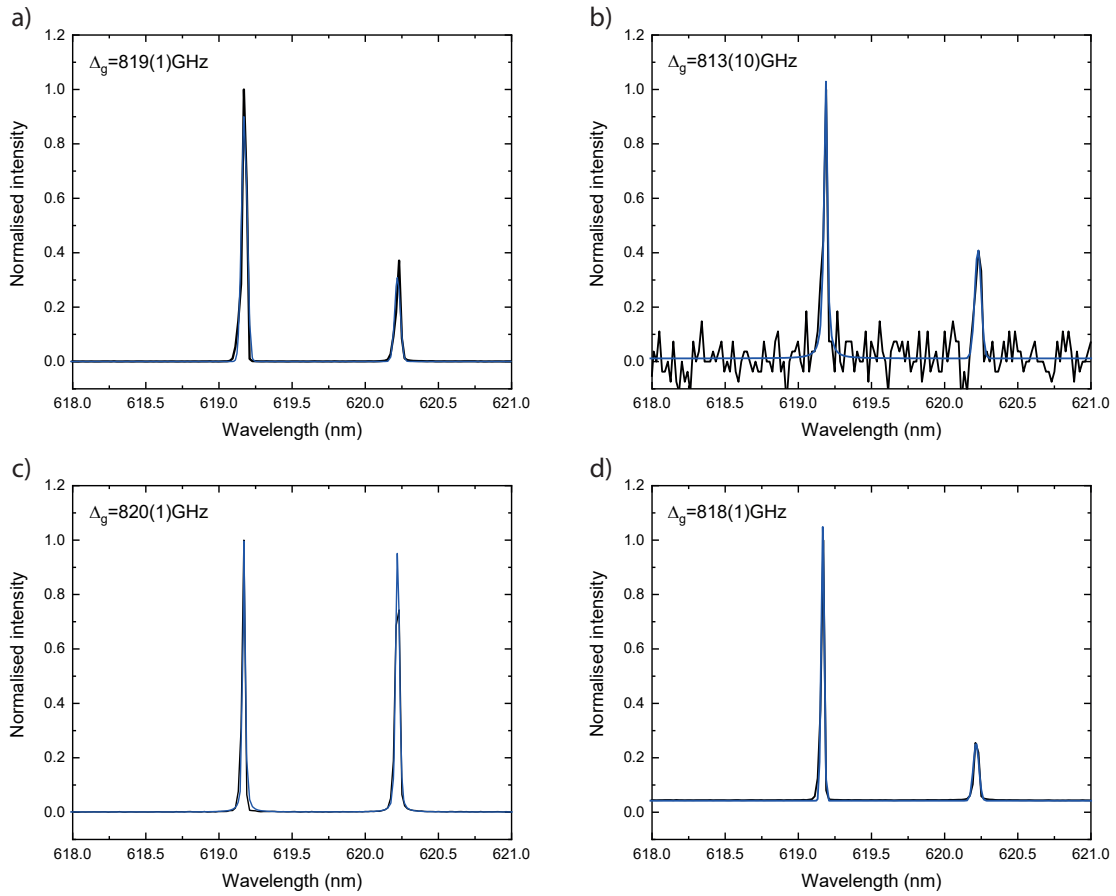

Figure 6.4: **Spectra of single SnV$^-$ centres:** Low temperature spectra of the fine-structure of single SnV$^-$ centres yield a ground state splitting of **a)** 819(1) GHz for emitter EA27, **b)** 813(10) GHz for emitter EA30, **c)** 820(1) GHz for emitter EA13 and **d)** 818(1) GHz for emitter EA11.

completion of the charge cycle explained in chapter 5. The time scale of the decay determined by the applied charge stabilisation laser power is 99.58(6) µs. Compared to emitter EA4, this is significantly shorter due to the laser power used for charge stabilisation being two orders of magnitude lower.

As it can be seen in each of the four detailed resonant autocorrelation measurements in Fig. 6.2, the dip resulting from antibunching is surrounded by decaying Rabi oscillations. These oscillations prove the coherent nature of the resonant excitation process, which are damped due to the decaying coherence of the excited state due to spontaneous photon emission. As it is theoretically expected (see sec. 2.2), the frequency of the Rabi oscillations increases linearly with the square root of the excitation laser power (Fig. 6.2f)). The slope of this increase amounts to 19.73(9) 2π MHz/nW$^{0.5}$.

We repeat the resonant autocorrelation measurements for two further emitters, employing a resonant laser power of 80 nW (100 nW) and a charge stabilisation laser power of 60 µW (70 µW) for EA11 (EA13). The emitted photons show strong antibunching, yielding $g^{(2)}(0) = 0.08(2)$ ($g^{(2)}(0) = 0.11(4)$), with the disparity from zero being explained by the dark counts and the jitter of the APDs. The charge stabilisation results also for these emitters in pronounced bunching of the photons, which decays with a time constant

of 290.3(2) µs (84.04(8) µs). It has to be emphasised that the values of the laser power used for the emitters EA11 and EA13 cannot be directly compared to the measurements conducted on EA27 and EA30 since the optical setup was improved in between the measurement runs. Therefore, the excitation and collection in the experiments with EA27 and EA30 is about a factor of 5 more efficient. Due to technical reasons, no autocorrelation of the photons being emitted by emitter EA30 is measured. However, the presence of only one narrow C-transition in PLE scans and only one dark resonance in CPT scans, which is demonstrated in the course of this chapter, as well as the geometrical isolation of the emitter in the sample are clear indicators that also EA30 is a single SnV^- centre.

6.1.2 Spectra

As a further highlight of the homogeneity obtained in the HPHT samples, this section compares the spectra at 1.7 K of the investigated emitters in Fig. 6.4. The ground state splittings as an indicator for strain imposed on the emitters in sample NI58 are 819(1) GHz (EA27), 813(10) GHz (EA30), 820(1) GHz (EA13) and 818(1) GHz (EA11). Within the margin of error, all of these ground state splittings overlap, which is a strong indicator that the strain within this sample is at least very homogeneously distributed. More likely the result of the HPHT annealing creates a marginally strained environment, thereby leaving the SnV^- centres for the most part unaffected by crystal strain, which is in agreement with the findings reported in sec. 4 within this thesis. We therefore suspect that the unstrained ground state splitting of the SnV^- centre is most likely determined by the average of these splittings amounting to about 818 GHz which is smaller than reported in literature [113, 176].

6.1.3 Excitation polarisation

In sec. 4.2.3, we characterised the absorption polarisation states of single SnV^- centre of the higher lying excited state. This section extends the characterisation to the resonant absorption dipole on the C-transition. The experiment is performed in a similar way as for the excitation of the A_{2u} state, the only difference is that the quarter wave plates are no longer necessary due to utilising improved optics. In a first step, the resonance frequency is determined in a PLE scan and subsequently the laser is stabilised to it using feedback from the wavemeter. While keeping the excitation power fixed, we send the excitation laser through a polariser in order to guarantee a linear polarisation state and rotate this state employing a HWP. For each position of the HWP, we record the count rate emitted into the PSB averaged over 10 s. The resulting dipoles for EA27 and EA13 are depicted in Fig. 6.5 and show a linear absorption dipole with high visibilities of 88 %, respectively 93 %. The visibilities are most likely limited by saturation effects and potentially by contributions of orthogonal dipoles being collected with the large NA objective. The axes in these graphs are not aligned to the axes of the sample as in sec. 4.2.3, but as every investigated emitter in the HPHT samples showed the same resonant absorption polarisation behaviour with high visibilities and the same or orthogonal direction, we assume the alignment of the dipole axis to be along the <111> axis.

6.1.4 Lifetime limited linewidth

The majority of protocols in QIP depends on the availability of indistinguishable photons from different quantum nodes that interfere at a beam splitter. This two-photon interference is diminished, as it is explained in sec. 2.3, by spectral diffusion and pure dephasing.

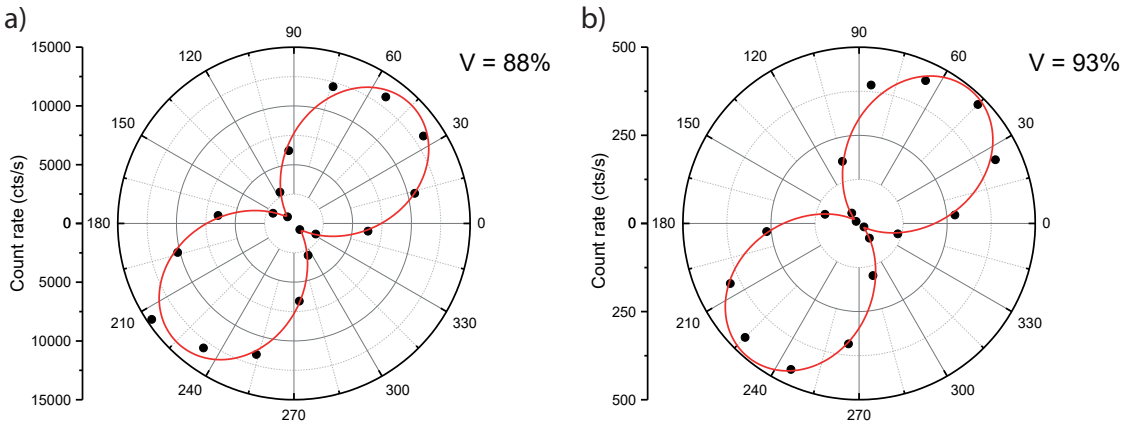

Figure 6.5: **Resonant absorption diople of single SnV$^-$ centres:** Measurement of the absorption dipole of emitter **a)** EA27 and **b)** EA13 under resonant excitation on the C-transition. The linear polarisation state of the inciding laser beam is rotated by a HWP and the count rate emitted into the PSB of the emitter is recorded and averaged over 10 s. Both emitters exhibit a linear absorption dipole with high visibilities.

Therefore, the first step on the road towards retrieving indistinguishable photons from a SnV$^-$ centre is the measurement of the transition linewidth. For an undisturbed, perfect system the linewidth is fully determined by the lifetime of the excited state as a cause of the quantum mechanical uncertainty principle. The spectrum is then called to be Fourier, lifetime or transform limited with linewidth ν_{FL}. For this reason, we measure the lifetime of the excited state of a EA4 by employing TCSPC. The excitation pulse at 532 nm is retrieved from the supercontinuum laser source. The excited state decays with a time constant of $\tau = 7.61(3)$ ns, which corresponds to $\nu_{\mathrm{FL}} = \frac{1}{2\pi\tau} = 20.9(1)$ MHz, see Fig. 6.6a). Subsequently, we use a resonant excitation power of 200 pW far below saturation, which is sufficiently low that electron capture does not occur in a single scan even though we do not apply a charge stabilisation laser. We scan this laser across the resonance of the C-transition and collect photons being emitted into the PSB. The resulting linewidth is 18(3) MHz, which is agreeing well with the lifetime limited linewidth within the margin of error. We therefore conclude that SnV$^-$ centres with lifetime limited linewidths can be found in HPHT samples. In [176], the authors report a mean linewidth of 57(17) MHz across several single centres in a LPLT annealed sample, while the linewidths found in [242] exceed 200 MHz in a similar sample. In the HPHT samples that are investigated throughout this thesis, the mean transition linewidth is about 31 MHz and almost no emitter with a linewidth larger than 35 MHz can be found, with or without charge stabilisation being applied. This is a further emphasis of the advantageous optical properties of SnV$^-$ centres in a diamond sample subject to HPHT annealing.

6.1.5 Long-term stability of optical resonances

While linewidths of single SnV$^-$ centres that are purely lifetime limited are presented in the previous section, it is important to keep in mind that this is a single-shot experiment. In any QIP application, the linewidth and line position needs to be stable over the course of hours and under the influence of a charge stabilisation laser being applied. We therefore conduct repeated PLE scans across the C-transition of single SnV$^-$ centres in sample NI58 and BOJO_001, thereby probing the linewidth and line position for the duration of up to

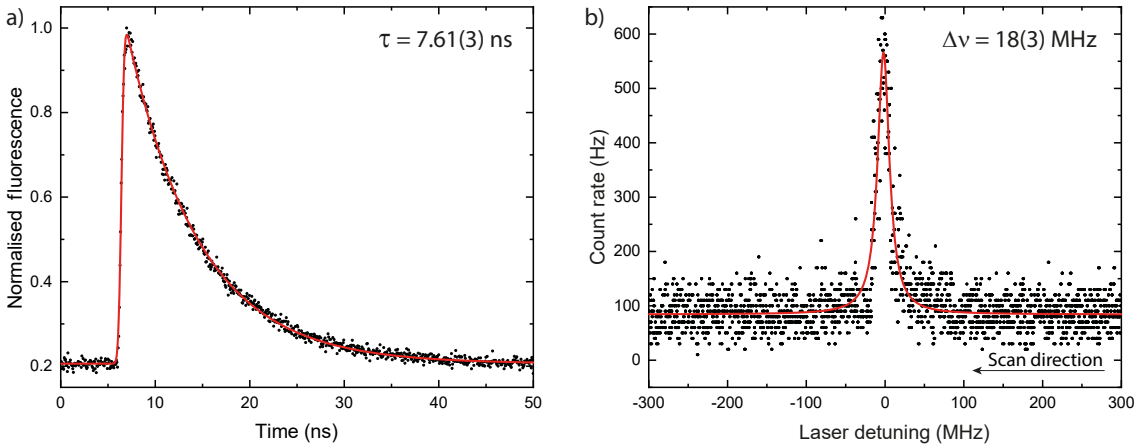

Figure 6.6: **Lifetime limited linewidth of a single SnV$^-$ centre: a)** TCSPC of a single SnV$^-$ centre, excited by laser pulses at a wavelength of 532(10) nm retrieved from the supercontinuum laser source. The lifetime of the excited state amounts to 7.61(3) ns, corresponding to a lifetime limited linedwidth $\nu_{\mathrm{FL}} = 20.9(1)$ MHz. **b)** Resonance scan at an excitation power of 200 pW across the C-transition of the same emitter, while collecting photons being emitted into the PSB. The linewidth is determined to be 18(3) MHz in excellent agreement with the Fourier limit.

an hour. It is important to distinguish two cases: The low and the higher power regime, defined by comparing the excitation power to the saturation power of the emitter. In a low power regime ($P \ll P_{\mathrm{sat}}$), electron capture will occur very rarely while the linewidth is almost not influenced by power broadening and therefore small spectral shifts can be resolved. This setting is suitable for quantifying the effect of spectral diffusion induced by the charge stabilisation laser itself. The latter impacts the charge environment, even in the case of no electron capture of the SnV$^-$ centre occuring, by excitation or ionisation of surrounding defects. These processes could introduce changes in the resonance position due to second-order Stark shifts [196, 197], see also sec. 2.1.6. In Fig. 6.7a) we measure the influence of the continuously applied charge stabilisation laser on the central frequency and linewidth of the C-transition for EA27 over 1 h with an excitation power $<$500 pW being a factor of four below the saturation power. The probability of electron capture in each line scan can be calculated from the time the excitation laser addresses the resonance within its FWHM, the extrapolation of the electron capture rate towards lower power (Fig. 5.3) and taking into account the lower excited state population at excitation powers below saturation. It amounts to about 20 % and thus in most of the scans presented in Fig. 6.1.5 no electron capture will occur. The resonance stays remarkedly stable over time, with the peak position exhibiting a standard deviation as low as 4(2) MHz. The summed spectrum over the full hour is broadened to 33 MHz in comparison to a lifetime limited linewidth of $\nu_{\mathrm{FL}} = 25$ MHz.

In the higher excitation power regime ($P \approx 5P_{\mathrm{sat}}$), we ensure that electron capture is continuously occuring in every single scan (more than 99 % probability that electron capture occurs more than 5 times per scan), while keeping the impact of power broadening as small as possible. The difference between the two experiments is that for the SnV$^-$ centre undergoing one full charge cycle the equilibrium of nearby charges set by the 445 nm laser is disturbed. Since the hole that is captured in step IV of the charge cycle can result from a different divacancy in each turn, the near-scale charge environment can potentially be changed. We therefore expect larger fluctuations in the resonance position for this setting.

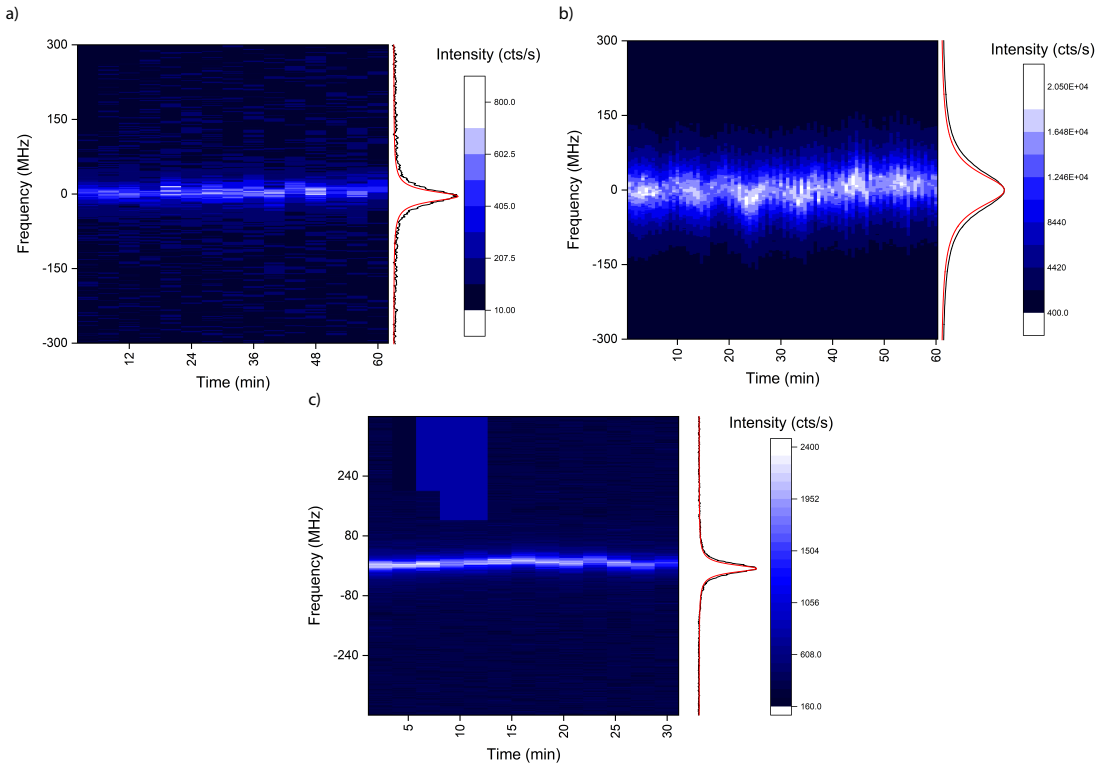

Figure 6.7: **Long-term stability of the optical resonances of single SnV^- centres: a)** Low excitation power (<500 pW) long-term PLE scan on emitter EA27 with a continuously applied charge stabilisation laser. The excitation power is chosen such that electron capture is highly unlikely to occur during the measurement and the linewidth is almost not subject to power broadening. The central frequency of the C-transition remains stable up to a standard deviation of 4(2) MHz throughout one hour. On the right side the comparison of the summation of all scans with a width of 33(2) MHz (black) and a Lorentzian (red) with a width corresponding to $\nu_{FL} = 25$ MHz is depicted. **b)** Repetition of the measurement on EA30 with an excitation power of 10 nW, ensuring electron capture within every scan, while limiting the effect of power broadening as much as possible. The charge state is actively stabilised throughout the whole measurement. The standard deviation of the shifts in the central resonance frequency is 10(2) MHz. On the right side the sum over all scans with a width of 103(2) MHz (black) is compared to a Lorentzian with a width corresponding to the power broadened linewidth of a single scan of 88 MHz. The small oscillatory shifts in the central frequency with a period of about 10 min are introduced by the air conditioning in the laboratory. **c)** Repetition of the measurement on EB1 in sample BOJO_001, using an excitation power of 1 nW and a slow scan rate that makes electron capture very probable in each scan. The centre frequency remains stable up to a standard deviation of 6(2) MHz over half an hour and the width of the summed scans is 31(2) MHz (black curve on the right) in comparison to 25(5) MHz of a Fourier limited Lorentzian (red curve on the right).

This experiment is conducted on EA30, as EA27 was no longer accessible due to malfunctioning of the used piezo positioners. As it is displayed in Fig. 6.7b), the resonance position remains stable up to a standard deviation as low as 10(2) MHz even for the case of continuous electron and subsequent charge-initialisation-laser induced hole capture over a full hour with an excitation power of 10 nW. The width of the summed spectrum amounts

to 103(2) MHz, while the power broadened linewidth of a single scan exhibits a width of 88 MHz. In the long-term graph it is furthermore possible to identify small oscillations in the central resonance frequency with a period of about 10 min. This timescale matches the cycle of our air conditioning in the laboratory. We identify the cause of these shifts by tiny alterations in the position of the blue laser focus on the sample with respect to the SnV^- centre. This effect can be also seen when slightly misaligning one mirror axis of the 445 nm laser path and is most likely caused by a spatial asymmetry in the charge distribution of the divacancies. In further experiments this effect can be used as a frequeny shift mechanism with a tuning range of a few tens to hundreds of MHz. This range is limited by non-perfect charge initialisation for a significantly misaligned charge-initialisation-laser, resulting in blinking of the fluorescence.

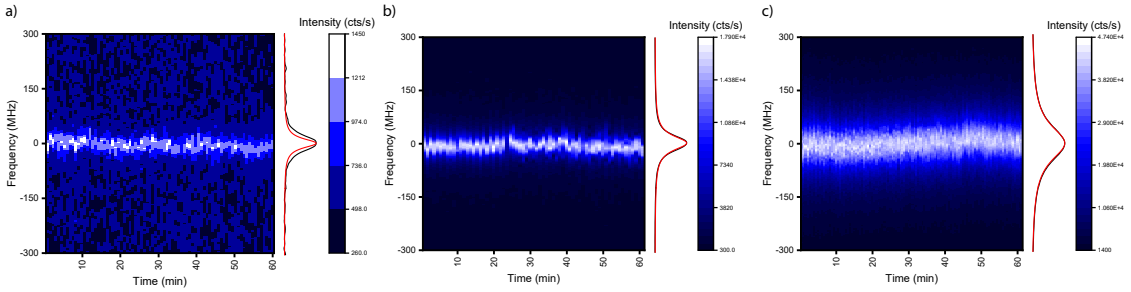

Figure 6.8: **Different excitation power regimes of long-term PLE:** We repeat the measurements conducted on the previous emitters on E1NI58 and highlight the different excitation power regimes. We choose the power to amount to **a)** $P = \frac{P_{sat}}{30}$, **b)** $P \approx P_{sat}$ and **c)** $P = 7P_{sat}$. In all three cases the resonance line stays remarkably stable over time and the sum over all scans is almost coinciding with the lifetime limited (**a**) respectively the average single scan linewidth (**b,c**).

In Fig. 6.7c) we repeat the experiment for a single emitter in sample BOJO_001 with an excitation power of 1 nW ($\approx P_{sat}$) and a slow scan speed, which leads to a probable electron capture within each scan. The line centre exhibits a standard deviation of 6(2) MHz over half an hour and the width of the sum over all scans is 31 MHz, slightly broader than the lifetime limited linewidth of 25(5) MHz. The large error bar is a result of the estimation of the lifetime from an autocorrelation measurement.
The high and low power measurements in sample NI58 were conducted on two different emitters, however, most of the SnV^- centres exhibit remarkable stable resonance lines. In Fig. 6.8 the long-term stability of the resonance position of emitter E1NI58 is depicted for an excitation power far below (factor 30), almost equal to (≈0.8) and above (factor 7) saturation power. Also here we see that the resonance lines are very stable over time. Concluding from this set of measurements on arbitrary emitters that were not preselected, we find that the charge initialisation of SnV^- centres in HPHT samples is a remarkable tool in order to obtain long-term stable, (close to) lifetime limited linewidths from single SnV^- centres. These results are in stark contrast to the frequency jumps for not perfectly charge stabilised SnV^- centres observed in [195, 197].
Regarding the application in QIP, we can deduce a two-photon HOM interference visibility from the measurement in Fig. 6.1.5a). We therefore assume that we either take two photons emitted by the same SnV^- centre but with an arbitrary, up to one hour long, time delay between the excitation times and overlap them at a FBS as described in sec. 2.3. Alternatively, the same visibility can be achieved taking two photons being emitted by two SnV^- centres that exhibit the same inhomogeneous broadening over time. The two cases

are equivalent, if the timescale τ_{SD} of the spectral diffusion correlation is way smaller than the time separation of photons which are brought to interference. This is a reasonable assumption, since charge fluctuations in the diamond lattice are typically very short lived. Using equation 2.97 with the parameters $\tau_r = 6.4\,\text{ns}$, $\sigma_0 = 6.7\,\text{MHz}$ (corresponds to the summed scan Voigt linewidth of 33 MHz being deconvoluted into a FWHM of 15.8 MHz for the Gaussian and 25 MHz for the Lorentzian part), $\Gamma \approx 0$, $\tau_{AE} = 0$, $\tau_{MZI} \gg \tau_{SD}$ and $\delta_t \approx 0$, we find a visibility of 89.4 %. This value is also in agreement with the findings in [231]. We would like to point out that such high visibility TPI is a crucial prerequisite for entangling two remote SnV^- centres and therefore of significant importance in QIP applications. It is also valid to assume that such two emitters being weakly affected by spectral diffusion can be identified in the samples as we here have demonstrated the long-term stability for three arbitrarily chosen SnV^- centres.

6.1.6 Pulsed Rabi oscillations

The Rabi oscillations observed in the autocorrelation measurements in sec. 6.1.1 are indicating the coherent excitation process upon addressing the C-transition on resonance. However, exploitation of this coherence in the experiment is only feasible when using optical pulses tailored such that a defined rotation on the Bloch sphere is implemented, e.g. a π-pulse. To this end we apply 100 ns long optical pulses resonant with the C-transition of emitter EA13 and collect the photons emitted into the PSB. As it can be seen in Fig. 6.9, Rabi oscillations between the lower orbital ground and excited state are induced by the optical pulse. We conduct this measurement for five different optical powers ranging from 300 nW up to 901 nW and find, as in the case of the autocorrelation measurements, that the Rabi frequency increases linearly with the square root of the excitation laser power. The slope of the increase amounts to $5.5(2)\,2\pi\,\text{MHz/nW}^{0.5}$. Even though Rabi oscillations are induced by the
optical pulses, their several nanoseconds long risetime induced by the used AOM (see sec. 3.2.2) is too slow to prevent significant overlap with the decoherence induced by the decay of the excited state due to its finite lifetime. Therefore, in order to achieve high fidelity π-pulses, amplitude modulation of optical pulses with an EOM will be required in future experiments.

6.2 Spin coherence and spin readout

6.2.1 Zeeman splitting

When applying a magnetic field, the degeneracy of the spin states of the SnV^- centre is lifted, which is described in detail in sec. 2.1.3. The four transitions between orbital states of the fine-structure split up into sixteen lines, eight of which correspond to SC transitions between levels of the same spin projection, while the other eight are SF transitions between states of orthogonal spin state projection. In a purely atomic system, the latter one are typically dipole forbidden, while for a colour centre like the SiV^- centre in diamond even at moderate magnetic field strengths and relatively small angular deviations between the symmetry axis of the defect and the magnetic field direction the impact of SF transitions on the spin dynamics is significant [36] as spin mixing occurs. For the SnV^- centre, we find a somewhat intermediate state between those situations. When only applying a magnetic field, the charge stabilisation and the resonant excitation laser, the PLE signal decreases with increasing field strength until it vanishes completely as soon as the SC transitions no longer overlap. This effect can be explained exemplarily for scanning the laser across

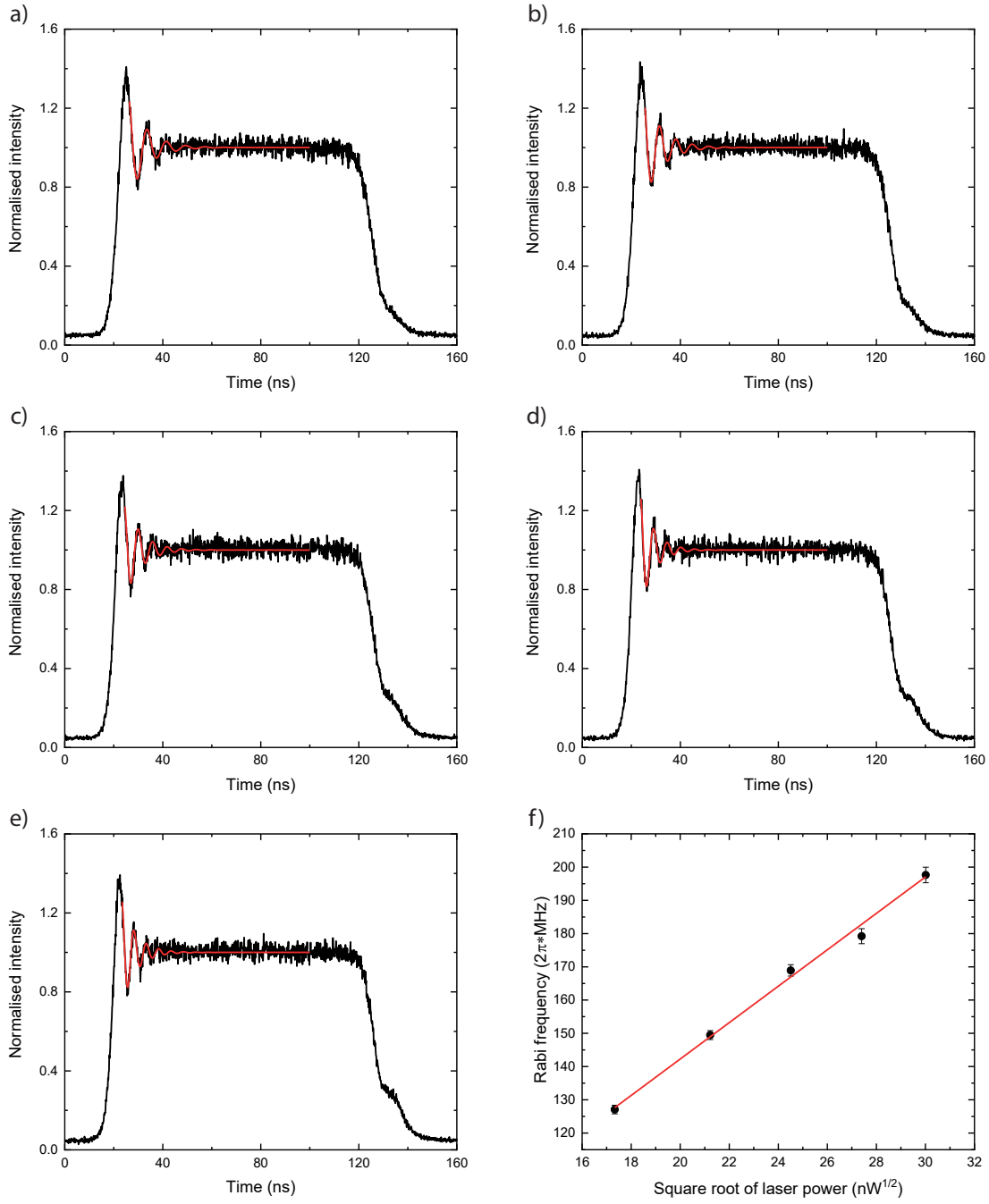

Figure 6.9: **Pulsed Rabi oscillations of emitter EA13:** Fluorescence response of emitter EA13 under power dependent pulsed excitation resonant with the C-transition. The resonant cw laser power is **a)** 300 nW, **b)** 450 nW, **c)** 601 nW, **d)** 751 nW and **e)** 901 nW. **f)** The Rabi frequency extracted from the individual measurements obeys the expected linear dependence on the square root of the laser power with a slope of $5.5(2)\,2\pi\,\mathrm{MHz/nW^{0.5}}$. The charge stabilisation laser power amounts to 200 µW for all experiments.

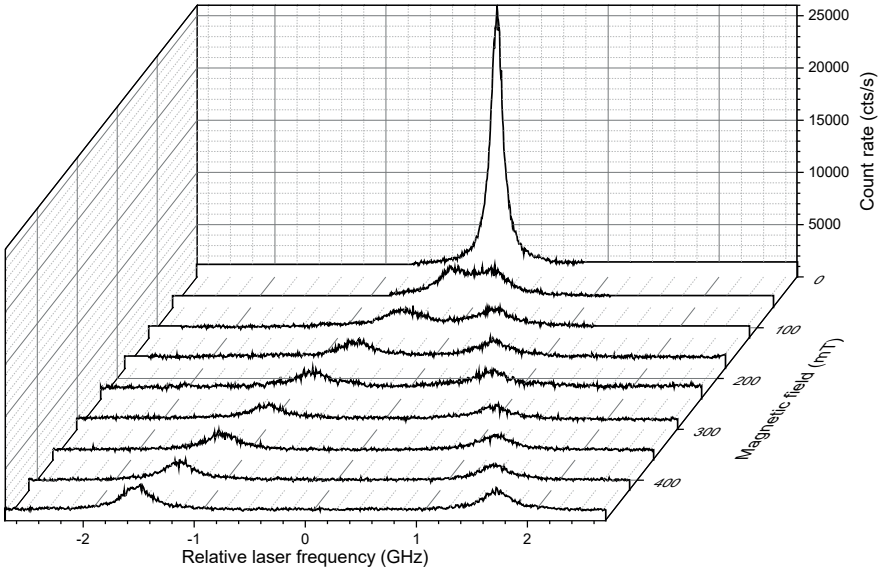

Figure 6.10: **Photoluminescence excitation scan of Zeeman split SC transitions:** For each applied magnetic field, the laser is scanned across the SC transitions A1 and B2 of emitter EA27. The applied charge stabilising laser is complemented by a repump laser at 532 nm which mitigates the effect of optical pumping to long-lived orthogonal spin states, as explained in the main text. The SF transitions cannot be observed due to a very low photon scattering probability.

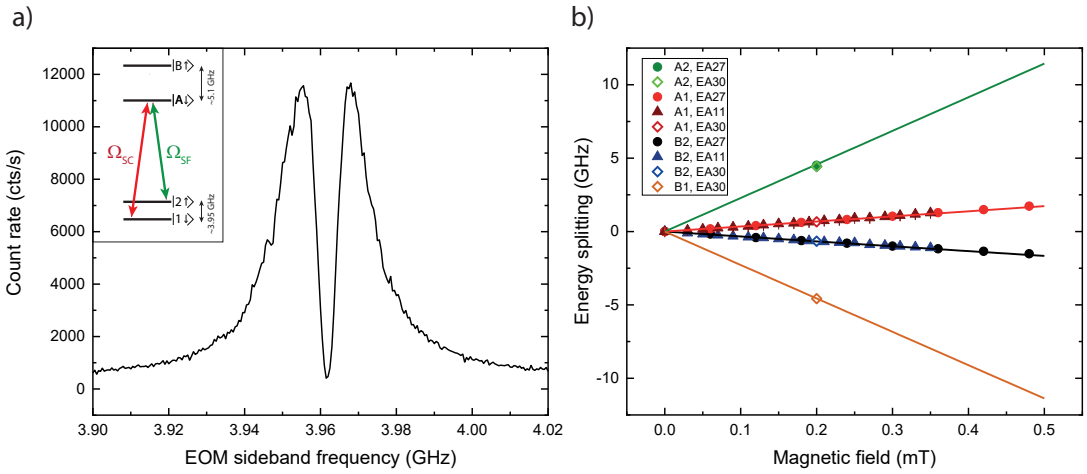

Figure 6.11: **CPT and Zeeman splitting of single charge stabilised SnV^- centres:** **a)** The laser carrier frequency is resonant to the SC transition A1 while the frequency of the EOPM sideband is scanned across the dark resonance of emitter EA30 at a magnetic field of B = 200 mT. The two peaks correspond to the dressed states introduced by the laser carrier while the dip at about 3.96 GHz is the dark resonance created by the sideband being resonant with the SF transition A2. **b)** The energy splittings extracted from the PLE and CPT measurements on EA27 and EA11 for different magnetic field strengths are depicted. For a fixed magnetic field strength of 200 mT the four transitions extracted for EA30 are inserted. The data is fitted using the model designed in [99], yielding a JT contribution of 5.1 % to the ground state and 50 % to the excited state splitting.

one of the SC transitions, e.g. transition A1. After a certain number of excitation and deexcitation cycles, a single decay event on the weaker SF transition A2 will flip the spin state. Since the spin state lifetime is on the order of milliseconds (will be explored in detail in sec. 6.2.2), the population of the SnV^- centre will reside for most of the time in state $|2\uparrow\rangle$. Consequently, almost no fluorescence can be observed. To overcome this problem we add a weak quasi-resonant repump laser at 532 nm, which leads to a finite amount of population in both states $|1\downarrow\rangle$ and $|2\uparrow\rangle$ due to optical pumping. Therefore, the Zeeman splitting of the SC transitions can be observed in PLE scans and is depicted in Fig. 6.10 for emitter EA27. However, the SF transitions cannot be measured directly, which we attribute to the fact that as soon as the SnV^- centre is excited on one of the SF transitions, the subsequent decay will be most likely on the corresponding SC transition and the centre is in a dark state. A reliable way of finding these SF transition is to apply two laser frequencies in a CPT scheme. We therefore set the laser carrier resonant to the SC transition A1, scan the sideband generated by the first harmonic of an EOPM across the SF transition A2 and collect photons emitted into the PSB. A characteristic CPT signal measured on EA30 is depicted in Fig. 6.11a). The two peaks correspond to the dressed states introduced by the laser on A1 and probed by the scanned sideband. The dark resonance at the centre determines the separation of $\Delta_{\uparrow\downarrow} = 3.96\,\mathrm{GHz}$ between the two spin ground states at a magnetic field of $B = 200\,\mathrm{mT}$ and an angle of 54.7° between the field axis and the symmetry axis of the centre. The shown data is averaged over 10 scans at a total laser power of 150 nW and a microwave power of −5 dBm amplified by about 32 dBm before being applied to the EOPM. In Fig. 6.11b), the extracted energy splittings of the SC transitions for EA27 and EA11 and the energy splitting of the SF transition obtained by CPT of EA27 are depicted. Furthermore, all splittings for EA30 at a fixed magnetic field strength of $B = 200\,\mathrm{mT}$ are shown. It is remarkable how well the transition frequencies of three randomly chosen emitters overlap, another sign of the advantageous homogeinity within HPHT treated samples. We fit the data using the SiV^- centre model implemented by C. Hepp et al. in [99], which we modify for the parameters of the SnV^- centre. The result is depicted in Fig. 6.11b). From the fit we extract a contribution of the JT effect of 5.1 % to the ground state splitting, while 94.9 % are introduced by the SO coupling. For the excited state 50 % of the splitting are due to the JT effect and 50 % due to spin orbit coupling. The tendency of stronger JT contribution within the excited state and a lower impact within the ground state agrees with the results reported in [176]. However, the JT contribution observed within this thesis is significantly stronger. It has to be emphasised, that the simulation cannot distinguish between the JT effect and the impact of strain induced by the large tin atom itself [99, 100]. Since we are confident that the diamond lattice itself is predominantly unstrained, we claim that the tin atom itself will give rise to the dominant strain contribution. This point is strengthend by the identical Zeeman splittings of three different emitters. On the contrary, in [176] the SnV^- centres are situated in an environment strained by still prevalent implantation damage and furthermore strain induced by nanofabrication of pillar structures. This strain can possibly counteract the JT effect or strain induced by the tin atom itself and thereby lead to different results of JT, respectively strain, contribution in ground and excited state.

6.2.2 Spin lifetime

The total spin coherence is determined by the decay of population between the spin states as well as effects such as fluctuating magnetic fields that affect only the phase of a coherent superposition. In order to determine the influence of these effects, we start by measuring the spin state lifetime T_1 for the lowest orbital ground state at a temperature of 1.7 K.

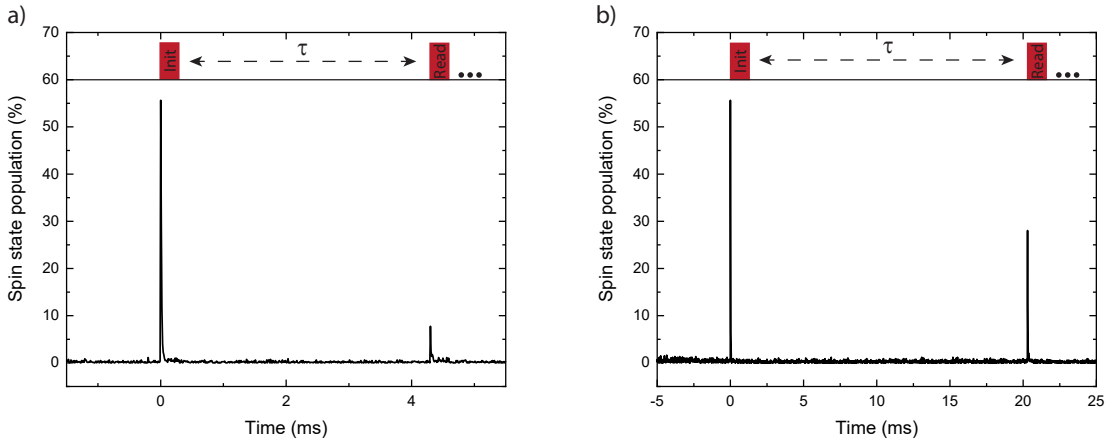

Figure 6.12: **Recovery of thermal spin state population:** The initialisation pulse resonant with the A1 transition initialises the spin state population in state $|2\uparrow\rangle$ via optical pumping. The height of the fluorescence response caused by this peak is used for normalisation to the spin state population in the thermal equilibrium. After exemplary waiting times of **a)** $\tau = 4\,\mathrm{ms}$ or **b)** $\tau = 20\,\mathrm{ms}$ the read pulse (resonant with A1) reads out the population decayed back into state $|1\downarrow\rangle$.

This is implemented by firstly applying a laser pulse resonant with the SC transition A1 and thereby initialising the spin state through optical pumping in state $|2\uparrow\rangle$. After a waiting time τ a second laser pulse resonant with transition A1 reads out the amount of population that decayed back to state $|1\downarrow\rangle$. The pulse sequence ends with a long waiting time of about 1 s, ensuring the return to a thermal equilibrium spin state population. The fluorescence response caused by the initialisation laser pulse is used as a normalisation for the population read out with the read laser pulse, see Fig. 6.12. It corresponds to a theoretically calculated value of 55.63 % of the total spin population in state $|1\downarrow\rangle$ for the given state splitting between $|1\downarrow\rangle$ and $|2\uparrow\rangle$, which is experimentally confirmed in sec. 6.2.3. By varying the time delay and fitting the recovery of the read peak height with a mono-exponential growth law, the T_1-time is extracted. In Fig. 6.13 the data obtained for EA27, EA30 and EA13 is depicted yielding spin lifetimes of $T_1 = 21(2)\,\mathrm{ms}$ and $T_1 = 22(5)\,\mathrm{ms}$ at a magnetic field of $B = 200\,\mathrm{mT}$ for EA27 and EA30, respectively. For EA13 the measurement yields $T_1 = 15(1)\,\mathrm{ms}$ at $B = 80\,\mathrm{mT}$. The negative charge state is maintained throughout the course of the experiment by application of a 10 ms charge initialisation pulse for EA27 and by continuous illumination for EA30 and EA13. These values are in the same order of magnitude as it is reported in [176].

6.2.3 Cyclicity and single-shot readout

In QIP applications, such as the realisation of a quantum repeater, many experimental protocols rely on "repetition until success" schemes. This means furthermore that real time processing of measurement results is necessary in order to quickly adapt to an occuring protocol error. Therefore, instead of averaging the results over the numerous repetitions of a measurement sequence and post processing the data, single-shot readout of qubit spin states is a crucial tool for application of the SnV^- centre in QIP. The foundation of this readout are cycling transitions on which a number of photons large enough to be clearly distinguishable from the dark count level can be scattered within a reasonably short time interval (Detailed theoretical description of the scheme is found in sec. 2.2.5). In this

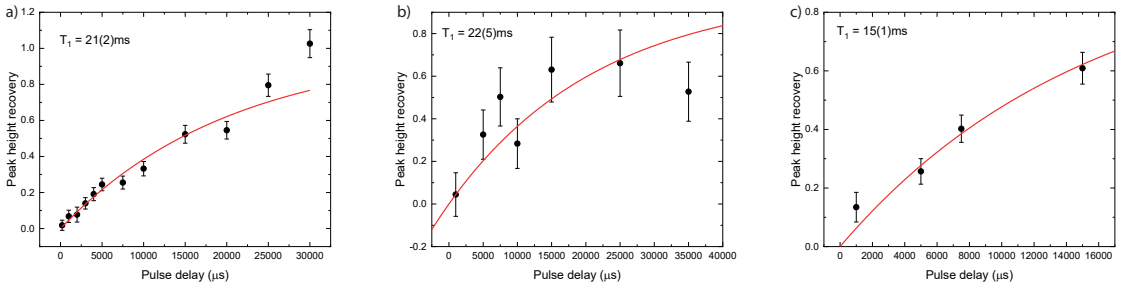

Figure 6.13: **Spin lifetime measurement of single SnV$^-$ centres:** The recovery of the fluorescence response peak caused by the read laser pulse is fitted with a mono-exponential growth law, yielding the spin lifetime of **a)** $T_1 = 21(2)$ ms for EA27, **b)** $T_1 = 22(5)$ ms for EA30 and **c)** $T_1 = 15(1)$ ms for EA13 at a temperature of 1.7 K. The applied magnetic field is B = 200 mT for EA27 and EA30, while it is reduced to B = 80 mT for EA13.

section, we experimentally probe the cyclicity of the SC transitions in the presence of a magnetic field with a moderate field strength of B = 200 mT. The B-field is applied with a large angle of 54.7° relative to the symmetry axis of the SnV$^-$ centre. For the SiV$^-$ centre, such a misalignment of the field angle leads to spin mixing and thereby a reduction of the cyclicity of the SC transitions [36]. However, owing to the large ground state splitting in between the orbital branches, spin mixing for the SnV$^-$ centre becomes only significant at much larger magnetic fields as the strength of it decreases with the square of the SO splitting, see eq. 2.38. In a first step, we probe the strength of the SF transitions via optical spin state pumping through the excited state, i.e by applying a laser pulse resonant to the SC transition A1 and recording the decay of the emitted fluorescence as it is shown in Fig. 6.14. To ensure that spurious excitation of the SnV$^-$ centre by residual laser power leaking through the AOM does not influence the experiment, we detune the laser by about 4 GHz and use the EOPM (−6.6 dBm unamplified microwave power) to bring the second harmonic sideband into resonance with transition A1. The measurement is conducted for two different total laser powers (40 nW and 500 nW) and fitted with the theoretical model described in sec. 2.2. The first free parameter is the ratio between laser power and Rabi frequency in the low power measurement. Since we know the ratio between the laser powers in the two experiments, the Rabi frequency in the high power measurement can be directly determined via the relation $\Omega_{\mathrm{HP}} = \sqrt{\frac{P_{\mathrm{high}}}{P_{\mathrm{low}}}}\Omega_{\mathrm{LP}}$. The second free parameter is the branching ratio η_{cycling} between the strength of the SC and SF transitions, which is introduced in sec. 2.2.5. The result is plotted in Fig. 6.14 and we find a branching ratio of $\eta_{\mathrm{cycling}} = 850(150)$, which is significantly larger than $\eta_{\mathrm{cycling}} = 80(5)$ reported in reference [114]. For the high power measurement we can easily compare whether the time scale of the exponential decay is in agreement with the theoretical predictions in sec. 2.2. In this case the pumping time scale should be almost saturated (compare Fig. 2.15) and we can calculate the branching ratio by dividing half of the pumping time scale by the lifetime. This yields a branching ratio of about 900 , which is closely matching the fitted value. Building on this promising result, we now investigate single shot spin state read-out. To this end, we use a two pulse laser sequence to first initialise the spin in state $|1\downarrow\rangle$ by a 200 µs long laser pulse resonant with the SC transition B2 and subsequently read out the population in $|1\downarrow\rangle$ by a 200 µs laser pulse resonant with the SC transition A1. The histogram over 11139 pulse sequences is depicted in Fig. 6.15a) and we find a spin initialisation efficiency of the first laser pulse of 98.9(4) % determined by the value of the mono-exponential fit to the fluorescence

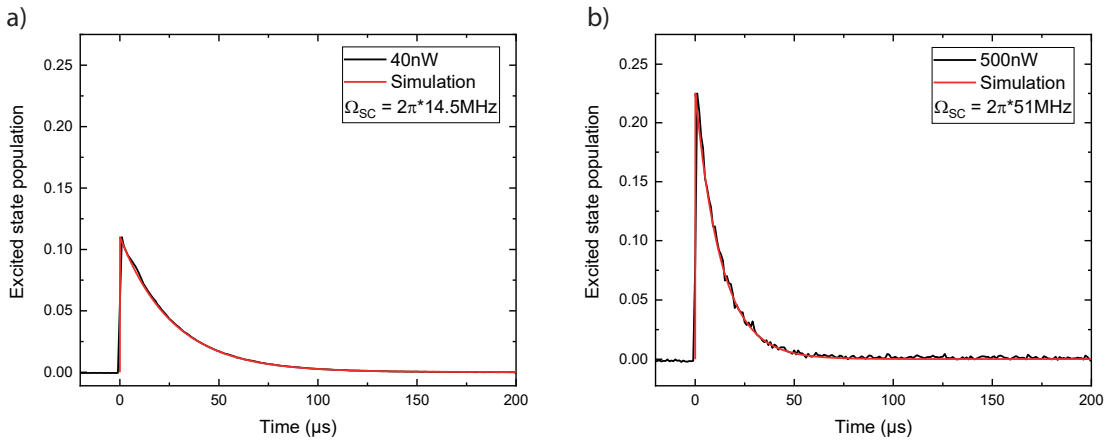

Figure 6.14: **Determination of the branching ratio between SC and SF transitions:** In order to determine the ratio between the strength of the SC and SF transitions we detune the laser carrier by about 4 GHz from the A1 transition and use an EOPM to bring one sideband into resonance with the SC A1 transition. This yields a laser pulse of 200 µs duration, which is long enough to ensure flipping of the spin state. We repeat the measurement for two different total laser powers of **a)** 40 nW and **b)** 500 nW. We fit the two datasets with the model derived in 2.2 and extract the two free parameters. The first one is the ratio between laser power and Rabi frequencies, the second one is the branching ratio amounting to $\eta = 850(150)$.

decay at the end of the pulse. The ratio of the height of both peaks amounts to 44.0(5) % which corresponds to the population in state $|2\uparrow\rangle$ in thermal equilibrium. This value matches the theoretically expected value of 44.37 % for the given magnetic field splitting and temperature of 1.7 K. We evaluate the emitted photons per pulse by dividing the sum over all photons in the histogram by the number of repetitions and find for each read pulse an average photon number of 1.21 (1.13) without (with) dark count substraction. As this number surpasses the threshold of 1 photon per pulse in the bright state, from which on a meaningful state assignment upon readout can be implemented, we evaluate the readout fidelity according to the definition derived in [68]. The threshold of a state readout to be assigned as bright state is set to 1 photon. In Fig. 6.15b) for each pulse in the measurement sequence the number of emitted photons is extracted, binned in a histogram and translated into a probability distribution through normalisation of the counts by the total pulse number. In comparison, the probability distribution of an equivalent time interval (lightly orange shaded area in Fig. 6.15) of the same length as the read pulse but where no laser is applied is depicted as an estimate of the dark state measurement. This approach is valid, as the initialisation efficiency is close to perfect and we correct the readout fidelity by the photons scattered by the remaining population. Following the protocol described in sec. 2.2.5 we can derive the readout error for the erroneous detection of the bright state ($|1\downarrow\rangle$) as dark ($|2\uparrow\rangle$) to be $\epsilon_B = 0.45$ in the case of the detection of one photon being set as the threshold for detecting a state as bright (see Fig. 6.15b)). This error is rather large due to the significant number of read out pulses on the bright state that contain no detected photon. On the other hand, the error for a dark state being detected as bright amounts only to $\epsilon_D = 0.08$, including the scattered photons caused by the remaining 1.1 % of population remaining after the state initialisation. This error is largely limited by the dark counts of the APDs. From both errors we calculate the average state readout error,

which is defined as $\epsilon = \frac{\epsilon_B + \epsilon_D}{2}$, yielding $\epsilon = 0.26$. The readout fidelity is directly correlated to this error and yields $\mathcal{F} = 1 - \epsilon = 0.74$. This fidelity of 74 % demonstrates the potential of the strongly cycling SC transitions of the SnV^- centre, as it surpasses the 50 % threshold from which on a meaningful single-shot readout is possible. Achievement of a high fidelity single-shot readout can be realised by improving the detection efficiency of photons. The detection efficiency of the current experiment can be derived in the following way: The 1.13 photons per pulse are detected upon emission into the PSB. Correcting this value by the DW factor yields 1.7 photons per pulse being emitted into the ZPL. Comparing the 1.7 photons to the 850(150) photons that have to be scattered due to the branching ratio until the spin is flipped yields the overall detection efficieny of the whole setup of 2.0(4) ‰. A main limiting factor is the low collection efficiency from unstructured bulk diamond due to total internal reflection in the high refractive index material and the modification of the dipole emission pattern of an emitter towards the medium with larger photon density of states. Straightforward means to improve this collection of photons are the use of photonic elements or optical cavities (for an overview see e.g. [184, 185]) such as optical antennas [186, 187], solid immersion lenses [125, 126], nanowires and -pillars [176, 188, 189] or photonic crystal cavities [128, 190, 191, 225, 262].

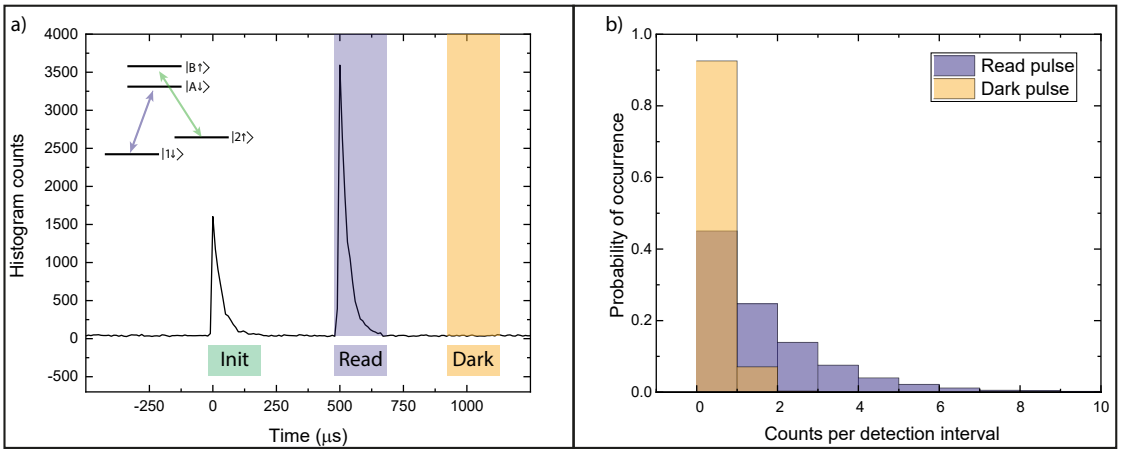

Figure 6.15: **Spin initialisation and single-shot readout of a charge stabilised SnV^- centre: a)** Histogram of the initialisation and readout sequence consisting of an initialisation pulse resonant with the SC transition B2 and a read pulse resonant with the SC transition A1. The pulse sequence is repeated 11139 times and an initialisation efficiency of 98.9 % into state $|1\downarrow\rangle$ is reached. For the read pulse, a mean photon number of 1.21 (1.13) without (with) dark substract is detected within the 200 µs long pulse interval. **b)** For the read pulse (blue) and a time interval of the same length were no laser pulse is applied (dark pulse, orange), a histogram of the photon number detected in each measurement run is extracted. This is translated into a probability distribution through normalisation by the total pulse number. Taking into account the photons caused by the non perfect state initialisation, the single-shot readout fidelity amounts to 74 % for the case of one photon being set as the threshold for a state to be detected as bright.

We can use the measurement of the detection efficiency in the above-mentioned way to compare the count rate we detect to the maximum possible count rate, which is limited by the excited state lifetime. Under resonant excitation we measure a saturation count rate in between 45 - 75 kHz emitted into the PSB, depending on the setup alignment. As the PSB contributes to 40 % of the photons emitted by the SnV^- centre (see sec. 4.3)

and the used optical filter (655-47 bandpass) transmits 76 % of the total PSB, the count rate detectable in our setup ranges from 148 kHz to 247 kHz. Correcting this value by the detection efficiency yields 62 - 145 MHz, which includes all photons emitted whether they are detected or not. The lifetime of the emitter could not be measured by the usual TCSPC scheme, as the supercontinuum laser source was not available at this time. However, the lifetime can be estimated by fitting the decay of the fluorescence at the end of a pulse generated by the AOM characterised in sec. 3.2.2. We extract a lifetime of $\tau = 7.5(9)$ ns, which is further confirmed by the simulations in the following section. In the case of only radiative decay channels contributing to the lifetime, it corresponds to a count rate of 133(21) MHz. Within the error bars, this value is in agreement with our experimental findings. However, the large error bars on this calculation can be easily minimised in future experiments by conducting a saturation measurement of the optical pumping time scale and extrapolate it to extract the branching ratio (see sec. 2.2.5). Furthermore, the lifetime and the saturation count rate need to be measured more precisely and the collection efficiency needs to be determined independently. The accuracy of the matching between the theoretical and experimental value for the count rate gives information about the quantum efficiency of the SnV^- centre. For unity quantum efficiency, the values need to match exactly, while for a quantum efficiency of 80 % as it is reported in [113], there will be a difference observable.

6.2.4 Spin dephasing time

The experiments in the previous sections demonstrate the potential of charge stabilised SnV^- centres with respect to long-term stable lifetime limited optical transitions, long spin lifetimes and single-shot spin state readout. However, the spin dephasing time of the ground state spin qubit remains elusive. This section is dedicated to filling in this gap by implementing an all optical CPT scheme. The necessary Lambda scheme is constituted by the SC (SF) transition between the ground state $|1\downarrow\rangle$ ($|2\uparrow\rangle$) and the excited state $|A\downarrow\rangle$. A magnetic field B = 200 mT is applied in an angle of 54.7° with respect to the symmetry axis of EA30.

Transition B1 is driven by the carrier frequency of our dye laser, whereas the second light field is generated by the first harmonic of the EOPM and scanned across transition A1. The count rate emitted into the PSB is recorded and a characteristic CPT signal is depicted in Fig. 6.16a). The black curve represents the measured data, while the solid red line is a fit using the theoretical model derived in sec. 2.2. On the high frequency side, the deviation of the fit from the data is caused by approaching the acceptance edge at 4 GHz of the microwave amplifier used. This leads to a decrease of the intensity in the first harmonic sideband and therefore effectively changes the Rabi frequency of the laser field scanned across transition A1 during the scan. The latter effect is not covered by our simulation. We nevertheless use this measurement for translating the measured count rate into excited state $|A\downarrow\rangle$ spin population. In the case of no magnetic field being applied a count rate of 45 kHz is emitted into the PSB for an excitation power far above saturation. This value corresponds to the limit of incoherent excitation between ground and excited state and consequently relates to 50 % of the population. Using this relation as a starting point, we fit the high power CPT signal in Fig. 6.16a) and retrieve an exact conversion factor between count rate and excited state population, which we use for the following measurements. Repetition of the experiment for strongly reduced laser powers and varying ratio between SC and SF field intensity yields a data set that we fit simultaneously in order to reduce the free parameters. These are the exact number of

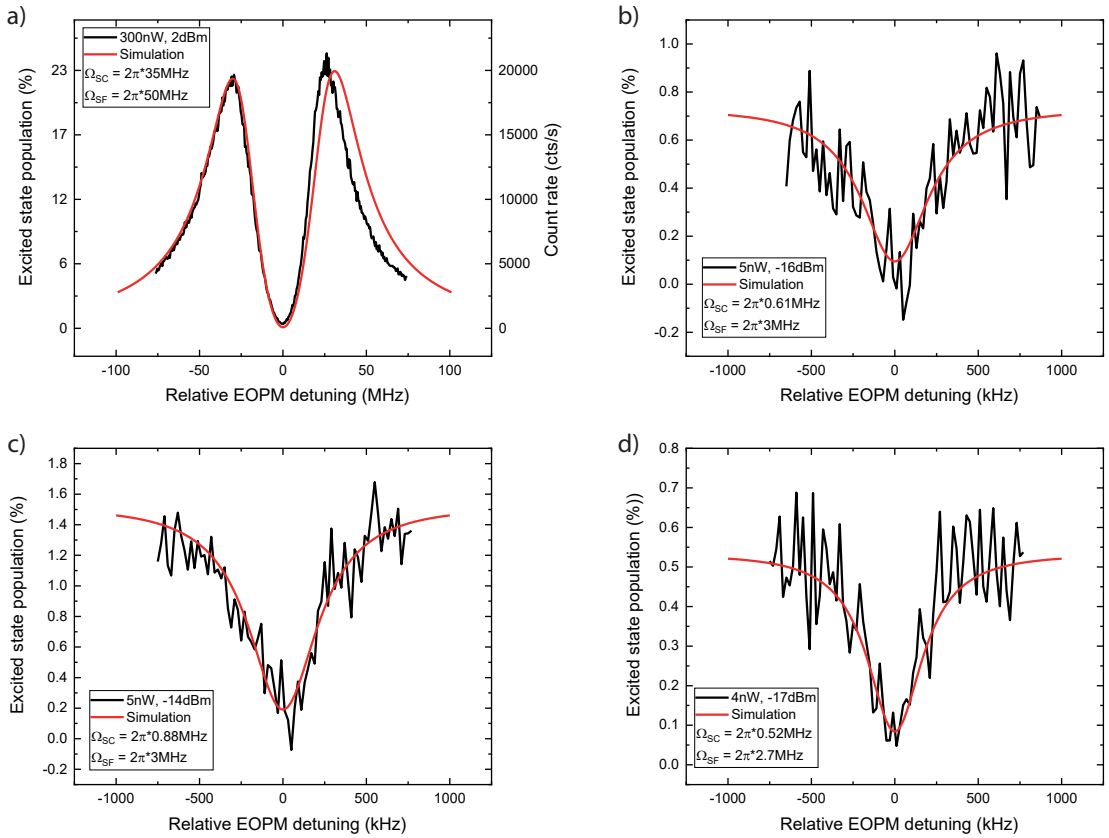

Figure 6.16: **Coherent population trapping of a charge stabilised single SnV^- centre: a)** CPT signal of EA30, which is retrieved in a measurement using 300 nW of total laser power. Fitting the data in black with the theoretical model derived in sec. 2.2 (red solid line) yields the conversion factor between the count rate emitted into the PSB and the excited state spin population of the SnV^- centre. On the high frequency side of the spectrum, the deviation of the fit from the data is explained by approaching the acceptance edge of the microwave amplifier. This leads to a decrease of the intensity in the first harmonic sideband driving transition A1, effectively changing the Rabi frequency during the measurement. The CPT signals in **b)**, **c)** and **d)** for reduced laser powers and varying ratio between SC and SF field intensity are used to reduce the amount of free parameters in the simulations. All stated microwave power values relate to the situation before amplification.

background fluorescence introduced by the charge stabilising laser, the dark counts of the APD and the ratio between experimental laser power and Rabi frequency in the simulation. In combination with the lowest power measurement depicted in Fig. 6.17, we eventually extract the ground state spin dephasing rate $\gamma_{SD} = 64(10)$ kHz. As discussed in sec. 2.2.6, the dephasing rate corresponds to a spin dephasing time of $T_2^* = 5(1)$ µs for EA30, a value slightly larger than reported in [114, 176]. This spin dephasing time is significantly longer than for the SiV^- centre ($T_2^* \approx 100$ ns) [106] and GeV^- centre ($T_2^* \approx 19$ ns) [108] at comparable temperatures as the SnV^- centre benefits from the large ground state splitting, thereby mitigating decoherence introduced by phonon driven transitions between the two lowest orbital fine-structure states (see sec. 2.1.4 for details on the decoherence mechanism). Additionally, the HPHT annealing furthermore reduced the amount of impurities and defects in the vicinity of the SnV^- centre, which can induce magnetic noise.

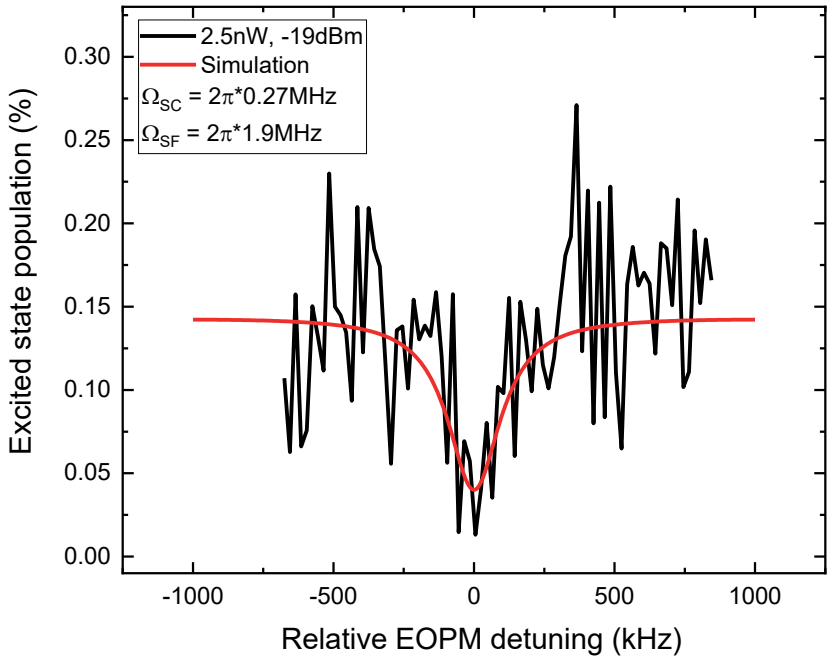

Figure 6.17: **Derivation of the ground state spin dephasing time of a charge stabilised single SnV^- centre:** Lowest laser power CPT measurement on emitter EA30. For a total power of 2.5 nW, 500 repetitions of the sideband scan yield the measurement data in black. The red solid line represents the fit of the theoretical model to the data. In addition with the measurements presented in Fig. 6.16, a ground state decoherence rate of $\gamma_{SD} = 64(10)$ kHz is extracted. This corresponds to a spin dephasing time of $T_2^* = 5(1)$ µs. The microwave power of -19 dBm used to generate the sideband is the value before amplification.

Chapter 7

Two-photon interference of photons emitted from single SnV^- centres

Contributions and copyright notice

The experiments conducted in this chapter were carried out under the supervision of C.B.. J.G., Robert Morsch (R.M., as part of his master thesis) and B.K. designed the setup and J.G. and R.M. performed the experiments. The temperature stabilisation of the filter lens was implemented by Tobias Bauer. The analysis of the data was carried out bei J.G. and R.M., while the TPI simulations were done by B.K., J.G. and R.M..

Within the course of the previous chapter, the promising long-term stability of the optical transitions of the SnV^- centre were investigated. In this chapter, we aim at exploiting this optical coherence of the emitted photons by characterising the two-photon interference of subsequently emitted photons of a single SnV^- centre. Therefore, the first part of this chapter is dedicated to the spectral filtering of the photons emitted by the investigated SnV^- centres and the achieved signal to background ratio. Subsequently, the single photon character of the emission is characterised by pulsed autocorrelation measurements and the lifetime of the excited state is extracted from TCSPC measurements. In a last characterisation step, we probe the impact of SD by scanning the resonance of the implemented filter setup across the emitted photons in order to extract the spectral linewidth. Eventually, we conclude the experiments by measuring the two-photon interference of subsequently emitted photons resulting from one SnV^- centre for two different emitters and evaluate the impact of spectral diffusion on the TPI visibility for photons being emitted with time delays up to about 350 ns.

7.1 Characterisation of the emitters

The theoretical foundation of TPI described in sec. 2.3 is based on the precise knowledge of a set of parameters that are needed to accurately simulate and evaluate acquired measurement data. Therefore, an in-depth characterisation of the single SnV^- centres under investigation is needed. This section is dedicated to revealing these properties starting with the SBR ratio after filtering of the C-transition and the extinction of the D-transition by the filter lens. Subsequently, the single photon emission is characterised by conducting pulsed autocorrelation measurements under the same conditions as in the TPI experiment. The section concludes by deriving the excited state lifetime and the impact of spectral

diffusion on time scales of the order of half an hour. All experiments within this section are conducted on sample BOJO_001.

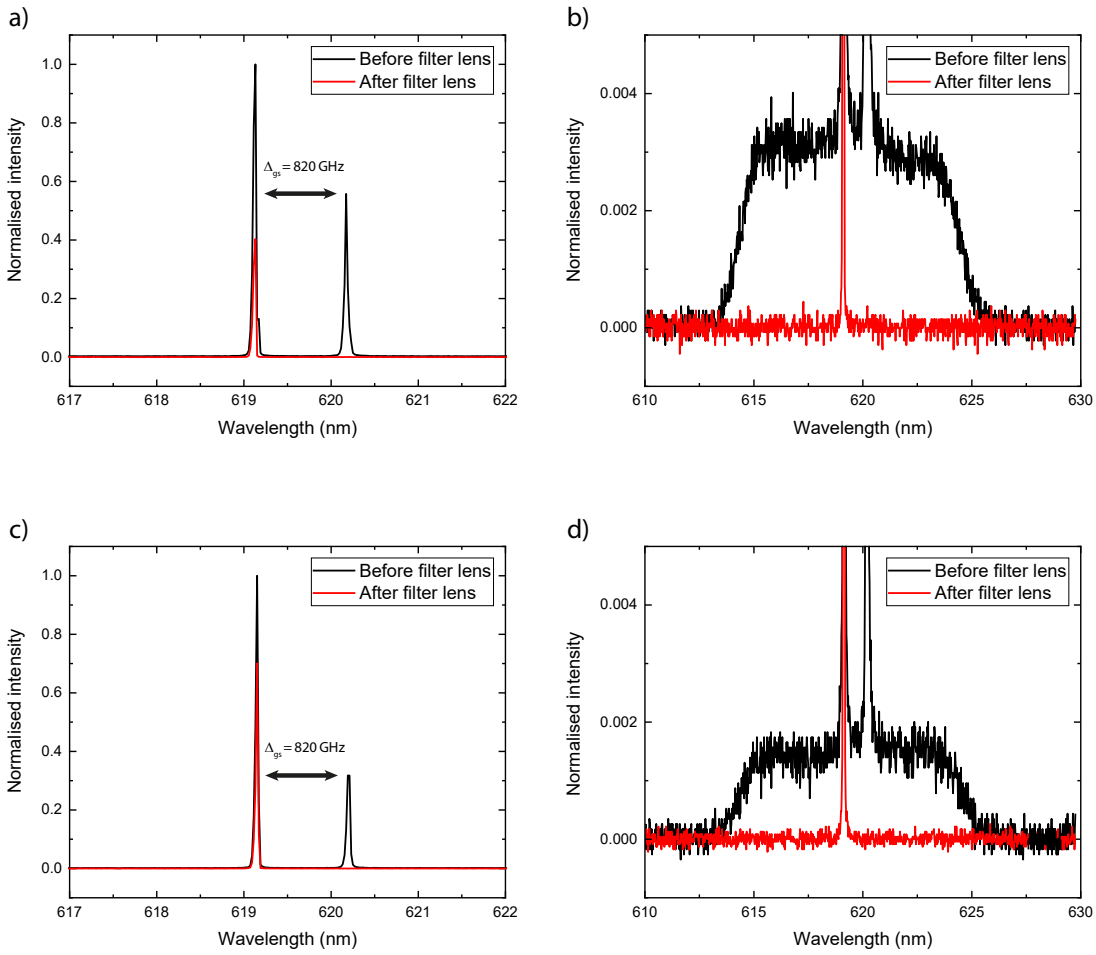

Figure 7.1: **Comparison of filtered and unfiltered spectra: a)** The unfiltered fine-structure spectrum of emitter EB2 in black is overlapped with the spectrum acquired after passing the filter lens setup. The filter setup is set resonant with the C-transition and the emission into the D-line is strongly suppressed (1:993(187)). **b)** Zoom into the lower part of the spectrum of emitter EB2. Before filtering, a significant background contribution within the transmission band of the applied optical bandpass filter is observed. This background is strongly suppressed by the filter lens and results in a SBR ratio of 43(2). **c)** and **d)** Repetition of the measurements for emitter EB3, resulting in an extinction of the emission from the D-transition too large to be reliably quantified in this measurement and a SBR ratio of 217(14).

7.1.1 Signal-to-background ratio

The SBR ratio is an important parameter for the description of the acquired data throughout the TPI measurements. We probe the SBR by measuring spectra of the emitters EB2 and EB3 at 1.7 K under two conditions: First we measure the spectrum under off-resonant excitation, revealing a ground state splitting of 820 GHz, which, in the course of this thesis, is assumed to relate close to the ideal case of an unstrained SnV^- centre. Subsequently, we filter the emission using the filter lens setup described in sec. 3.2.3. In Fig. 7.1a) and c) the

direct comparison for EB2, respectively EB3, between the filtered and unfiltered spectra is shown. The effect of the filter lens is clearly visible, as the C-transition strongly dominates the spectrum after the filter setup. However, the transmission for emitter EB2 is only about 35 % due to the filter setup being not in its final optimised state. For emitter EB3 a total transmission of 62 % is measured. We evaluate the extinction of the D-transition by comparing the counts in the same spectral region before and after filtering and taking into account the total transmission through the filter setup. For emitter EB2 the extinction amounts to 1:993(187), while for emitter EB3 the extinction is too large (at least 5000) to distinguish a contribution of the residual D-transition from the noise of the data set. The latter is in agreement with the theoretical extinction ratio (about 12000) measured in sec. 3.2.3 of the finalised filter setup, while the mismatch for emitter EB2 results most likely from imperfect coupling to the filter lens. In Fig. 7.1b) and d) a magnification of the spectra is displayed. For the unfiltered emission a significant background contribution resulting from fluorescence of defects in the diamond lattice is observed. The edges in the spectrum of the background emission are a result of the applied bandpass filter (620(10) nm). The filter lens strongly reduces this background contribution. More precisely, when summing up the full spectral range of the filtered spectrum in which background emission is observed before the filter lens, we find a SBR ratio of 43(2) for emitter EB2, respectively 217(14) for emitter EB3. It is difficult to distinguish between non perfect dark substract of the spectrometer and real background induced by the optical excitation, which is the reason why we do not correct for imperfect dark substract and consider these values to be lower bounds. Even so, a maximum of 2.3 % of the photons contributing to the TPI statistic will be erroneous and therefore their impact is very limited.

7.1.2 Lifetime

The exact knowledge of the excited state lifetime is crucial in order to precisely evaluate TPI measurements. We therefore employ TCSPC and use the same excitation and filter condition as for the pulsed autocorrelation and TPI measurements described below. The excitation pulses are retrieved from the supercontinuum laser source, with the repetition rate for both emitters being set to about 37 MHz. The excitation wavelength is set to 480(120) nm, where 120 nm denotes the spectral bandwidth, and the fluorescence response is detected by recording the photons being emitted upon decay via the C-transition, which is carved out by the filter lens setup (see sec. 3.2.3). The depicted measurements in Fig. 7.3 suprisingly reveal a rising edge that cannot be explained by the excitation pulse width and the APD jitter. For all emitters under investigation in sample NI58, no such rising edge was detected in TCSPC lifetime determination. While the exact origin of this rising edge could not be revealed in the course of this thesis, we attribute it to a population jitter that is induced by the time constant τ_{AE} of the decay from the A_{2u} excited state (see sec. 4.4) into the E_g excited state of the SnV^- centre (Fig. 7.2). The TCSPC measurements thus need to be fitted by the convolution of this time dependent population of the excited state, the APD jitter and

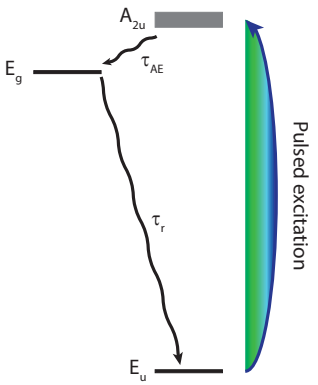

Figure 7.2: **Reduced level scheme:** The excitation pulse populates the A_{2u} excited state, which decays into the E_g excited state (time constant τ_{AE}), resulting in a population jitter. The subsequent radiative ZPL decay (time constant τ_r) leaves the emitter in the E_u ground state.

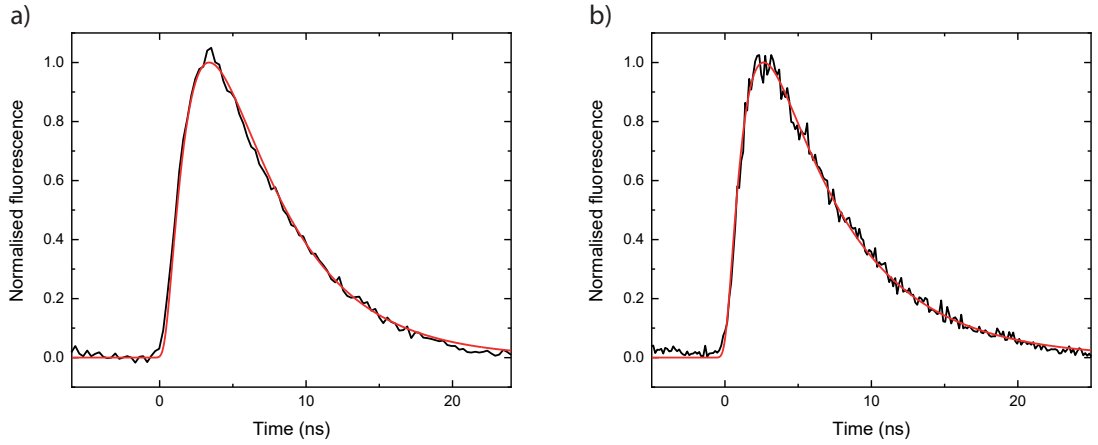

Figure 7.3: **Lifetime measurement of the investigated single SnV^- centres:** The excited state lifetime τ_r is measured by employing TCSPC. The excitation pulse is retrieved from the supercontinuum laser source and the photons emitted upon decay via the C-transition are spectrally carved out using the filter lens setup and detected by APDs. A significant rising edge as a result of population of the E_g excited state by decay from the higher excited A_{2u} state with a time constant of τ_{AE} is visible. The measurements yield **a)** $\tau_{AE} = 1.7(1)$ ns and $\tau_r = 5.0(3)$ ns for EB2 and **b)** $\tau_{AE} = 1.09(8)$ ns and $\tau_r = 5.8(2)$ ns for EB3.

the exponential decay of the excited state into the ground state. This yields a population jitter time constant $\tau_{AE} = 1.7(1)$ ns ($\tau_{AE} = 1.09(8)$ ns) for emitter EB2 (EB3). The excited state decay time constant amounts to $\tau_r = 5.0(3)$ ns ($\tau_r = 5.8(2)$ ns).

7.1.3 Pulsed autocorrelation measurement

In order to quantify the single photon emission character of the defects under investigation and the impact of background from the sample on the TPI measurements, we conduct pulsed autocorrelation measurements using the same excitation and filter setting as in the actual TPI measurements and described in the previous section. The first FBS in the unbalanced MZI (see sec. 3.2.3) is used for generating the same HBT setting in a fibre based manner as it is described in sec. 3.2.4 for free space application. The fibre outputs of the FBS are directly connected to the APDs and the resulting autocorrelation measurement is depicted in Fig. 7.4. As a proof of the single photon nature of the emitted photons, the peak at zero time delay is discriminated, yielding a value of $g^{(2)}(0) = 0.12$ ($g^{(2)}(0) = 0.09$) for EB2 (EB3) without dark count substraction of the APDs. This value is extracted from the fit, which takes into account the population jitter and lifetime determined in the previous section, and the dark count contribution of the ADPs. We calculate the latter according to the formula

$$bg = d_1 \cdot c_2 + d_2 \cdot c_1 + d_1 \cdot d_2 \tag{7.1}$$

derived in appendix C in [230]. The dark count rate of each APD is defined as $d_{1/2}$ and the count rate resulting from the emitter on each APD is denoted as $c_{1/2}$. The only free parameters of the fit are the amplitude of the neighbouring peaks as well as the amplitude of the central peak. Taking into account the APD dark count contribution, which can be also accounted for in the TPI measurements, results in a corrected value of $g^{(2)}(0) = 0.01$ ($g^{(2)}(0) = 0.02$). The time overlap of the neighbouring peaks exactly explains the residual

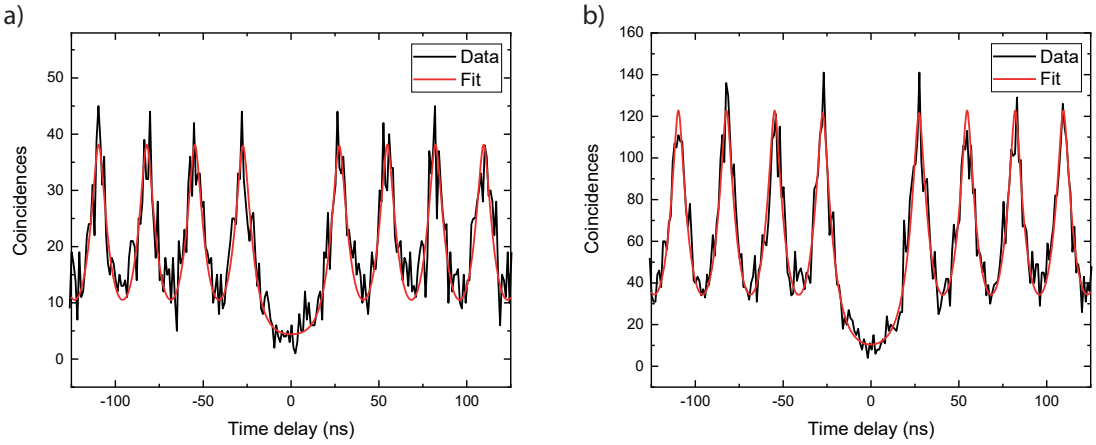

Figure 7.4: **Pulsed autocorrelation measurement:** The single photon character of the photons emitted into the C-transition after filtering them with the filter lens setup is quantified in an autocorrelation measurement. The excitation and detection settings are the same as in the subsequently performed TPI experiments. From the fits to the data, we extract **a)** $g^{(2)}(0) = 0.12$ for EB2 and **b)** $g^{(2)}(0) = 0.09$ for EB3 without correcting for the dark counts of the APDs. The correction for the latter yields $g^{(2)}(0) = 0.01$, respectively $g^{(2)}(0) = 0.02$, with the deviation from zero being fully explained by the residual overlap of the two neighbouring peaks.

deviation from zero. We can therefore conclude that the investigated SnV^- centres are perfect single photon emitters.

7.1.4 Spectral diffusion

The SD of optical transitions is one of the most common sources that limit the visibility of two-photon interference. It can be quantified by measuring the spectral linewidth of the emitted photons. In contrast to sec. 6.1.5, where the absorption linewidth is characterised in PLE scans, we are here interested in the linewidth of the emitted photons decaying via the C-transition upon quasi-resonant, pulsed excitation. The main difference is that the charge environment will be influenced by the laser powers in the milliwatt regime that have to be applied for efficient quasi-resonant excitation. Furthermore, the diamond material will be heated up by the intense laser pulses. In order to investigate the effect, we use the temperature tunability of the filter lens (see sec. 3.2.3) and scan the resonance of the filter lens across the photons decaying via the C-transition. From the recorded spectrum constituted by transmitted photon counts, we can derive the linewidth in units of Kelvin. Since the coefficient between temperature and filter lens resonance position is quantified in sec. 3.2.3, we can directly relate temperature to frequency. We fit the spectrum using a Voigt fit, where we set the Lorentzian part fixed to the FWHM of the pure filter lens (354 MHz) and assume the SD to be Gaussian distributed, which is to be expected for a random stochastic process. Fitting the Gaussian part of the Voigt profile in Fig. 7.5a) yields a Gaussian SD width of $\Delta_G = 273(15)$ MHz for EB2 in the case of an excitation pulse at a wavelength of 532(10) nm retrieved from the supercontinuum laser source. This linewidth represents the spectral diffusion on the time scale of about half an hour, with the speed of the scan being limited by the temperature tuning of the filter lens. Since this linewidth is about a factor of 8.5 larger than the lifetime limit of 32(2) MHz and the excitation wavelength is imperfect for the simultaneous stabilisation of

the charge state (see chap. 5), we suspect that SD induced by charge fluctuations is one source of the broadening. Repetition of the measurement with an excitation wavelength of 460(120) nm, which includes the blue frequencies suitable for the charge stabilisation reduces the Gaussian linewidth to 238(8) MHz, see Fig. 7.5b). The origin of the remaining broadening is most likely residual SD originating from the large laser powers applied and furthermore the heating effect that we introduce by using an average power of 20 mW, which will be explored further in the following sections. For EB3, we characterise the emission in Fig. 7.5c) for an excitation wavelength of 480(120) nm and find the Gaussian linewidth to be 198(9) MHz.

7.2 Two-photon interference

7.2.1 Indistinguishable consecutive photons

The measurement of the indistinguishability of single photons emitted from a SnV^- centre utilises the setup described in sec. 3.2.3. The excitation delay τ_{exc} of the pulses created by the supercontinuum laser source is given by the repetition rate of about 37 MHz and amounts to about 27 ns. We match the lengths of the fibres within the long and short arm to compensate for an integer number of the excitation delay. The standard configuration is compensating for $3\tau_{exc}$, due to the fibre length wrapped around the fibre stretcher. However, an additional fibre can be added into the short arm in order to overlap photons separated by $1\tau_{exc}$. For maximum separation, a fibre spool of about 50 m additional fibre length can be introduced in the long arm, increasing the photon separation to $13\tau_{exc}$.
Since the count rate of emitter EB2 is rather low (about 2 kcts/s at a repetition rate of 37 MHz) due to the filter lens setup being in the non optimised state, we only characterise photons separated by $3\tau_{exc}$ in the lowest loss standard MZI configuration. We use the polarisation control to maximise the classical visibility of the MZI in order to set the polarisation states of the photons interfering at the second FBS in parallel to each other. Furthermore, the high classical visibilities that we achieve assure that, in addition to the polarisation mode, also the spatial mode overlap inside the FBS is large. A typical measurement for this case is analysed in sec. 3.2.3. The supercontinuum laser source excitation wavelength is set to 480(120) nm in order to minimise the effect of SD as explained in the section above. In Fig. 7.6a) the result of the TPI and the fit according to the model described in sec. 2.3 is depicted. As expected, the central peak at zero time delay is strongly diminished due to TPI interference. Furthermore, the reduced peak height of the third neighbouring peak is in agreement with the photon separation by $3\tau_{exc}$, which is explained in detail in sec. 2.3.3. The fit of the data is performed in the following way: We insert the lifetime and the population jitter as fixed values, which are measured independently as explained in the previous sections. Furthermore, we calculate the background according to equation 7.1. Finally, the repetition rate γ_{rep} of the excitation pulses and the known theoretical relative peak height pattern are kept constant. This leaves only two free and independently fitted parameters, namely the amplitude of the peaks and the influence of SD and PD. The peak amplitude is fitted by taking into account a significant number of neighbouring peaks, but neglecting the central peak. The SD is fitted taking into account only the time interval of $[-\tau_{exc}, \tau_{exc}]$ around the central peak. This procedure is chosen to minimise the influence of the two free parameters on each other. As it can be seen, the model describes the measurement data accurately. In Fig. 7.6b), we display the comparison of the fit (in red) with three theoretical cases of interest. In green, the case for distinguishable photons states the clear difference between this case and what we observe in the experiment. In blue, the

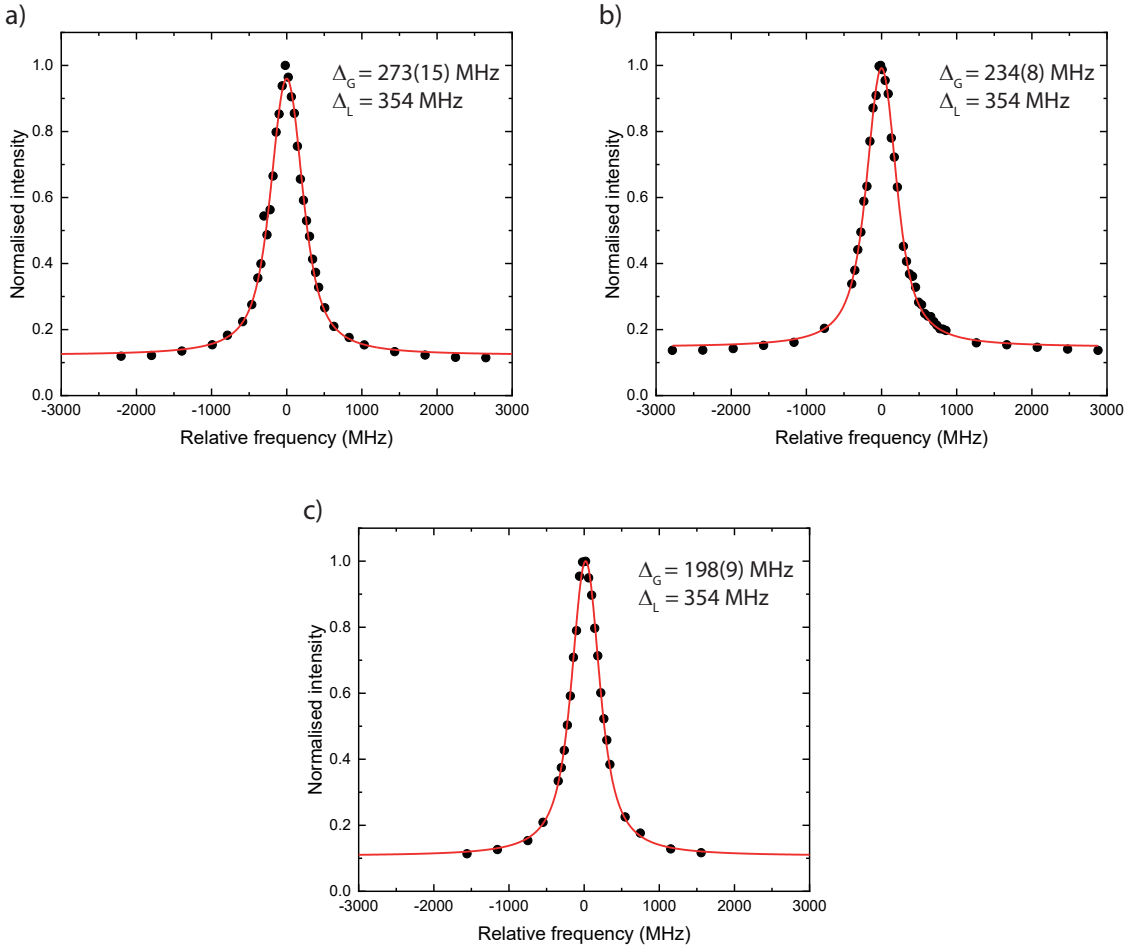

Figure 7.5: **SD upon quasi-resonant, pulsed excitation:** The SD of the photons emitted upon decay via the C-transition is quantified by scanning the filter lens resonance across the photon spectrum and recording the transmitted photons. The width of the close to Lorentzian filter lens resonance of 354 MHz is set fixed and the total spectrum of the transmission is fitted with a Voigt profile, with the Gaussian contribution to the width as a free parameter describing the random process of SD. **a)** For EB2 under 532(10) nm pulsed excitation the SD width amounts to $\Delta_G = 273(15)$ MHz. **b)** Excitation with 460(120) nm reduces the charge noise and thus leads to a decreased width of 238(8) MHz. **c)** The SD width in the case of excitation with 480(120) nm amounts to 198(9) MHz. The remaining broadening is most likely caused by residual SD and heating of the diamond upon the strong pulsed excitation.

optimal case in our experiment is displayed, in which the visibility is limited to 75 % due to the uncertainty in arrival time introduced by the population jitter τ_{AE}. The dark grey line presents the perfect case of a single SnV^- centre exhibiting no population jitter and perfectly indistinguishable photons with 100 % visibility. To the latter case we compare our measurements and thus extract the value of the visibility that is actually achievable in any quantum communication protocol. For this, the visibility of the full photon wave package is the figure of merit that is of interest. In order to retrieve it from our measurement data, we first fit the data and subsequently integrate over the full fit in a time interval $\gg \tau_{\mathrm{r}}$, including several neighbouring peaks. This ensures to account for 99.99 % of the photon wavepackage contributing to the TPI. From the integration, we substract the value that we get from summing up the perfect case (I = 100 %, V = 100 %) over the same time interval, yielding the area of the remaining peak $\mathrm{A_{rem}}$. The same we do for the distinguishable case (I = 0 %, V = 0 %) and again substract the integration of the perfect case, which we label $\mathrm{A_{dist}}$. We can calculate the visibility in accordance to the formula

$$\mathrm{V} = 1 - \frac{\mathrm{A_{rem}}}{\mathrm{A_{dist}}}, \tag{7.2}$$

as we expect the area of the peak describing the TPI to be reduced by a factor of $1 - \mathrm{V}$ compared to the distinguishable case, see sec. 2.3. The equality $\mathrm{A_{dist}} = (1 - \mathrm{V})\mathrm{A_{rem}}$ directly leads to equation 7.2. For EB2, we find a visibility of the full photon wave package of 45.7(6.4)% for a photon separation of $3\tau_{\mathrm{exc}}$. In literature, the visibility is oftentimes

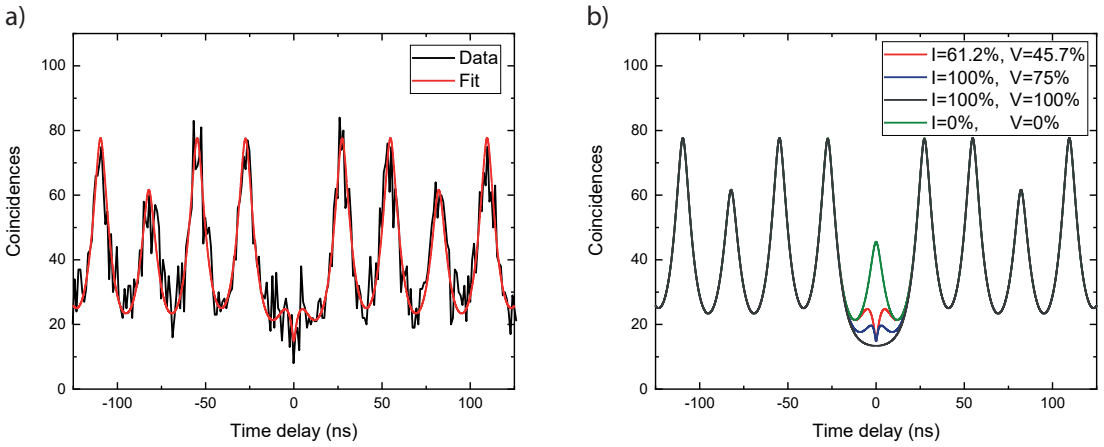

Figure 7.6: **TPI of photons emitted by EB2: a)** Measurement of the TPI of photons emitted by EB2 under pulsed, quasi-resonant excitation with a time separation of $3\tau_{\mathrm{exc}}$. As is characteristic, the heights of the peaks at $3\tau_{\mathrm{exc}}$ time delay are only two third of the amplitude of the other neighbouring peaks. Furthermore, the central peak is strongly diminished due to TPI. The data (black solid line) is fitted (red solid line) according to the model described in sec. 2.3. **b)** Comparison of the fit to the optimal case (grey) of a TPI visibility of 100 %, the case of the visibility being only limited by the population jitter τ_{AE} (blue) and the case of orthogonal polarisation states (green) of the interfering photons. By comparison of the fit to the optimal case, we extract a visibility of V = 45.7(6.4)% for the full photon wave package. Taking into account the population jitter and the slight mismatch of the photon arrival time at the FBS yields an indistinguishability of I = 61.2(12.3)% limited only by SD and/or PD.

stated for a certain filter window in time including only a fraction of the full photon wave package contributing to the TPI. This increases the visibility, as it carves out the interference dip at zero time delay. However, in any quantum communication protocol it reduces the efficiency as only photons interfering in the defined time window will be taken into account. Due to the interference relying on two separate photons, this effect scales quadratically. In Fig. 7.7a) the effective visibility is plotted against the percentage of the area of the photon wave package that is taken into account. It surpasses 75 % for filtering only half, respectively 90 % for filtering about twenty percent of the photon wave package. This comes along with an increased measurement time by a factor of four, respectively 25 (see Fig. 7.7b)). Therefore, depending on the protocol that should be implemented and its requirements regarding speed and fault tolerance, the filter window can be adjusted to the desired size.

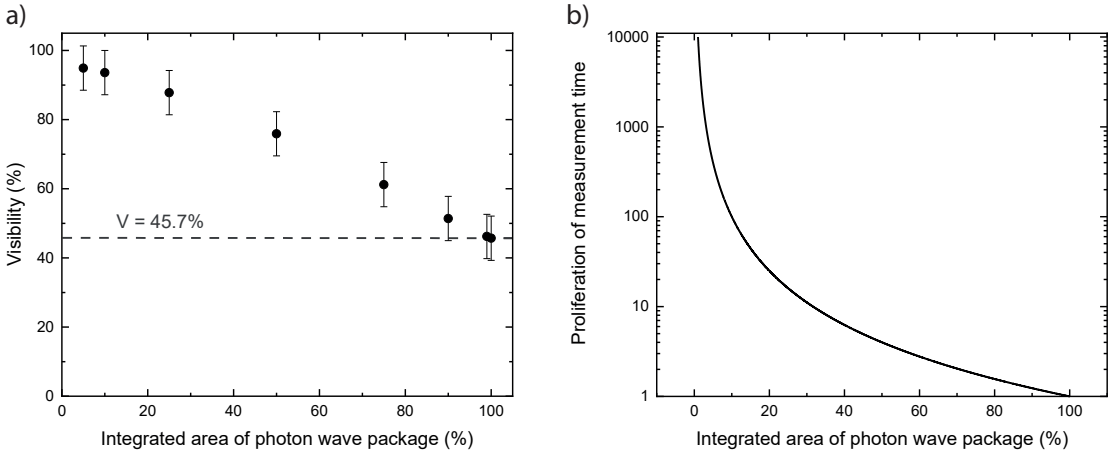

Figure 7.7: **Visibility and proliferation of measurement time dependence on time filtering: a)** The visibility of TPI can be increased by time filtering around zero time delay by a certain percentage of the photon wave packages. For EB2, only about 20 % of the wave package can be taken into account in order to surpass a visibility of 90 %. However, as depicted in **b)**, time filtering proliferates the measurement time quadratically due to two photons contributing to the interference. For the beforementioned filtering of one fifth of the photons, this yields an 25fold increased measurement time.

While the visibility is the figure of merit in any communication protocol, it is also interesting to evaluate how indistinguishable the photons are without avoidable experimental imperfections that impact the measurements. The first such error source is the compensation of the excitation delay within the unbalanced MZI, which is imperfect due to variations of the refractive index for different fibre batches and a finite error bar on the order of 5 mm in our protocol for cutting and splicing fibers to the correct length. We characterise the delay mismatch by TCSPC of single photons from a SnV^- centre, once for the photons passing the short and a second time for passing the long arm of the interferometer. The results are shown in Fig. 7.8 for compensation of a photon separation of $1\tau_{\mathrm{exc}}$, $3\tau_{\mathrm{exc}}$ and $13\tau_{\mathrm{exc}}$. We find a mismatch δt of 263(23) ps, 289(22) ps and 65(25) ps for the three situations, which impair the visibility slightly (see sec. 2.3).

The second imperfection is the timing jitter induced by the population of the excited state with the time constant τ_{AE} according to sec. 7.1.2. In future experiments, this effect can be straightforwardly compensated for by using excitation pulses resonant with the C-transition and TPI of photons being emitted upon decay via the D-transition. The impact

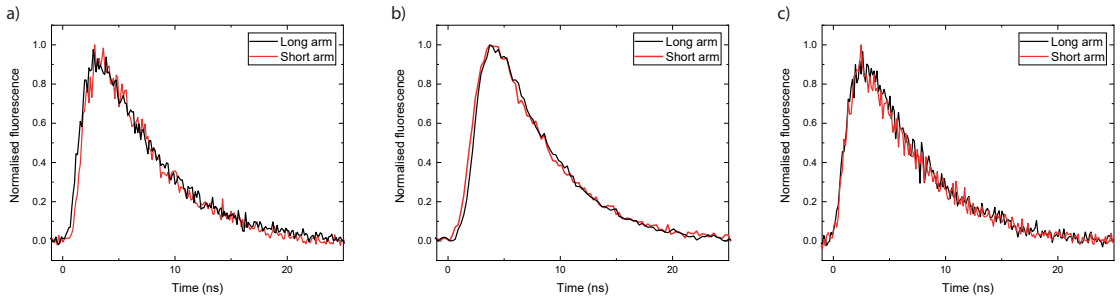

Figure 7.8: **Compensation of excitation delay in the MZI:** Measurement of the compensation of the time delay in the unbalanced MZI. Depicted are the photon wave packages after passing the long arm (black), respectively the short arm (red) for the compensation of **a)** $1\tau_{\mathrm{exc}}$, **b)** $3\tau_{\mathrm{exc}}$ and **c)** $13\tau_{\mathrm{exc}}$. The compensation is exact up to a residual timing mismatch δt of 263(23) ps, 289(22) ps and 65(25) ps.

of this population jitter on the visibility is discussed in sec. 2.3 and results, in combination with the timing mismatch and according to equation 2.97, in a visibility reduced by a factor of

$$\kappa(\tau_{\mathrm{AE}}, \delta t) = \frac{\tau_r^2 \exp(-\frac{|\delta t|}{\tau_r}) - \tau_r \tau_{\mathrm{AE}} \exp(-\frac{|\delta t|}{\tau_{\mathrm{AE}}})}{(\tau_r^2 - \tau_{\mathrm{AE}}^2)}. \tag{7.3}$$

We define the indistinguishability I as the achievable visibility if no experimental imperfections would be present. Thus, we can calculate it as

$$I = \frac{V}{\kappa(\tau_r, \delta t)} \tag{7.4}$$

yielding a value of I = 61.2(12.3)%. The remaining deviation from optimal indistinguishability is caused either by SD or PD. The impact of the two factors can in principle be distinguished, as they result in slightly different shapes of the TPI interference pattern. However, due to the limited statistics obtainable in reasonably long measurement time, the line shape cannot be unambiguously identified. We therefore fit the measurement taking only SD into account, as introduction of PD results in an additional free parameter but does not improve the accuracy of the fit. Furthermore, the measurements on EB3 below further justify the exclusion of PD. The fit yields a width of $\sigma_0 = 25(8)$ MHz, where we assume SD to be constant due to the fact that we cannot distinguish its impact with the visibility being only measured for one photon separation.
Due to the comparably low count rates of emitter EB2 and the corresponding measurement time of about 9.5 h, the filter setup was further optimised as described in sec. 3.2.3 and a higher NA objective (MPLN100x, Olympus) was used for the investigations on emitter EB3 afterwards. For this emitter, we find a count rate of about 3.2 kcts/s at a repetition rate of 37 MHz, reducing the measurement duration by about a factor of 2.5 in order to obtain a similar statistics as for EB2. Furthermore, we repeat the TPI experiment for all three sets of possible compensation delays that can be inserted into the unbalanced MZI. In Fig. 7.9 the results are depicted in the same fashion as for emitter EB2 above. For a compensation delay of $1\tau_{\mathrm{exc}}$, the visibility for the full photon wavepackage is limited to V = 37.8(4.1)% corresponding to a SD linewidth of $\sigma_0 = 37(7)$ MHz, while the maximum of visibility that can be reached with the population jitter τ_{AE} for this emitter is 84.2 %. For longer time separations between the interfering photons, the visibility amounts to V = 34.5(3.3)% and the SD linewidth to $\sigma_0 = 42(6)$ MHz ($3\tau_{\mathrm{exc}}$) and V = 33.8(4.6)%, $\sigma_0 = 43(10)$ MHz ($13\tau_{\mathrm{exc}}$).

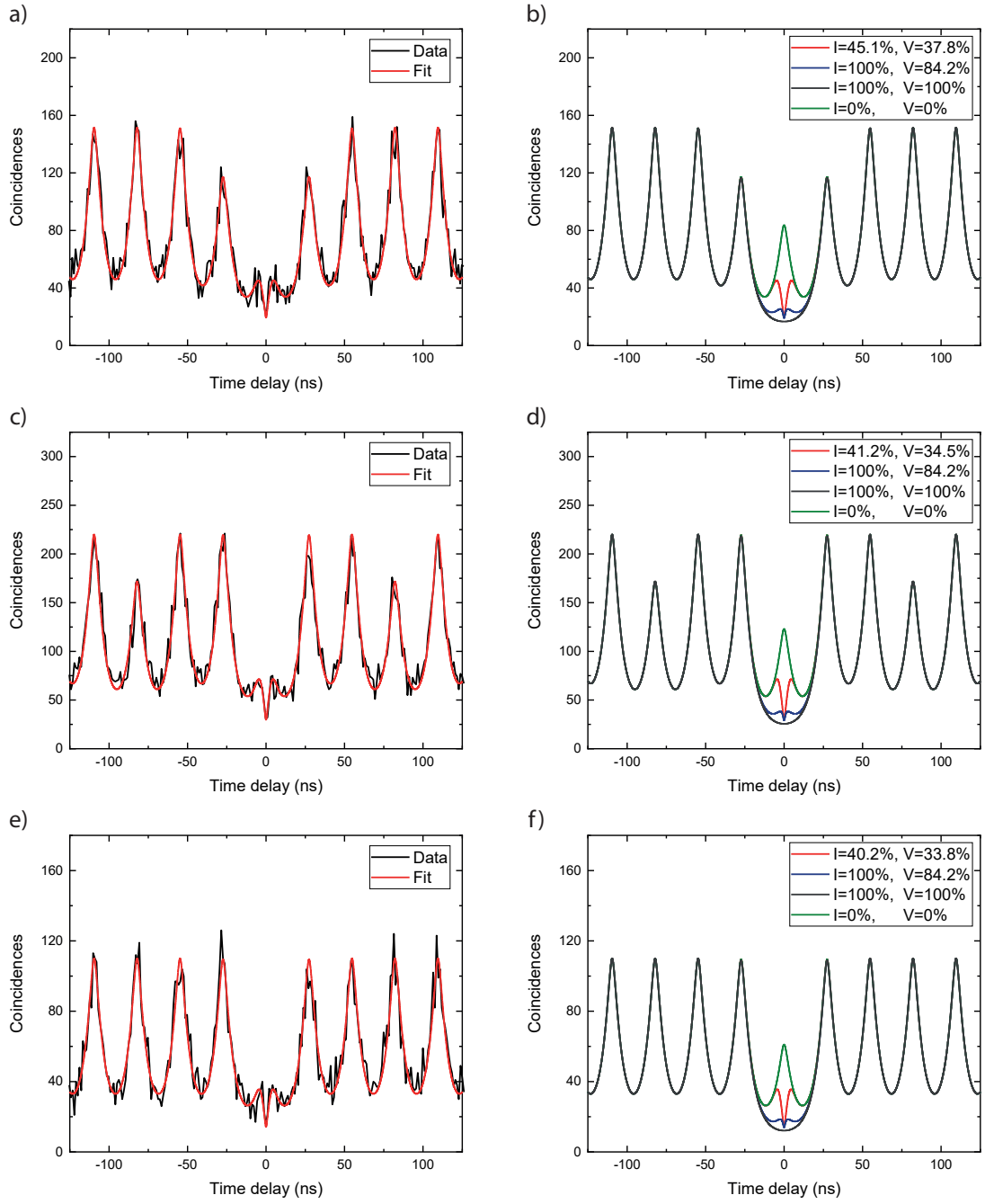

Figure 7.9: **TPI of photons emitted by EB3:** Measurements of the TPI at a MZI delay of **a)** $1\tau_{\text{exc}}$, **c)** $3\tau_{\text{exc}}$ and **e)** $13\tau_{\text{exc}}$ for photons emitted by EB3. In **b)**, **d)** and **f)** the comparison to the same extremal cases of interests as before is depicted, yielding V $=37.8(4.1)\%$, I$=45.1(4.1)\%$, V $=34.5(3.3)\%$, I$=41.2(4.1)\%$ and V $=33.8(4.6)\%$, I$=40.2(4.1)\%$.

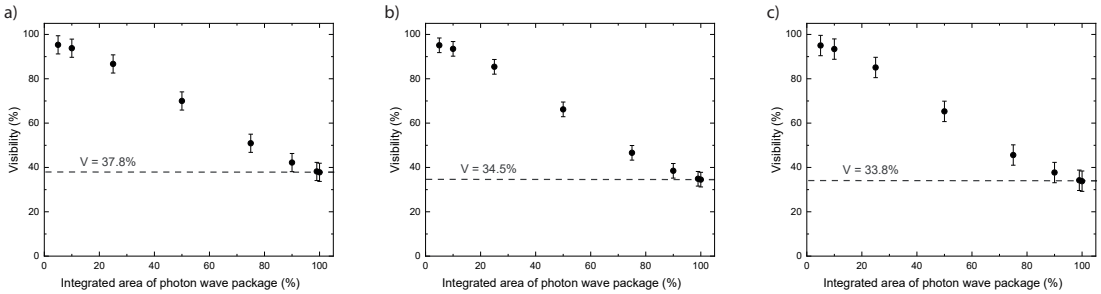

Figure 7.10: **Visibility dependence on time filtering:** The increase of the visibility of the TPI with narrower time filtering of the photon wave package contributing to the interference is depicted for the three delay cases **a)** $1\tau_{\mathrm{exc}}$, **b)** $3\tau_{\mathrm{exc}}$ and **c)** $13\tau_{\mathrm{exc}}$. As before, this comes with the tradeoff of longer integration times in any quantum communication protocol.

For all three cases, the effect of time filtering on the visibility is depicted in Fig. 7.10, yielding comparable results as for emitter EB2. All fits are carried out taking only the effect of SD into account, as it fits the shape of the TPI significantly better than the effect of PD. In Fig. 7.11 the comparison of the fits for the case of $3\tau_{\mathrm{exc}}$ is depicted. While the TPI is fitted well by the SD fit, the effect of PD overestimates the height of the peak and slightly underestimates the interference dip width. This effect, as illustrated for $3\tau_{\mathrm{exc}}$, occurs for all delay settings and is the reason why all fits are conducted including only the effect of SD.

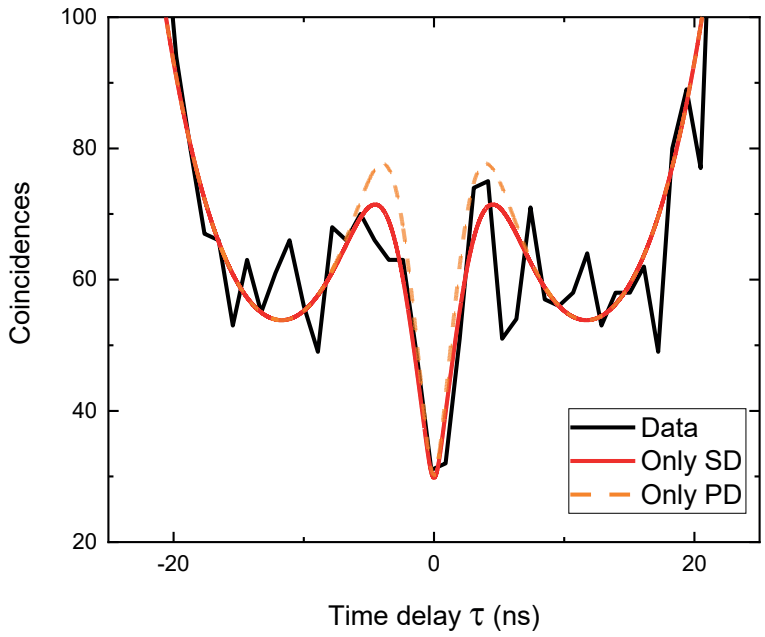

Figure 7.11: **Comparison of fitting SD or PD:** The dataset (black solid line) of the TPI retrieved on EB3 with a time delay of $3\tau_{\mathrm{exc}}$ is fitted once using SD as the free fitting parameter (red solid line) and a second time taking only PD into account. As it is valid for all excitation time delays, the fit relying only on PD significantly overestimates the peak height, while the dip width is slightly underestimated. The fit relying on SD reproduces the data more accurate.

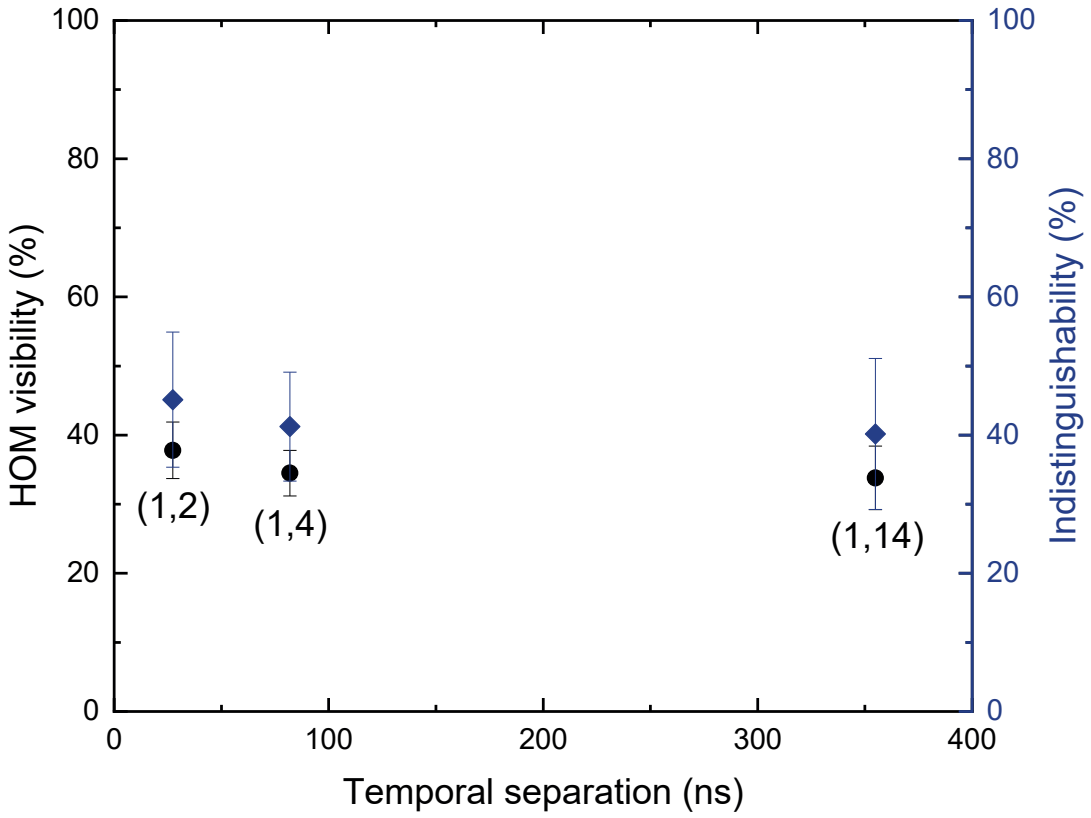

Figure 7.12: **Visibility and indistinguishability dependence on photon time separation:** Depicted are the visibility (black dots) as well as the indistinguishability (blue diamonds) of the photons emitted by EB3 against the time separation between the interfering photons. No significant decrease of visibility (indistinguishability) can be observed up to time delays exceeding 350 ns, which indicates at least two time scales contributing to the reduction of photon coherence. A rapid decoherence process reduces the visibility (indistinguishability) already on times shorter than 27 ns to below 40 % (50 %), corresponding to a SD linewidth of $\sigma_0 = 37(7)$ MHz. For the underlying spectral diffusion process we neglect any time dependence as this process obviously happens on a time scale $\tau_{SD} \ll \tau_{MZI}$. However, a second very slow process, the impact of which we cannot unveal on the time scales accessible in the TPI experiment, broadens the photon emission line on a minutes time scale to 198(9) MHz as found in sec. 7.1.4.

For all three settings, we extract the indistinguishabiliy using equation 7.4 as before and plot it together with the visibility in dependence on the time separation between two photons in Fig. 7.12. While the photons for a time separation of $13\tau_{exc}$ are delayed by more than 350 ns, no significant impact on the measured visibility respectively the indistinguishability is observed. This means that two separate effects are limiting the indistinguishability of the emitted photons: One fast effect that is responsible for the reduction of the indistinguishability I below 50 % even for photons being emitted about 27 ns apart from each other, corresponding to a spectral diffusion linewidth of about $\sigma_0 = 35$ MHz. The second effect has to occur on longer time scales than we can experimentally resolve in the TPI experiments and will lead to the broadening of the linewidth of the emitted photons to the measured FWHM linewidth of 198(9) MHz (corresponding to $\sigma_0 = 84(4)$ MHz) by scanning the filter lens in sec. 7.1.4, which takes about half an hour. While PD seems to be

a valid candidate for the fast process, especially since it occurs due to thermal heating of the diamond with the laser pulses, we are not confident identifying it as the source of the reduced visibilities, because, as mentioned above, it reproduces the data sets significantly worse than taking into accounts only SD. Therefore, we suspect two different processes of SD to limit the visibility. The fast process seems to occur only for higher laser powers, as we could not find indication of it in the long-term PLE scans discussed in sec. 6.1.5. It might be that upon the irradiation with large laser power multi-photon ionisations lead to a fluctuating charge environment which broaden the resonance by SD and thus lead to the decrease in visibility. The slower process is most likely due to SD on a slow time scale, which we could also distinguish for lower charge stabilisation and excitation powers in the long-term PLE scans, however, the broadening effect is more pronounced in the case of the quasi-resonant excitation scheme with large laser powers utilised in the TPI experiments. While we cannot rule out PD as the fast process mechanism due to thermal effects caused by the laser radiation, the effect of temperature on the TPI visibility can be investigated in future experiments by using resonant excitation of the SnV^- centres, which circumvents the population jitter τ_{AE} as well as heating effects due to the low laser power needed for π- pulse excitation. Temperature dependent measurement of the visibility will then give further insight on the decoherence mechanism.

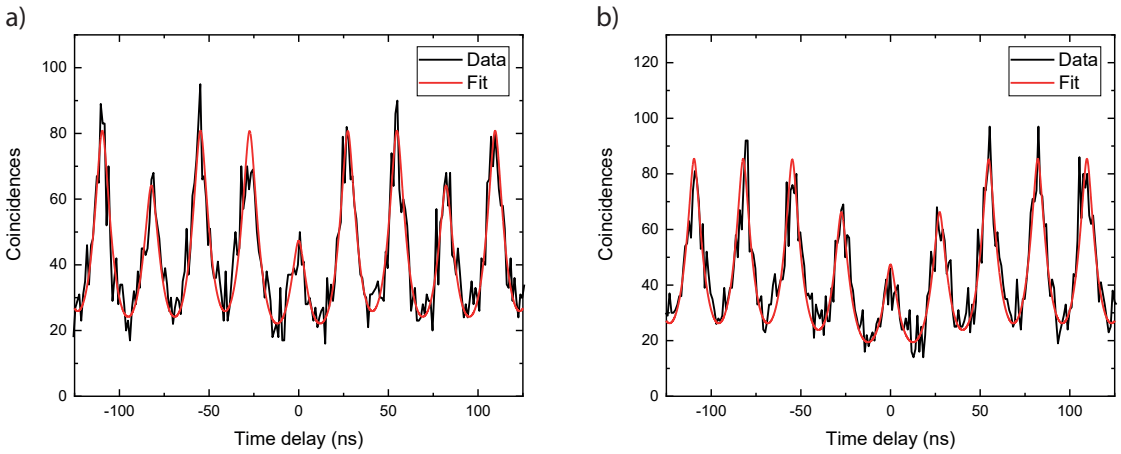

Figure 7.13: **TPI with distinguishable single photons:** The polarisation control in the long arm of the imbalanced MZI is used to set the polarisation states of the two photons orthogonal to each other at the second FBS. The resulting interference pattern is depicted for **a)** EB2 with a compensation delay of $3\tau_{exc}$ and **b)** EB3 with a compensation delay of $1\tau_{exc}$ used. The central peak is clearly observed and undiminished in comparison to the case of photons with parallel polarisation states. The data is fitted very well by the theoretical case of vanishing TPI with $I = 0\,\%$, $V = 0\,\%$. When leaving SD as a free parameter, the fit yields visibilities that cover $I = 0\,\%$, $V = 0\,\%$ within the margin of error.

7.2.2 Distinguishable consecutive photons

The measurement results above are exhibiting clear indication of TPI, however, proof of the interference pattern being the result of TPI interference can only be made by comparing the measurements to the case of the photons being distinguishable. In the imbalanced MZI used, rendering the photons distinguishable is straightforward. The polarisation control in the long arm of the interferometer can be used to set the polarisation state of the early photon orthogonal to the late photon when arriving at the second FBS. This is indicated

by a strongly reduced visibility of the classical interference fringes when laser light is sent through the interferometer (see sec. 3.2.3).
We repeat the TPI experiments for both single photon emitters for one delay setting each. For emitter EB2, the time delay is set to $3\tau_{\mathrm{exc}}$, while for emitter EB3 it is only $1\tau_{\mathrm{exc}}$. The results of the measurements are depicted in Fig. 7.13, where a clear central peak is observed and well fitted by the model with I = 0 %, V = 0 %. However, when leaving SD as a free parameter, the fit yields visibilities below 5 % with 0 % being covered by the error bars. Therefore, we conclude that no significant TPI is taking place and we are indeed measuring the classical pattern of non-interfering, distinguishable single photons. With this, we are sure to have measured and quantified the TPI of single photons resulting from SnV^- centres in diamond in the previous sections.

Chapter 8

Summary & Outlook

The first part of this chapter is dedicated to summarise the experimental achievements demonstrated within this thesis. It is followed by a potential roadmap sketching pathways to further explore and exploit the applicability of the SnV^- centre as a quantum bit.

Summary

During the course of this thesis, we extended the understanding of the SnV^- centre significantly by thorough spectroscopic investigations, the unravelling of its charge dynamics, exploration of its superior optical and spin coherence and even implementation of two-photon interference. These results lay the foundation to utilising the SnV^- centre in future applications and thus the main results are summarised in the following.

Spectroscopy

Within this thesis we explored the promising potential of the SnV^- centre in diamond as a quantum bit for application in QIP. This required a thorough study of its fundamental properties by spectroscopic means, aiming at fulfilling the first criterion of DiVincenzo of well characterising a potential qubit system. We found the SnV^- centre to be a pure and bright single photon emitter, the radiative lifetime of which is significantly influenced by the proximity to the diamond surface due to the change in the density of photonic states. Investigation of the temperature dependence of the linewidth and line position of the ZPL resonances revealed a dominant coupling of the SnV^- centre to a_{1g} symmetric phonons. Additionally, we confirmed the importance of mitigation of implantation induced lattice damage by comparison of SnV^- centres' photoluminescence spectra in samples annealed at 2100 °C and about 8 GPa, respectively at 1200 °C and in vacuum. Only in the HPHT annealed samples, SnV^- centres with narrow inhomogeneous ZPL distributions were found and even comparable between different samples, while the ZPLs are spread over several nanometers in LPLT treated samples. In these HPHT annealed samples, we measured the polarisation of the photon emission of single SnV^- centres, which confirmed the alignment of the centres along the <111> crystallographic axis of the diamond host lattice. Additionally, a characterisation of ground state splittings of several single emitters in a low-strained sample led to the conclusion that the value for an unstrained single SnV^- centre amounts to $\Delta_g = 818$ GHz. A further evaluation of the phononic sideband structure yielded remarkable overlap with the theoretically predicted spectrum, again confirming the electron-phonon interactions being dominated by phonons of a_{1g} symmetry. An additional indication of this was found by temperature dependent characterisation of the

Debye-Waller factor. The latter was quantified in our work to amount to 60 % of the total emitted photons being coherently emitted into the ZPL. We extended the understanding of the level structure of the SnV^- centre even further by spectroscopically investigating a higher lying excited state, which produced evidence that excitation at a wavelength of about 530 nm is resonant to an A_{2u} symmetric state broadened by coupling of the electron orbital to the diamond valence band states.

Charge cycle

After the spectroscopic characterisation of the SnV^- centre we started to unveil its charge dynamics. Under resonant excitation, the fluorescence of single SnV^- centres is terminated permanently, which we could attribute to a charge transfer to the doubly negative dark charge state SnV^{2-} induced by a single photon process. In a systematic study on the fluorescence enhancement of a resonantly excited ensemble of SnV^- centres when adding a second light field, we succeeded in determining the optimal wavelength for radiation induced recovery of the desired singly negative charge state SnV^-. Again, this was originating from a single photon process and we could retrieve evidence from the shape of the wavelength dependent charge stabilisation measurement that the process is based on driving the charge transition of the neutral divacancy to its negatively charged state. Eventually, these results enabled us to deduce a full four step charge cycle model of the SnV centre: First, a photon resonant with its ZPL of about 2 eV excites the SnV^- centre. In a second step, a subsequent 2 eV laser photon promotes an electron from the valence band to the lowest orbital of the SnV^- centre turning it into its optically inactive SnV^{2-} charge state. The third step consists of the charge transition of the neutral divacancy to its negatively charged state being induced by a photon with an energy exceeding 2.4 eV and leaving a hole in the valence band. Eventually, the hole migrates towards the colour centre, where it recombines with an electron from an orbital of the SnV^{2-} centre and thus closes the charge cycle by yielding the desired SnV^- charge state. This charge cycle is potentially universal to all G4V centres, which we could undermine by demonstrating a similar fluorescence enhancement of an ensemble of SiV^- centres under resonant excitation in dependence of the wavelength of a second light field added. Eventually, we exploited this understanding of the charge dynamics by demonstrating highly efficient (up to 97 %) and rapid (as fast as 10 µs) charge initialisation of the SnV^- centre.
The fundamental understanding of the charge processes enabled us to furthermore explore the optical coherence of single SnV^- centres. We confirmed the charge stabilised centres to be very pure single photon emitters by autocorrelation measurements on the stream of emitted photons. The coherent nature of the excitation process in these measurements was revealed as Rabi-oscillations being damped by the decoherence related to the excited state's radiative decay. We furthermore revealed by polarisation spectroscopy that the optically accessible C-transition exhibits a clear dipole pattern.

Optical and spin coherence

A major finding of this work was providing evidence of resonance linewidths of the SnV^- centre being fully limited by the lifetime of the excited state, which is of utmost importance in many QIP applications. Moreover, the optical coherence of the resonances of several SnV^- centres was found to be long-term stable up to an hour of measurement when applying the deduced charge stabilisation. This is an outstanding discovery for emitters situated in solid state material and a crucial finding for realisation of an efficient optical photon-qubit interface. In a first step to applicability, we exploited the optical coherence

by measuring pulsed Rabi-oscillations between an orbital ground and excited state.

Subsequently, we started investigating the spin coherence of single SnV^- centres by measuring the Zeeman splittings for varying magnetic field strengths, where we discovered a remarkable reproducibility for different emitters in the HPHT annealed samples. The latter is outstanding for colour centres hosted in a solid material, where typically large variations of strain influence the transition frequencies. We quantified the spin lifetime of the lowest orbital ground state's Zeeman split qubit to range between $T_1 = 15-22\,\mathrm{ms}$ at magnetic fields of $80-200\,\mathrm{mT}$ even though the large angle of 54.7° between magnetic field and symmetry axis of the defect centre allowed for spin mixing. In a further step, we explored the cyclicity of the spin-conserving transitions via optical pumping and unveiled a branching ratio of $\eta_{\mathrm{cycling}} = 850(150)$ being one order of magnitude larger than previously reported in LPLT annealed samples [114]. We exploited this feature by implementing a single-shot readout scheme as an important tool to measure the spin state in real time processing protocols. The fidelity of the readout amounted to $\mathcal{F} = 74\,\%$ in a $200\,\mu\mathrm{s}$ readout interval demonstrating meaningful and fast readout. Additionally, we extracted an initialisation efficiency of about 99 % within a time window of $200\,\mu\mathrm{s}$ with both these findings leading to fulfillment of the second and the fifth of DiVincenzo's criteria. As a further important measure, implementation of a coherent population trapping scheme enabled us to quantify the spin dephasing time to be $T_2^* = 5(1)\,\mu\mathrm{s}$, which is about a factor of four larger than reported in previous studies [114,176]. We thus demonstrated an important step towards fulfillment of the long relevant decoherence times put forth in the third DiVincenzo criterion.

Two-photon interference

In the final part of the thesis, we focussed on a further step towards realising the additional criterion of an efficient optical photon-qubit interface. Towards this end, we quantified the two-photon interference of photons retrieved from well characterised and absolutely pure single photon emitters. We therefore implemented an imbalanced Mach-Zehnder interferometer delaying emitted photons such as to compensate for the delay between the optical excitation pulses. This led to a fourth of the photons being overlapped at a 50:50 fibre-based beam splitter and brought to interference. We were able to determine the characteristic diminished coincidence rate at the output ports of the beam splitter inherent to partly indistinguishable photons. The extracted visibilities ranged from about 34 % up to 46 % for the full wavepackage of the photons being brought to interference. These were partly limited by avoidable technical imperfections as well as a timing jitter induced by the optical excitation into a higher lying excited state and its subsequent decay. Correcting for these effects, indistinguishabilities in between 40 % to 61 % were extracted from our fitting model. The remaining disparity from unity is most likely explained by a fast spectral diffusion process being introduced by the large amount of laser power necessary in the non-resonant excitation scheme used. We probed the time scale of the spectral diffusion by interfering photons delayed by 27 ns up to 351 ns, however, no significant decrease of the visibilities in this time window could be revealed. In contrast to this, we observed a significant broadening of the emitted photons linewidth on timescales of about half an hour, indicating an additional slow spectral diffusion effect. All of these effects should be avoidable in future experiments by switching to a resonant excitation scheme in which excitation pulses are carved from a continuous wave laser by an electro-optical amplitude modulator.

Conclusion

In conclusion, we have demonstrated the SnV^- centre in diamond to be an outstanding candidate for realisation of a qubit or quantum network node system in future QIP applications. It excels in terms of emitting highly coherent photons predominantly into its zero-phonon line over hourlong measurement times. Furthermore, by utilising the charge cycle scheme derived within this work, its desired negative charge state can be prepared on demand. The latter enables exploitation of the highly cycling transitions observable even in magnetic fields exhibiting a large angle with respect to the symmetry axis of the charge stabilised defect, allowing for efficient spin state initialisation and readout. For the SnV^- centre, long spin dephasing times of the qubit states can be reached at liquid helium temperatures of about 1.7 K, posing a significant improvement over the SiV^- centre as the currently most heavily researched G4V centre. Additionally, two-photon interference of photons emitted by SnV^- centres was demonstrated and thus photon-mediated entanglement of remote centres can be realised in future experiments. The next steps on the path towards applicability of the SnV^- centre in QIP is sketched in the following outlook.

Outlook

Based on the discoveries made within this thesis, we would like to highlight several pathways on improving and extending the performance of the SnV^- centre. Within this work, we demonstrated improved spin dephasing times by optically addressing a charge stabilised SnV^- centre in a coherent population scheme, however, pulsed control of the spin qubit was complicated by the large difference in transition strengths of spin-flipping (SF) and spin-conserving (SC) transitions. In a different study, this branching ratio was found to be smaller by one order of magnitude due to residual strain, thus simplifying coherent control [114]. Nevertheless, the demonstrated visibilities in Raman-Rabi oscillations and Ramsey interference experiments were limited. It is furthermore desirable to use unstrained emitters, as we could demonstrate within our work that their optical and spin properties are remarkably similar, thereby addressing the need for homogeneous and scalable quantum systems. We therefore conducted simulations on the Raman-Rabi transfer efficiency reachable using a typical set of parameters determined in this thesis. The schematic of the transfer is rather simple: It consists of one laser field addressing the SC A1 and another being applied to the SF A2 transition (see Fig. 8.1a)). Both of them can be off-resonant by the single-photon detuning Δ from the excited state, however, they need to be in two-photon resonance, meaning that they are detuned by the same amount. For the simulation of the transfer we prepare the qubit in state $|2\uparrow\rangle$ and apply both laser fields with equal Rabi frequency. The latter is important as simulations indicate the highest transfer efficiency for this scenario. In the case of a branching ratio of $\eta_{\text{cycling}} = 850$ this means that the laser power driving the SF transition needs to be almost three orders of magnitude larger than for driving the SC transition to achieve this aim. While this is not a fundamental problem it nevertheless complicates the transfer, as the strong laser applied to the SF transition will scatter photons off-resonantly on the SC transition. This results in a boundary condition on the Rabi frequency of the SF laser field. While larger Rabi frequencies are desirable as a fast transfer minimises the effect of dephasing within the ground state qubit, we set the limit to be such that the SF laser field causes only one percent of the total spin population to be scattered on the SC transition. The simulated transfer curve in Fig. 8.1a) yields the optimum for what would be achievable in the parameter regime explored within this thesis. The branching ratio is set to $\eta_{\text{cycling}} = 850$, the qubit splitting to $\Delta_{12} \approx 4\,\text{GHz}$

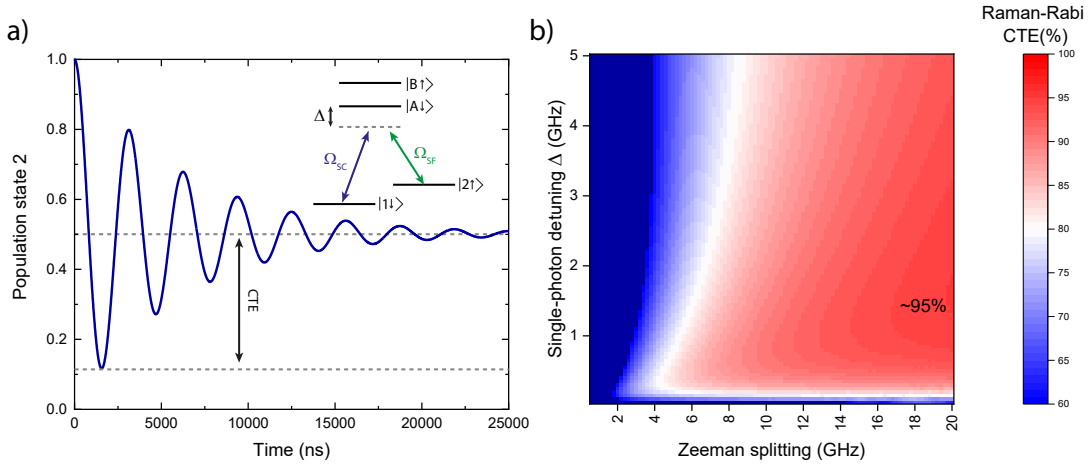

Figure 8.1: **Raman-Rabi transfer within the spin qubit of a SnV^- centre: a)** Simulation of a Raman-Rabi transfer between the spin qubit states of the SnV^- centre for typical parameters obtained in this thesis, specified in the main text. The Rabi-frequency of the laser field addressing the SF transition has to be kept small in order to avoid off-resonant photon scattering on the SC transition. Optimising the detuning of both lasers from resonance yields a CTE of about 79 % at a value of $\Delta \approx 350\,\mathrm{MHz}$. **b)** The CTE is simulated for variation of the detuning Δ and the qubit Zeeman splitting under the assumption that all parameters are invariant to changes in the magnetic field.

corresponding to a magnetic field of about 200 mT and the spin lifetime, respectively dephasing time, to $T_1 = 20\,\mathrm{ms}$ and $T_2^* = 5\,\mu\mathrm{s}$. The detuning corresponding to the optimal transfer efficiency amounts to $\Delta \approx 350\,\mathrm{MHz}$ for the Rabi frequencies at this setting being limited to $\Omega_{SF} = \Omega_{SC} = 15\,\mathrm{MHz}$. We define the coherent transfer efficiency (CTE) as the difference between the incoherent limit of 50 % population in each of the states and the first minimum of the oscillation. In order to quantify it in an intuitive manner, we normalise the obtained value by the incoherent limit. This definition is motivated by the fact that it covers the full impact of the decoherence within the transfer time, whereas simply taking the difference between the starting value of unity and the first minimum underestimates the effect. The CTE can be understood as the part of the transferred population which still retains the coherence information encoded in the Rabi oscillation. In the given case, the CTE amounts to about 79 %, which leaves the possibility for improvement. In Fig. 8.1b), we therefore display the CTE in dependence of the qubit splitting and the detuning Δ assuming that the parameters for the SnV^- centre do not change with the different magnetic field strengths needed for splitting up the qubit. The latter is a simplification as spin mixing will impact the branching ratio and the spin lifetime, however, discovering the full parameter set of the SnV^- centre's spin qubit for varying magnetic fields is subject to future studies. Nevertheless, the simulation gives an indication that it will be worth to explore the spin properties of the SnV^- centre in the presence of higher magnetic fields, which potentially have to be aligned to the symmetry axis of the defect in order to minimise the effects of spin mixing. On the other hand, spin mixing can potentially reduce the branching ratio and thus enabling faster and more efficient Raman-Rabi transfer, however, it will be hampering the qubit intialisation and single-shot readout as well as potentially reducing the spin coherence.

Having realised highly efficient Raman-Rabi transfer enables the coherent rotation of population from one to the other qubit state. However, the full control over the realisable

qubit superpositions requires control over the phase between the two states too. This can be done by means of Raman-Ramsey interference, which is straightforward to implement after having acquired the tool set given by the Raman-Rabi transfer. The whole sequence consists of two subsequent Raman-Rabi $\frac{\pi}{2}-$pulses separated by a variable time delay τ. Within the waiting time in between the pulses, the qubit states acquire a relative phase to each other as their absolute frequencies differ in energy by the Zeeman splitting. Thus, controlling the pulse separation precisely is equivalent to setting the desired phase relation between the two qubit states.
This full control over the single qubit space can then be exploited in order to decouple the spin states from their environment. In the most simple way, this is realised by application of a $\pi-$pulse in the middle of the Raman-Ramsey sequence and thus realising a Hahn-Echo measurement. The inversion of the population in the middle of the sequence leads to a rephasing in the case that the influential factor in the environment causing a dephasing remained constant over this time. Varying the delay and recording the populations of the spin states at the end of the sequence yields a first indication of realisable quantum memory times. Moreover, this sequence as well as other more complex decoupling schemes are ideally suited to reveal coupling of the electron spin to the magnetic field induced by nuclear spins in the proximity of the colour centre due to collapses observable in the echo signal [263]. This coupling can be exploited by careful timing of the echo sequences and enables the transfer of information to a nuclear spin [264], which can be either incorporated in a nearby ^{13}C or even the impurity atom of the SnV^- centre itself when choosing a tin isotope carrying a nuclear momentum. These nuclear spins are typically very long-lived and thus perfect candidates for a quantum memory [90]. Furthermore, several of these neighbouring quantum memorys can be set up as a register, enabling multimode operation mediated by a single SnV^- centre. The latter has been demonstrated by utilising the NV^- centre [90], however, no nuclear register has so far been implemented by means of a G4V centre as communication medium.
A further tool being required in QIP is the possibility of generating spin-photon entanglement. A suitable scheme for realising the entanglement with the SnV^- centre is adapted from reference [265] and depicted in Fig. 8.2. The spin qubit is firstly prepared in a coherent 50:50 superposition by a Raman-Rabi $\frac{\pi}{2}-$pulse, reading

$$\psi_{\text{init}} = \frac{|1\downarrow\rangle + |2\uparrow\rangle}{\sqrt{2}}.$$

Subsequently, an optical $\pi-$pulse on the A1 transition is applied so that in the case of the qubit being in state $|1\downarrow\rangle$ a photon with linear polarisation, here assumed to be horizontal, will be generated by the following decay on the C-transition. The sequence evolves, which is labelled path A in Fig. 8.2, by the photon being routed to an optical path in which its polarisation is rotated by 90° into the vertical state. Meanwhile, a Raman-Rabi $\pi-$pulse inverts the population of the spin qubit and the subsequently applied $\pi-$pulse on the A1 transition will therefore be off-resonant with any dipole-allowed transition and thus no further photon is generated. In the case that the qubit remained in state $|2\uparrow\rangle$ in the beginning of the sequence, no photon is generated in the first step. After application of the Raman-Rabi $\pi-$pulse, the $\pi-$pulse resonant with the A1 transition will now lead to an excitation and the generated horizontally polarised photon is routed to a second optical pathway. Its pathlength is shorter compared to the photon travelling in path A by exactly the amount of time needed for realisation of the Raman-Rabi $\pi-$pulse. Thus, the photons will arrive at the same time at a polarising beam splitter where they are overlapped. As both pathways are taken with the same likelihood, this results in the spin-photon entangled

state

$$\Psi_{\mathrm{SP}} = \frac{|1\downarrow\rangle\,|\mathrm{H}\rangle + |2\uparrow\rangle\,|\mathrm{V}\rangle}{2}$$

where detecting a photon being horizontally polarised in the output of the PBS means that the spin qubit is in state $|1\downarrow\rangle$, while a vertically polarised photon corresponds to the spin state $|2\uparrow\rangle$. However, there are certain difficulties to circumvent in this scheme.

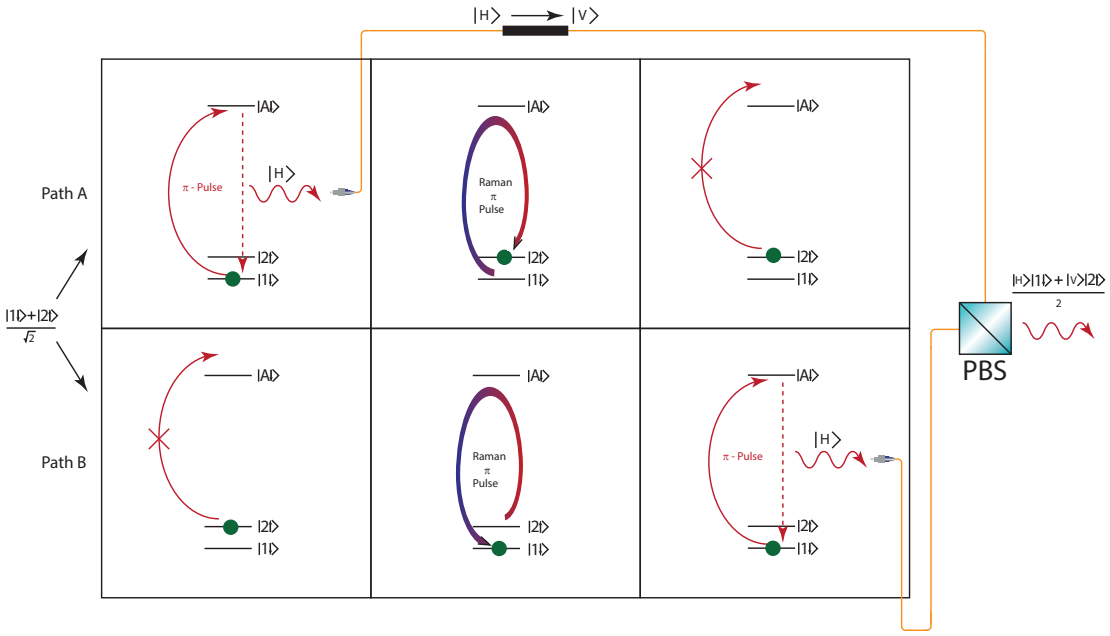

Figure 8.2: **Scheme for realising spin-photon entanglement with a SnV$^-$ centre:** After preparation of the SnV$^-$ centre's spin qubit in a coherent 50:50 superposition, an optical $\pi-$pulse resonant with the SC transition A1 is applied. If the qubit is read-out in state $|1\downarrow\rangle$, a horizontally polarised photon is emitted and switched to a optical pathway were the polarisation state is rotated to be vertical. Subsequently, the qubit states are inverted by a Raman-Rabi $\pi-$pulse and an additional $\pi-$pulse resonant with A1 is applied, which is now off-resonant and thus will not scatter a photon. For the case that the qubit was in state $|2\uparrow\rangle$ at the beginning of the sequence, it will end up in state $|1\downarrow\rangle$ at the end and thus the resonant pulse on A1 will produce a photon which is routed to a different pathway. The pathlenghts of both photons are matched so that they arrive simultaneously at a polarising beam splitter, where they are overlapped. The procedure generates spin-photon entanglement between the polarisation state of the photon and the qubit state of the SnV$^-$ centre. The figure is adapted for application to the SnV$^-$ centre with permission from reference [265].

First of all, it is difficult to separate the $\pi-$pulse resonant with the A1 transition from the emitted single photon as their frequencies are the same. There are several possibilities to overcome this problem, for example using an ultrashort excitation pulse, way shorter than the excited state lifetime, and gating the detectors measuring the photons in order to exclude laser photons. A second possibility is to use crossed polarisers in the excitation and the detection pathway, however, this means losing a significant amount of emitted single photons. A similar approach relies on application of the $\pi-$pulse to the SF transition A2 instead of A1, since the decay will most likely occur on the SC transition A1. In this case

the photon can be spectrally separated from the laser photons. However, unfortunately the large laser power required for a short $\pi-$rotation on transition A2 is significantly larger than for the SC transitions and potentially leads to off-resonant scattering effects. A more elegant approach is replacing the $\pi-$pulse on the A1 transition with a two-photon based $\pi-$pulse with a laser operating around 1240 nm. In this case, excitation and detection can be separated by means of standard optical filters. A further difficulty apart from the detection is the fast routing of the photons in path A and B to their respective optical pathways, which is challening but can be achieved using fast acousto- or electro-optical modulators.
By overcoming these difficulties, successful realisation of spin-photon entanglement will enable photon-mediated remote entanglement between distant SnV^- centres and thus the realisation of two-qubit gates as a basic requirement in quantum computing and quantum communication.
The scheme of implementing spin-photon entanglement can be extended even further for the generation of photonic cluster states. The basic principle is described in references [266, 267] and is simply based on the repetition of the spin-photon entanglement scheme described above. In that way, subsequently emitted photons will be entangled with each other, forming a cluster state. The size of this one-dimensional cluster state is ultimately only limited by the spin coherence time of the qubit. However, an efficient realisation of the protocol relies on photon extraction with close to unity collection efficiency. Even more restricting, the photons have to decay predominantly on the C transition instead of decays into the higher orbital ground state or even the phononic sideband. It is thus a crucial requirement having the SnV^- centre situated in a cavity which enhances solely the decay via transition C. This is a further boundary condition as it means that the cavity linewidth has to be significantly narrower than the ground state splitting of about 820 GHz. In addition to the narrow linewidth, the coupling needs to be strong enough so that the decay via transition A1 is ensured. These demands pose significant challenges for the fabrication of nanophotonic devices, however, their successful realisation would enable many more improvements such as enhancing the single-shot readout speed and fidelity significantly. Even more fascinating, by additional application of quantum frequency conversion [268,269] even hybrid entanglement with different quantum network nodes such as $^{40}Ca^+$ ions could be realised.

Bibliography

[1] Arute, F. *et al.* Quantum supremacy using a programmable superconducting processor. *Nature* **574**, 505–510 (2019). URL https://doi.org/10.1038/s41586-019-1666-5.

[2] Riedel, M. F., Binosi, D., Thew, R. & Calarco, T. The european quantum technologies flagship programme. *Quantum Science and Technology* **2**, 030501 (2017). URL https://doi.org/10.1088/2058-9565/aa6aca.

[3] Acín, A. *et al.* The quantum technologies roadmap: a european community view. *New Journal of Physics* **20**, 080201 (2018). URL https://doi.org/10.1088/1367-2630/aad1ea.

[4] Ludlow, A. D., Boyd, M. M., Ye, J., Peik, E. & Schmidt, P. O. Optical atomic clocks. *Rev. Mod. Phys.* **87**, 637–701 (2015). URL https://link.aps.org/doi/10.1103/RevModPhys.87.637.

[5] Degen, C. L. Scanning magnetic field microscope with a diamond single-spin sensor. *Applied Physics Letters* **92**, 243111 (2008). URL https://doi.org/10.1063/1.2943282.

[6] Balasubramanian, G. *et al.* Nanoscale imaging magnetometry with diamond spins under ambient conditions. *Nature* **455**, 648–651 (2008). URL https://doi.org/10.1038/nature07278.

[7] Marchiori, E. *et al.* Nanoscale magnetic field imaging for 2D materials. *Nature Reviews Physics* **4**, 49–60 (2022). URL https://doi.org/10.1038/s42254-021-00380-9.

[8] Oelker, E. *et al.* Demonstration of $4.8\text{x}10^{-17}$ stability at 1s for two independent optical clocks. *Nature Photonics* **13**, 714–719 (2019). URL https://doi.org/10.1038/s41566-019-0493-4.

[9] Celano, U. *et al.* Probing magnetic defects in ultra-scaled nanowires with optically detected spin resonance in nitrogen-vacancy center in diamond. *Nano Letters* **21**, 10409–10415 (2021). URL https://doi.org/10.1021/acs.nanolett.1c03723. PMID: 34882420.

[10] Georgescu, I. M., Ashhab, S. & Nori, F. Quantum simulation. *Rev. Mod. Phys.* **86**, 153–185 (2014). URL https://link.aps.org/doi/10.1103/RevModPhys.86.153.

[11] Feynman, R. P. Simulating physics with computers. *International Journal of Theoretical Physics* **21**, 467–488 (1982). URL https://doi.org/10.1007/BF02650179.

[12] Bernien, H. *et al.* Probing many-body dynamics on a 51-atom quantum simulator. *Nature* **551**, 579–584 (2017). URL https://doi.org/10.1038/nature24622.

[13] Zhang, J. *et al.* Observation of a many-body dynamical phase transition with a 53-qubit quantum simulator. *Nature* **551**, 601–604 (2017). URL https://doi.org/10.1038/nature24654.

[14] Chiu, C. S. *et al.* String patterns in the doped hubbard model. *Science* **365**, 251–256 (2019). URL https://www.science.org/doi/abs/10.1126/science.aav3587.

[15] Nichols, M. A. *et al.* Spin transport in a mott insulator of ultracold fermions. *Science* **363**, 383–387 (2019). URL https://www.science.org/doi/abs/10.1126/science.aat4387.

[16] Brown, P. T. *et al.* Bad metallic transport in a cold atom fermi-hubbard system. *Science* **363**, 379–382 (2019). URL https://www.science.org/doi/abs/10.1126/science.aat4134.

[17] Cirac, J. I. & Zoller, P. Goals and opportunities in quantum simulation. *Nature Physics* **8**, 264–266 (2012). URL https://doi.org/10.1038/nphys2275.

[18] Altman, E. *et al.* Quantum simulators: Architectures and opportunities. *PRX Quantum* **2**, 017003 (2021). URL https://link.aps.org/doi/10.1103/PRXQuantum.2.017003.

[19] Nielsen, M. A. & Chuang, I. L. *Quantum Computation and Quantum Information: 10th Anniversary Edition* (Cambridge University Press, 2010).

[20] Horodecki, R., Horodecki, P., Horodecki, M. & Horodecki, K. Quantum entanglement. *Rev. Mod. Phys.* **81**, 865–942 (2009). URL https://link.aps.org/doi/10.1103/RevModPhys.81.865.

[21] de Leon, N. P. *et al.* Materials challenges and opportunities for quantum computing hardware. *Science* **372**, eabb2823 (2021). URL https://www.science.org/doi/abs/10.1126/science.abb2823.

[22] Zhang, G., Cheng, Y., Chou, J.-P. & Gali, A. Material platforms for defect qubits and single-photon emitters. *Applied Physics Reviews* **7**, 031308 (2020). URL https://doi.org/10.1063/5.0006075.

[23] Xia, T. *et al.* Randomized benchmarking of single-qubit gates in a 2D array of neutral-atom qubits. *Phys. Rev. Lett.* **114**, 100503 (2015). URL https://link.aps.org/doi/10.1103/PhysRevLett.114.100503.

[24] Wang, Y., Kumar, A., Wu, T.-Y. & Weiss, D. S. Single-qubit gates based on targeted phase shifts in a 3D neutral atom array. *Science* **352**, 1562–1565 (2016). URL https://www.science.org/doi/abs/10.1126/science.aaf2581.

[25] Bruzewicz, C. D., Chiaverini, J., McConnell, R. & Sage, J. M. Trapped-ion quantum computing: Progress and challenges. *Applied Physics Reviews* **6**, 021314 (2019). URL https://doi.org/10.1063/1.5088164.

[26] Gustavsson, S. *et al.* Improving quantum gate fidelities by using a qubit to measure microwave pulse distortions. *Phys. Rev. Lett.* **110**, 040502 (2013). URL https://link.aps.org/doi/10.1103/PhysRevLett.110.040502.

[27] Barends, R. *et al.* Superconducting quantum circuits at the surface code threshold for fault tolerance. *Nature* **508**, 500–503 (2014). URL https://doi.org/10.1038/nature13171.

[28] Michler, P. *Quantum Dots for quantum information technologies* (Springer AG, 2017).

[29] Siyushev, P. *et al.* Coherent properties of single rare-earth spin qubits. *Nature Communications* **5**, 3895 (2014). URL https://doi.org/10.1038/ncomms4895.

[30] Raha, M. *et al.* Optical quantum nondemolition measurement of a single rare earth ion qubit. *Nature Communications* **11**, 1605 (2020). URL https://doi.org/10.1038/s41467-020-15138-7.

[31] Castelletto, S. & Boretti, A. Silicon carbide color centers for quantum applications. *Journal of Physics: Photonics* **2**, 022001 (2020). URL https://doi.org/10.1088/2515-7647/ab77a2.

[32] Pezzagna, S. & Meijer, J. Quantum computer based on color centers in diamond. *Applied Physics Reviews* **8**, 011308 (2021). URL https://doi.org/10.1063/5.0007444.

[33] Ruf, M., Wan, N. H., Choi, H., Englund, D. & Hanson, R. Quantum networks based on color centers in diamond. *Journal of Applied Physics* **130**, 070901 (2021). URL https://doi.org/10.1063/5.0056534.

[34] Becker, J. N. & Becher, C. Coherence properties and quantum control of silicon vacancy color centers in diamond. *physica status solidi (a)* **214**, 1700586 (2017). URL https://onlinelibrary.wiley.com/doi/abs/10.1002/pssa.201700586.

[35] DiVincenzo, D. P. The physical implementation of quantum computation. *Fortschritte der Physik* **48**, 771–783 (2000). URL https://onlinelibrary.wiley.com/doi/pdf/10.1002/1521-3978(200009)48:9/11<771::AID-PROP771>3.0.CO;2-E.

[36] Sukachev, D. D. *et al.* Silicon-vacancy spin qubit in diamond: A quantum memory exceeding 10 ms with single-shot state readout. *Phys. Rev. Lett.* **119**, 223602 (2017). URL https://link.aps.org/doi/10.1103/PhysRevLett.119.223602.

[37] Becker, J. N. *et al.* All-optical control of the silicon-vacancy spin in diamond at millikelvin temperatures. *Phys. Rev. Lett.* **120**, 053603 (2018). URL https://link.aps.org/doi/10.1103/PhysRevLett.120.053603.

[38] Diedrich, F., Bergquist, J. C., Itano, W. M. & Wineland, D. J. Laser cooling to the zero-point energy of motion. *Phys. Rev. Lett.* **62**, 403–406 (1989). URL https://link.aps.org/doi/10.1103/PhysRevLett.62.403.

[39] Valenzuela, S. O. *et al.* Microwave-induced cooling of a superconducting qubit. *Science* **314**, 1589–1592 (2006). URL https://www.science.org/doi/abs/10.1126/science.1134008.

[40] Ristè, D., van Leeuwen, J. G., Ku, H.-S., Lehnert, K. W. & DiCarlo, L. Initialization by measurement of a superconducting quantum bit circuit. *Phys. Rev. Lett.* **109**, 050507 (2012). URL https://link.aps.org/doi/10.1103/PhysRevLett.109.050507.

[41] Shor, P. W. Scheme for reducing decoherence in quantum computer memory. *Phys. Rev. A* **52**, R2493–R2496 (1995). URL https://link.aps.org/doi/10.1103/PhysRevA.52.R2493.

[42] Steane, A. M. Error correcting codes in quantum theory. *Phys. Rev. Lett.* **77**, 793–797 (1996). URL https://link.aps.org/doi/10.1103/PhysRevLett.77.793.

[43] Roffe, J. Quantum error correction: an introductory guide. *Contemporary Physics* **60**, 226–245 (2019). URL https://doi.org/10.1080/00107514.2019.1667078.

[44] Campbell, E. T., Terhal, B. M. & Vuillot, C. Roads towards fault-tolerant universal quantum computation. *Nature* **549**, 172–179 (2017). URL https://doi.org/10.1038/nature23460.

[45] Barenco, A. *et al.* Elementary gates for quantum computation. *Phys. Rev. A* **52**, 3457–3467 (1995). URL https://link.aps.org/doi/10.1103/PhysRevA.52.3457.

[46] Monroe, C., Meekhof, D. M., King, B. E., Itano, W. M. & Wineland, D. J. Demonstration of a fundamental quantum logic gate. *Phys. Rev. Lett.* **75**, 4714–4717 (1995). URL https://link.aps.org/doi/10.1103/PhysRevLett.75.4714.

[47] Pirandola, S. *et al.* Advances in quantum cryptography. *Adv. Opt. Photon.* **12**, 1012–1236 (2020). URL http://opg.optica.org/aop/abstract.cfm?URI=aop-12-4-1012.

[48] Wehner, S., Elkouss, D. & Hanson, R. Quantum internet: A vision for the road ahead. *Science* **362**, eaam9288 (2018). URL https://www.science.org/doi/abs/10.1126/science.aam9288.

[49] Acín, A. *et al.* Device-independent security of quantum cryptography against collective attacks. *Phys. Rev. Lett.* **98**, 230501 (2007). URL https://link.aps.org/doi/10.1103/PhysRevLett.98.230501.

[50] Kok, P. *et al.* Linear optical quantum computing with photonic qubits. *Rev. Mod. Phys.* **79**, 135–174 (2007). URL https://link.aps.org/doi/10.1103/RevModPhys.79.135.

[51] Brecht, B., Reddy, D. V., Silberhorn, C. & Raymer, M. G. Photon temporal modes: A complete framework for quantum information science. *Phys. Rev. X* **5**, 041017 (2015). URL https://link.aps.org/doi/10.1103/PhysRevX.5.041017.

[52] Ramelow, S., Ratschbacher, L., Fedrizzi, A., Langford, N. K. & Zeilinger, A. Discrete tunable color entanglement. *Phys. Rev. Lett.* **103**, 253601 (2009). URL https://link.aps.org/doi/10.1103/PhysRevLett.103.253601.

[53] Olislager, L. *et al.* Frequency-bin entangled photons. *Phys. Rev. A* **82**, 013804 (2010). URL https://link.aps.org/doi/10.1103/PhysRevA.82.013804.

[54] Reimer, C. *et al.* Generation of multiphoton entangled quantum states by means of integrated frequency combs. *Science* **351**, 1176–1180 (2016). URL https://www.science.org/doi/abs/10.1126/science.aad8532.

[55] Mair, A., Vaziri, A., Weihs, G. & Zeilinger, A. Entanglement of the orbital angular momentum states of photons. *Nature* **412**, 313–316 (2001). URL https://doi.org/10.1038/35085529.

[56] Loss, D. & Sukhorukov, E. V. Probing entanglement and nonlocality of electrons in a double-dot via transport and noise. *Phys. Rev. Lett.* **84**, 1035–1038 (2000). URL https://link.aps.org/doi/10.1103/PhysRevLett.84.1035.

[57] Awschalom, D. *et al.* Development of quantum interconnects (QuICs) for next-generation information technologies. *PRX Quantum* **2**, 017002 (2021). URL https://link.aps.org/doi/10.1103/PRXQuantum.2.017002.

[58] Wei, S.-H. *et al.* Towards real-world quantum networks: a review. *arXiv:2201.04802* (2022).

[59] Bouwmeester, D. *et al.* Experimental quantum teleportation. *Nature* **390**, 575–579 (1997). URL https://doi.org/10.1038/37539.

[60] Takeoka, M., Guha, S. & Wilde, M. M. Fundamental rate-loss tradeoff for optical quantum key distribution. *Nature Communications* **5**, 5235 (2014). URL https://doi.org/10.1038/ncomms6235.

[61] Pirandola, S., Laurenza, R., Ottaviani, C. & Banchi, L. Fundamental limits of repeaterless quantum communications. *Nature Communications* **8**, 15043 (2017). URL https://doi.org/10.1038/ncomms15043.

[62] Wootters, W. K. & Zurek, W. H. A single quantum cannot be cloned. *Nature* **299**, 802–803 (1982). URL https://doi.org/10.1038/299802a0.

[63] Briegel, H.-J., Dür, W., Cirac, J. I. & Zoller, P. Quantum repeaters: The role of imperfect local operations in quantum communication. *Phys. Rev. Lett.* **81**, 5932–5935 (1998). URL https://link.aps.org/doi/10.1103/PhysRevLett.81.5932.

[64] Atatüre, M., Englund, D., Vamivakas, N., Lee, S.-Y. & Wrachtrup, J. Material platforms for spin-based photonic quantum technologies. *Nature Reviews Materials* **3**, 38–51 (2018). URL https://doi.org/10.1038/s41578-018-0008-9.

[65] Harty, T. P. *et al.* High-fidelity preparation, gates, memory, and readout of a trapped-ion quantum bit. *Phys. Rev. Lett.* **113**, 220501 (2014). URL https://link.aps.org/doi/10.1103/PhysRevLett.113.220501.

[66] Wang, Y. *et al.* Single-qubit quantum memory exceeding ten-minute coherence time. *Nature Photonics* **11**, 646–650 (2017). URL https://doi.org/10.1038/s41566-017-0007-1.

[67] Brown, K. R. *et al.* Single-qubit-gate error below 10^{-4} in a trapped ion. *Phys. Rev. A* **84**, 030303 (2011). URL https://link.aps.org/doi/10.1103/PhysRevA.84.030303.

[68] Myerson, A. H. *et al.* High-fidelity readout of trapped-ion qubits. *Phys. Rev. Lett.* **100**, 200502 (2008). URL https://link.aps.org/doi/10.1103/PhysRevLett.100.200502.

[69] Pfister, A. D., Salz, M., Hettrich, M., Poschinger, U. G. & Schmidt-Kaler, F. A quantum repeater node with trapped ions: a realistic case example. *Applied Physics B* **122**, 89 (2016). URL https://doi.org/10.1007/s00340-016-6362-7.

[70] Kjaergaard, M. *et al.* Superconducting qubits: Current state of play. *Annual Review of Condensed Matter Physics* **11**, 369–395 (2020). URL https://doi.org/10.1146/annurev-conmatphys-031119-050605.

[71] Krantz, P. *et al.* Single-shot read-out of a superconducting qubit using a Josephson parametric oscillator. *Nature Communications* **7**, 11417 (2016). URL https://doi.org/10.1038/ncomms11417.

[72] Neuwirth, J. *et al.* Quantum dot technology for quantum repeaters: from entangled photon generation toward the integration with quantum memories. *Materials for Quantum Technology* **1**, 043001 (2021). URL https://doi.org/10.1088/2633-4356/ac3d14.

[73] Paul, M. *et al.* Single-photon emission at 1.55 μm from MOVPE-grown InAs quantum dots on InGaAs/GaAs metamorphic buffers. *Applied Physics Letters* **111**, 033102 (2017). URL https://doi.org/10.1063/1.4993935.

[74] Anderson, M. *et al.* Quantum teleportation using highly coherent emission from telecom C-band quantum dots. *npj Quantum Information* **6**, 14 (2020). URL https://doi.org/10.1038/s41534-020-0249-5.

[75] Press, D., Ladd, T. D., Zhang, B. & Yamamoto, Y. Complete quantum control of a single quantum dot spin using ultrafast optical pulses. *Nature* **456**, 218–221 (2008). URL https://doi.org/10.1038/nature07530.

[76] Tomm, N. *et al.* A bright and fast source of coherent single photons. *Nature Nanotechnology* **16**, 399–403 (2021). URL https://doi.org/10.1038/s41565-020-00831-x.

[77] Zhong, M. *et al.* Optically addressable nuclear spins in a solid with a six-hour coherence time. *Nature* **517**, 177–180 (2015). URL https://doi.org/10.1038/nature14025.

[78] Kindem, J. M. *et al.* Control and single-shot readout of an ion embedded in a nanophotonic cavity. *Nature* **580**, 201–204 (2020). URL https://doi.org/10.1038/s41586-020-2160-9.

[79] Serrano, D. *et al.* Ultra-narrow optical linewidths in rare-earth molecular crystals. *Nature* **603**, 241–246 (2022). URL https://doi.org/10.1038/s41586-021-04316-2.

[80] Bhatnagar, M. & Baliga, B. Comparison of 6H-SiC, 3C-SiC, and Si for power devices. *IEEE Transactions on Electron Devices* **40**, 645–655 (1993). URL https://doi.org/10.1109/16.199372.

[81] Babin, C. *et al.* Fabrication and nanophotonic waveguide integration of silicon carbide colour centres with preserved spin-optical coherence. *Nature Materials* **21**, 67–73 (2021). URL https://doi.org/10.1038/s41563-021-01148-3.

[82] Anderson, C. P. *et al.* Five-second coherence of a single spin with single-shot readout in silicon carbide. *Science Advances* **8**, eabm5912 (2022). URL https://www.science.org/doi/abs/10.1126/sciadv.abm5912.

[83] Udvarhelyi, P. *et al.* Vibronic states and their effect on the temperature and strain dependence of silicon-vacancy qubits in 4H-SiC. *Phys. Rev. Applied* **13**, 054017 (2020). URL https://link.aps.org/doi/10.1103/PhysRevApplied.13.054017.

[84] Kalb, N., Humphreys, P. C., Slim, J. J. & Hanson, R. Dephasing mechanisms of diamond-based nuclear-spin memories for quantum networks. *Phys. Rev. A* **97**, 062330 (2018). URL https://link.aps.org/doi/10.1103/PhysRevA.97.062330.

[85] Herbschleb, E. D. *et al.* Ultra-long coherence times amongst room-temperature solid-state spins. *Nature Communications* **10**, 3766 (2019). URL https://doi.org/10.1038/s41467-019-11776-8.

[86] Abobeih, M. H. *et al.* One-second coherence for a single electron spin coupled to a multi-qubit nuclear-spin environment. *Nature Communications* **9**, 2552 (2018). URL https://doi.org/10.1038/s41467-018-04916-z.

[87] Rong, X. *et al.* Experimental fault-tolerant universal quantum gates with solid-state spins under ambient conditions. *Nature Communications* **6**, 8748 (2015). URL https://doi.org/10.1038/ncomms9748.

[88] Irber, D. M. *et al.* Robust all-optical single-shot readout of nitrogen-vacancy centers in diamond. *Nature Communications* **12**, 532 (2021). URL https://doi.org/10.1038/s41467-020-20755-3.

[89] Maurer, P. C. *et al.* Room-temperature quantum bit memory exceeding one second. *Science* **336**, 1283–1286 (2012). URL https://www.science.org/doi/abs/10.1126/science.1220513.

[90] Bradley, C. E. *et al.* A ten-qubit solid-state spin register with quantum memory up to one minute. *Phys. Rev. X* **9**, 031045 (2019). URL https://link.aps.org/doi/10.1103/PhysRevX.9.031045.

[91] Cramer, J. *et al.* Repeated quantum error correction on a continuously encoded qubit by real-time feedback. *Nature Communications* **7**, 11526 (2016). URL https://doi.org/10.1038/ncomms11526.

[92] Xu, Z., qi Yin, Z., Han, Q. & Li, T. Quantum information processing with closely-spaced diamond color centers in strain and magnetic fields. *Opt. Mater. Express* **9**, 4654–4668 (2019). URL http://opg.optica.org/ome/abstract.cfm?URI=ome-9-12-4654.

[93] Bassett, L. C., Heremans, F. J., Yale, C. G., Buckley, B. B. & Awschalom, D. D. Electrical tuning of single nitrogen-vacancy center optical transitions enhanced by photoinduced fields. *Phys. Rev. Lett.* **107**, 266403 (2011). URL https://link.aps.org/doi/10.1103/PhysRevLett.107.266403.

[94] Tamarat, P. *et al.* Stark shift control of single optical centers in diamond. *Phys. Rev. Lett.* **97**, 083002 (2006). URL https://link.aps.org/doi/10.1103/PhysRevLett.97.083002.

[95] Pompili, M. *et al.* Realization of a multinode quantum network of remote solid-state qubits. *Science* **372**, 259–264 (2021). URL https://science.sciencemag.org/content/372/6539/259.

[96] Hensen, B. *et al.* Loophole-free bell inequality violation using electron spins separated by 1.3 kilometres. *Nature* **526**, 682 EP – (2015). URL https://doi.org/10.1038/nature15759.

[97] Faraon, A., Barclay, P. E., Santori, C., Fu, K.-M. C. & Beausoleil, R. G. Resonant enhancement of the zero-phonon emission from a colour centre in a diamond cavity. *Nature Photonics* **5**, 301–305 (2011). URL https://doi.org/10.1038/nphoton.2011.52.

[98] Riedel, D. *et al.* Deterministic enhancement of coherent photon generation from a nitrogen-vacancy center in ultrapure diamond. *Phys. Rev. X* **7**, 031040 (2017). URL https://link.aps.org/doi/10.1103/PhysRevX.7.031040.

[99] Hepp, C. *et al.* Electronic structure of the silicon vacancy color center in diamond. *Phys. Rev. Lett.* **112**, 036405 (2014). URL https://link.aps.org/doi/10.1103/PhysRevLett.112.036405.

[100] Thiering, G. & Gali, A. Ab initio magneto-optical spectrum of group-IV vacancy color centers in diamond. *Phys. Rev. X* **8**, 021063 (2018). URL https://link.aps.org/doi/10.1103/PhysRevX.8.021063.

[101] Bhaskar, M. K. *et al.* Experimental demonstration of memory-enhanced quantum communication. *Nature* **580**, 60–64 (2020). URL https://doi.org/10.1038/s41586-020-2103-5.

[102] Rogers, L. J. *et al.* Multiple intrinsically identical single-photon emitters in the solid state. *Nature Communications* **5**, 4739 (2014). URL https://doi.org/10.1038/ncomms5739.

[103] Sipahigil, A. *et al.* Indistinguishable photons from separated silicon-vacancy centers in diamond. *Phys. Rev. Lett.* **113**, 113602 (2014). URL https://link.aps.org/doi/10.1103/PhysRevLett.113.113602.

[104] Sipahigil, A. *et al.* An integrated diamond nanophotonics platform for quantum-optical networks. *Science* **354**, 847–850 (2016). URL https://science.sciencemag.org/content/354/6314/847.

[105] Nguyen, C. T. *et al.* Quantum network nodes based on diamond qubits with an efficient nanophotonic interface. *Phys. Rev. Lett.* **123**, 183602 (2019). URL https://link.aps.org/doi/10.1103/PhysRevLett.123.183602.

[106] Metsch, M. H. *et al.* Initialization and readout of nuclear spins via a negatively charged silicon-vacancy center in diamond. *Phys. Rev. Lett.* **122**, 190503 (2019). URL https://link.aps.org/doi/10.1103/PhysRevLett.122.190503.

[107] Bradac, C., Gao, W., Forneris, J., Trusheim, M. E. & Aharonovich, I. Quantum nanophotonics with group IV defects in diamond. *Nature Communications* **10**, 5625 (2019). URL https://doi.org/10.1038/s41467-019-13332-w.

[108] Siyushev, P. *et al.* Optical and microwave control of germanium-vacancy center spins in diamond. *Phys. Rev. B* **96**, 081201 (2017). URL https://link.aps.org/doi/10.1103/PhysRevB.96.081201.

[109] Nguyen, M. *et al.* Photodynamics and quantum efficiency of germanium vacancy color centers in diamond. *Advanced Photonics* **1**, 1 – 7 (2019). URL https://doi.org/10.1117/1.AP.1.6.066002.

[110] Bhaskar, M. K. *et al.* Quantum nonlinear optics with a germanium-vacancy color center in a nanoscale diamond waveguide. *Phys. Rev. Lett.* **118**, 223603 (2017). URL https://link.aps.org/doi/10.1103/PhysRevLett.118.223603.

[111] Høy Jensen, R. *et al.* Cavity-enhanced photon emission from a single germanium-vacancy center in a diamond membrane. *Phys. Rev. Applied* **13**, 064016 (2020). URL https://link.aps.org/doi/10.1103/PhysRevApplied.13.064016.

[112] Boldyrev, K., Mavrin, B., Sherin, P. & Popova, M. Bright luminescence of diamonds with Ge-V centers. *Journal of Luminescence* **193**, 119–124 (2018). URL https://www.sciencedirect.com/science/article/pii/S0022231317308207.

[113] Iwasaki, T. *et al.* Tin-vacancy quantum emitters in diamond. *Phys. Rev. Lett.* **119**, 253601 (2017). URL https://link.aps.org/doi/10.1103/PhysRevLett.119.253601.

[114] Debroux, R. *et al.* Quantum control of the tin-vacancy spin qubit in diamond. *Phys. Rev. X* **11**, 041041 (2021). URL https://link.aps.org/doi/10.1103/PhysRevX.11.041041.

[115] Tchernij, S. D. *et al.* Spectral features of Pb-related color centers in diamond – a systematic photoluminescence characterization. *New Journal of Physics* **23**, 063032 (2021). URL https://doi.org/10.1088/1367-2630/ac038a.

[116] Ditalia Tchernij, S. *et al.* Single-photon emitters in lead-implanted single-crystal diamond. *ACS Photonics* **5**, 4864–4871 (2018). URL https://doi.org/10.1021/acsphotonics.8b01013.

[117] Trusheim, M. E. *et al.* Lead-related quantum emitters in diamond. *Phys. Rev. B* **99**, 075430 (2019). URL https://link.aps.org/doi/10.1103/PhysRevB.99.075430.

[118] Zhou, Y. *et al.* Direct writing of single germanium vacancy center arrays in diamond. *New Journal of Physics* **20**, 125004 (2018). URL https://doi.org/10.1088/1367-2630/aaf2ac.

[119] Wang, P., Taniguchi, T., Miyamoto, Y., Hatano, M. & Iwasaki, T. Low-temperature spectroscopic investigation of lead-vacancy centers in diamond fabricated by high-pressure and high-temperature treatment. *ACS Photonics* **8**, 2947–2954 (2021). URL https://doi.org/10.1021/acsphotonics.1c00840.

[120] Jahnke, K. D. *et al.* Electron–phonon processes of the silicon-vacancy centre in diamond. *New Journal of Physics* **17**, 043011 (2015). URL https://doi.org/10.1088%2F1367-2630%2F17%2F4%2F043011.

[121] Müller, T. *et al.* Optical signatures of silicon-vacancy spins in diamond. *Nature Communications* **5**, 3328 (2014). URL https://doi.org/10.1038/ncomms4328.

[122] Stoneham, A. M. Non-radiative transitions in semiconductors. *Reports on Progress in Physics* **44**, 1251–1295 (1981). URL https://doi.org/10.1088/0034-4885/44/12/001.

[123] Rogers, L. How far into the infrared can a colour centre in diamond emit? *Physics Procedia* **3**, 1557–1561 (2010). URL https://www.sciencedirect.com/science/article/pii/S1875389210002221.

[124] Hadden, J. P. *et al.* Strongly enhanced photon collection from diamond defect centers under microfabricated integrated solid immersion lenses. *Applied Physics Letters* **97**, 241901 (2010). URL https://doi.org/10.1063/1.3519847.

[125] Marseglia, L. *et al.* Nanofabricated solid immersion lenses registered to single emitters in diamond. *Applied Physics Letters* **98**, 133107 (2011). URL https://doi.org/10.1063/1.3573870.

[126] Jamali, M. *et al.* Microscopic diamond solid-immersion-lenses fabricated around single defect centers by focused ion beam milling. *Review of Scientific Instruments* **85**, 123703 (2014). URL https://doi.org/10.1063/1.4902818.

[127] Riedrich-Möller, J. *et al.* Nanoimplantation and purcell enhancement of single nitrogen-vacancy centers in photonic crystal cavities in diamond. *Applied Physics Letters* **106**, 221103 (2015). URL https://doi.org/10.1063/1.4922117.

[128] Jung, T. *et al.* Spin measurements of NV centers coupled to a photonic crystal cavity. *APL Photonics* **4**, 120803 (2019). URL https://doi.org/10.1063/1.5120120.

[129] Nguyen, C. T. *et al.* An integrated nanophotonic quantum register based on silicon-vacancy spins in diamond. *Phys. Rev. B* **100**, 165428 (2019). URL https://link.aps.org/doi/10.1103/PhysRevB.100.165428.

[130] Dolde, F. *et al.* Room-temperature entanglement between single defect spins in diamond. *Nature Physics* **9**, 139–143 (2013). URL https://doi.org/10.1038/nphys2545.

[131] Hunold, L. *et al.* Scalable creation of deep silicon-vacancy color centers in diamond by ion implantation through a 1-μm pinhole. *Advanced Quantum Technologies* **4**, 2100079 (2021). URL https://onlinelibrary.wiley.com/doi/abs/10.1002/qute.202100079.

[132] Tchernij, S. D. *et al.* Single-photon-emitting optical centers in diamond fabricated upon Sn implantation. *ACS Photonics* **4**, 2580–2586 (2017). URL https://doi.org/10.1021/acsphotonics.7b00904.

[133] Wan, N. H. *et al.* Large-scale integration of artificial atoms in hybrid photonic circuits. *Nature* **583**, 226–231 (2020). URL https://doi.org/10.1038/s41586-020-2441-3.

[134] Lindner, S. *et al.* Strongly inhomogeneous distribution of spectral properties of silicon-vacancy color centers in nanodiamonds. *New Journal of Physics* **20**, 115002 (2018). URL http://dx.doi.org/10.1088/1367-2630/aae93f.

[135] Iwasaki, T. *et al.* Germanium-vacancy single color centers in diamond. *Scientific Reports* **5**, 12882 (2015). URL https://doi.org/10.1038/srep12882.

[136] Görlitz, J. *et al.* Spectroscopic investigations of negatively charged tin-vacancy centres in diamond. *New Journal of Physics* **22**, 013048 (2020). URL https://doi.org/10.1088/1367-2630/ab6631.

[137] Gardill, A. *et al.* Probing charge dynamics in diamond with an individual color center. *Nano Letters* **21**, 6960–6966 (2021). URL https://doi.org/10.1021/acs.nanolett.1c02250.

[138] Görlitz, J. *et al.* Coherence of a charge stabilised tin-vacancy spin in diamond. *arXiv:2110.05451, accepted for publication at npj quantum information* (2021).

[139] de Lange, G., Wang, Z. H., Ristè, D., Dobrovitski, V. V. & Hanson, R. Universal dynamical decoupling of a single solid-state spin from a spin bath. *Science* **330**, 60–63 (2010). URL https://www.science.org/doi/abs/10.1126/science.1192739.

[140] Ishikawa, T. *et al.* Optical and spin coherence properties of nitrogen-vacancy centers placed in a 100 nm thick isotopically purified diamond layer. *Nano Letters* **12**, 2083–2087 (2012). URL https://doi.org/10.1021/nl300350r.

[141] Schreck, M., Gsell, S., Brescia, R. & Fischer, M. Ion bombardment induced buried lateral growth: the key mechanism for the synthesis of single crystal diamond wafers. *Scientific Reports* **7**, 44462 (2017). URL https://doi.org/10.1038/srep44462.

[142] Ohno, K. *et al.* Engineering shallow spins in diamond with nitrogen delta-doping. *Applied Physics Letters* **101**, 082413 (2012). URL https://doi.org/10.1063/1.4748280.

[143] McLellan, C. A. *et al.* Patterned formation of highly coherent nitrogen-vacancy centers using a focused electron irradiation technique. *Nano Letters* **16**, 2450–2454 (2016). URL https://doi.org/10.1021/acs.nanolett.5b05304.

[144] Huang, Z. *et al.* Diamond nitrogen-vacancy centers created by scanning focused helium ion beam and annealing. *Applied Physics Letters* **103**, 081906 (2013). URL https://doi.org/10.1063/1.4819339.

[145] Ohno, K. *et al.* Three-dimensional localization of spins in diamond using ^{12}C implantation. *Applied Physics Letters* **105**, 052406 (2014). URL https://doi.org/10.1063/1.4890613.

[146] Chen, Y.-C. *et al.* Laser writing of coherent colour centres in diamond. *Nature Photonics* **11**, 77–80 (2017). URL https://doi.org/10.1038/nphoton.2016.234.

[147] Neu, E. *et al.* Single photon emission from silicon-vacancy colour centres in chemical vapour deposition nano-diamonds on iridium. *New Journal of Physics* **13**, 025012 (2011). URL https://doi.org/10.1088%2F1367-2630%2F13%2F2%2F025012.

[148] De Feudis, M. *et al.* Large-scale fabrication of highly emissive nanodiamonds by chemical vapor deposition with controlled doping by SiV and GeV centers from a solid source. *Advanced Materials Interfaces* **7**, 1901408 (2020). URL https://onlinelibrary.wiley.com/doi/abs/10.1002/admi.201901408.

[149] Westerhausen, M. T. *et al.* Controlled doping of GeV and SnV color centers in diamond using chemical vapor deposition. *ACS Applied Materials & Interfaces* **12**, 29700–29705 (2020). URL https://doi.org/10.1021/acsami.0c07242.

[150] Neu, E. *et al.* Narrowband fluorescent nanodiamonds produced from chemical vapor deposition films. *Applied Physics Letters* **98**, 243107 (2011). URL https://doi.org/10.1063/1.3599608.

[151] Shimazaki, K. *et al.* Fabrication of detonation nanodiamonds containing silicon-vacancy color centers by high temperature annealing. *physica status solidi (a)* **218**, 2100144 (2021). URL https://onlinelibrary.wiley.com/doi/abs/10.1002/pssa.202100144.

[152] Schell, A. W. *et al.* A scanning probe-based pick-and-place procedure for assembly of integrated quantum optical hybrid devices. *Review of Scientific Instruments* **82**, 073709 (2011). URL https://doi.org/10.1063/1.3615629.

[153] Bolshakov, A. *et al.* Photoluminescence of SiV centers in single crystal CVD diamond in situ doped with Si from silane. *physica status solidi (a)* **212**, 2525–2532 (2015). URL https://onlinelibrary.wiley.com/doi/abs/10.1002/pssa.201532174.

[154] Ziegler, J. F., Ziegler, M. & Biersack, J. SRIM - the stopping and range of ions in matter (2010). *Nuclear Instruments and Methods in Physics Research Section B: Beam Interactions with Materials and Atoms* **268**, 1818–1823 (2010). URL https://www.sciencedirect.com/science/article/pii/S0168583X10001862. 19th International Conference on Ion Beam Analysis.

[155] Pezzagna, S. *et al.* Nanoscale engineering and optical addressing of single spins in diamond. *Small* **6**, 2117–2121 (2010). URL https://onlinelibrary.wiley.com/doi/abs/10.1002/smll.201000902.

[156] Schröder, T. *et al.* Scalable focused ion beam creation of nearly lifetime-limited single quantum emitters in diamond nanostructures. *Nature Communications* **8**, 15376 (2017). URL https://doi.org/10.1038/ncomms15376.

[157] Shinada, T., Okamoto, S., Kobayashi, T. & Ohdomari, I. Enhancing semiconductor device performance using ordered dopant arrays. *Nature* **437**, 1128–1131 (2005). URL https://doi.org/10.1038/nature04086.

[158] Jamieson, D. N. *et al.* Controlled shallow single-ion implantation in silicon using an active substrate for sub-20-keV ions. *Applied Physics Letters* **86**, 202101 (2005). URL https://doi.org/10.1063/1.1925320.

[159] Groot-Berning, K. *et al.* Deterministic single-ion implantation of rare-earth ions for nanometer-resolution color-center generation. *Phys. Rev. Lett.* **123**, 106802 (2019). URL https://link.aps.org/doi/10.1103/PhysRevLett.123.106802.

[160] Groot-Berning, K., Jacob, G., Osterkamp, C., Jelezko, F. & Schmidt-Kaler, F. Fabrication of ^{15}NV- centers in diamond using a deterministic single ion implanter. *New Journal of Physics* **23**, 063067 (2021). URL https://doi.org/10.1088/1367-2630/ac0753.

[161] Räcke, P., Spemann, D., Gerlach, J. W., Rauschenbach, B. & Meijer, J. Detection of small bunches of ions using image charges. *Scientific Reports* **8**, 9781 (2018). URL https://doi.org/10.1038/s41598-018-28167-6.

[162] Chen, Y.-C. *et al.* Laser writing of individual nitrogen-vacancy defects in diamond with near-unity yield. *Optica* **6**, 662–667 (2019). URL http://www.osapublishing.org/optica/abstract.cfm?URI=optica-6-5-662.

[163] Fröch, J. E. *et al.* Versatile direct-writing of dopants in a solid state host through recoil implantation. *Nature Communications* **11**, 5039 (2020). URL https://doi.org/10.1038/s41467-020-18749-2.

[164] Goss, J. P., Jones, R., Breuer, S. J., Briddon, P. R. & Öberg, S. The twelve-line 1.682 eV luminescence center in diamond and the vacancy-silicon complex. *Phys. Rev. Lett.* **77**, 3041–3044 (1996). URL https://link.aps.org/doi/10.1103/PhysRevLett.77.3041.

[165] Thiering, G. & Gali, A. Characterization of oxygen defects in diamond by means of density functional theory calculations. *Phys. Rev. B* **94**, 125202 (2016). URL https://link.aps.org/doi/10.1103/PhysRevB.94.125202.

[166] Neu, E., Fischer, M., Gsell, S., Schreck, M. & Becher, C. Fluorescence and polarization spectroscopy of single silicon vacancy centers in heteroepitaxial nanodiamonds on iridium. *Phys. Rev. B* **84**, 205211 (2011). URL https://link.aps.org/doi/10.1103/PhysRevB.84.205211.

[167] D'Haenens-Johansson, U. F. S. *et al.* Optical properties of the neutral silicon split-vacancy center in diamond. *Phys. Rev. B* **84**, 245208 (2011). URL https://link.aps.org/doi/10.1103/PhysRevB.84.245208.

[168] Wahl, U. *et al.* Direct structural identification and quantification of the split-vacancy configuration for implanted Sn in diamond. *Phys. Rev. Lett.* **125**, 045301 (2020). URL https://link.aps.org/doi/10.1103/PhysRevLett.125.045301.

[169] Stacey, A. *et al.* Depletion of nitrogen-vacancy color centers in diamond via hydrogen passivation. *Applied Physics Letters* **100**, 071902 (2012). URL https://doi.org/10.1063/1.3684612.

[170] Hepp, C. *Electronic structure of the silicon vacancy color center in diamond*. Ph.D. thesis, Universität des Saarlandes (2014).

[171] Gali, A. & Maze, J. R. Ab initio study of the split silicon-vacancy defect in diamond: Electronic structure and related properties. *Phys. Rev. B* **88**, 235205 (2013). URL https://link.aps.org/doi/10.1103/PhysRevB.88.235205.

[172] Häußler, S. *et al.* Photoluminescence excitation spectroscopy of SiV^- and GeV^- color center in diamond. *New Journal of Physics* **19**, 063036 (2017). URL https://doi.org/10.1088%2F1367-2630%2Faa73e5.

[173] Walker, J. Optical absorption and luminescence in diamond. *Reports on Progress in Physics* **42**, 1605–1659 (1979). URL https://doi.org/10.1088/0034-4885/42/10/001.

[174] Ham, F. S. Dynamical Jahn-Teller effect in paramagnetic resonance spectra: Orbital reduction factors and partial quenching of spin-orbit interaction. *Phys. Rev.* **138**, A1727–A1740 (1965). URL https://link.aps.org/doi/10.1103/PhysRev.138.A1727.

[175] Ekimov, E. A. *et al.* Germanium-vacancy color center in isotopically enriched diamonds synthesized at high pressures. *JETP Letters* **102**, 701–706 (2015). URL https://doi.org/10.1134/S0021364015230034.

[176] Trusheim, M. E. *et al.* Transform-limited photons from a coherent tin-vacancy spin in diamond. *Phys. Rev. Lett.* **124**, 023602 (2020). URL https://link.aps.org/doi/10.1103/PhysRevLett.124.023602.

[177] Davies, G. The Jahn-Teller effect and vibronic coupling at deep levels in diamond. *Reports on Progress in Physics* **44**, 787–830 (1981). URL https://doi.org/10.1088/0034-4885/44/7/003.

[178] Gaebel, T. *et al.* Stable single-photon source in the near infrared. *New Journal of Physics* **6**, 98–98 (2004). URL https://doi.org/10.1088/1367-2630/6/1/098.

[179] Becker, J. N., Görlitz, J., Arend, C., Markham, M. & Becher, C. Ultrafast all-optical coherent control of single silicon vacancy colour centres in diamond. *Nature Communications* **7**, 13512 EP – (2016). URL https://doi.org/10.1038/ncomms13512. Article.

[180] Sohn, Y.-I. *et al.* Controlling the coherence of a diamond spin qubit through its strain environment. *Nature Communications* **9**, 2012 (2018). URL https://doi.org/10.1038/s41467-018-04340-3.

[181] Sigalas, M. M. & Economou, E. N. Elastic and acoustic wave band structure. *Journal of Sound and Vibration* **158**, 377–382 (1992). URL https://www.sciencedirect.com/science/article/pii/0022460X92900597.

[182] Kushwaha, M. S., Halevi, P., Dobrzynski, L. & Djafari-Rouhani, B. Acoustic band structure of periodic elastic composites. *Phys. Rev. Lett.* **71**, 2022–2025 (1993). URL https://link.aps.org/doi/10.1103/PhysRevLett.71.2022.

[183] Fuchs, P. *Theoretische und praktische Implementierung nanophotonischer Strukturen in Diamant.* Master's thesis, Universität des Saarlandes (2016).

[184] Mi, S., Kiss, M., Graziosi, T. & Quack, N. Integrated photonic devices in single crystal diamond. *Journal of Physics: Photonics* **2**, 042001 (2020). URL https://doi.org/10.1088/2515-7647/aba171.

[185] Janitz, E., Bhaskar, M. K. & Childress, L. Cavity quantum electrodynamics with color centers in diamond. *Optica* **7**, 1232–1252 (2020). URL http://opg.optica.org/optica/abstract.cfm?URI=optica-7-10-1232.

[186] Fuchs, P., Jung, T., Kieschnick, M., Meijer, J. & Becher, C. A cavity-based optical antenna for color centers in diamond. *APL Photonics* **6**, 086102 (2021). URL https://doi.org/10.1063/5.0057161.

[187] Karamlou, A., Trusheim, M. E. & Englund, D. Metal-dielectric antennas for efficient photon collection from diamond color centers. *Opt. Express* **26**, 3341–3352 (2018). URL http://opg.optica.org/oe/abstract.cfm?URI=oe-26-3-3341.

[188] Hausmann, B. J. M. *et al.* Fabrication of diamond nanowires for quantum information processing applications. *Diamond and Related Materials* **19**, 621–629 (2010). URL https://www.sciencedirect.com/science/article/pii/S0925963510000312.

[189] Babinec, T. M. *et al.* A diamond nanowire single-photon source. *Nature Nanotechnology* **5**, 195–199 (2010). URL https://doi.org/10.1038/nnano.2010.6.

[190] Barth, M., Nüsse, N., Löchel, B. & Benson, O. Controlled coupling of a single-diamond nanocrystal to a photonic crystal cavity. *Opt. Lett.* **34**, 1108–1110 (2009). URL http://opg.optica.org/ol/abstract.cfm?URI=ol-34-7-1108.

[191] Knall, E. N. *et al.* Efficient source of shaped single photons based on an integrated diamond nanophotonic system. *arXiv:2201.02731* (2022).

[192] Aslam, N., Waldherr, G., Neumann, P., Jelezko, F. & Wrachtrup, J. Photo-induced ionization dynamics of the nitrogen vacancy defect in diamond investigated by single-shot charge state detection. *New Journal of Physics* **15**, 013064 (2013). URL https://doi.org/10.1088/1367-2630/15/1/013064.

[193] Chen, D. *et al.* Optical gating of resonance fluorescence from a single germanium vacancy color center in diamond. *Phys. Rev. Lett.* **123**, 033602 (2019). URL https://link.aps.org/doi/10.1103/PhysRevLett.123.033602.

[194] Pfaff, W. *et al.* Unconditional quantum teleportation between distant solid-state quantum bits. *Science* **345**, 532–535 (2014). URL https://www.science.org/doi/abs/10.1126/science.1253512.

[195] Rugar, A. E. *et al.* Narrow-linewidth tin-vacancy centers in a diamond waveguide. *ACS Photonics* **7**, 2356–2361 (2020). URL https://doi.org/10.1021/acsphotonics.0c00833.

[196] Aghaeimeibodi, S., Riedel, D., Rugar, A. E., Dory, C. & Vučković, J. Electrical tuning of tin-vacancy centers in diamond. *Phys. Rev. Applied* **15**, 064010 (2021). URL https://link.aps.org/doi/10.1103/PhysRevApplied.15.064010.

[197] De Santis, L., Trusheim, M. E., Chen, K. C. & Englund, D. R. Investigation of the Stark effect on a centrosymmetric quantum emitter in diamond. *Phys. Rev. Lett.* **127**, 147402 (2021). URL https://link.aps.org/doi/10.1103/PhysRevLett.127.147402.

[198] Neu, E. K. *Silicon vacancy color centers in chemical vapor deposition diamond: New insights into promising solid state single photon sources.* Ph.D. thesis, Universität des Saarlandes (2012).

[199] Becker, J. N. *Silicon Vacancy Colour Centres in Diamond: Coherence Properties and Quantum Control.* Ph.D. thesis, Universität des Saarlandes (2017).

[200] Clark, C. D., Kanda, H., Kiflawi, I. & Sittas, G. Silicon defects in diamond. *Phys. Rev. B* **51**, 16681–16688 (1995). URL https://link.aps.org/doi/10.1103/PhysRevB.51.16681.

[201] Collins, A. T., Allers, L., Wort, C. J. H. & Scarsbrook, G. A. The annealing of radiation damage in De Beers colourless CVD diamond. *Diamond and Related Materials* **3**, 932–935 (1994). URL https://www.sciencedirect.com/science/article/pii/0925963594903026.

[202] Dietrich, A. *et al.* Isotopically varying spectral features of silicon-vacancy in diamond. *New Journal of Physics* **16**, 113019 (2014). URL https://doi.org/10.1088%2F1367-2630%2F16%2F11%2F113019.

[203] Gorokhovsky, A. A., Turukhin, A. V., Alfano, R. R. & Phillips, W. Photoluminescence vibrational structure of Si center in chemical-vapor deposited diamond. *Applied Physics Letters* **66**, 43–45 (1995). URL https://doi.org/10.1063/1.114176.

[204] Allers, L. & Collins, A. T. Photoconductive spectroscopy of diamond grown by chemical vapor deposition. *Journal of Applied Physics* **77**, 3879–3884 (1995). URL https://doi.org/10.1063/1.358566.

[205] Rose, B. C. *et al.* Observation of an environmentally insensitive solid-state spin defect in diamond. *Science* **361**, 60–63 (2018). URL https://www.science.org/doi/abs/10.1126/science.aao0290.

[206] Zhang, Z.-H. *et al.* Optically detected magnetic resonance in neutral silicon vacancy centers in diamond via bound exciton states. *Phys. Rev. Lett.* **125**, 237402 (2020). URL https://link.aps.org/doi/10.1103/PhysRevLett.125.237402.

[207] Green, B. L. *et al.* Electronic structure of the neutral silicon-vacancy center in diamond. *Phys. Rev. B* **99**, 161112 (2019). URL https://link.aps.org/doi/10.1103/PhysRevB.99.161112.

[208] Neu, E., Agio, M. & Becher, C. Photophysics of single silicon vacancy centers in diamond: implications for single photon emission. *Opt. Express* **20**, 19956–19971 (2012). URL http://opg.optica.org/oe/abstract.cfm?URI=oe-20-18-19956.

[209] Turukhin, A. V., Liu, C.-H., Gorokhovsky, A. A., Alfano, R. R. & Phillips, W. Picosecond photoluminescence decay of Si-doped chemical-vapor-deposited diamond films. *Phys. Rev. B* **54**, 16448–16451 (1996). URL https://link.aps.org/doi/10.1103/PhysRevB.54.16448.

[210] Musale, D., Sainkar, S. & Kshirsagar, S. Raman, photoluminescence and morphological studies of Si- and N-doped diamond films grown on Si(100) substrate by hot-filament chemical vapor deposition technique. *Diamond and Related Materials* **11**, 75–86 (2002). URL https://www.sciencedirect.com/science/article/pii/S0925963501005210.

[211] Singh, S. & Catledge, S. A. Silicon vacancy color center photoluminescence enhancement in nanodiamond particles by isolated substitutional nitrogen on (100) surfaces. *Journal of Applied Physics* **113**, 044701 (2013). URL https://doi.org/10.1063/1.4783958.

[212] Beveratos, A., Brouri, R., Gacoin, T., Poizat, J.-P. & Grangier, P. Nonclassical radiation from diamond nanocrystals. *Phys. Rev. A* **64**, 061802 (2001). URL https://link.aps.org/doi/10.1103/PhysRevA.64.061802.

[213] Jantzen, U. *et al.* Nanodiamonds carrying silicon-vacancy quantum emitters with almost lifetime-limited linewidths. *New Journal of Physics* **18**, 073036 (2016). URL https://doi.org/10.1088/1367-2630/18/7/073036.

[214] Evans, R. E., Sipahigil, A., Sukachev, D. D., Zibrov, A. S. & Lukin, M. D. Narrow-linewidth homogeneous optical emitters in diamond nanostructures via silicon ion implantation. *Phys. Rev. Applied* **5**, 044010 (2016). URL https://link.aps.org/doi/10.1103/PhysRevApplied.5.044010.

[215] Bar-Gill, N., Pham, L. M., Jarmola, A., Budker, D. & Walsworth, R. L. Solid-state electronic spin coherence time approaching one second. *Nature Communications* **4**, 1743 EP – (2013). URL https://doi.org/10.1038/ncomms2771. Article.

[216] Medford, J. *et al.* Scaling of dynamical decoupling for spin qubits. *Phys. Rev. Lett.* **108**, 086802 (2012). URL https://link.aps.org/doi/10.1103/PhysRevLett.108.086802.

[217] Maity, S. *et al.* Coherent acoustic control of a single silicon vacancy spin in diamond. *Nature Communications* **11**, 193 (2020). URL https://doi.org/10.1038/s41467-019-13822-x.

[218] Maity, S. *et al.* Coherent coupling of mechanics to a single nuclear spin. *arXiv:2107.10961* (2021).

[219] Palyanov, Y. N., Kupriyanov, I. N., Borzdov, Y. M. & Surovtsev, N. V. Germanium: a new catalyst for diamond synthesis and a new optically active impurity in diamond. *Scientific Reports* **5**, 14789 (2015). URL https://doi.org/10.1038/srep14789.

[220] Palyanov, Y. N., Kupriyanov, I. N., Borzdov, Y. M., Khokhryakov, A. F. & Surovtsev, N. V. High-pressure synthesis and characterization of Ge-doped single crystal diamond. *Crystal Growth & Design* **16**, 3510–3518 (2016). URL https://doi.org/10.1021/acs.cgd.6b00481.

[221] Nahra, M. *et al.* Single germanium vacancy centers in nanodiamonds with bulk-like spectral stability. *AVS Quantum Science* **3**, 012001 (2021). URL https://doi.org/10.1116/5.0035937.

[222] Thiering, G. & Gali, A. The (eg ⊗ eu) ⊗ Eg product Jahn-Teller effect in the neutral group-IV vacancy quantum bits in diamond. *npj Computational Materials* **5**, 18 (2019). URL https://doi.org/10.1038/s41524-019-0158-3.

[223] Kumar, S. *et al.* Fluorescence enhancement of a single germanium vacancy center in a nanodiamond by a plasmonic Bragg cavity. *The Journal of Chemical Physics* **154**, 044303 (2021). URL https://doi.org/10.1063/5.0033507.

[224] Lühmann, T. *et al.* Charge-state tuning of single SnV centers in diamond. *ACS Photonics* **7**, 3376–3385 (2020). URL https://doi.org/10.1021/acsphotonics.0c01123.

[225] Rugar, A. E. *et al.* Quantum photonic interface for tin-vacancy centers in diamond. *Phys. Rev. X* **11**, 031021 (2021). URL https://link.aps.org/doi/10.1103/PhysRevX.11.031021.

[226] Shore, B. W. *Manipulating Quantum Structures Using Laser Pulses* (Cambridge University Press, 2011).

[227] Am-Shallem, M., Levy, A., Schaefer, I. & Kosloff, R. Three approaches for representing lindblad dynamics by a matrix-vector notation. *arXiv:1510.08634* (2015).

[228] Loudon, R. *The quantum theory of light* (Oxford University Press, 2000), 3 edn.

[229] Foot, C. J. *Atomic Physics* (Oxford University Press, 2005).

[230] Kambs, B. *Quantum frequency conversion of indistinguishable photons from independent solid state emitters.* Ph.D. thesis, Universität des Saarlandes (2019).

[231] Kambs, B. & Becher, C. Limitations on the indistinguishability of photons from remote solid state sources. *New Journal of Physics* **20**, 115003 (2018). URL https://doi.org/10.1088/1367-2630/aaea99.

[232] Morsch, R. *Erzeugung ununterscheidbarer Einzelphotonen mit Zinn-Fehlstellenzentren in Diamant.* Master's thesis, Universität des Saarlandes (2021).

[233] Brańkczyk, A. M. Hong-Ou-Mandel Interference. *arXiv:1711.00080* (2017).

[234] Wildfeuer, C. F., Lund, A. P. & Dowling, J. P. Strong violations of Bell-type inequalities for path-entangled number states. *Phys. Rev. A* **76**, 052101 (2007). URL https://link.aps.org/doi/10.1103/PhysRevA.76.052101.

[235] Knill, E., Laflamme, R. & Milburn, G. J. A scheme for efficient quantum computation with linear optics. *Nature* **409**, 46–52 (2001). URL https://doi.org/10.1038/35051009.

[236] Legero, T., Wilk, T., Kuhn, A. & Rempe, G. Time-resolved two-photon quantum interference. *Applied Physics B* **77**, 797–802 (2003). URL https://doi.org/10.1007/s00340-003-1337-x.

[237] Glauber, R. J. The quantum theory of optical coherence. *Phys. Rev.* **130**, 2529–2539 (1963). URL https://link.aps.org/doi/10.1103/PhysRev.130.2529.

[238] McHale, J. L. *Molecular Spectroscopy* (Boca Raton, 2017).

[239] Bylander, J., Robert-Philip, I. & Abram, I. Interference and correlation of two independent photons. *The European Physical Journal D - Atomic, Molecular, Optical and Plasma Physics* **22**, 295–301 (2003). URL https://doi.org/10.1140/epjd/e2002-00236-6.

[240] Meschede, D. *Wellenoptik* (Springer Spektrum, 2015).

[241] Lesik, M. *et al.* Perfect preferential orientation of nitrogen-vacancy defects in a synthetic diamond sample. *Applied Physics Letters* **104**, 113107 (2014). URL https://doi.org/10.1063/1.4869103.

[242] Rugar, A. E., Dory, C., Sun, S. & Vučković, J. Characterization of optical and spin properties of single tin-vacancy centers in diamond nanopillars. *Phys. Rev. B* **99**, 205417 (2019). URL https://link.aps.org/doi/10.1103/PhysRevB.99.205417.

[243] Mohtashami, A. & Koenderink, A. F. Suitability of nanodiamond nitrogen–vacancy centers for spontaneous emission control experiments. *New Journal of Physics* **15**, 043017 (2013). URL https://doi.org/10.1088%2F1367-2630%2F15%2F4%2F043017.

[244] Inam, F. A., Edmonds, A. M., Steel, M. J. & Castelletto, S. Tracking emission rate dynamics of nitrogen vacancy centers in nanodiamonds. *Applied Physics Letters* **102**, 253109 (2013). URL https://doi.org/10.1063/1.4812711.

[245] Arend, C., Becker, J. N., Sternschulte, H., Steinmüller-Nethl, D. & Becher, C. Photoluminescence excitation and spectral hole burning spectroscopy of silicon vacancy centers in diamond. *Phys. Rev. B* **94**, 045203 (2016). URL https://link.aps.org/doi/10.1103/PhysRevB.94.045203.

[246] Hizhnyakov, V., Boltrushko, V., Kaasik, H. & Sildos, I. Strong Jahn-Teller effect in the excited state: Anomalous temperature dependence of the zero-phonon line. *The Journal of Chemical Physics* **119**, 6290–6295 (2003). URL https://doi.org/10.1063/1.1603216.

[247] Hizhnyakov, V., Boltrushko, V., Kaasik, H. & Sildos, I. Phase relaxation in the vicinity of the dynamic instability: anomalous temperature dependence of zero-phonon line. *Journal of Luminescence* **107**, 351 – 358 (2004). URL http://www.sciencedirect.com/science/article/pii/S0022231303002035.

[248] Hizhnyakov, V., Kaasik, H. & Sildos, I. Zero-phonon lines: The effect of a strong softening of elastic springs in the excited state. *phys. stat. sol. (b)* **234**, 644–653 (2002). URL https://doi.org/10.1002/1521-3951(200211)234:2<644::AID-PSSB644>3.0.CO;2-E.

[249] Alkahtani, M. *et al.* Tin-vacancy in diamonds for luminescent thermometry. *Applied Physics Letters* **112**, 241902 (2018). URL https://doi.org/10.1063/1.5037053.

[250] Londero, E., Thiering, G., Razinkovas, L., Gali, A. & Alkauskas, A. Vibrational modes of negatively charged silicon-vacancy centers in diamond from ab initio calculations. *Phys. Rev. B* **98**, 035306 (2018). URL https://link.aps.org/doi/10.1103/PhysRevB.98.035306.

[251] Brand, J., Weinzierl, G. & Friedrich, J. Single mode electron-phonon coupling and optical lineshape analysis on a naphtalene x trap system. *J. Chem. Phys. Lett.* **84**, 197–200 (1981). URL https://doi.org/10.1016/0009-2614(81)85400-0.

[252] Plakhotnik, T., Doherty, M. W., Cole, J. H., Chapman, R. & Manson, N. B. All-optical thermometry and thermal properties of the optically detected spin resonances of the NV^- center in nanodiamond. *Nano Letters* **14**, 4989–4996 (2014). URL https://doi.org/10.1021/nl501841d.

[253] Deák, P., Aradi, B., Kaviani, M., Frauenheim, T. & Gali, A. Formation of NV centers in diamond: A theoretical study based on calculated transitions and migration of nitrogen and vacancy related defects. *Phys. Rev. B* **89**, 075203 (2014). URL https://link.aps.org/doi/10.1103/PhysRevB.89.075203.

[254] Pu, A., Avalos, V. & Dannefaer, S. Negative charging of mono-and divacancies in IIa diamonds by monochromatic illumination. *Diamond and Related Materials* **10**, 585–587 (2001). URL https://www.sciencedirect.com/science/article/pii/S0925963500004416.

[255] Slepetz, B. & Kertesz, M. Divacancies in diamond: a stepwise formation mechanism. *Phys. Chem. Chem. Phys.* **16**, 1515–1521 (2014). URL http://dx.doi.org/10.1039/C3CP53384K.

[256] Lühmann, T. *et al.* Screening and engineering of colour centres in diamond. *Journal of Physics D: Applied Physics* **51**, 483002 (2018). URL https://doi.org/10.1088/1361-6463/aadfab.

[257] Dobrinets, I. A., Vins, V. G. & Zaitsev, A. M. *HPHT-treated diamonds*, vol. 181 (Springer-Verlag Berlin Heidelberg, 2013). URL https://www.springer.com/gp/book/9783642374890.

[258] Davies, G., Lawson, S. C., Collins, A. T., Mainwood, A. & Sharp, S. J. Vacancy-related centers in diamond. *Phys. Rev. B* **46**, 13157–13170 (1992). URL https://link.aps.org/doi/10.1103/PhysRevB.46.13157.

[259] Clark, C. D., Ditchburn, R. W. & Dyer, H. B. The absorption spectra of irradiated diamonds after heat treatment. *Proceedings of the Royal Society of London. Series A, Mathematical and Physical Sciences* **237**, 75–89 (1956). URL http://www.jstor.org/stable/99989.

[260] Torelli, M. D. *et al.* High temperature treatment of diamond particles toward enhancement of their quantum properties. *Frontiers in Physics* **8** (2020). URL https://www.frontiersin.org/article/10.3389/fphy.2020.00205.

[261] Zaitsev, M. *Optical Properties of Diamond* (Springer, 2001).

[262] Kuruma, K. *et al.* Coupling of a single tin-vacancy center to a photonic crystal cavity in diamond. *Applied Physics Letters* **118**, 230601 (2021). URL https://doi.org/10.1063/5.0051675.

[263] Childress, L. *et al.* Coherent dynamics of coupled electron and nuclear spin qubits in diamond. *Science* **314**, 281–285 (2006). URL https://www.science.org/doi/abs/10.1126/science.1131871.

[264] Taminiau, T. H., Cramer, J., van der Sar, T., Dobrovitski, V. V. & Hanson, R. Universal control and error correction in multi-qubit spin registers in diamond. *Nature Nanotechnology* **9**, 171–176 (2014). URL https://doi.org/10.1038/nnano.2014.2.

[265] Vasconcelos, R. *et al.* Scalable spin-photon entanglement by time-to-polarization conversion. *npj Quantum Information* **6**, 9 (2020). URL https://doi.org/10.1038/s41534-019-0236-x.

[266] Lindner, N. H. & Rudolph, T. Proposal for pulsed on-demand sources of photonic cluster state strings. *Phys. Rev. Lett.* **103**, 113602 (2009). URL https://link.aps.org/doi/10.1103/PhysRevLett.103.113602.

[267] Schwartz, I. *et al.* Deterministic generation of a cluster state of entangled photons. *Science* **354**, 434–437 (2016). URL https://www.science.org/doi/abs/10.1126/science.aah4758.

[268] Kumar, P. Quantum frequency conversion. *Opt. Lett.* **15**, 1476–1478 (1990). URL http://opg.optica.org/ol/abstract.cfm?URI=ol-15-24-1476.

[269] Huang, J. & Kumar, P. Observation of quantum frequency conversion. *Phys. Rev. Lett.* **68**, 2153–2156 (1992). URL https://link.aps.org/doi/10.1103/PhysRevLett.68.2153.

Publications

Research articles

Articles resulting from research work discussed within this thesis

- J. Görlitz, D. Herrmann, P. Fuchs, T. Iwasaki, T. Taniguchi, D. Rogalla, D. Hardeman, P.-O. Colard, M. Markham, M. Hatano and C. Becher, "Coherence of a charge stabilised tin-vacancy spin in diamond", *arxiv, accepted for publication at npj quantum information,* 2110.05451 (2021).

- J. Görlitz, D. Herrmann, G. Thiering, P. Fuchs, M. Gandil, T. Iwasaki, T. Taniguchi, M. Kieschnick, J. Meijer, M. Hatano, A. Gali and C. Becher, "Spectroscopic investigations of negatively charged tin-vacancy centres in diamond", *New Journal of Physics* **22**, 013048 (2020).

Articles created during the course of my PhD which are not discussed within this thesis

- T. Jung, J. Görlitz, B. Kambs, C. Pauly, N. Raatz, R. Nelz, E. Neu, A. M. Edmonds, M. Markham, F. Mücklich, J. Meijer, and C. Becher, "Spin measurements of NV centers coupled to a photonic crystal cavity", *APL Photonics* **4**, 120803 (2019). **Invited article**

- C. Weinzetl*, J. Görlitz*, J. N. Becker*, I. A. Walmsley, E. Poem, J. Nunn, and C. Becher, "Coherent control and wave mixing in an ensemble of silicon vacancy centers in diamond", *Physical Review Letter* **122**, 063601 (2019).
*These authors contributed equally

- R. Nelz, J. Görlitz, D. Herrmann, A. Slablab, M. Challier, M. Radtke, M. Fischer, S. Gsell, M. Schreck, C. Becher, and E. Neu, "Toward wafer-scale diamond nano- and quantum technologies", *APL Materials* **7**, 011108 (2019).

Danksagung

Abschließend möchte ich an dieser Stelle all denjenigen Personen danken, die auf unterschiedlichste Art und Weise zum Gelingen dieser Arbeit beigetragen haben.

Zuvorderst möchte ich meinem Doktorvater Prof. Dr. Christoph Becher danken, der mich über die gesamte Dauer meiner Promotion gefördert und gefordert hat. Besonders erwähnenswert finde ich die immer offene Tür und die Bereitschaft auch vermeintlich kleinere und technische Problemstellungen ausgiebig zu diskutieren. Auch wenn ich die Arbeitsgruppe nun verlasse, freue ich mich auf die wegen Corona lange versprochenene und verschobene Gartenparty eingeladen zu werden.

Ein herzlicher Dank geht an Dr. Florian Kaiser, sowohl für die Begutachtung meiner Promotion als auch für die ausgiebige Diskussion hinsichtlich der Stabilisierung von elektrooptischen Amplitudenmodulatoren.

In diesem Sinne möchte ich mich bei der Vielzahl an wissenschaftlichen Kollaborationspartnern bedanken, die diese Arbeit überhaupt erst möglich gemacht haben. Innerhalb Deutschland waren das Michael Kieschnick im Speziellen und Jan Meijers Arbeitsgruppe im Allgemeinen, die immer einen Weg gefunden haben unsere vielzähligen Wünsche für Ionenimplantationen in einer sehr angenehmen Arbeitsatmosphäre und mit großem Know-How zu realisieren. Ein großes Dankeschön an euch! Im Bereich der hochenergetischen Ionenimplantation möchte ich mich herzlichst bei Detlef Rogalla und dem Team des RUBION dafür bedanken, dass wir Zinn tief genug in Diamant implantieren konnten um anschließend das sehr wichtige HPHT Ausheizen durchführen zu können.

Regarding the HPHT annealing, I would like to send a big thank you to Takayuki Iwasaki, Takashi Taniguchi and Mutsuko Hatano in Japan for providing the HPHT annealed sample NI58, which is the basis of about 90 % of the results obtained within this thesis. In the same run, thanks also to Element Six in the UK, especially to David Hardeman, Pierre-Olivier Colard and Matthew Markham for conducting the HPHT annealing on sample BOJO_001, a sample that I suspect to be of great importance in future work.

Being a group of experimentalists, it was very helpful to be in regular contact with Gergő Thiering and Adam Gali, the probably most frequented theoreticians in the field of G4V centres and beyond. I thank you very much for your valuable input and the time and effort spent on the long discussions we had.

Kommen wir also zu der hart arbeitenden Bevölkerung des E2.6: Ein großer Dank an Stefan Löw, der sich auch von solchen Kleinigkeiten wie dem regulären Renteneintritt nicht davon abbringen lässt weiter an die Uni zu kommen und unermüdlich an den komplexesten Schaltungen tüftelt. An der gesamten Uni gibt es keinen Mitarbeiter, der seine Arbeit so präzise und ausführlich dokumentiert und auch jahrzentealte Aufschriften auf Anhieb wiederfindet. Ein riesiges Dankeschön geht auch an die Mitarbeiter der Feinmechanikwerkstatt, die keine noch so wilde Solidworkszeichnung als unmachbar abtun und diese dann auch noch akkurat umsetzen. Ein ganz besonderer Dank geht an Peter Wagner, der seine Arbeit grundsätzlich früher fertigstellt als geplant und immer einen Ausweg parat hat, wenn sich doch

mal ein Denkfehler in der Solidworksdatei eingeschlichen hat. Genauso möchte ich Gereon Pink herausstellen, der nicht nur schnell und genau arbeitet sondern mit dem man auch gut feiern kann. Danke auch an Armin Seel, für das Kühlwasserlegen und das Anfertigen der enorm aufwändigen Schutzboxen um unsere optischen Aufbauten. Besonders herauszustellen sind die beiden Werkstattsleiter Titan Monostori und Michael Schmidt die den Laden am Laufen halten und gehalten haben. Ich danke der ganzen Werkstatttruppe für die Jahresabschlüsse bei euch unten, die immer ein absolutes Highlight waren!

Womit wir schließlich bei unserer Arbeitsgruppe angekommen wären. An allererster Stelle möchte ich mich bei Elke Huschens bedanken, die als unsere Sekretärin über den größten Teil meiner Promotion immer da war, für jedes Problem eine Lösung hatte und die Stimmung massiv aufgelockert hat mit ihrer gut gelaunt, spitzzüngigen Art. Wir vermissen dich alle, auch wenn wir dir deine Rente natürlich von Herzen gönnen. Liebe Nina Apfelbaum, auch dir danke ich vielmals für deinen riesigen Einsatz und die sehr angenehmen, herrlich fachfremden, Gespräche zwischendurch, sowie deine Bewerbungstipps.

In meiner Doktorarbeit hatte ich das Privileg drei herausragende Studenten zu betreuen: Hier möchte ich Marlon Schäfer für den großen Einsatz in seiner Bachelorarbeit danken, wenn auch von diesem themenfremden Einschub keine Messung den Weg in diese Arbeit finden konnte. Ein riesiges Dankeschön geht an meinen ehemaligen Masteranden Dennis Herrmann, dessen betriebener enormer Arbeitsaufwand manchmal aufgrund seiner unaufgeregten Art diesen zu präsentieren untergeht. Insbesondere Kapitel 4 würde ohne deinen sehr großen Beitrag anders aussehen und auch nach Abschluss deiner Masterarbeit habe ich sehr gern mit dir zusammen gearbeitet. Ich bin froh, dass mit dir ein engagierter Nachfolger bereitsteht, die noch ausstehende kohärente Kontrolle zu realisieren. Ich vermute fast, dass das noch zum Leeren einiger Fantaflaschen in Nachtschichten führen wird, daher ein weiser und vollkommen neuer Rat hier meinerseits: Das Leben ist eins der Schwierigsten! Mit Robert Morsch hatte ich das Vergnügen einen guten Freund nicht nur während der Bachelor- sondern auch der Masterarbeit anzuleiten. Das hat, was in meinen Augen absolut nicht selbstverständlich ist, enorm gut geklappt, wenn man von Scheren-BNC Kabel-Faserwitzen einmal absieht die mich fast zum Herzinfarkt geführt hätten. Ich danke dir für eine äußerst heitere Zeit im Labor und außerhalb, für Korrekturlesen der TPI Teile meiner Dissertation und generell dass de so e gudda Burschi bisch. Ich möchte dir hier noch etwas wirklich Wertvolles für den weiteren Lebensweg mitgeben: CHILL! hehe. Es macht Spaß euch beide, Dennis und Robert, in Aktion zu erleben sowohl zwischenmenschlich als auch wie ihr die Experimente im Labor voran treibt!

Ein großes Dankeschön auch an Philipp Fuchs, der einen großen Beitrag dazu geleistet hat, dass seit Beginn meiner Doktorarbeit die Zusammenarbeit und die Rücksichtsnahme innerhalb der Arbeitsgruppe deutlich intensiviert wurden. Danke auch für die unzähligen Probereinigungen, Implantations- und Ladungszyklusdiskussionen und das (nicht gänzlich altruistische ;-)) Erhalten des notwendigen Zuckerpegels der AG sowohl als Süßigkeitenlieferant als auch als Eintreiber mitzubringender Kuchen bei arbiträren Anlässen. Vielen Dank ebenfalls an Anna Fuchs, die sich selbst beim tausendsten aufgetauchten Problem wieder mit mir auf Dichtematrixmodelldiskussionen eingelassen hat! Außerdem danke ich dir für einen herrlichen Eselkalender, der lange Zeit die Wand unseres Büros geschmückt hat und die dazugehörigen Ausführungen die man in einem Büchlein “Eselwissen für alle Fälle” zusammenfassen könnte und die stets sehr zur Erheiterung beigetragen haben. Ein weiteres großes Dankeschön geht an Benjamin Kambs, von der fachlichen Seite her wegen der Einführung in dein TPI Modell, Teilbetreuung von Robert, Rat und Tat bei der Ausdehnung deines Modells auf unsere Experimente und das Korrekturlesen von Teilen der Arbeit. Abgesehen davon danke ich dir dafür, dass du ein uner-

müdlicher, äußerst kreativer Hutbauer und Verteidigungsvorbereiter bist (Der "Bell-Test" wird der Arbeitsgruppe noch lange in Erinnerung bleiben!!) und das auch in moralisch durchaus anspruchsvollen Situationen. Generell schätze ich deinen klaren Wertekompass, deine ruhige Art und deinen äußerst albernen Humor (Der Schubladentausch ist bis heute noch nicht zur Gänze verziehen :-P). Um das Thema Hutbauen und Verteidigungen aufzugreifen: Ein großes Dankeschön an Matthias Bock, der einer der maßgeblichen Antreiber war warum die Doktorhüte unserer AG einen legendären Status haben. Unabhängig von der Situation bist du geborenener Optimist ("Perfeeeeeekt"), zudem Joggingmotivator auf Konferenzen und Anstifter zu langen Abenden ("Gehsche ger?", "Mir würde aach noch e Runde trinken, awa ufs Haus!").

Bleiben wir also bei den Ehemaligen: Alexander Bommer alias Bombi, du bleibst in der AG unvergessen und ich persönlich verdanke dir vor allem anderen, dass du allzu große Euphorie meinerseits verhindert hast und mich damit auf die Schrecken der zweiten Phase der Promotion vorbereitet hast ;-). Abgesehen davon üben wir immer noch von Zeit zu Zeit für den Arbeitsgruppenchor und ich habe bis zum Schluss der Dissertation von deinen Powerpoint- und Originkniffen profitiert! Danke auch an Thomas Jung für die gute Zusammenarbeit zu Beginn meiner Promotion bei der Inbetriebnahme des Kryos, der uns doch einige Kopfschmerzen bereitet hat, und der Vermessung deiner photonischen Kristalle. Dein unerschütterlicher Optimismus ("Das wird super") ist mir in guter Erinnerung geblieben. Ebenfalls danke ich Richard Nelz und Elke Neu für die Geräteleihgaben wie Weißlichtlaser, Mikrowellenquellen und -komponenten als auch die vielen guten Gespräche (Elke) und netten Pöbeleien (Richard).

Um zurück zur aktuellen Besetzung zu kommen: Ein großes Dankeschön an Günther Marchand, der grundsätzlich bei allem hilft, ob das jetzt Reparatur von Wasserwächtern, Ernährungs- und Fitnesstips (Sonnenblumenkernhack mompf mompf) oder Albernheiten beim Mittagessen an der frischen Luft sind. Ähnlich hilfsbereit ist Tobias Bauer, ich danke dir sehr für dein kompromissloses Einspringen bei allem wo Not am Mann ist! Vielen Dank auch für die Motorisierung unserer Wellenplatten, Oszitipps und deine entspannte Art ("STREEEEEESS"). Finalement, je tiens à remercier Morgane Gandil, qui a apporté une contribution précieuse à la réalisation des expérimentations dans le chapitre 4. Merci beaucoup!

Es mag überraschen, aber die wenigsten Doktoranden überleben die Strapazen einer Promotion ohne ein gesundes soziales Umfeld unbeschadet. In meinem Fall möchte ich allen meinen Freunden die in dieser oftmals stressigen Phase für mich da waren danken. Besonders rauszustellen ist da wie so oft in meinem Leben Felix, den ich einfach unglaublich schätze und der grundsätzlich stets darauf bedacht ist, dass ich es nicht übertreibe, wobei er dabei mehr auf Arbeitsbelastung als auf Feiern abzielt. Ein dicker Bussi!

Abschließend will ich meiner gesamten Familie und der Familie meiner Frau Svea ein riesiges Danke aussprechen. In egal welcher Lebenslage seid ihr für mich da und ertragt auch einen gestressten und überarbeiteten Johannes. Vielen Dank liebe Katharina & Philipp & Merle und Lea & Fredo für euren Support reichend von Zuspruch, nützlichen "Chillaufrufen", Bekochung und Unterbringung in Notlagen. Ein ganz großer Dank geht an meine Eltern, Elke und Christoph, die für mich ein Riesenhalt im Leben sind und uns Kinder immer und bei allem unterstützen. Fühlt euch alle sehr fest von mir gedrückt. Zu guter Letzt geht meine innige Liebe und unfassbare Dankbarkeit an meine Frau Svea, die ein Rückhalt in belastenden Phasen ist, mit ihrer gelassenen Art einen perfekten Gegenpol zu mir bildet und bei der ich schlicht zu Hause bin. Ohne dich wäre diese Dissertation nicht möglich gewesen oder um es in der von dir vorgeschlagenen Kurzfassung meiner Danksagung zu formulieren: Ich danke meiner Frau.

Die Höhen und Tiefen dieser Promotion lassen sich abschließend in einem Zitat von Blaise Pascal zusammenfassen:

Die Natur hat Vollkommenheit, um zu zeigen, dass sie das Abbild Gottes ist und Mängel, um zu zeigen, dass sie nur das Abbild ist.

Danke!